The Physical Layer for Low Power Wide Area Networks: A Study of Combined Modulation and Coding Associated with an Iterative Receiver

Yoann Roth

Communauté
UNIVERSITÉ Grenoble Alpes

THÈSE

Pour obtenir le grade de

DOCTEUR DE LA COMMUNAUTÉ UNIVERSITÉ GRENOBLE ALPES

Spécialité : **Signal, Image, Parole, Télécoms**

Arrêté ministériel : 25 mai 2016

Présentée par

Yoann ROTH

Thèse dirigée par **Laurent Ros** et codirigée par **Jean-Baptiste Doré**

Préparée au sein du **CEA-LETI**

dans l'École Doctorale **d'Électronique, Électrotechnique, Automatique et Traitement du Signal (EEATS)**

The Physical Layer for Low Power Wide Area Networks: A Study of Combined Modulation and Coding Associated with an Iterative Receiver

Thèse soutenue publiquement le 10 juillet 2017, devant le jury composé de :

Pr. Michel JÉZÉQUEL
Professeur à Télécom Bretagne, Brest, président

Pr. Charly POULLIAT
Professeur à l'INP-ENSEEIHT, Toulouse, rapporteur

Pr. Didier LE RUYET
Professeur au CNAM, Paris, rapporteur

Pr. Stephan TEN BRINK
Professeur à l'université de Stuttgart, examinateur

Pr. Jean-Marc BROSSIER
Professeur à Grenoble-INP, examinateur

Dr. Guillaume VIVIER
Deputy CTO de Sequans Communications, examinateur

Dr. Laurent ROS
Maître de conférence HDR à Grenoble-INP, directeur de thèse

Dr. Jean-Baptiste DORÉ
Docteur-ingénieur de recherche CEA, encadrant

Mr. Vincent BERG
Ingénieur de recherche CEA, invité

En mémoire de ma maman,

Sylvie Havard
1954-2016

Acknowledgements

Cette première page est l'occasion pour moi de remercier les personnes sans qui ce travail n'aurait pas pu être mené à bout. La thèse est un long exercice parsemé d'embûches et de doutes, mais c'est aussi une expérience enrichissante en connaissances et en rencontres.

En premier lieu, je tiens à remercier Jean-Baptiste Doré pour son encadrement tout au long de ces trois années. Merci pour tes conseils, ta patience et ton expertise. Tu as toujours su m'aiguiller et trouver comment relancer ma motivation. Un merci également à Vincent Berg, qui a toujours pris le temps de suivre mon travail et a partagé ses précieuses connaissances techniques. Enfin, merci à Laurent Ros, qui a su parfaitement diriger cette thèse. Tu as toujours réussi à trouver le temps de t'intéresser à mon travail et su proposer des discussions pertinentes. Merci également pour tes relectures assidues de tout mon travail.

Je tiens également à remercier mon jury de thèse, le président Michel Jézéquel, les rapporteurs Charly Poulliat et Didier Le Ruyet, et les examinateurs Stephan Ten Brink, Jean-Marc Brossier et Guillaume Vivier, qui m'ont fait l'honneur de juger mon travail et qui ont tous su proposer des discussions très intéressantes.

Merci aussi à l'ensemble des équipes LCOI et LSHD du CEA Leti, qui m'ont accueillies tout au long de ces trois ans. Merci à tous les permanents, y compris Valerian, Mickaël, Benoît I, Valentin, Antonio, Patrick, Manu, Benoît II, François, Lionel, Xavier, Dimitri. Merci aussi aux non permanents, doctorants et stagiaires qui sont passés dans le labo, Elodie, Ludovic, Simon, Jimmy, Gourab, Truong, Tushar, Ioan, Quin, Baher, Minh, Jessica, Remun, Nicolas, Moises, et tout ceux que j'oublie. Merci à Robin, pour tes conseils et ta soif de partager tes connaissances. Grand merci à l'ancien bureau, Jérém et David, pour ces innombrables pauses cafés. Finalement, merci à mes deux derniers co-bureaux, Sylvie pour m'avoir laissé une place entre les cartons et Arturo pour ramener du bon café ! Merci aussi à Alexandre, Pierre et Marc qui m'ont accueillis dans leur bureau au Gipsa pour mes derniers mois de thèse.

Un autre merci à tout ceux qui m'entourent ou m'ont entouré, Nicolas et Julie, Robin, Denis, Azul, Cyril et Dany, Aurèle, mais aussi Megan et Bea. Merci aussi au groupe, Nathan, Mathieu, Sergio et Pierre, pour me permettre de profiter de faire de la musique et de me changer les idées. Merci aussi à ma famille qui m'a toujours soutenu : Thérèse et Bernard, Bertrand et Agnès, Isabelle et Michel, Annie et Philippe, et tout mes cousins et cousines. Merci à vous Gaël, Camille et Paul, Guillaume et Elena, et merci à toi mon papa pour ton soutien sans faille et pour m'avoir inspiré à poursuivre des études. Merci aussi à ma petite mamie dont je suis très fier. Enfin, merci à toi ma maman. Tu es partie bien trop vite et sans toi rien n'aurait été possible.

Last but not least, thank you, Rachel, for everything. Thanks for your patience during the redaction of my thesis and for your countless proofreadings. Spending time with you is always awesome and you are an amazing woman. I'm more than happy to plan on spending the rest of my life with you, I love you.

Abstract

More than 10% of the Internet-of-Things (IoT) connections are expected to be realized through Low Power Wide Area (LPWA) networks, representing several billions of connected devices. Several industrial solutions have been developed and a standardization process is ongoing. The low levels of sensitivity and low data rate required for the long range communication are achieved by the means of two strategies: a narrow-band strategy and a low spectral efficiency strategy. Considering the limits of the information theory, additional gains in the communication's energy efficiency can be achieved. Nonetheless, a trade-off between spectral efficiency and energy efficiency should always be made. Reliable transmission with high energy efficiency will necessarily result in poor spectral efficiency, and in comparison, a system with a higher spectral efficiency has to consume more energy to transmit the same amount of bits with the same arbitrary level of error.

This work considers the low spectral efficiency strategy. The combination of orthogonal modulations and a powerful channel code is studied. The scheme, so-called Turbo-FSK, associates the low spectral efficiency of Frequency Shift Keying (FSK) with the energy efficiency gain of a turbo receiver. Low levels of spectral efficiency can be achieved while optimizing the use of the available resource. The parameters of the scheme are optimized using a classic tool for iterative receivers, the EXtrinsic Information Transfer (EXIT) chart. Performance of Turbo-FSK compared to existing LPWA solutions demonstrates the potential of the proposed solution to achieve low levels of sensitivity and to outperform existing schemes. However, the restrictions on low levels of spectral efficiency reduces the number of possible applications for the scheme. By introducing a linear component in the alphabet and a puncturing procedure, flexibility in spectral efficiency is achieved. A large range of spectral efficiencies can be obtained while maintaining performance close to the channel capacity theoretical limit. Eventually, more practical scenarios are considered for evaluating the performance of the scheme. Frequency selective channels are considered and an encapsulation in a Fast Fourier Transform (FFT)-based system is implemented. Various indicators are studied and the Turbo-FSK scheme is compared to well-known technologies, such as schemes using Orthogonal Frequency Division Multiplexing (OFDM) associated with a powerful Forward Error Correction (FEC) scheme, namely Turbo Code (TC).

Résumé

Dans le contexte de l'Internet des Objets (IoT), on estime à plus de 10% la proportion de connexions réalisées via les réseaux longue portée bas débit, représentant ainsi plusieurs milliards d'objets connectés. Afin de satisfaire les exigences en termes de sensibilité et de réduction du débit, deux approches sont généralement envisagées : l'approche bande étroite, et l'approche faible efficacité spectrale. En comparant les performances des systèmes existants à la limite théorique issue de la théorie de l'information et démontrée par Shannon, on constate qu'un gain en performance est atteignable, tout en travaillant toujours à de faibles niveaux de sensibilité. La théorie de l'information permet d'affirmer qu'un compromis entre l'efficacité spectrale et l'efficacité énergétique doit toujours être fait. Ainsi, une haute efficacité énergétique s'obtiendra au détriment d'une efficacité spectrale faible. À l'inverse, un système fonctionnant à une haute efficacité spectrale devra utiliser plus d'énergie pour transmettre le même nombre de bits et atteindre le même taux d'erreur.

Ce travail s'intéresse à l'approche faible efficacité spectrale. En partant des modulations orthogonales, qui permettent d'atteindre la limite théorique de Shannon à des efficacités spectrales très faibles, et des processus turbo, qui atteignent d'excellentes performances à des efficacités spectrales élevées, l'utilisation conjointe d'une modulation orthogonale et d'un code correcteur associés à un récepteur itératif dans une technique dénommée Turbo-FSK est étudiée. Les différents paramètres de la technique sont optimisés en utilisant un outil classique des processus itératifs, l'Extrinsic Information Transfer (EXIT) chart. Les performances mesurées démontrent que la technique permet bien d'atteindre de très faibles niveaux de sensibilité et répond aux critères des réseaux longue portée bas débit. Cependant, la technique ne dispose de point de fonctionnement qu'à de très faibles valeurs d'efficacité spectrale : pour certaines applications ou si la portée nécessaire est réduite, il peut être bénéfique pour le système d'augmenter son efficacité spectrale. Ceci est rendu possible grâce à l'introduction d'une composante linéaire dans l'alphabet de modulation et d'un mécanisme de poinçonnage spécifique à la technique dans une version flexible appelée Coplanar Turbo-FSK. L'étude de l'influence des paramètres et des performances sur un canal à bruit blanc additif gaussien permet en effet de conclure sur la flexibilité de l'efficacité spectrale du système, tout en fonctionnant proche de la limite théorique. Finalement, l'étude jusqu'ici théorique est étendue à un contexte plus pratique, où des canaux sélectifs en fréquences sont considérés. Une encapsulation du système utilisant une architecture OFDM est considérée, et différentes mesures caractéristiques des systèmes de télécommunication sont évaluées. Les résultats sont confrontés à la solution Narrow-Band IoT proposée par l'organisme 3GPP et démontrent ici encore le potentiel de la solution Turbo-FSK pour les réseaux longue portée bas débit.

Résumé étendu

L'ambition de la cinquième génération de réseaux mobiles, la 5G, n'est pas que d'augmenter les débits atteignables, mais également d'offrir de nouvelles applications [2]. Une de ces applications est l'Internet des Objets (Internet-of-Things (IoT) en anglais) [3], qui vise à connecter une grande variété d'objets (capteurs, actionneurs, …) à l'Internet. On estime à plus de 25 milliards le nombre d'objets connectés à l'IoT [4]. Parmi ces nombreuses connexions, 10% d'entre elles se feront par les réseaux longue portée basse consommation (Low Power Wide Area (LPWA) en anglais) [6].

L'objectif des communications pour ce type de réseaux est d'atteindre une longue portée tout en conservant un émetteur (l'objet) peu complexe. La longue portée s'obtient en s'assurant que la technologie utilisée permet au récepteur de retrouver le paquet d'information même à de très faibles niveaux de sensibilité. Deux approches sont alors communément envisagées : l'approche bande étroite, où l'on minimise le bruit récupéré en considérant seulement une faible bande de fréquence pour le signal, et l'approche faible efficacité spectrale. Pour cette seconde approche, une technique courante est l'utilisation d'un facteur de répétition, qui permettra d'obtenir un gain de Rapport Signal-à-Bruit (RSB) au niveau du récepteur. L'efficacité spectrale peut également être réduite tout en augmentant l'efficacité énergétique du système en considérant l'utilisation d'un codage correcteur d'erreur.

Une autre technique étudiée ici concerne l'utilisation d'une modulation orthogonale. Pour ce type de modulation, l'efficacité spectrale décroît avec la taille de l'alphabet M tandis que l'efficacité énergétique augmente. Il est d'ailleurs possible de démontrer que ce type de modulation atteint la meilleure efficacité énergétique (i.e. l'énergie par bit minimum atteignable) possible pour une transmission fiable selon le théorème de la capacité de Claude Shannon [7] pour une taille d'alphabet infinie. Cette solution n'est cependant pas viable puisque l'efficacité spectrale tendrait également vers 0. Il est alors intéressant de considérer l'utilisation de codes concaténés décodés itérativement. Ces schémas, inventés au début des années 90 [8], permettent d'approcher la capacité du canal à haut rendement.

Cette thèse s'intéresse à l'utilisation conjointe de modulations orthogonales et d'un récepteur itératif dans le contexte des réseaux LPWA. En combinant les propriétés des deux techniques, on s'attachera à démontrer qu'il est possible d'obtenir de très faibles niveaux de sensibilité et d'optimiser l'efficacité de la ressource énergétique et spectrale. Ce résumé décrit le contenu du document, chapitre par chapitre.

1 Introduction aux réseaux longue portée bas débit

Afin d'assurer une longue portée pour la communication, le récepteur doit avoir une très faible sensibilité. La sensibilité est définie comme le niveau de puissance minimum nécessaire pour obtenir un taux d'erreur arbitraire. Elle est alors exprimée

$$(P_{\text{req}})^{\text{dBm}} = \text{RSB}_{\text{req}}^{\text{dB}} + 10\log_{10}(B) + 10\log_{10}\left(N_0 \cdot 10^3\right) + 10\log_{10}(F)\,. \tag{1}$$

où $\text{RSB}_{\text{req}}^{\text{dB}}$ est le RSB (exprimé en dB) requis pour obtenir le niveau d'erreur considéré, B est la bande (en Hz), N_0 la densité spectrale de puissance du bruit et F le facteur de bruit du récepteur. Alors que la valeur de N_0 dépend de la température et que le facteur de bruit dépend de la conception du récepteur, on voit apparaître les deux approches possible afin de réduire la sensibilité :

- Réduire la bande B du signal ;
- Réduire le niveau de fonctionnement en RSB, grâce à des algorithmes de réception avancés.

La première approche revient à utiliser des signaux à bande étroite. C'est notamment la stratégie choisie par la société Sigfox [46]. Même si le niveau de RSB nécessaire pour le taux d'erreur considéré reste élevé, la faible bande permet d'obtenir des faibles niveaux de sensibilité. Cependant, d'autres problématiques apparaissent, comme la détection du signal (les conséquences d'une faible erreur en fréquence peuvent être très négatives) ou la longue durée nécessaire pour émettre un paquet d'information de taille donnée. La seconde approche considère une réduction du niveau

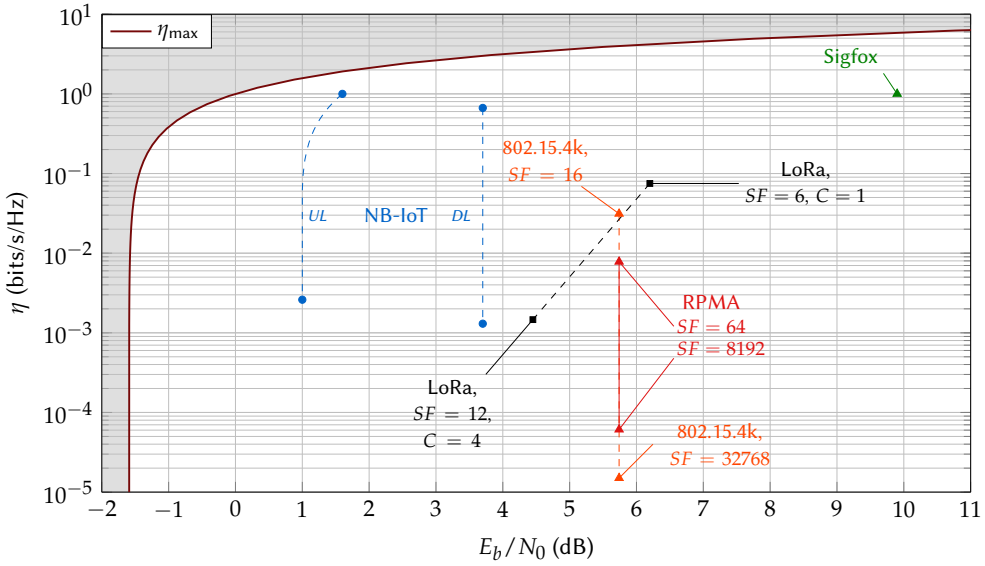

FIGURE 1 – *Efficacité spectrale versus E_b/N_0 requis pour obtenir un TEB de 10^{-5}. Différentes solutions dédiées aux réseaux LPWA sont représentées ainsi que l'efficacité spectrale maximum atteignable telle que donnée par l'équation* (2).

de bruit nécessaire pour le taux d'erreur considéré. Une technique couramment utilisée est le facteur de répétition. Ainsi, répéter λ fois le signal permet un gain de traitement égal à $10 \cdot \log_{10}(\lambda)$ dB au niveau du récepteur. Cette répétition se fait au détriment d'une réduction du débit d'un même facteur λ, réduisant donc l'efficacité spectrale de la technique. D'autres techniques peuvent également être envisagées telle que l'utilisation d'un codage canal, qui réduit le débit mais également le niveau de rapport de l'énergie d'un bit sur la densité spectrale de puissance du bruit, noté E_b/N_0 et appelé RSB d'un bit, nécessaire pour un même taux d'erreur.

Contrairement à l'utilisation d'un codage canal, l'utilisation de la répétition seule ne permet pas d'augmenter l'efficacité énergétique du système, qui est inversement proportionnelle à E_b/N_0. Claude Shannon a défini le débit maximum atteignable (appelé capacité) pour un canal de transmission [7]. On peut déduire de cette limite le E_b/N_0 minimum atteignable pour une efficacité spectrale donnée, ou inversement du niveau maximum d'efficacité spectrale atteignable pour un E_b/N_0 donné. Cette efficacité spectrale maximum, notée η_{max}, s'exprime

$$\eta_{max} = \log_2\left(1 + \frac{E_b}{N_0} \cdot \eta_{max}\right). \tag{2}$$

Le E_b/N_0 minimum, noté $(E_b/N_0)_{min}$, s'exprime lui

$$\left(\frac{E_b}{N_0}\right)_{min} = \frac{2^{\eta} - 1}{\eta}, \tag{3}$$

où η est l'efficacité spectrale considérée. Un système avec un point de fonctionnement proche de ces valeurs maximum utilise d'une façon efficace la ressource énergétique et spectrale.

On s'intéresse à plusieurs solutions dédiées aux réseaux LPWA. 4 solutions sont étudiées : Sigfox, basée sur des signaux bande étroite [46] ; LoRa, basée des modulations orthogonales [47, 48] ; RPMA, basée sur le standard 802.15.4K [52, 54] qui utilise le facteur de répétition, et la standardisation (en cours) faite par le 3rd Generation Partnership Project (3GPP), le Narrow-Band IoT (NB-IoT) [56, 57], qui utilise un Turbo Code (TC). Pour chacune des solutions, la technologie utilisée est implémentée dans un modèle Matlab qui va permettre d'estimer le E_b/N_0 nécessaire afin d'obtenir un Taux d'Erreur Binaire (TEB) égal à 10^{-5}. Les différentes technologies fonctionnent à des niveaux d'efficacité spectrale divers, puisqu'elles considèrent différentes approches.

Sur la Figure 1, on représente l'efficacité spectrale en fonction du E_b/N_0 requis pour toutes les technologies. L'efficacité spectrale maximum atteignable en fonction de E_b/N_0 donnée par l'équation (2) est également représentée. Pour les technologies proposant différents modes de fonctionnement, on représente le mode avec l'efficacité spectrale maximum et le mode avec l'efficacité spectrale minimum. On constate que la technologie Sigfox, puisqu'elle adopte l'approche bande étroite, se distingue clairement des autres solutions. Le NB-IoT s'approche de plus de la limite, grâce à l'utilisation du TC. Les autres solutions sont plus éloignées de la limite.

Ces résultats montrent que les technologies actuelles qui utilisent la deuxième approche (réduire l'efficacité spectrale afin d'obtenir de faibles niveaux de sensibilité) tendent à être toujours à plusieurs dB de la limite donnée

par Shannon. Il serait préférable d'utiliser une technologie qui permettrait à la fois de réduire l'efficacité spectrale mais aussi de se rapprocher de la limite. Ceci est obtenu grâce à la technique proposée dans ce travail, dénommée Turbo-FSK.

2 La technique Turbo-FSK

La technique Turbo-FSK repose sur l'utilisation d'une modulation orthogonale associée à un codage correcteur. Les modulations orthogonales ont pour propriété d'avoir une efficacité spectrale décroissante avec la taille de l'alphabet M tandis que l'efficacité énergétique augmente. Lorsque M tend vers l'infini, on peut montrer que ce type de modulation atteint la capacité de Shannon [15]. En utilisant un codage correcteur basé sur un récepteur itératif, on s'approche de la capacité tout en utilisant des tailles d'alphabet raisonnables.

Le chapitre décrit d'abord les réflexions ayant menées à la mise au point de la technique. Entre autres, la technologie Turbo-Hadamard [65] reposant sur le même principe (mais utilisant un alphabet orthogonal par codes binaires) est présentée. Pour le contexte des réseaux LPWA, l'utilisation d'une modulation à enveloppe constante se révèle très bénéfique à la fois pour la consommation de l'émetteur mais aussi pour le coût de l'amplificateur de puissance en bout de chaine de transmission. La modulation de fréquence Frequency Shift Keying (FSK) est alors considérée.

La technique Turbo-FSK en elle-même est ensuite présentée. Le transmetteur est basé sur la combinaison d'un code convolutif, l'accumulateur, et d'une modulation orthogonale de taille M, la FSK. L'ajout du code convolutif permet de relier les mots de code consécutifs entre eux, et ainsi de générer une structure dans la séquence émise qui pourra être utilisée par un processus probabiliste au niveau du récepteur. Cette structure peut se représenter grâce à un treillis. Le transmetteur génère λ séquences représentant toutes le même paquet d'information de taille Q, mais avec différentes fonctions d'entrelaçement. Le récepteur Turbo-FSK est ensuite décrit. Les vraisemblances de tout les mots de code des λ séquences sont calculées, puis utilisées comme métrique dans le treillis. Pour chaque séquence et en utilisant l'information *a priori* provenant du décodage des autres séquences, le décodeur turbo utilise l'algorithme du BCJR (du nom des inventeurs, Bahl, Cocke, Jelinek et Rajiv [31]) afin de calculer les probabilités *a posteriori*. Les développements mathématiques des expressions du récepteur sont présentées, ainsi que l'architecture du récepteur. Ce dernier peut se décomposer comme une tête de réception réalisant la détection des symboles FSK et d'un turbo décodeur. Les échanges d'information extrinsèques entre le décodage des différentes séquences sont également décrits mathématiquement, puis une version sous optimale de l'algorithme de décodage, basée sur l'approximation max-log, est présentée. Les performances de la Turbo-FSK sont ensuite présentées. Une architecture alternative du récepteur est étudiée, et permet de conclure sur la nécessité pour le décodeur d'utiliser la métrique "orthogonal" lors du décodage du treillis (alors qu'une métrique binaire peut être envisagée). Aussi, la technique dispose de trois paramètres : la taille d'alphabet M, le nombre de répétitions λ et la taille d'entrelaceur Q (qui est égale à la taille du bloc d'information). L'évolution des performances en fonction des paramètres révèle une dépendance non triviale. Ainsi, une optimisation des paramètres en fonction de l'efficacité énergétique est envisagée.

Afin d'optimiser les paramètres de la technique, un outil d'analyse des processus itératif, l'EXtrinsic Information Transfer (EXIT) chart, est utilisé. Il permet d'observer les échanges d'information dans le décodeur et de prédire son comportement pour un certain niveau de bruit. Il est également possible de déterminer le seuil du décodeur, i.e. le niveau de E_b/N_0 minimum nécessaire pour qu'un décodage correct soit possible. L'outil est présenté en annexe Appendix D, et son adaptation à la technique Turbo-FSK est étudiée. L'interprétation de l'outil est expliquée, et une évaluation des performances asymptotiques est réalisée. Pour chaque couple de paramètres M et λ, le seuil du récepteur est déterminé. D'après les résultats, le couple de paramètres qui permet de minimiser le E_b/N_0 correspond à $M = 512$ et $\lambda = 3$.

L'analyse est ensuite étendue à des configurations où la taille de bloc est égale à 1000 bits. Les performances Turbo-FSK en terme de TEB sont estimées et permettent de constater qu'une perte moyenne de 1dB est subie à cause de la réduction de la taille de bloc. Les performances sont ensuite comparées à la limite de Shannon. Avec la configuration optimale, les performances asymptotiques de la Turbo-FSK se trouvent à moins de 0.29dB de la limite de Shannon. En considérant une taille de bloc de 1000 bits, la Turbo-FSK avec les paramètres optimaux est à 1.35dB de la limite. Finalement, les performances sont comparées à des schémas de transmission existant. Trois techniques sont sélectionnées : le standard 802.15.4k [52], utilisé par la technologie RPMA ; une solution reposant sur le principe de la technologie LoRa [51], et enfin le NB-IoT [56, 59], qui est en cours de standardisation. Cette dernière technologie repose sur l'utilisation d'un turbo code. Chacune des techniques est paramétrée afin que l'efficacité spectrale soit la même pour toutes les techniques. Le Taux d'Erreur Paquet (TEP) en fonction du RSB est représenté sur la Figure 2, sous l'hypothèse d'un canal à Bruit Blanc Additif Gaussien (BBAG). On constate que les solutions turbo codée (Turbo-FSK et NB-IoT) nécessitent des taux de RSB plus faibles pour atteindre un même niveau de TEP, comparé aux autres solutions. La Turbo-FSK avec ces paramètres permet un gain additionnel de 1dB par rapport au NB-IoT, pour un TEP de 10^{-2}.

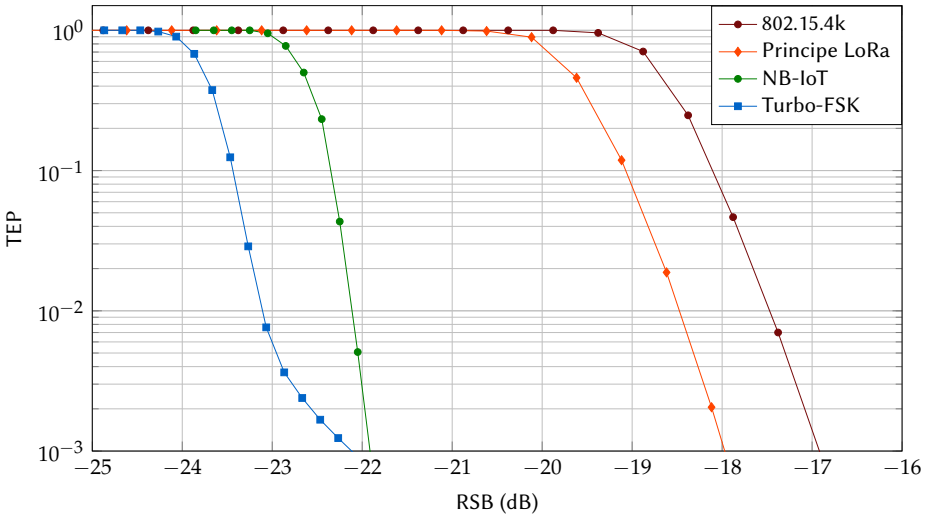

FIGURE 2 – *Performance en TEP des solutions comparées, sous l'hypothèse d'un canal BBAG.*

La technique Turbo-FSK répond aux contraintes de la couche physique des réseaux LPWA. Le système a été optimisé et permet d'obtenir des gains en niveaux de sensibilité par rapport aux solutions existantes, tout en offrant une enveloppe constante. Toutefois, le système tel que conçu ne permet que d'atteindre des efficacités spectrales faibles. Une généralisation de la technique est alors étudiée.

Les travaux de ce chapitre ont été publiés dans le journal *Elsevier Compte Rendu de Physique* [83]. La technique Turbo-FSK a été présentée à SPAWC'15 [84], et l'optimisation à ISTC'16 [86]. La comparaison à l'état de l'art a été présentée à CROWNCOM'16 [85].

3 Augmentation de la flexibilité de l'efficacité spectrale

Avoir une efficacité spectrale flexible permet à une technique de correspondre à un plus large nombre d'applications. Dans ce sens, on s'intéresse dans ce chapitre à étudier des techniques permettant d'augmenter l'efficacité spectrale de la Turbo-FSK tout en conservant de bonnes performances. Pour ce faire, deux techniques sont intégrées au système : l'utilisation d'une modulation différente et l'introduction d'un mécanisme de poinçonnage.

Une nouvelle modulation, mélangeant modulations orthogonale et linéaire, est présentée. Elle repose sur l'utilisation d'une totalité de $N_\perp$ sous-espaces orthogonaux, où dans chaque ensemble se trouvent N_L symboles complexes. Il y a au total $M = N_L N_\perp$ symboles. Les N_L symboles d'un même sous-espace appartiennent donc au même plan complexe, tandis que des symboles de deux sous-espaces distincts sont orthogonaux. Cette modulation, appelée Orthogonal with Coplanar Subsets (OCS) modulation, mélange les propriétés des modulations orthogonales et des modulations linéaires, autant au niveau des performances que de l'efficacité spectrale. La définition de la modulation est indépendante du choix de la modulation orthogonale et de la modulation linéaire. Le calcul de la vraisemblance d'un symbole est présenté, et quelques performances sont proposées. L'analyse de la modulation n'est pas approfondie car on s'intéresse surtout à son utilisation dans le contexte Turbo-FSK.

La Turbo-FSK est généralisée au principe de la Coplanar Turbo-FSK, qui utilise une modulation OCS où la modulation orthogonale est choisie comme étant de la FSK et la modulation linéaire est une modulation de phase, la Phase Shift Keying (PSK). On s'assure ainsi de conserver une enveloppe constante. Le transmetteur est d'abord présenté, notamment le mécanisme de poinçonnage. Afin de conserver les propriétés de la technique, il est nécessaire de poinçonner des mots binaires entiers (contrairement aux techniques classiques où les bits sont poinçonnés un à un). Ainsi, le poinçonnage réduit globalement le nombre de symboles de modulation OCS transmis. Le taux de poinçonnage est noté R_p. Le treillis est également introduit. A l'instar de la Turbo-FSK, où toutes les branches du treillis sont orthogonales entre elles, certaines branches ne sont plus orthogonales dans le cas de la Coplanar Turbo-FSK. L'association des mots de codes de l'alphabet aux branches du treillis aura donc une influence sur les performances. Le récepteur Coplanar Turbo-FSK est finalement présenté, réutilisant la vraisemblance de la modulation OCS calculée auparavant. L'architecture du récepteur est présentée, montrant notamment les étapes supplémentaires requises par l'ajout des deux fonctionnalités.

La Coplanar Turbo-FSK dispose d'un certain nombre de degrés de liberté : le choix de l'association des mots de code sur le treillis ; le nombre de sous-espaces orthogonaux $N_\perp$; la taille de la modulation linéaire N_L ; le nombre

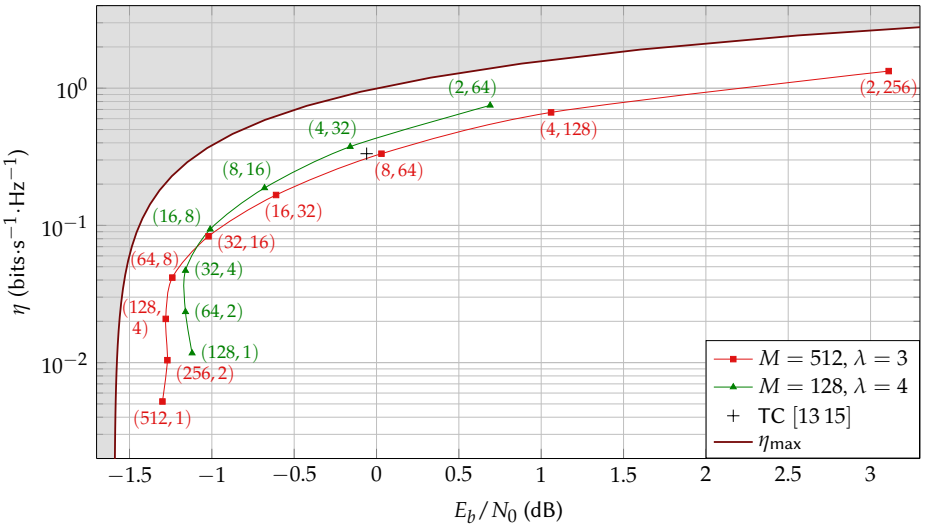

FIGURE 3 – *Efficacité spectrale versus E_b/N_0 de seuil pour différentes valeurs de M et λ, et pour différentes combinaisons de $N_\perp$ et N_L. L'efficacité spectrale maximum atteignable telle que donnée par l'équation* (2) *est également représentée.*

d'étages du transmetteur λ et le taux de poinçonnage R_p. Étant donné qu'une optimisation en prenant en compte tout les paramètres se révèle difficilement réalisable, on choisit d'étudier seulement certains aspects de la technique. L'influence du choix de l'association des symboles sur le treillis est étudiée, et montre qu'il est préférable de conserver un certain ratio d'orthogonalité entre les transitions du treillis. L'utilisation d'une modulation linéaire différente, où une variation d'amplitude est possible, est envisagée, mais les résultats montrent que la modulation PSK mène à de meilleurs résultats dans la majorité des configurations. L'étude du poinçonnage montre la perte en performance associée à l'augmentation de l'efficacité spectrale, mais également qu'il est possible de jouer sur le taux de poinçonnage pour réduire le plancher d'erreur des performances. Enfin, la confrontation des performances du système à la limite de Shannon montre bien la capacité de la Coplanar Turbo-FSK à rester proche de la limite tout en proposant une plus large gamme d'efficacités spectrales. Sur la Figure 3, les seuils du décodeur pour différentes tailles d'alphabets et différentes valeurs de λ sont représentés avec l'efficacité spectrale maximum atteignable. Différentes combinaisons de tailles de modulation orthogonale et de modulation linéaire sont représentées. Sur la courbe, les couples $(N_\perp, N_L)$ sont indiqués. On voit qu'il est possible d'augmenter l'efficacité spectrale et de conserver de bonnes performances, proches de la capacité de Shannon.

L'introduction d'un nouvel alphabet de modulation et d'un mécanisme de poinçonnage permet bien d'augmenter l'efficacité spectrale du système. Les performances restent proches de la capacité de Shannon. Cependant, l'analyse du système se révèle complexe. Ainsi, il est possible qu'une configuration offrant de meilleures performances comparées à la Turbo-FSK existe.

La technique Coplanar Turbo-FSK a été breveté [88]. Elle est également le sujet d'un article prochainement soumis [87].

4 Comparaison avec les solutions existantes

Dans les études et comparaisons réalisées jusqu'à présent, des scénarios très théoriques étaient envisagés, comme l'utilisation du canal BBAG. Dans ce chapitre, on cherche à étudier les techniques présentées (Turbo-FSK et Coplanar Turbo-FSK) dans des scénarios plus proches de conditions pratiques. On considère notamment la simulation de canaux sélectifs en fréquence, où encore l'implémentation d'approximations pour le récepteur.

Afin de comparer les systèmes dans des conditions équitables, on considère la même implémentation dans une architecture Orthogonal Frequency Division Multiplexing (OFDM), i.e. basée sur un transmetteur utilisant une Inverse Fast Fourier Transform (IFFT) et un récepteur utilisant une Fast Fourier Transform (FFT). Trois systèmes, utilisant tous le même turbo code, sont choisis pour comparaison : le Turbo Coded Orthogonal Frequency Division Multiplexing (TC-OFDM), le Turbo Coded Single Carrier Frequency Division Multiple Access (TC-SC-FDMA) et la Turbo Coded Frequency Shift Keying (TC-FSK). Deux différentes versions de la Turbo-FSK sont considérées : la Coplanar Turbo-FSK, et la Coplanar Turbo-ZC, une variante où l'alphabet orthogonal est construit à partir de séquences à enveloppe constantes, les séquences de Zadoff-Chu (ZC). Tous les systèmes sont présentés, depuis la technique de construction du signal émis jusqu'à l'architecture du démodulateur/décodeur. Le calcul de la vraisemblance est d'abord présenté pour le cas général du système OFDM, et la formule exacte pour chaque technique en est déduite.

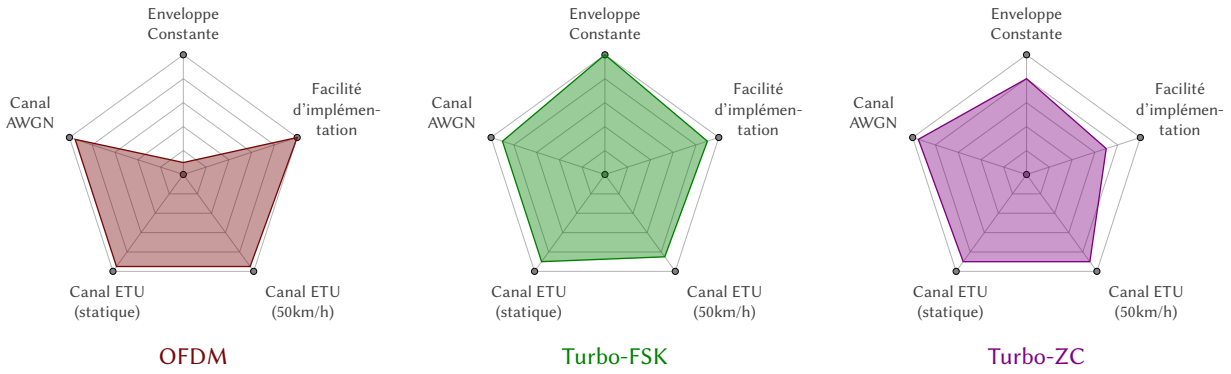

FIGURE 4 – *Performance des schémas comparés pour un scénario bas débit.*

Afin d'analyser les performances des différentes techniques, deux scénarios sont considérés. Le premier scénario est dit bas débit, car le débit binaire de chacune des techniques est égal à 8kbps. Le deuxième scénario est dit haut débit avec 46kbps. À chaque scénario sont associés différents paramètres pour chacune des modulations. On s'assure cependant que l'efficacité spectrale est la même pour toutes les techniques lorsqu'un scénario est considéré. On suppose également une synchronisation et estimation de canal parfaites. Plusieurs éléments sont alors étudiés. Les variations de l'enveloppe sont mesurées grâce à l'Instantaneous-to-Average Power Ratio (IAPR), qui donne le rapport de puissance instantanée sur la puissance moyenne du signal. On retrouve bien que les techniques utilisant la FSK ont une enveloppe constante. La technique TC-OFDM démontre les plus grandes variations d'amplitudes, un effet connu pour cette modulation. Les performances sous canal BBAG sont également étudiées. Pour ce canal, certaines techniques sont équivalentes, et la technique TC-OFDM offre les meilleures performances, même si la Turbo-FSK présente des performances comparables (à environ 0.2dB). Les canaux sélectifs en fréquence sont ensuite étudiés. On considère le cas statique et le cas où le transmetteur et le récepteur bougent l'un par rapport à l'autre. Dans le cas statique, la technique TC-OFDM offre les meilleures performances grâce à sa diversité spectrale. Les techniques Coplanar Turbo-FSK et Coplanar Turbo-ZC ont des performances comparables à la TC-OFDM. Lorsqu'une taille plus importante de modulation linéaire N_L est considérée, on constate que l'utilisation d'une modulation à base de séquences ZC permet de mieux utiliser la diversité spectrale par rapport à la modulation FSK. En cas de mobilité, la redondance offerte par toutes les techniques permet de s'approcher des performances TC-OFDM. Ici encore, la modulation Coplanar Turbo-ZC offre des performances plus intéressantes que la Coplanar Turbo-FSK. Finalement, la complexité des différentes techniques est estimée grâce aux expressions mathématiques du récepteur. Les quantités d'additions et de multiplications de chaque technique sont comparées à celles de la TC-OFDM. On constate alors que dans le scénario bas débit, la Turbo-FSK n'implique que 20% d'augmentation de complexité par rapport à la TC-OFDM. En revanche, lorsque la taille d'alphabet M augmente, l'augmentation de complexité devient très importante. Les résultats des comparaisons sont synthétisés dans des représentations à cinq axes. La comparaison entre TC-OFDM, Turbo-FSK et Turbo-ZC pour le scénario bas débit est représentée Figure 4. On constate que la Turbo-FSK permet d'obtenir des performances relativement proches de la TC-OFDM tout en offrant une enveloppe constante. La Turbo-ZC reste une alternative intéressante de part sa résistance dans les canaux sélectifs en fréquences et lorsque des tailles de modulation linéaire importantes sont considérées.

La comparaison dans des conditions plus proches des systèmes pratiques permet encore une fois d'avoir un aperçu du potentiel de la technique Turbo-FSK. Son enveloppe constante offre un bénéfice majeur car cela réduit les contraintes de sélection de l'amplificateur présent en fin de chaine de transmission. Toutefois, l'étude pourrait être étendue à des cas où la synchronisation du système est considérée, et où l'estimation du canal est effectivement réalisée.

Les travaux de ce chapitre vont être présentés dans un article en cours de préparation [100]. Par ailleurs, un implémentation sur composants bas coûts à été réalisée, permettant de conclure sur la viabilité de la technique Turbo-FSK même en considérant des architectures à faibles capacités de calculs [101].

CONCLUSION

Obtenir de faibles niveaux de sensibilité est crucial pour obtenir la longue portée des réseaux LPWA. Un faible débit de donnée doit être considéré, et deux approches sont généralement envisagées : l'approche bande étroite et l'approche faible efficacité spectrale. Les travaux présentés dans cette thèse concernent la seconde approche. Grâce à une combinaison de modulation orthogonale, code convolutif, répétition et décodage itératif, un système

fonctionnant à efficacité énergétique proche de la limite définie par Shannon a été proposé. De faibles niveaux de sensibilité peuvent alors être obtenus. La technique a été optimisée, comparée aux solutions existantes, puis améliorée pour atteindre une plus grande plage d'efficacités spectrales. La comparaison à des systèmes sophistiqués tel que la TC-OFDM démontre que la solution permet bien de répondre aux contraintes de ce type de réseaux, même lorsque des canaux sélectifs en fréquence sont considérés, tout en répondant également à certains critères de mise en œuvre comme la propriété d'enveloppe constante. Cette propriété est particulièrement intéressante dans le contexte de l'IoT, où la consommation énergétique de l'objet doit être optimisée.

Publications

Patents

- **"Transmission/Reception System Based on the Use of a Joint Orthogonal and Linear Modulation"**
  "Système d'émission/réception utilisant une modulation conjointe orthogonale-linéaire"
  Filed in March 2017

International Journal Communications

- **"Turbo-FSK, a Physical Layer for Low-Power Wide-Area Networks: Analysis and Optimization"**
  Yoann Roth, Jean-Baptiste Doré, Laurent Ros and Vincent Berg
  Elsevier Comptes Rendus Physique, 2017.
  www.sciencedirect.com/science/article/pii/S163107051630158X
- **"Coplanar Turbo-FSK: a Flexible and Power Efficient Modulation for the Internet-of-Things"**
  Yoann Roth, Jean-Baptiste Doré, Laurent Ros and Vincent Berg
  To be submitted, 2017.

International Conference Communications

- **"Turbo-FSK: A New Uplink Scheme for Low Power Wide Area Networks"**
  Yoann Roth, Jean-Baptiste Doré, Laurent Ros and Vincent Berg
  2015 IEEE 16th International Workshop on Signal Processing Advances in Wireless Communications (SPAWC), Stockholm, Sweden, 2015.
- **"A Comparison of Physical Layers for Low Power Wide Area Networks"**
  Yoann Roth, Jean-Baptiste Doré, Laurent Ros and Vincent Berg
  11th EAI International Conference on Cognitive Radio Oriented Wireless Networks (Crowncom), Grenoble, France, 2016.
- **"EXIT Chart Optimization of Turbo-FSK: Application to Low Power Wide Area Networks"**
  Yoann Roth, Jean-Baptiste Doré, Laurent Ros and Vincent Berg
  9th International Symposium on Turbo Codes & Iterative Information Processing 2016 (ISTC'16), Brest, France, 2016.
- **"Implementation and Analysis of a Turbo-FSK Transceiver for a New Low Power Wide Area Physical Layer"**
  Jérémy Estavoyer, Yoann Roth, Jean-Baptiste Doré and Vincent Berg
  2016 International Symposium on Wireless Communication Systems (ISWCS): Special sessions (ISWCS'2016 - Special sessions), Poznan, Poland, 2016.
- **"Contenders for Low Power Wide Area Network in OFDM Frameworks"**
  Yoann Roth, Jean-Baptiste Doré, Laurent Ros and Vincent Berg
  To be submitted, 2017.

French Conference Communications

- **"Turbo-FSK : une nouvelle technique de communication montante pour les réseaux longue portée basse consommation"**
  Yoann Roth, Jean-Baptiste Doré, Laurent Ros and Vincent Berg
  Colloque Gretsi, Lyon, France, Sept. 2015.
- **"Nouvelle technique de communication pour les réseaux longue portée basse consommation : optimisation et comparaison"**
  Yoann Roth, Jean-Baptiste Doré, Laurent Ros and Vincent Berg
  Journées scientifiques de l'URSI 2016, Rennes, France, Avril 2016.

Contents

List of Figures

List of Tables

List of Acronyms

2G · second generation

3GPP · 3rd Generation Partnership Project

3G · third generation

4G · fourth generation

5G · fifth generation

ADC · Analog-to-Digital Converter

APP · *A Posteriori* Probability

APSK · Amplitude Phase-Shift Keying

AWGN · Additive White Gaussian Noise

BCJR · Bahl, Cocke, Jelinek and Raviv

BER · Bit Error Rate

BICM · Bit-Interleaved Coded Modulation

BPSK · Binary Phase Shift Keying

CAZAC · Constant Amplitude Zero Auto-Correlation

CCDF · Complementary Cumulative Distribution Function

CFO · Carrier Frequency Offset

CP · Cyclic Prefix

CRC · Cyclic Redundancy Check

CSI · Channel State Information

CSS · Chirp Spread Spectrum

DBPSK · Differential Binary Phase Shift Keying

DFT · Discrete Fourier Transform

DL · Downlink

DSSS · Direct Sequence Spread Spectrum

ETSI · European Telecommunications Standards Institute

ETU · Extended Typical Urban

EXIT · EXtrinsic Information Transfer

FEC · Forward Error Correction

FFT · Fast Fourier Transform

FIR · Finite Impulse Response

FSK · Frequency Shift Keying

IAPR · Instantaneous-to-Average Power Ratio

ICI · Inter-Carrier Interference

IDFT · Inverse Discrete Fourier Transform

IEEE · Institute of Electrical and Electronics Engineers

IFFT · Inverse Fast Fourier Transform

IoT · Internet-of-Things

ISI · Inter-Symbol Interference

ISM · Industrial, Scientific and Medical

LDPC · Low Density Parity Check

LLR · Log Likelihood Ratio

LPWA · Low Power Wide Area

LR-WPAN · Low-Rate Wireless Personal Area Networks

LTE · Long Term Evolution

M2M · Machine-to-Machine

MAP · Maximum *A Posteriori*

MI · Mutual Information

ML · Maximum Likelihood

MMSE · Minimum Mean Square Error

NB-IoT · Narrow-Band IoT

OCS · Orthogonal with Coplanar Subsets

OFDM · Orthogonal Frequency Division Multiplexing

OSI · Open System Interconnection

PAM · Pulse Amplitude Modulation

PAPR · Peak to Average Power Ratio

PA · Power Amplifier

PCCC · Parallel Concatenated Convolutional Code

PDF · Probability Density Function

PER · Packet Error Rate

PHY · Physical

PPM · Pulse Position Modulation

PSK · Phase Shift Keying

QAM · Quadrature Amplitude Modulation

QoS · Quality of Service

QPSK · Quadrature Phase Shift Keying

RF · Radio Frequency

RPMA · Random Phase Multiple Access

RSC · Recursive Systematic Convolutional

RX · Receiver

SC-FDMA · Single Carrier Frequency Division Multiple Access

SF · Spreading Factor

SNR · Signal-to-Noise Ratio

SOVA · Soft-Output Viterbi Algorithm

TBCC · Tail Biting Convolutional Code

TC-FSK · Turbo Coded Frequency Shift Keying

TC-OFDM · Turbo Coded Orthogonal Frequency Division Multiplexing

TC-SC-FDMA · Turbo Coded Single Carrier Frequency Division Multiple Access

TC · Turbo Code

TX · Transmitter

UL · Uplink

ZC · Zadoff-Chu

ZF · Zero-Forcing

Introduction

In the 90's, digital communications for mobile phones were introduced with the second generation (2G) of wireless telephone technology. Data services like text messages were already included, allowing users to exchange text, pictures and multimedia. Over the years, the success of the Internet and the increasing demand in connectivity required evolutions of the technology, and has induced the creation of a third and fourth generation (3G, 4G) of mobile cellular networks. Since the 2G, the various evolutions aimed for higher rates and better user Quality of Service (QoS). Now that 4G (also referred to as Long Term Evolution (LTE)) is almost deployed world wide [1] with peak data rates of 1 giga-bits per second (Gbps), the fifth generation (5G) is in the process of being developed. This next generation is not only predicted to increase the data rate, but to also enhance existing applications, such as Machine-to-Machine (M2M) communications, or include several new use cases [2], such as the Internet-of-Things (IoT) [3].

The IoT is the concept that every-day life objects could be connected via the Internet. The notion of connected objects has many applications for devices such as cellphones, sensors, wearable devices, components of machines, etc. The concept also relies on the aspect that enabling this technology will unveil new, unexpected applications. Several billions of objects are expected to be connected [4], with an estimation of a ratio of connected devices per person above 6 by 2020 [5]. While most of the connections are done using cellular networks or legacy networks such as WiFi or Bluetooth, there is a gap between local wireless networks and cellular networks that will need to be filled. This is the problem addressed by Low Power Wide Area (LPWA) networks [6]. Out of the 25 billion estimated connections for the IoT, more than 10% are expected to be LPWA connections [4], demonstrating the potential market for this new network.

The key to LPWA connectivity is to achieve long range transmission. The receiver needs to reach low levels of sensitivity, which is dependent on the data rate. Therefore, long range communication is only possible when associated with a low data rate. Most of the current technologies dedicated to LPWA solutions or the ongoing standardization by the 3rd Generation Partnership Project (3GPP) rely on one of two possible strategies to lower the data rate. The first strategy is to reduce the level of captured noise by dealing with narrow-band signaling. The second strategy is to reduce the spectral efficiency of the technique used, *e.g* with the use of a Spreading Factor (SF), or with the use of channel coding.

Regarding this second strategy, the use of orthogonal modulations combines both a reduction of spectral efficiency and a gain in energy efficiency. These modulations are actually shown to attain, for an infinite size of alphabet, the best achievable energy efficiency (i.e. the minimum achievable energy per bit) according to the ultimate capacity limit as defined by Claude Shannon [7]. Since reaching the best energy efficiency implies a spectral efficiency tending toward 0, such a realization is unpractical. But there are other ways to increase energy efficiency. The invention of the Turbo Code (TC) in 1993 [8] offered a practical system with the ability to outperform all channel coding techniques. Based on an iterative receiver, the legitimacy of the scheme was rapidly demonstrated. It was shown to approach the channel capacity closer than any existing schemes. Other techniques such as Low Density Parity Check (LDPC) [9] and Polar codes [10] have been discovered since, but TCs are still used in numerous applications.

The work presented in this thesis addresses the problem of the physical layer for LPWA networks. Repetition is a widely used technique to reduce the spectral efficiency and to achieve low levels of sensitivity. However, it does not improve the energy efficiency. The pairing of 4 elements is considered to improve the energy efficiency: orthogonal modulations, convolutional coding, repetition and iterative decoding. The combination of modulation and coding structures the sequence, and the association with iterative decoding of the various repetition improves the energy efficiency. The process closely approaches the minimum achievable E_b/N_0 at low levels of spectral efficiency. Extensive comparison to existing LPWA solutions demonstrates the high potential of the solution.

Review of the Chapter Contents

The **first chapter** is dedicated to the introduction of the LPWA networks. After a review of the general context of this thesis, the key system parameters used throughout the thesis are introduced. It includes the definition of sensitivity, a key measurement for the long range capacity of a system. The two main techniques allowing a system to reach low levels of sensitivity are also reviewed. The main elements of a transmission system are then introduced: the transmission channel, the modulation and associated demodulation, and Forward Error Correction (FEC) or channel coding. This includes the description of the orthogonal modulation and probabilistic demodulation, along with a review of the FEC techniques, from block codes to the powerful TCs. Finally, a description of existing LPWA solutions is presented, along with some performance in terms of achievable sensitivity levels. Throughout the chapter, the different techniques are directly confronted to the limit as defined by Shannon.

In the **second chapter**, the design of a new technique, so-called Turbo-FSK, is presented. The origins of the scheme are first presented. The principle is then extensively described, from the transmitter procedure to the derivations of the receiver operations. Typical performance is also presented. The optimization of the Turbo-FSK parameters regarding the required level of E_b/N_0 is then investigated. It is done through the use of the EXtrinsic Information Transfer (EXIT) chart tool, which is first introduced and studied for the Turbo-FSK scheme. The asymptotic performance of the scheme is assessed and the parameters minimizing the E_b/N_0 are found. The analysis is then extended to short packet sizes and confronted with the maximum achievable spectral efficiency as defined by Shannon's limit. Performance of the Turbo-FSK using the optimum parameters under AWGN channel is then compared to existing LPWA solutions. The results demonstrate the potential gain in sensitivity of the solution and the effectiveness of the combination of orthogonal modulation and channel coding associated to a specific turbo receiver.

A generalization of the Turbo-FSK, so-called Coplanar Turbo-FSK, is studied in the **third chapter**. As the original Turbo-FSK only allows low levels of spectral efficiency, two features are introduced to overcome the lack of flexibility in the system. The first feature concerns the design of the alphabet of modulation. The so-called Orthogonal with Coplanar Subsets (OCS) modulation is introduced and consists of an orthogonal alphabet which includes linear components. The second feature is the specification of a puncturing procedure to reduce the number of transmitted symbols. The transmitter and receiver of the Coplanar Turbo-FSK scheme are described. The various features of the scheme are then studied: the influence of the choice of mapping on the trellis, the impact of the size of the linear modulation, the effects of puncturing and the evolution of the spectral efficiency with the parameters, specifically with the size of the alphabet.

The **fourth chapter** focuses on the study of the previously designed system under more practical scenarios and implementation. The system is compared to common modulation techniques such as Orthogonal Frequency Division Multiplexing (OFDM), Single Carrier Frequency Division Multiple Access (SC-FDMA) and FSK associated with a powerful TC. A spread spectrum orthogonal alphabet for the Coplanar Turbo-FSK is also considered as an element of comparison. A global simulation chain has been implemented on top of an OFDM transceiver. After descriptions of the transmitter and receiver procedures for each of the 5 compared schemes, the two tested scenarios and the associated parameters for the various schemes are presented. For each scheme, the signal envelope variations are estimated. For each scenario, performance under various channels is also evaluated, including frequency-selective channels. Both static and mobility conditions are considered, in order to assess the performance of the designed system under more realistic signal propagation conditions. Eventually, key parameters indicators are discussed and a synthesis is presented. It illustrates to which scenarios the proposed scheme is more adapted to.

CHAPTER 1

Introduction to Low Power Wide Area Networks

Chapter contents

This chapter is dedicated to the introduction of concepts and existing solutions for Low Power Wide Area (LPWA) networks. All the technical elements presented are used in the next chapters. After introducing the general LPWA context, the key system parameters for telecommunication systems are introduced, as they will be used throughout this paper. The main elements of the Physical (PHY) layer are presented, such as the principles of modulation and Forward Error Correction (FEC), along with an historical overview of the techniques. Finally, the existing industrial solutions dedicated to LPWA networks are reviewed.

1.1 Low Power Wide Area Networks

In order to introduce LPWA networks and the associated requirements, an overview of the existing telecommunication networks is presented. Some of the inherent problems of legacy networks that conflict with LPWA requirements are also outlined.

In a cellular network, devices (*e.g* cellphones) are endpoints. In order to communicate, they must connect to the network. This network access is done by communicating through gateways, also called base stations. A schematic view of the connection between the endpoint and the base station is given in Figure 1.1. Each base station serves a specific number of users, and offers a spectral resource, shared between the users. The base station coverage, the cell, can be of various sizes. In urban areas, the density of devices is high, and the base station coverage is reduced so that each user can have enough resources. However, in rural areas, this density decreases, and the cell can be larger. For the Long Term Evolution (LTE), the urban area cell has a typical radius of few kilometers, while rural area cells can have a radius of several tens of kilometers. As the device is an endpoint, it needs to communicate with the base station to send or receive new packets. In order to ensure a low latency when a packet needs to be sent or received, the device and the base station almost constantly exchange synchronization signals. The communication scheme is said to be synchronized. This communication is continuous, and induces an overhead in the communication. One of the drawbacks of the procedure is when the device does not transmit or emit a large quantity of packet. If for example, the device communicates with the base station during 1% of the time in one day, the synchronization procedure would be ongoing and useless for 99% of the time, inducing a waste of energetic and spectral resource. Energy seems to be wasted at the device and base station level, as the radio stays on without the necessity of sending data packets, and the spectral waste corresponds to the useless exchanges of synchronization packets. For cellular networks, concessions in terms of coverage and device consumption are accepted, as one of the main concerns is the Quality of Service (QoS) offered to the users. For example, low latency and high data rate can be main criteria for the users' satisfaction.

LPWA networks concern new applications with new requirements, such as smart-metering of water consumption. This application would require a new battery solution, preferably with a long life duration to avoid frequent changes. As discussed, when a rural situation is considered, a large coverage for the base station is required. This is also a financial benefit for the network access provider, as reducing the total number of base stations reduces its cost. The water metering sensors only send small amounts of information (a few bytes of data would suffice the consumption and the date), and they do so only once a week or once a month. The amount of exchanged data over the period is very low. The use of a cellular network may be inefficient due to the large amount of overhead required for synchronization; a sporadic access is preferred, where the node enters into a sleeping mode after data transmission. The coverage offered by the cellular network may also not be large enough, a wider cell range should

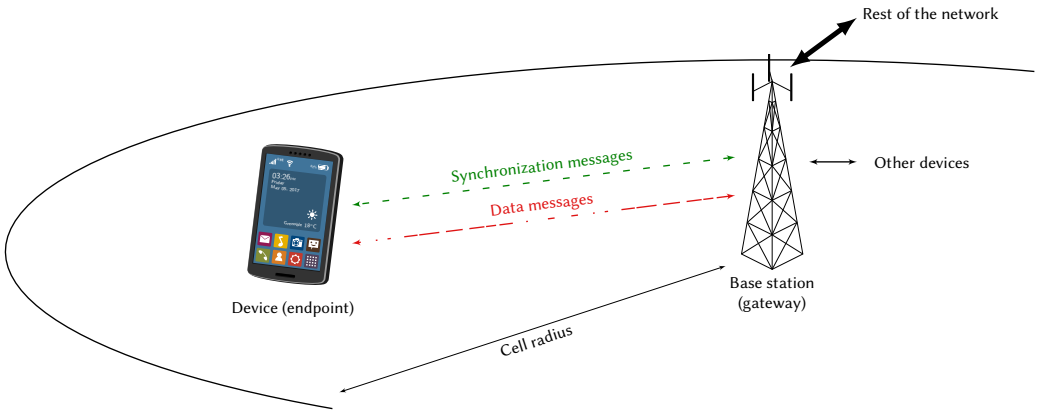

Figure 1.1 – *Schematic of the cellular network architecture.*

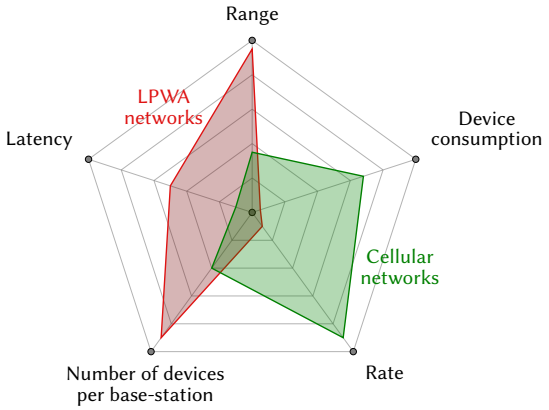

FIGURE 1.2 – *Requirements for cellular networks (3G, 4G) and LPWA networks.*

be considered. This simple example illustrates the need for a new LPWA network. These networks are commonly characterized by some key features [11]:

- Long range communication, allowing a reduced number of base station deployment compared to legacy cellular networks;
- Long battery life for the devices (up to 10 years);
- Low throughput communication;
- Low cost devices;
- Massive number of devices connected to a single base station;

The requirements of both cellular (third generation (3G) and fourth generation (4G)) and LPWA networks is presented in Figure 1.2. Compared to cellular networks, the latency constraint of LPWA networks is relaxed and the high rate requirement is replaced by long range and low device consumption. The figure also emphasizes the opposite requirements of the two technologies.

The Internet-of-Things (IoT) concerns a lot of applications, and it is accepted that legacy cellular networks will still be a solution for some use cases (for example, non-energy constrained problems which require high data rates), but the potential market for LPWA networks is compelling.

1.2 Key System Parameters

A communication link is composed of a transmitter that sends a signal containing the information, a transmission medium (also called channel), which can be the air, and a receiver. The receiver will try to retrieve the information from the received signal, and may succeed depending on the distortion that happened to the signal during its transition through the channel. When it comes to characterizing the performance of a communication link, both experimental and theoretical criteria can be chosen. This section is dedicated to the presentation of these key system parameters, and how they are related.

1.2.1 Long Range and Sensitivity

The ability for LPWA to communicate over long distances is a key feature. When considering a free path loss, the distance at which the transmitter and the receiver can communicate depends on several factors, which are summarized by the basic form of the Friis transmission equation [12]

$$P_r = P_t G_t G_r \left(\frac{\lambda_w}{4\pi d}\right)^2, \tag{1.1}$$

where P_t (resp. P_r) is the power at the transmitter side (resp. the receiver side), G_t (resp. G_r) the antenna gain of the transmitter (resp. the receiver), λ_w the wavelength of the transmitter signal and d the distance between the transmitter and the receiver. In order to characterize a communication system, engineers rely on the sensitivity. It is defined as the minimum received power signal required to achieve an arbitrary level of error. This quantity is thus the power P_{req} for which the receiver will be able to retrieve the error free data sent at the other side of the

communication link (or at the transmitter). When under this value, the power level is such that the resulting error level is higher than tolerated.

By allowing only the received power and the distance to vary, Equation (1.1) simplifies to $P_r = C_{st}/d^2$, with C_{st} a constant value. Sensitivity is reached when $P_r = P_{req}$, inducing a specific distance for which the communication achieves the arbitrary level of error. Long range can thus be achieved when the system can work at very low levels of sensitivity, turning the problem of long range into that of lowering the level of sensitivity. Several techniques are used to do so, and to clearly understand the reasons for each approach, some concepts need to first be presented.

A simple definition of the power of a signal is

$$P = E_b R, \tag{1.2}$$

where E_b is the energy of one bit, expressed in Watt·s and R the binary rate, expressed in bit·s^{-1}. The power P is thus expressed in Watts. Introducing the value $E_{b\,\mathrm{req}}$ as the energy per bit required for the arbitrary level of error, the sensitivity can be expressed

$$P_{\mathrm{req}} = E_{b\,\mathrm{req}} R. \tag{1.3}$$

In this equation, $E_{b\,\mathrm{req}}$ depends only on the technique used to transmit the information. This equation gives the most simple and true approach to reducing the sensitivity level: reduce the data rate R.

The receiver, as any electronic device, is subject to thermal noise [13]. This electronic noise is due to the thermal agitation of the electrons, and is proportional to the ambient temperature. The noise power can be expressed

$$P_n = N_0 B, \tag{1.4}$$

where $N_0 = k_B T$ with k_B the Boltzmann's constant (equal to $1.3806 \cdot 10^{-23}$ Joules·K^{-1}), T the temperature in Kelvins. B is the bandwidth of the signal, in Hz. P_n is expressed in Watt, or Joules·s^{-1}. The quantity N_0 is commonly referred to as the noise power spectral density.

In order to characterize the noise versus the signal power, we define the Signal-to-Noise Ratio (SNR) as

$$\mathrm{SNR} = \frac{P}{P_n} = \frac{P}{N_0 B}. \tag{1.5}$$

Typical receivers also present some imperfections that affect the SNR. In order to characterize the loss compared to an ideal receiver, the noise factor F is introduced, with $F \geq 1$ [13]. When the receiver is considered ideal, the noise factor is taken to equal 1.

A new expression of the sensitivity, including the noise factor of the receiver and expressed in W, can be derived as

$$P_{\mathrm{req}} = \mathrm{SNR}_{\mathrm{req}} \cdot N_0 \cdot B \cdot F, \tag{1.6}$$

where $\mathrm{SNR}_{\mathrm{req}}$ is the ratio between the sensitivity as defined in Equation (1.3) and the noise power given Equation (1.4).

As we usually deal with small values for P_{req}, it is common to express the power in dBm, using the conversion

$$(P_{\mathrm{req}})^{\mathrm{dBm}} = 10 \log_{10}\left(\frac{P_{\mathrm{req}}}{10^{-3}}\right), \tag{1.7}$$

where the division by 10^{-3} stands for the fact that we consider the ratio of the power (in Watt) over 1mW. More generally, we choose to represent any ratio in dB, or 10 times the base 10 logarithm of the power ratio.

The sensitivity in dBm is given by

$$(P_{\mathrm{req}})^{\mathrm{dBm}} = \mathrm{SNR}_{\mathrm{req}}^{\mathrm{dB}} + 10 \log_{10}(B) + 10 \log_{10}\left(N_0 \cdot 10^3\right) + 10 \log_{10}(F). \tag{1.8}$$

The quantity $10 \log_{10}\left(N_0 \cdot 10^3\right)$ is often taken equal to -174dBm, which is its value for $T \simeq 288$K ($\simeq 15$°C). The noise factor expressed in dB is called the noise figure N_F. For the rest of the document, we will consider (unless stated otherwise) that the front end of the receiver does not add any additional noise, and thus has a noise figure $N_F = 0$dB. Typical noise figures can range from 1 to 15dB when not considering deep space applications [13].

1.2.2 Spectral Efficiency, Energy Efficiency and Long Range Strategies

Using Equation (1.2) and the expression of the SNR given in Equation (1.5), the SNR can also be expressed as

$$\mathrm{SNR} = \frac{E_b}{N_0} \cdot \eta, \tag{1.9}$$

where

$$\eta = \frac{R}{B} \tag{1.10}$$

is the spectral efficiency, a positive value expressed in bits·s^{-1}·Hz^{-1}. The value E_b/N_0 is the ratio of the energy of one bit over the noise power spectral density. This value is closely related to the energy efficiency of the system, which can be defined as [14]

$$\varepsilon = \frac{1}{E_b} = \frac{1}{N_0 \cdot \frac{E_b}{N_0}}. \tag{1.11}$$

It is expressed in bits·J^{-1}. Following this definition, the energy efficiency is inversely proportional to E_b/N_0. Having a high required E_b/N_0 is equivalent to have a low energy efficiency, and, alternatively, an energy efficient system will have a low required E_b/N_0.

Considering a specific technique that has a certain required SNR for an arbitrary level of error, Equation (1.9) means that the technique will achieve this level of error with a specific energy efficiency and a certain spectral efficiency. The sensitivity can be expressed differently with

$$(P_{\mathrm{req}})^{\mathrm{dBm}} = \left(\frac{E_b}{N_0}\right)^{\mathrm{dB}}_{\mathrm{req}} + 10\log_{10}(R) + 10\log_{10}\left(N_0 \cdot 10^3\right). \tag{1.12}$$

This expression shows three possible ways to lower the sensitivity level:

- Reduce the noise spectral density by reducing the temperature;
- Reduce the data rate R;
- Reduce the E_b/N_0 value required for the level of error.

While influencing the temperature might somehow be a difficult solution, except by ensuring a proper cooling of the receiver, the two other terms are essential when it comes to the major strategies to lower the sensitivity.

Reducing the data rate can be done through two different methods: as bandwidth and spectral efficiency are related with $R = \eta B$, it is possible to reduce one of the two to affect the data rate. One strategy is then to use narrow band signaling, i.e. reducing the data rate by using only a small bandwidth. This strategy comes with issues, including the necessity to have precise oscillators, as a minor frequency offset can induce the loss of the narrow band signal. Another strategy relies on relaxing the spectral efficiency, for example by repeating the message λ times. The spectral efficiency is divided by λ, and so is the data rate. Reducing the spectral efficiency while keeping the bandwidth constant induces an increase of the signal duration.

The required E_b/N_0 for a level of error depends on how the technique is designed. Reducing its value thus implies the replacement of some elements of the technique or the use of more sophisticated reception algorithms. In the next section, the design of transmission techniques is presented, and schemes with very low levels of required E_b/N_0 are introduced.

1.2.3 Channel Capacity and Maximum Achievable Spectral Efficiency

The channel capacity (also called Shannon's limit) was introduced by Claude Shannon in 1948 [7], and remains one of the fundamental results of information theory. It is defined as the maximum achievable rate for a given bandwidth and level of SNR, with an arbitrarily small level of error. The classical expression of the capacity C for an Additive White Gaussian Noise (AWGN) channel is given by

$$C = B\log_2(1 + \mathrm{SNR}), \tag{1.13}$$

where C is expressed in bits·s^{-1}. The rate R of any reliable technique of transmission is upper bounded by the capacity, and getting close to it has been the purpose of countless research efforts. Reaching the limit rate for a given bandwidth and SNR would signify that the resource is used in the most efficient way possible. Summarily, having a system close to the capacity would render enormous benefits in this context.

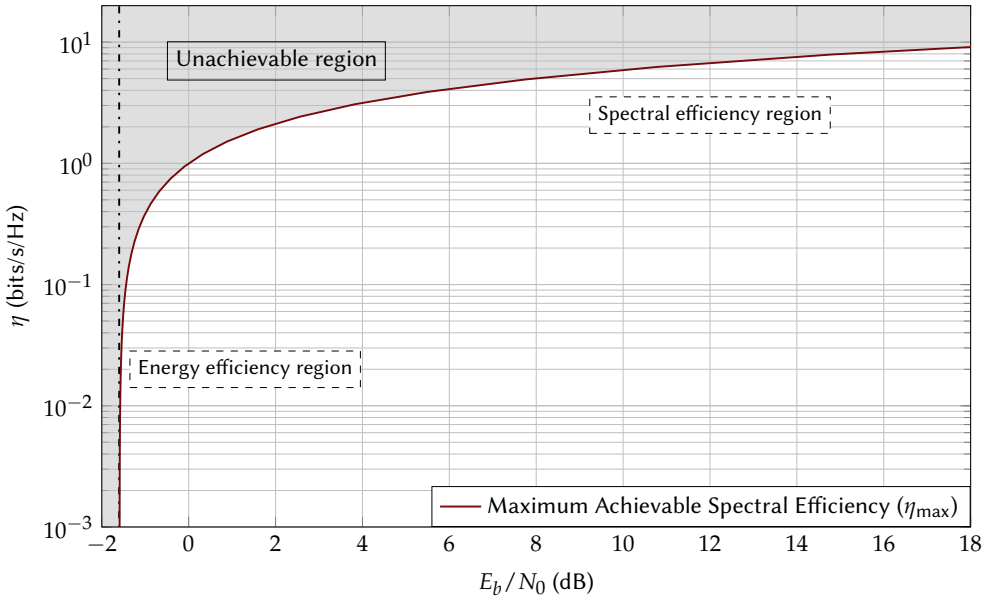

FIGURE 1.3 – *The maximum spectral efficiency according to the channel capacity from Equation* (1.15)*, versus* E_b/N_0.

In order to express the limit using the quantities previously defined, we normalize the channel capacity by the bandwidth to get $\eta_{\max} = C/B$, the maximum achievable spectral efficiency. The limit becomes

$$\eta_{\max} = \log_2(1 + \mathrm{SNR}). \tag{1.14}$$

Using the SNR definition given in Equation (1.5), the maximum spectral efficiency for a given E_b/N_0 must satisfy

$$\eta_{\max} = \log_2\left(1 + \frac{E_b}{N_0} \cdot \eta_{\max}\right). \tag{1.15}$$

It is also possible to express the minimum achievable E_b/N_0 for a given spectral efficiency, denoted $(E_b/N_0)_{\min}$, with

$$\left(\frac{E_b}{N_0}\right)_{\min} = \frac{2^{\eta} - 1}{\eta}. \tag{1.16}$$

Since $(E_b/N_0)_{\min}$ is an increasing function of the spectral efficiency η, it is lower bounded when η tends toward 0. This ultimate limit can be shown to be equal to $(E_b/N_0)_{\lim} = \log(2)$, or $\simeq -1.59$dB. When considering a system with a given spectral efficiency, the required E_b/N_0 must be superior to the $(E_b/N_0)_{\min}$ given by Equation (1.16). Following the definition of the energy efficiency given in Equation (1.11), the maximum achievable energy efficiency is given by $\varepsilon_{\max} = (N_0 \log(2))^{-1}$ bits·J^{-1}.

In Figure 1.3, the maximum achievable spectral efficiency has been depicted versus E_b/N_0. The operating zone of any reliable communication system must be in the area under the curve, which is generally divided into two main regions [15, p. 284]. The first region is the spectral efficiency region. In this area, spectral efficiency is high (> 1) while the E_b/N_0 is high as well. This region concerns techniques designed for very high data rates without considering the energy efficiency as a major constraint. In the second region, the energy efficiency region, the level of E_b/N_0 is low (inducing a high energy efficiency ε) but so is the spectral efficiency. This area concerns techniques for which the energy efficiency constraint is very high, while a lower data rate is required, or more bandwidth usage is accepted.

The channel capacity leads then to limitations on the maximum achievable spectral efficiency for a given E_b/N_0, or the minimum E_b/N_0 required (alternatively the maximum energy efficiency) for a given spectral efficiency. From the information theory, the conclusion is that a trade-off between the spectral efficiency and the energy efficiency must always be made. Reliable transmission with high energy efficiency will necessarily result in poor spectral efficiency, and in comparison, a system with a higher spectral efficiency has to consume more energy to transmit the same amount of bits with the same arbitrary level of error.

1.2.4 Constant Envelope and Power Amplifier

The Power Amplifier (PA) is one of the last elements of the transmission chain. It converts the low-level signal to a high-power signal to be transmitted through the transmitter antenna [16, 17]. This critical component turns out to

be a high energy consumer, and selecting an efficient PA is a major concern when designing a Radio Frequency (RF) system [18].

While different classes or types of PAs can be selected, their transfer function may be characterized by three regions:

- the linear region, where the output is equal to the input times the gain factor,
- the non-linear region, where the output is a non-linear function of the input,
- the saturation region, where the output is constant whatever the input.

If the input signal power varies over time, a certain backoff needs to be considered in order to avoid entering the non-linear or saturation regions, which would induce distorsions of the signal.

The Complementary Cumulative Distribution Function (CCDF) of the Peak to Average Power Ratio (PAPR) is widely used in the literature as a performance criterion. It is defined as the probability that the PAPR exceeds a given level P_0 during a specific time interval with

$$\mathrm{CCDF}\left[\mathrm{PAPR}\left(B_l\right)\right] = \Pr\left(\mathrm{PAPR}\left(B_l\right) > P_0\right), \tag{1.17}$$

where

$$\mathrm{PAPR}(B_l) = \frac{\max\limits_k \left[|x(k)|^2\right]}{E\left[|\boldsymbol{x}|^2\right]}, \tag{1.18}$$

B_l is the block index corresponding to the time interval, $\boldsymbol{x}$ is the time signal and $x(k)$ the samples of the signal in the block with $k \in \{0, \ldots, N_{\text{block}} - 1\}$, where N_{block} is the size of the considered block B_l. E is the expectation operator.

The CCDF of the PAPR is a representation that only considers one extreme value (the sample with the highest instantaneous power). It is more relevant to consider all the samples that have a power above the threshold P_0 [19] (for example, all the samples that would reach the non-linear region of the PA induce distorsions). This measure is the Instantaneous-to-Average Power Ratio (IAPR). The CCDF of the IAPR is given by

$$\mathrm{CCDF}\left[\frac{|x(k)|^2}{E\left[|\boldsymbol{x}|^2\right]}\right] = \Pr\left(\frac{|x(k)|^2}{E\left[|\boldsymbol{x}|^2\right]} > P_0\right). \tag{1.19}$$

When a signal is said to have a constant envelope, its instantaneous signal power is a constant, so that both the PAPR and the IAPR are equal to 0dB. At the PA level, this means that no backoff is necessary as the power does not vary. The PA can operate at its most efficient configuration, thus maximizing its energy efficiency. Also, the use of a non-linear PA can be considered, as this type of PA has better efficiency at lower costs.

1.3 The Physical Layer

In telecommunications, the way two or more entities communicate is usually described through means of a protocol. This corresponds to a set of rules and standards that defines the structure of the communication, its syntax and semantics. To ensure a successful communication, the protocol is decomposed into layers, where each layer communicates to the layer above and under it only. Because the layers are independent, problems or errors are contained in each layer, simplifying the design of the protocol. One widely applied model, Open System Interconnection (OSI) model, decomposes protocols in 7 layers, each one having a specific purpose. For example, the highest layer is the Application Layer, that interacts directly with the user. On the opposite, the PHY layer is the layer that interacts with the transmission medium, which may consists in wires, coaxial cable, radio link, or else. The purpose of the PHY layer is to convert the raw information bits coming from the upper layers into a physical signal to be transmitted over the transmission medium. The layer also needs to be able to perform the reverse operation, and to retrieve the data bits from the received signal.

The communication between two PHY layers is modeled by a transmission system, represented in Figure 1.4. It is usually decomposed in three main parts: a transmitter, a transmission channel and a receiver. The transmitter needs to have a RF front end in order to emit an analog signal at high frequencies. In this document, a simplified baseband model is considered. The transmitter and receiver analog baseband signals are modelled by complex sampled signals. Effects introduced by the RF front end are included in the channel model and assumed to be linear.

In this section, the description of the different techniques used in the PHY layer, both at the transmitter and the receiver side, will be reviewed. When considering binary values, two representations may be used: the unipolar representation 0 and 1 or the polar representation $+1$ and -1 (respectively).

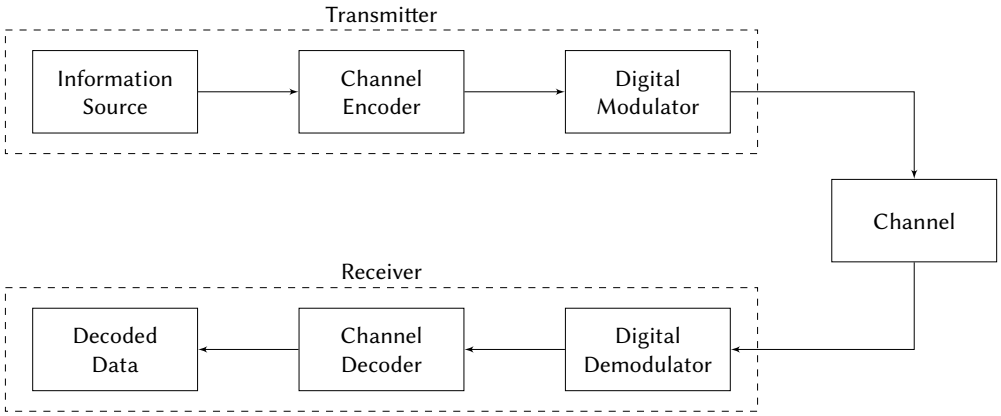

FIGURE 1.4 – *The transmission system model.*

1.3.1 CHANNEL

The physical transmission medium between the transmitter and the receiver is represented by the channel. Several models can be chosen for the channel, in order to reflect the different possible sources of impairment. For our model, the steps of transposition to carrier frequency at the transmitter, and down conversion at the receiver, are considered perfect. The signals are sampled at the Nyquist-Shannon rate, with a time interval $T_c = 1/B$, where B is the analog bandwidth (around the carrier frequency) of the transmitted signal. The considered channel model is depicted in Figure 1.5. We assume that the information source consists in Q bits, and that encoding and modulation steps have been performed. The input of the channel is the vector $\boldsymbol{x}$, and its output is the vector $\boldsymbol{y}$. The size of both vectors is N_{ch}. $\boldsymbol{x}$ (resp. $\boldsymbol{y}$) represent the discrete-time base-band signal (i.e. the complex envelope) of the transmitter (resp. the receiver). The vectors are composed of complex values and are defined as

$$\begin{aligned}\boldsymbol{x} &= [x_0, x_1, \ldots, x_{N_{\text{ch}}-1}] = \{x_k\}_{k\in\{0,\ldots,N_{\text{ch}}-1\}} \\ \boldsymbol{y} &= [y_0, y_1, \ldots, y_{N_{\text{ch}}-1}] = \{y_k\}_{k\in\{0,\ldots,N_{\text{ch}}-1\}}.\end{aligned}$$

The input vector $\boldsymbol{x}$ is affected by a filter, which represents the possibility to receive several versions of the transmitted signal with various gains. This is a linear model of the channel. The output $\boldsymbol{g}$ of the filter can be expressed, with $k \in \{0, \ldots, N_{\text{ch}} - 1\}$

$$g(k) = \sum_{l=0}^{L_{\text{ch}}-1} h(l)x(k-l), \tag{1.20}$$

where $\boldsymbol{h}$ is the channel impulse response, a complex vector with L_{ch} elements, representing the gain of each possible paths. Equation (1.20) can be seen as the convolution of the signal with the channel vector.

After the channel filter, AWGN is added to the signal $\boldsymbol{g}$. This noise represents the thermal noise intrinsic to any electronic device. The received signal $\boldsymbol{y}$ is expressed

$$\boldsymbol{y} = \boldsymbol{g} + \boldsymbol{\nu}, \tag{1.21}$$

where the elements ν_k of $\boldsymbol{\nu}$ follow a circularly-symmetric and zero mean complex normal distribution. The terms ν_k are independent and their distribution is given by

$$p(\nu_k) = \frac{1}{2\pi\sigma_{\text{ch}}^2} \exp\left\{-\frac{1}{2\sigma_{\text{ch}}^2}|\nu_k|^2\right\}, \tag{1.22}$$

where the variance is equal to $\sigma_{\text{ch}}^2 = N_0 B$.

When $L_{\text{ch}} = 1$ and $h(0) = 1$, the filter has no effect and $\boldsymbol{g} = \boldsymbol{x}$ (i.e. only the direct path without any gain is received). In this case, the output of the channel is only the sum of the input signal and the AWGN noise. We will refer to this case as the AWGN channel.

The energy of the discrete signal $\boldsymbol{x}$ is denoted $E_{\boldsymbol{x}}$ and expressed

$$E_{\boldsymbol{x}} = T_c \cdot \sum_{k=0}^{N_{\text{ch}}-1} |x_k|^2, \tag{1.23}$$

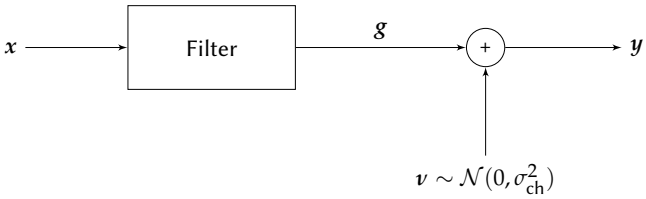

FIGURE 1.5 – *The channel model considered.*

where T_c is the time duration of one sample (or chip). $E_{\boldsymbol{x}}$ is expressed in Watt·s. As the signal carries Q information bits, we can consider the energy of one information bit E_b, and express the energy of the signal as

$$E_{\boldsymbol{x}} = Q \cdot E_b. \tag{1.24}$$

As the duration of the signal $\boldsymbol{x}$ is $N_{\text{ch}} T_c$, the data rate is equal to $R = Q/(N_{\text{ch}} T_c)$ and expressed in bits·s^{-1}. The power of the signal is the energy of the signal averaged over the duration of the signal, hence its expression

$$P_{\boldsymbol{x}} = \frac{E_{\boldsymbol{x}}}{N_{\text{ch}} T_c} = \frac{Q E_b}{N_{\text{ch}} T_c} = R \cdot E_b = \eta \cdot B \cdot E_b. \tag{1.25}$$

1.3.2 Digital Modulation

In digital communication systems, the conversion from digital binary values to physical waveforms is performed with digital modulation. At the transmitter side, the digital modulator maps a set of M binary digits to a complex waveform, and hence needs a set of $M = 2^m$ waveforms, also called the modulation alphabet and denoted $\boldsymbol{\mathcal{A}}$. When the mapping is done without taking into consideration the previous waveform, the modulation is said to be memoryless; otherwise the modulator is said to have memory. Considering a digital baseband model, the waveforms are represented in their sampled version, which for disambiguation will be called symbols. The sampling time is denoted T_c, and T_s is the symbol time. A symbol is a sequence of T_s/T_c chips. Since $\log_2(M)$ information bits are sent during T_s, the data rate is

$$R = \frac{\log_2(M)}{T_s}. \tag{1.26}$$

In the channel, the signal is corrupted by various types of noise sources. The digital demodulator, present at the receiver side, will process the received signal and estimate which symbol was sent, in order to recover the transmitter binary sequence modulated at the first place.

The main characteristics that should be considered for the design of a digital modulation are the choice of modulation alphabet, the mapping on the alphabet, and the conception of the demodulator. Two main types of modulation are presented here: the linear modulations and the orthogonal modulations. Only memoryless modulations are considered.

1.3.2.1 Linear Modulations

The alphabet of a linear modulation consists in linear variation of a basic waveform. The variations can be in amplitude, in phase, or both. A simple example of linear amplitude modulation is the 2-Pulse Amplitude Modulation (PAM), where the modulation alphabet is composed of 2 symbols $s_0 = +V$ and $s_1 = -V$, with V a real value. When $V = 1$, the 2-PAM can be seen as a phase modulation with an alphabet $\boldsymbol{\mathcal{A}}$ of size 2 equal to

$$s_0 = e^{j0} \qquad s_1 = e^{j\pi},$$

where the two phase shifts are 0 and π. This is the Binary Phase Shift Keying (BPSK) modulation. Using this modulation, only one bit can be represented per symbol. More bits can be represented by a symbol by increasing the size of the alphabet. For the Phase Shift Keying (PSK) modulation, this is done by allowing M phase shifts, thus enabling a symbol to carry $\log_2(M)$ information bits. Another example of linear modulation is the Quadrature Phase Shift Keying (QPSK), which combines two BPSK modulations, one in the real dimension and the other in the imaginary dimension. This modulation is equivalent to a 4-Quadrature Amplitude Modulation (QAM), which combines both amplitude and phase modulation.

The alphabet of a linear modulation is usually represented by its constellation, or the plot of the imaginary part (the quadrature component) of all the symbols of the alphabet versus their respective real part (the in-phase component). Examples of constellation for usual linear modulations are given in Figure 1.6. For every constellation, Gray Mapping was applied. With this mapping, for a certain symbol, the closest symbols only differ by one bit. If the

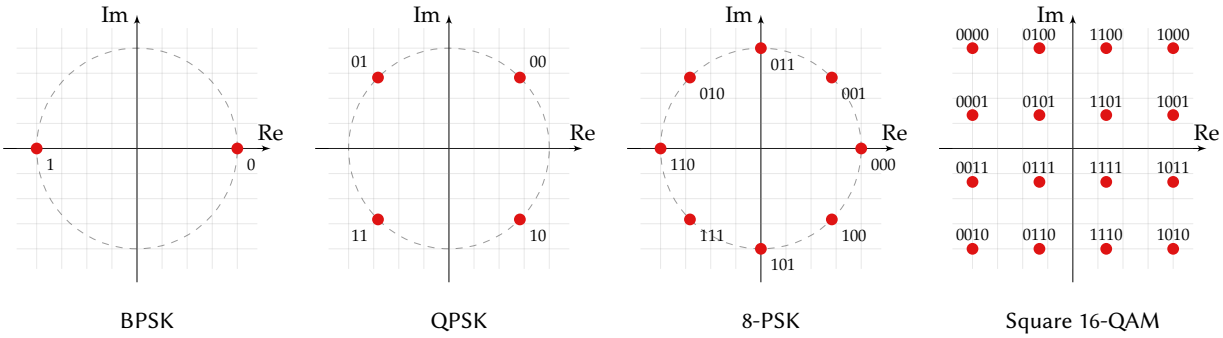

FIGURE 1.6 – *Examples of constellations for common linear modulations, with Gray Mapping.*

demodulator chooses one of the closest symbols instead of the correct symbol, the number of incorrectly detected bits is reduced compared to another mapping.

In order to avoid interference between consecutive symbols, the Nyquist criterion must be respected [15, p. 72]. The criterion imposes a minimum bandwidth equal to $B = 1/T_s$, which leads to $T_s = T_c$ following the definition of the bandwidth. This means that one symbol is composed of only one chip, and with the rate definition of Equation (1.26), the maximum spectral efficiency for linear modulations is equal to

$$\eta = \log_2(M). \tag{1.27}$$

1.3.2.2 Orthogonal Modulations

The alphabet $\boldsymbol{\mathcal{A}}$ of an orthogonal modulation must satisfy the orthogonality condition. The M symbols $\boldsymbol{s}$ of the alphabet are composed of M complex elements. When considering two symbols $\boldsymbol{s}^i \in \boldsymbol{\mathcal{A}}$ and $\boldsymbol{s}^j \in \boldsymbol{\mathcal{A}}$ (and thus $\{i, i'\} \in \{0, \dots, M-1\}^2$), the alphabet $\boldsymbol{\mathcal{A}}$ is orthogonal if

$$\langle \boldsymbol{s}^i, \boldsymbol{s}^{i'} \rangle = \begin{cases} A_i & \text{if } i = i' \\ 0 & \text{if } i \neq i' \end{cases}, \tag{1.28}$$

where $A_i \in$ and $\langle \, . \, , \, . \, \rangle$ is the complex scalar product, defined by

$$\langle \boldsymbol{x}, \boldsymbol{y} \rangle = \sum_k x_k \overline{y_k}, \tag{1.29}$$

with $\overline{y_k}$ the complex conjugate of y_k. The orthogonality condition can be orthonormal, i.e. $A_i = A$, under the condition that $\|\boldsymbol{s}^i\| = \|\boldsymbol{s}^j\|$, where $\|\boldsymbol{x}\|$ is the Euclidean norm of the vector $\boldsymbol{x}$, defined by

$$\|\boldsymbol{s}\| = \sqrt{\sum_k |x_k|^2}. \tag{1.30}$$

In order to satisfy the orthogonality condition (1.28), elements of the alphabet must be represented on M dimensions. For example, the symbol time could be divided into M slots, and each symbol of the alphabet would correspond to the vector where only one of the position is switched to 1, giving a total of M symbols. For this example, the orthogonality condition is expressed in the time domain. This orthogonal modulation is denominated Pulse Position Modulation (PPM).

Another example of orthogonal modulation is the FSK. For this type of modulation, the orthogonality is expressed in the frequency domain. The FSK mapping, symbols, waveforms and shaped spectrum are represented in Figure 1.7 for $M = 4$. Here, Gray Mapping was chosen. The alphabet of the FSK can be obtained using the Discrete Fourier Transform (DFT) matrix, defined as

$$\boldsymbol{W}_M = \left\{ \omega^{ki} \right\}_{\substack{k=0,1,\dots,M-1 \\ i=0,1,\dots,M-1}}, \tag{1.31}$$

with $\omega = e^{-j\frac{2\pi}{M}}$ the M-th root of unity. FSK symbols then correspond to row (or columns) of the matrix $\boldsymbol{W}_M$. The shaped spectrum represented in Figure 1.7 is given after rectangular windowing of the time signal. Before this time truncation and shaping steps, each codeword corresponds to a pure frequency.

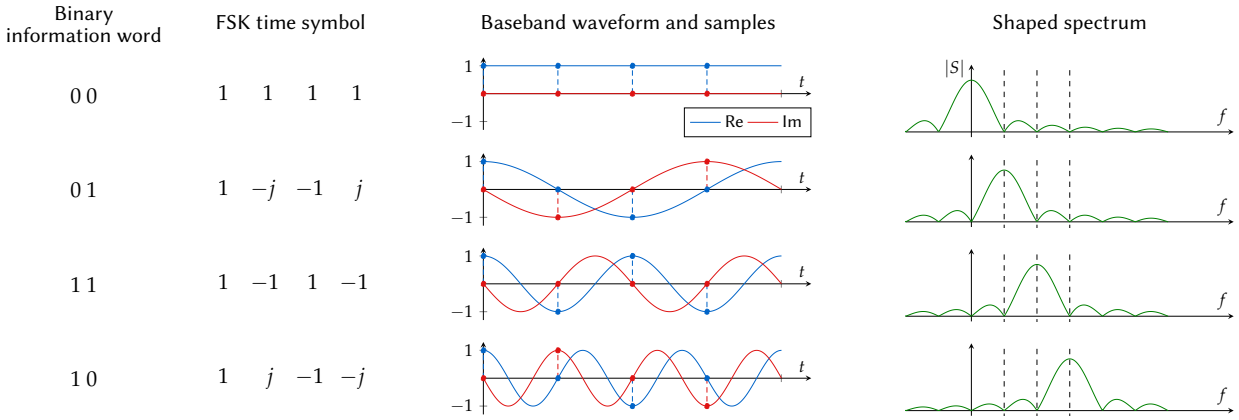

FIGURE 1.7 – *Example of Gray Mapping of a 4-FSK modulation, with representation of the oversampled time waveform and the spectrum S after time-domain rectangular shaping.*

Each orthogonal waveform contains $\log_2(M)$ information bits. However, the symbols are composed of M complex values, required to represent the M dimensions of the modulation. This condition will induce a signal of duration $T_s = MT_c$, and thus a data rate of $R = \log_2(M)/(MT_c)$. As the bandwidth is equal to $B = 1/T_c$, the spectral efficiency of the modulation is equal to

$$\eta = \frac{\log_2(M)}{M}. \tag{1.32}$$

When compared to linear modulations of alphabet size M, the spectral efficiency of an orthogonal modulations of the same alphabet size M is thus divided by M. This means that for a same rate R, the required bandwidth is increased by a factor of M.

1.3.3 Demodulation

The purpose of the demodulator is to estimate the received symbol from the observation acquired from the channel. In this section, the derivations of various demodulators and performance of some modulations are presented. The transmission of one symbol $\boldsymbol{s}$ taken from the alphabet is considered, and $\boldsymbol{r}$ is the noisy symbol received from the AWGN channel. The symbols are vectors composed of N_c chips, with $N_c \geq 1$, depending on the choice of modulation.

1.3.3.1 Maximum Likelihood Decision

The demodulator must be designed in the way that minimizes the symbol error probability, defined as the probability of not choosing the correct symbol. In order to do so, the *A Posteriori* Probability (APP) of having the possible symbol $\boldsymbol{s}^i$, with $i \in \{0, \ldots, M-1\}$, given the observation $\boldsymbol{r}$ is considered. It is expressed as $\Pr\left(\boldsymbol{s}^i \,\middle|\, \boldsymbol{r}\right)$. There are M possible symbols, and the Maximum *A Posteriori* (MAP) criterion consists in selecting the symbol having the maximum APP. This criterion is shown to minimize the probability of error. The APP can be expressed, using Bayes' rule, as

$$\Pr\left(\boldsymbol{s}^i \,\middle|\, \boldsymbol{r}\right) = \frac{p\left(\boldsymbol{r} \,\middle|\, \boldsymbol{s}^i\right) \Pr\left(\boldsymbol{s}^i\right)}{p\left(\boldsymbol{r}\right)}, \tag{1.33}$$

where $p\left(\boldsymbol{r} \,\middle|\, \boldsymbol{s}^i\right)$ is the conditional Probability Density Function (PDF) of observing $\boldsymbol{r}$ while $\boldsymbol{s}^i$ was sent, also called the likelihood function. $\Pr\left(\boldsymbol{s}^i\right)$ is the *a priori* probability of having the symbol $\boldsymbol{s}^i$, and the denominator can be seen as a normalization term, and is independent of which signal was transmitted.

When symbols are considered equally probable *a priori*, i.e. when $\Pr\left(\boldsymbol{s}^i\right) = 1/M \,\forall i$, the MAP criterion simplifies into finding the symbol $\boldsymbol{s}^i$ that maximizes the likelihood: this is the Maximum Likelihood (ML) criterion. In this case, the estimated symbol is thus given by

$$\hat{\boldsymbol{s}} = \left\{ s_i \,\middle|\, \max_{i \in \{0,\ldots,M-1\}} p\left(\boldsymbol{r} \,\middle|\, \boldsymbol{s}^i\right) \right\}. \tag{1.34}$$

In the case of AWGN channel with variance σ_{ch}^2, the likelihood can be expressed

$$\begin{aligned} p\left(\boldsymbol{r} \,\middle|\, \boldsymbol{s}^i\right) &= \prod_{k=0}^{N_c-1} p\left(r_k \,\middle|\, s_k^i\right) \\ &= \prod_{k=0}^{N_c-1} \frac{1}{2\pi\sigma_{\text{ch}}^2} \exp\left\{-\frac{1}{2\sigma_{\text{ch}}^2}\|r_k - s_l^i\|^2\right\}, \end{aligned} \tag{1.35}$$

where the Euclidean distance between two complex numbers z_a and z_b is defined by

$$\|z_a - z_b\| = \sqrt{\left(\text{Re}\left(z_a\right) - \text{Re}\left(z_b\right)\right)^2 + \left(\text{Im}\left(z_a\right) - \text{Im}\left(z_b\right)\right)^2}. \tag{1.36}$$

When a linear modulation at the minimum bandwidth is used, the symbol $\boldsymbol{s}$ is composed of one chip, i.e. $N_c = 1$. The likelihood is expressed

$$p\left(r \,\middle|\, s^i\right) = \frac{1}{2\pi\sigma_{\text{ch}}^2} \exp\left\{-\frac{1}{2\sigma_{\text{ch}}^2}\|r - s^i\|^2\right\}, \tag{1.37}$$

and the ML decision becomes

$$\hat{r} = \left\{ s_i \,\middle|\, \min_{i\in\{0,\ldots,M-1\}} \|r - s_i\| \right\}. \tag{1.38}$$

The ML detector will thus search for the closest symbol in the constellation. This search can be also seen as dividing the constellation into M regions, called Voronoi regions, and searching in which region is the received symbol [20, p. 173].

When an orthogonal modulation is used, we have $N_c = M$. The signal can be demodulated in a coherent or a non-coherent way, in which case the phase of the received signal is assumed unknown. The coherent demodulation is treated first. The Euclidean distance of Equation (1.35) can be expressed

$$\begin{aligned} \|r_k - s_k^i\|^2 &= \left(\text{Re}\left(r_k\right) - \text{Re}\left(s_k^i\right)\right)^2 + \left(\text{Im}\left(r_k\right) - \text{Im}\left(s_k^i\right)\right)^2 \\ &= \left(\text{Re}\left(r_k\right)^2 + \text{Im}\left(r_k\right)^2\right) + \left(\text{Re}\left(s_k^i\right)^2 + \text{Im}\left(s_k^i\right)^2\right) - 2\left(\text{Re}\left(r_k\right)\text{Re}\left(s_k^i\right) + \text{Im}\left(r_k\right)\text{Im}\left(s_k^i\right)\right) \\ &= |r_k|^2 + |s_k^i|^2 - 2\,\text{Re}\left(r_k \cdot \overline{s_k^i}\right). \end{aligned} \tag{1.39}$$

thus giving a likelihood equal to

$$\begin{aligned} p\left(\boldsymbol{r} \,\middle|\, \boldsymbol{s}^i\right) &= \left(\frac{1}{2\pi\sigma_{\text{ch}}^2}\right)^M \prod_{k=0}^{M-1} \exp\left\{-\frac{1}{2\sigma_{\text{ch}}^2}\left(|r_k|^2 + |s_k^i|^2 - 2\,\text{Re}\left(r_k \cdot \overline{s_k^i}\right)\right)\right\} \\ &= \left(\frac{1}{2\pi\sigma_{\text{ch}}^2}\right)^M \exp\left\{-\frac{1}{2\sigma_{\text{ch}}^2}\sum_{k=0}^{M-1}|r_k|^2\right\} \exp\left\{-\frac{1}{2\sigma_{\text{ch}}^2}\sum_{k=0}^{M-1}|s_k^i|^2\right\} \exp\left\{\frac{1}{\sigma_{\text{ch}}^2}\sum_{k=0}^{M-1}\text{Re}\left(r_k \cdot \overline{s_k^i}\right)\right\} \\ &= \left(\frac{1}{2\pi\sigma_{\text{ch}}^2}\right)^M \exp\left\{-\frac{\|\boldsymbol{r}\|^2}{2\sigma_{\text{ch}}^2}\right\} \exp\left\{-\frac{\|\boldsymbol{s}^i\|^2}{2\sigma_{\text{ch}}^2}\right\} \exp\left\{\frac{1}{\sigma_{\text{ch}}^2}\text{Re}\left(\langle \boldsymbol{r}, \boldsymbol{s}^i\rangle\right)\right\}, \end{aligned} \tag{1.40}$$

where $\|\boldsymbol{r}\|$ is the Euclidean norm of the M dimensional vector $\boldsymbol{r}$, defined Equation (1.30).

Assuming that $\|s^i\| = C_{\text{st}}$, $\forall i \in \{0, \ldots, M-1\}$, where C_{st} is a constant with $C_{\text{st}} \in \mathbb{R}$ (i.e. an orthonormal alphabet), the three first terms of (1.40) are equal $\forall i$. The ML decision is now expressed

$$\hat{r} = \left\{ \boldsymbol{s}^i \,\middle|\, \max_{i\in\{0,\ldots,M-1\}} \text{Re}\left(\langle \boldsymbol{r}, \boldsymbol{s}^i\rangle\right) \right\}. \tag{1.41}$$

The ML detector performs the correlation of the received symbol over all the symbols from the alphabet, and searches for the correlation with the maximum real part. Since the signal is represented in M dimensions, the correlation with the i-th symbol of the alphabet represents the projection on the i-th dimension.

The case of non-coherent demodulation is treated in Appendix A. The ML decision is given by

$$\hat{r} = \left\{ \boldsymbol{s}^i \,\middle|\, \max_{i\in\{0,\ldots,M-1\}} \left|\langle \boldsymbol{r}, \boldsymbol{s}^i\rangle\right| \right\}, \tag{1.42}$$

meaning that the ML detector performs the correlation over the possible symbols, and searches for the maximum of the modulus of all the correlations. When ML decision is performed, by definition, a decision is made and all the possibilities of the alphabet but one are ignored. Another strategy can be chosen, which is to give a probabilistic value of the information bits depending on the observation of all the possible symbols.

1.3.3.2 Probabilistic Demodulation

In a probabilistic demodulator, the output consists of a probabilistic representation of the information bits. Assuming that r is the observation of the bit, the probabilistic representation of the bit is given by the Log Likelihood Ratio (LLR)

$$L(b) = \log \frac{p\left(r \mid b = +1\right)}{p\left(r \mid b = -1\right)}, \tag{1.43}$$

where $p\left(r \mid b = +1\right)$ (resp. $p\left(r \mid b = -1\right)$) is the likelihood that the bit b is equal to 1 (resp. -1). The sign of $L(b)$ gives the bit value (also called "hard value"), and the magnitude of $L(b)$ gives the reliability of the bit value.

In an alphabet, each symbol is associated to an information word containing $\log_2(M)$ bits, with the probability of the value of one bit tied to multiple symbols. For example, with the mapping given in Figure 1.7, the probability that the first bit is equal to 0 is given by the probability of having of the first symbol $\boldsymbol{s}^0$ (equal to $[1\,1\,1\,1]$ and associated to the information word $[0\,0]$) and the probability of having the second symbol $\boldsymbol{s}^1$ (equal to $[1\ -j\ -1\ 1]$ and associated to the information word $[0\,1]$), given the observation (i.e. the received symbol) $\boldsymbol{r}$. This gives the expression

$$\Pr\left(b_0 = 1 \mid \boldsymbol{r}\right) = \Pr\left(\boldsymbol{s}^0 \,\middle|\, \boldsymbol{r}\right) + \Pr\left(\boldsymbol{s}^1 \,\middle|\, \boldsymbol{r}\right). \tag{1.44}$$

The probability $\Pr\left(\boldsymbol{s}^i \,\middle|\, \boldsymbol{r}\right)$, $i \in \{0, \ldots, M-1\}$ is the APP of having the symbols $\boldsymbol{s}^i$ given the observation $\boldsymbol{r}$, presented previously.

This expression can be extended to any size of modulation and any information bit b_n with $n \in \{0, \ldots, \log_2(M) - 1\}$. We denote $\mathcal{B}_1^n$ (resp. $\mathcal{B}_{-1}^n$) the group of symbols which encodes an information word for which the bit b_n is equal to 1 (resp. -1). For the example of Figure 1.7, we have $\mathcal{B}_1^0 = \{\boldsymbol{s}^0, \boldsymbol{s}^1\}$. The APP of the value of the bit b_n given the received symbol is expressed with [21]

$$\Pr\left(b_n = u \mid \boldsymbol{r}\right) = \sum_{i \in \mathcal{B}_u^n} \Pr\left(\boldsymbol{s}^i \,\middle|\, \boldsymbol{r}\right), \tag{1.45}$$

where u is equal to 1 or -1. The log-APP ratio of the bit b_n is expressed

$$\log \frac{\Pr\left(b_n = +1 \mid \boldsymbol{r}\right)}{\Pr\left(b_n = -1 \mid \boldsymbol{r}\right)} = \log \sum_{i \in \mathcal{B}_1^n} \Pr\left(\boldsymbol{s}^i \,\middle|\, \boldsymbol{r}\right) - \log \sum_{i \in \mathcal{B}_{-1}^n} \Pr\left(\boldsymbol{s}^i \,\middle|\, \boldsymbol{r}\right), \tag{1.46}$$

and is equal to the LLR when the two values of the bit are equally probable, following Equation (1.33).

Alternatively, the LLR of b_n is expressed using the likelihood of the symbols with

$$L(b_n) = \log \sum_{i \in \mathcal{B}_1^n} p\left(\boldsymbol{r} \,\middle|\, \boldsymbol{s}^i\right) - \log \sum_{i \in \mathcal{B}_{-1}^n} p\left(\boldsymbol{r} \,\middle|\, \boldsymbol{s}^i\right). \tag{1.47}$$

For the case of BPSK modulation with an AWGN channel, r is a scalar and the two possible symbols are $+1$ and -1. The LLR are expressed, using Equation (1.37), with

$$\begin{aligned} L(b_n) &= \log\left(\frac{1}{\sqrt{2\pi}\sigma_{\text{ch}}} \exp\left\{-\frac{1}{2\sigma_{\text{ch}}^2}(r-1)^2\right\}\right) - \log\left(\frac{1}{\sqrt{2\pi}\sigma_{\text{ch}}} \exp\left\{-\frac{1}{2\sigma_{\text{ch}}^2}(r+1)^2\right\}\right) \\ &= -\frac{1}{2\sigma_{\text{ch}}^2}\left((r-1)^2 - (r+1)^2\right) \\ &= \frac{2r}{\sigma_{\text{ch}}^2}. \end{aligned} \tag{1.48}$$

For the case of orthogonal modulation with coherent detection and an AWGN channel, the LLR can then be expressed, using (1.40) and Equation (1.47), as

$$L(b_n) = \log \sum_{i \in \mathcal{B}_1^n} \exp\left\{\frac{1}{\sigma_{\text{ch}}^2} \text{Re}\left(\langle \boldsymbol{r}, \boldsymbol{s}^i \rangle\right)\right\} - \log \sum_{i \in \mathcal{B}_{-1}^n} \exp\left\{\frac{1}{\sigma_{\text{ch}}^2} \text{Re}\left(\langle \boldsymbol{r}, \boldsymbol{s}^i \rangle\right)\right\}. \tag{1.49}$$

1.3.3.3 Probability of Error

A modulation performance may be estimated by the probability of having binary errors after demodulation $\Pr(e)$. When considering an AWGN channel, the probability can be derived in its closed form or at the least an approximation can be given. For one of the simplest modulation, the BPSK modulation, this probability of error is given by [15, p. 271]

$$\Pr(e) = \frac{1}{2}\operatorname{erfc}\left(\sqrt{\frac{E_b}{N_0}}\right), \tag{1.50}$$

where erfc is a decreasing function defined as

$$\operatorname{erfc}(x) = \int_x^{+\infty} \frac{2}{\sqrt{\pi}} e^{-z^2} dz. \tag{1.51}$$

This confirms the intuition that when E_b/N_0 (which is equal to the SNR for BPSK modulation) is increased, the probability of error is reduced.

For M-PSK with Gray mapping, the probability of error is approximated by [15, p. 273]

$$\Pr(e) \simeq \frac{1}{\log_2(M)}\operatorname{erfc}\left(\sqrt{\log_2(M)\frac{E_b}{N_0}} \cdot \sin\left(\frac{\pi}{M}\right)\right), \tag{1.52}$$

while in the case of M-QAM modulation and assuming a square shape of the constellation, the probability of error is approximated with [22]

$$\Pr(e) \simeq \frac{\sqrt{M}-1}{\sqrt{M}\log_2\left(\sqrt{M}\right)}\operatorname{erfc}\left(\sqrt{\frac{3\log_2(M)}{2(M-1)}\frac{E_b}{N_0}}\right). \tag{1.53}$$

For the case of M-ary orthogonal modulation with coherent detection, the details of the computations of the probability of error are given in Appendix B. The probability is expressed

$$\Pr(e) = \frac{M}{2(M-1)\sqrt{2\pi}}\int_{-\infty}^{+\infty}\left[1-\left(1-\frac{1}{2}\operatorname{erfc}\left(\frac{y}{\sqrt{2}}\right)\right)^{M-1}\right]\exp\left\{-\frac{1}{2}\left(y-\sqrt{\log_2(M)\frac{E_b}{N_0}}\right)^2\right\}dy, \tag{1.54}$$

with a union bound defined as [15, p. 263] [20, p. 239]

$$\Pr(e) \leq \frac{M-1}{2}\operatorname{erfc}\left(\sqrt{\frac{\log_2(M)}{2}\frac{E_b}{N_0}}\right). \tag{1.55}$$

In Figure 1.8, the spectral efficiencies and the E_b/N_0 required to reach a probability of error of $\Pr(e) = 10^{-5}$ have been depicted for various sizes of M-ary linear and orthogonal modulations, using the closed form expressions. The maximum achievable spectral efficiency, as defined by Equation (1.15), is also represented. For the linear modulations, the M-PSK and M-QAM, increasing the size of the alphabet allows for better spectral efficiency, but also increases the required E_b/N_0. The QAM modulation is more energy efficient than the PSK, since for the same spectral efficiency, the required E_b/N_0 is reduced (for example, for $M = 16$ or 4 bits·s^{-1}·Hz^{-1}, the E_b/N_0 gain of using QAM modulation instead of PSK is 4dB).

For orthogonal modulations, performance as a function of the size of alphabet M follows a different trend; when M is increased, the spectral efficiency decreases, as explained by the expression of η in Equation (1.32). However, the value of E_b/N_0 required decreases. The modulation becomes more and more energy efficient, at the expense of the spectral efficiency reduction. The symbol error probability $\Pr(e_s)$ of orthogonal modulation can be shown to be bounded, for large values of M and under the condition $\frac{E_b}{N_0} > \log 2$, by [15, p. 388]

$$\Pr(e_s) < \exp\left\{-\log_2(M)\left(\sqrt{\frac{E_b}{N_0}}-\sqrt{\log 2}\right)^2\right\}. \tag{1.56}$$

Hence $\lim_{M\to\infty}\Pr(e_s) = 0$ providing that E_b/N_0 is superior to $\log 2 \simeq 0.693 = -1.59\,\text{dB}$, which is the E_b/N_0 limit of the channel capacity when $\eta \to 0$ (cf Section 1.2.3). This means that the M-ary orthogonal modulations reach the channel capacity with the best achievable energy efficiency when the size of M tends to infinity. However, an infinite size of M induces a spectral efficiency tending toward 0, making this solution practically unrealistic, as an infinite bandwidth would be required for a fixed rate R (or, alternatively, an infinite time would be required to transmit a given number of bits).

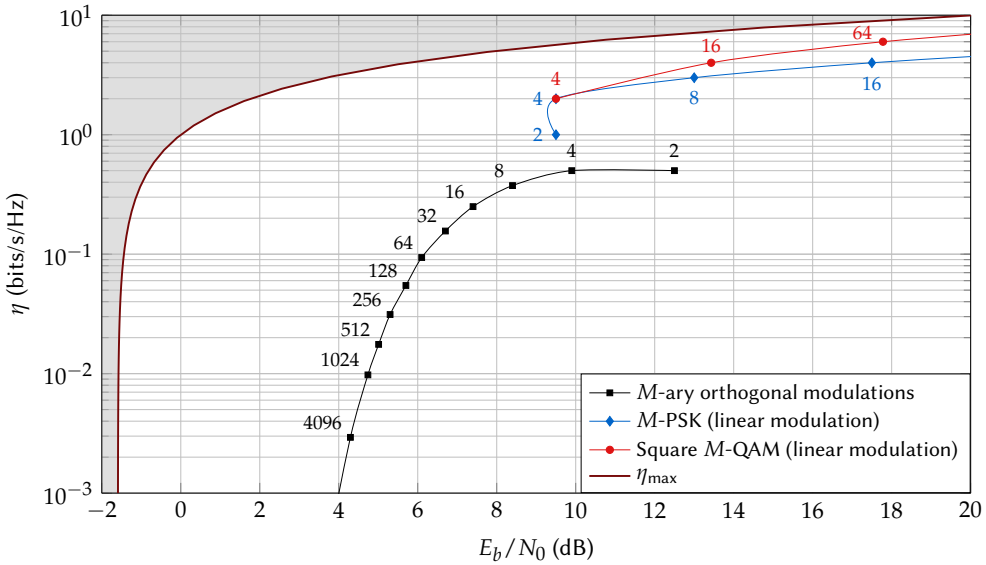

FIGURE 1.8 – *Comparison of the spectral efficiency and the required E_b/N_0 for bit probability of error $\Pr(e) = 10^{-5}$ of linear and orthogonal modulations, under the AWGN channel. The maximum achievable spectral efficiency according to the channel capacity from* (1.15) *is also represented.*

1.3.4 Forward Error Correction

As previously presented, the signal is affected by noise during its transmission in the channel. After demodulation, bit errors may be present in the information packet. In order to avoid these errors, redundancy bits can be added to the information source at the transmitter side, so that the receiver can detect and correct the errors that may have happened during the transmission. This is FEC, also called channel coding. In Figure 1.4, FEC is realized by the Encoder at the transmitter side, and the Decoder at the receiver side. We assume the number of information bits is equal to Q. One of the simplest forms of redundancy is repetition of the information bits. For example, if the information word to send is 010 ($Q = 3$), the encoder will repeat each bit three times, and send 000111000. At the receiver side, the different repetitions are recombined, and errors can be detected. If the word 000**1**01000 is received after hard demodulation for example (with one error in bold), the receiver can still conclude that the information word 010 was sent. This simple form of redundancy is called the repetition code. Other codes can be used, and depending on the choice of code, a specific number of errors can be detected or corrected in a single codeword, i.e. a group of bit at the output of the encoder (the 3 repeated bits for the previous example). A code is often characterized by its *code rate*, i.e. the rate of the input information bits over the encoded bits (equal to $1/3$ for the example).

Since the formulation of the channel capacity by Shannon, channel coding strived to increase the energy efficiency of the communication system as close as possible to the limit [23]. In this section, some channel coding strategies are presented, from the early block codes to the capacity approaching Turbo Codes (TCs) [8]. For all computations, we assume BPSK modulation and AWGN channel, and the polar representation of the bits (± 1) is used.

1.3.4.1 Block codes

The repetition code previously presented belongs to a family of codes called "block codes". A block code associates an information word of length q to a codeword of length N_c, giving a code rate $R_c = q/N_c$. One important characteristic of a code is its minimum distance $d_{\min}$, defined as the minimum of all Hamming distances between the codewords. The Hamming distance between two binary vectors $\boldsymbol{x}$ and $\boldsymbol{y}$ of length N_c is defined by

$$d = \sum_{k=0}^{N_c-1} |x_k - y_k|, \tag{1.57}$$

which is the number of positions at which the corresponding elements of the vectors are different.

This distance $d_{\min}$ gives the detection and correction capabilities of the code, as the number of possible error detected is equal to $d_{\min} - 1$ and the number of errors that can be corrected is equal to $\lfloor (d_{\min} - 1)/2 \rfloor$ [15, p. 413], where $\lfloor \cdot \rfloor$ denotes the floor operator.

For the repetition code of size N_c, the alphabet of codewords consists of two codewords: all 0's and all 1's. One bit is associated to one codeword of length N_c and the code rate is $R_c = 1/N_c$. The Hamming distance between the

b_0	b_1		h_0	h_1	h_2	h_3	
1	1	$\rightarrow$	1	1	1	1	$\boldsymbol{h}^0$
−1	1	$\rightarrow$	1	−1	1	−1	$\boldsymbol{h}^1$
1	−1	$\rightarrow$	1	1	−1	−1	$\boldsymbol{h}^2$
−1	−1	$\rightarrow$	1	−1	−1	1	$\boldsymbol{h}^3$

FIGURE 1.9 – *Mapping of the Hadamard code for $M = 4$.*

two codewords is N_c, thus this code can detect $N_c - 1$ errors and correct $\lfloor (N_c - 1)/2 \rfloor$. Despite the poor code rate, repetition code is very often used, as it gives correction capabilities with ultra low complexity requirements.

A well known example of block code is the Hamming Code. Developed by Richard W. Hamming in 1950 [24], this was one of the first error-correcting codes. In the initial form of the code, information bits are grouped by $q = 4$, and three redundancy bits are computed as the parity of some of the initial 4 bits. Codewords are hence composed of the 4 information bits (called the systematic bits), and 3 redundancy bits (the parity bits). The code rate is 4/7, and its minimum distance is equal to $d_{\min} = 3$. This code can then detect 2 errors and correct 1.

Orthogonal codes are also a family of block codes, for which the alphabet of codewords is orthogonal. If M is the alphabet size, and $\{i, j\}^2 \in \{0, \ldots, M-1\}^2$, the orthogonality condition can be expressed

$$\langle \boldsymbol{c}^i, \boldsymbol{c}^{i'} \rangle = \begin{cases} M & \text{if } i = i' \\ 0 & \text{if } i \neq i' \end{cases}, \tag{1.58}$$

where $\boldsymbol{c}^i$ and $\boldsymbol{c}^{i'}$ are codewords from the alphabet, represented as row vectors of size M. This definition of orthogonality is strictly equivalent to the one given in Equation (1.28), and the definition of the scalar product Equation (1.29) is the same, but the elements c_k^i and c_k^j, with $k \in \{0, \ldots, M-1\}$ are equal to ± 1. The Hadamard code is an orthogonal block code, and its alphabet is constructed using the Hadamard matrix $\boldsymbol{H}_M$, defined recursively with

$$\boldsymbol{H}_M = \begin{bmatrix} \boldsymbol{H}_{M/2} & \boldsymbol{H}_{M/2} \\ \boldsymbol{H}_{M/2} & -\boldsymbol{H}_{M/2} \end{bmatrix} \tag{1.59}$$

and $\boldsymbol{H}_1 = 1$. The matrix size is $M \times M$, with M a power of 2. The alphabet is thus composed of M codewords of length M. Codewords are chosen as rows or columns of the matrix $\boldsymbol{H}_M$, and denoted $\boldsymbol{h}^i$, $i \in \{0, \ldots, M-1\}$. As the alphabet contains M codewords, each codeword is associated to an information word of size $\log_2(M)$, giving a code rate of $R_c = \log_2(M)/M$. Every codeword has a Hamming weight equal to $M/2$ and the minimum distance of the code is $M/2$. The code can detect $M/2 - 1$ errors and correct $(M-2)/4$ errors. For the case $M = 4$, the Hadamard alphabet and its mapping are given in Figure 1.9. One can notice that the column h_1 is equal to b_0, while the column h_2 is equal to b_1. The code is said to be systematic, as its output includes the uncoded input message.

1.3.4.2 Probabilistic Decoding of Block Codes

The decoding procedure of block code can be done using different strategies, but the optimal decoding is done through MAP decoding. If we consider the demodulated codeword $\boldsymbol{r}$ of length N_c, the APP of having the codeword $\boldsymbol{c}^i$ given the observation is [21]

$$\Pr\left(\boldsymbol{c}^i \,\middle|\, \boldsymbol{r}\right) = \frac{\Pr\left(\boldsymbol{c}^i\right)}{p\left(\boldsymbol{r}\right)} \prod_{k=0}^{N_c-1} p\left(r_k \,\middle|\, c_k^i\right), \tag{1.60}$$

following Bayes' rule. The term c_k^i refers to the value of the bit at index k c_k for the i-th codeword. More generally, we can refer to the position c_k, and the LLR of the bit c_k is expressed

$$L(c_k) = \log \frac{p\left(r_k \,|\, c_k = +1\right)}{p\left(r_k \,|\, c_k = -1\right)}. \tag{1.61}$$

If $\Pr\left(c_k = +1\right) = \Pr\left(c_k = -1\right) = 1/2$ then $p\left(r_k \,|\, c_k = +1\right) + p\left(r_k \,|\, c_k = -1\right) = 2p\left(r_k\right)$, and

$$p\left(r_k \,|\, c_k = +1\right) = 2p\left(r_k\right) \frac{e^{L(c_k)}}{1 + e^{L(c_k)}} = 2p\left(r_k\right) \frac{e^{-\frac{1}{2}L(c_k)} e^{\frac{3}{2}L(c_k)}}{\left(1 + e^{-L(c_k)}\right) e^{L(c_k)}} = 2p\left(r_k\right) \frac{e^{-L(c_k)/2}}{1 + e^{-L(c_k)}} e^{L(c_k)/2}, \tag{1.62}$$

which can be generalized for both values $u = \pm 1$ using

$$p\left(r_k \mid c_k = u\right) = \vartheta(c_k)\, e^{L(c_k)u/2}, \tag{1.63}$$

with

$$\vartheta(c_k) = 2p\left(r_k\right) \frac{e^{-L(c_k)/2}}{1 + e^{-L(c_k)}}. \tag{1.64}$$

As the bit c_k takes the value c_k^i for the i-th codeword, the APP is expressed

$$\begin{aligned}
\Pr\left(\boldsymbol{c}^i \,\middle|\, \boldsymbol{r}\right) &= \frac{\Pr\left(\boldsymbol{c}^i\right)}{p\left(\boldsymbol{r}\right)} \prod_{k=0}^{N_c-1} p\left(r_k \,\middle|\, c_k = c_k^i\right) \\
&= \frac{\Pr\left(\boldsymbol{c}^i\right)}{p\left(\boldsymbol{r}\right)} \prod_{k=0}^{N_c-1} \vartheta(c_k) \exp\left\{\frac{L(c_k)c_k^i}{2}\right\} \\
&= \frac{\Pr\left(\boldsymbol{c}^i\right)}{p\left(\boldsymbol{r}\right)} \left(\prod_{k=0}^{N_c-1} \vartheta(c_k)\right) \exp\left\{\frac{1}{2} \sum_{k=0}^{N_c-1} L(c_k)c_k^i\right\}.
\end{aligned} \tag{1.65}$$

When all the codewords are equally probable, the decision of the codeword is expressed

$$\hat{c} = \left\{ \boldsymbol{c}^i \,\middle|\, \max_{i \in \{0,\ldots,M-1\}} \sum_{k=0}^{N_c-1} L(c_k)c_k^i \right\}. \tag{1.66}$$

where M is the alphabet size. This is equivalent to a ML decision. Once the codeword is estimated, the associated information word is chosen.

A probabilistic output of the decoder can also be computed, very much like the probabilistic output of the demodulator, with

$$L(b_n) = \log \sum_{i \in \mathcal{B}_1^n} \Pr\left(\boldsymbol{c}^i \,\middle|\, \boldsymbol{r}\right) - \log \sum_{i \in \mathcal{B}_{-1}^n} \Pr\left(\boldsymbol{c}^i \,\middle|\, \boldsymbol{r}\right). \tag{1.67}$$

where $\mathcal{B}_1^n$ (resp. $\mathcal{B}_{-1}^n$) is the set of codewords which encode an information word for which the bit b_n is equal to 1 (resp. -1).

For the case of repetition, there are only two codewords of size N_c (equal to the number of repetition): $11\ldots1$ or $-1\ -1\ \cdots -1$. The output LLR is easily shown to be

$$L(b_n) = \sum_{k=0}^{N_c-1} L(c_k). \tag{1.68}$$

It is possible to consider a non-probabilistic input for the decoder. This case refers to hard decoding, and is by definition less efficient than the ML decoding. Classic hard decoding procedures are syndrome decoding or minimizing the Hamming distance.

1.3.4.3 Convolutional Codes

Another widely used family of codes are the convolutional codes. Their invention is credited to Peter Elias in 1955 [25]. Unlike block codes where two consecutive codewords do not share information, convolution introduces the notion of memory in the code. To introduce this type of code, a simple convolutional code, the accumulator is presented. Its encoder is given in Figure 1.10 (a). The Q input bits are sequentially encoded, and for each input bit the encoder outputs the input bit (the systematic bits) and the result of the binary sum of the input and the content of the memory (the parity bit). The memory is then updated with the value of the parity bit. The overall rate of the accumulator is then $1/2$. The use of the memory bonds two consecutive codewords. The constraint length of a convolutional code is denoted with K (for the accumulator, $K = 2$), and its number of memories is denoted D with $D = K - 1$.

Alternatively, a convolutional code can be represented as a finite state machine. The input changes the states, which are the different configurations of the memory units. In the case of the accumulator, the memory has two states, either the value 0 is stored, or the value 1. The transitions between the different states depending on the input are represented by a trellis. The trellis of the accumulator is given in Figure 1.10 (b). On each transition, the

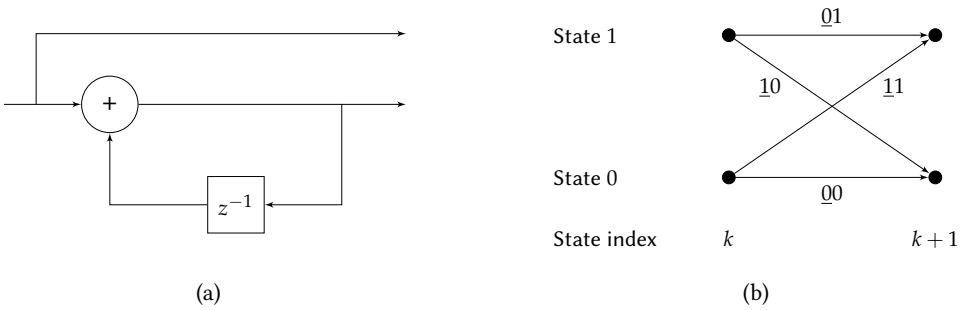

FIGURE 1.10 – *Encoder (a) and trellis (b) of the accumulator.*

output codeword is labeled and the systematic bit (i.e. the input) is underlined. The alphabet of codewords is thus of size 4, and an input value of 1 switches the state of the memory.

The initial and final states of the memory units can be chosen to be equal to a specific value, *e.g* 0. As the state of the memory depends on the input information word which is of length Q, it is not possible to predict the final state of the memory; however, it is possible to append some extra input bits which will force the memory back to the 0-state. This choice of configuration for the initial and final states is referred to as zero-tailed termination. For the accumulator, 2 extra bits need to be outputed for the memory to go back in the 0-state. The effective rate of the accumulator is then

$$R_c = \frac{Q}{2Q+2}, \tag{1.69}$$

which is lower than $1/2$, but can be approximated to $1/2$ for large values of Q. In order to avoid these extra bits, tail biting encoding can be considered [26], where the initial and final states have a similar but unknown value. This is done by setting the memory units as equal to the value of the $K-1$ last input bits.

A convolutional encoder is usually characterized by generators, which describe the way the input bit and the memories are combined to give the output bit. Another rate $1/2$ convolutional encoder is presented in Figure 1.11 (a). If b is the input bit and z^{-i}, $i \in \{1,2,3\}$ the memories, the output of the first adder F is given by the vector product $f = [b\ z^{-1}\ z^{-2}\ z^{-3}] \otimes [1\,0\,1\,1]^\intercal$, where $\otimes$ is the binary product. The binary vector $[1\,0\,1\,1]^\intercal$ can be represented in octal by 13, and is the feedback generator. The output of the adder G is given by $g = [f\ z^{-1}\ z^{-2}\ z^{-3}] \otimes [1\,1\,0\,1]^\intercal$, where the binary vector $[1\,1\,0\,1]^\intercal$ is 15 in octal: this is the feedforward generator. The code is thus represented by the two polynomials [13 15], and each polynomial is of length $K+1$. The example is a Recursive Systematic Convolutional (RSC) code. The first output is the input bit, and the structure of the encoder consists in a feedback loop. The code with the same generators can be represented in its non-recursive and non-systematic form.

The trellis of the [13 15] code is given in Figure 1.11 (b). Since there are 3 memories, the memory units can be in $2^3 = 8$ different configurations, hence the 8 different states in the trellis. From each state, two different transitions are possible: if the input is 0 (dashed line), or if the input is 1 (plain line). There are 16 possible transition. As there are two outputs, there are also 4 different codewords, which means that each codeword is the output corresponding to 4 transitions. In order to set the memory units back to the 0 state, 3 additional bits must be encoded (or 3 extra codewords must be transmitted). The rate of the code is

$$R_c = \frac{Q}{2Q+6}. \tag{1.70}$$

A generalization of the definition of the convolutional code can be done. When considering q inputs and N_c outputs ($q = 1$ and $N_c = 2$ for the [13 15] example), the code is characterized by $q \times N_c$ generators, and the rate is given by $R_c = q/N_c$ (without considering the trellis termination). The length of the polynomial vectors is K, equal to the constraint length, and there are $D = K-1$ memories. The trellis has 2^D states and $2^q \times 2^D$ transitions. D extra input bits must be appended to close the trellis (i.e. set it back to the 0-state).

1.3.4.4 Trellis Decoding of Convolutional Codes

As presented for the block codes, the optimal way of decoding convolutional code is using ML decoding. Because of the use of memories, the code cannot be decoded like a block code. A specific information bit sequence of size Q gives a specific output, which means that 2^Q different encoded sequences are possible. ML decoding would require the comparison of these 2^Q sequences, which is highly unpractical when the value of Q increases. Elias in [25] made the same conclusion, but in 1967 Andrew Viterbi proposed an efficient algorithm [27] which uses the trellis

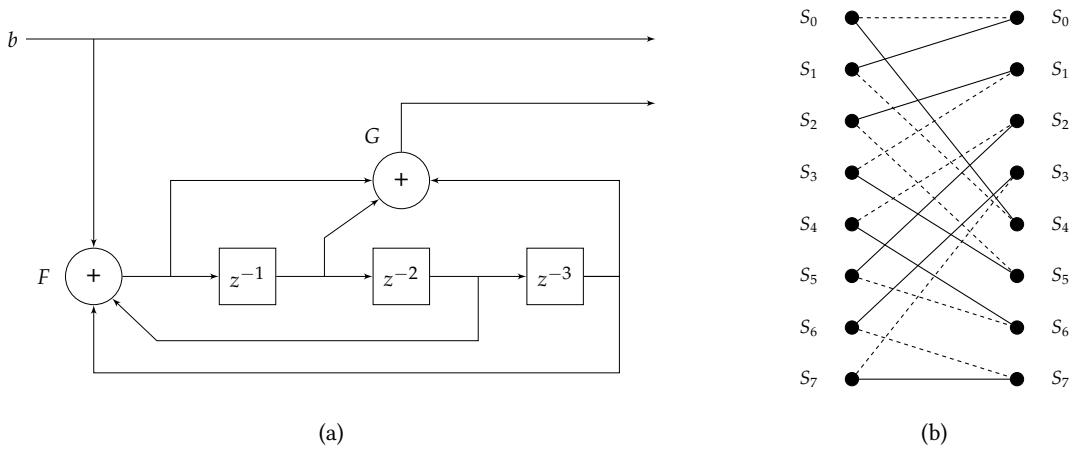

FIGURE 1.11 – *Encoder (a) and trellis (b) of the* [13 15] *convolutional code in its recursive form*

structure of the convolutional code to asymptotically achieve ML performance. As it demonstrates significantly better performance than block codes, convolutional code has been widely used for numerous applications [28], including space communications [29], and is still used nowadays in numerous communication systems.

The principle of the Viterbi algorithm is to estimate, given the received codewords, what is the most likely path through the trellis. In order to do so, the algorithm computes branch and path metrics, obtained using the Hamming distance of the received codewords with the possible codewords. Moving forward in the trellis, the algorithm will sequentially save a survivor path, the most likely one according to the metric used. Eventually, only one path through the whole trellis is chosen and the information bit sequence corresponding to this path is selected as output. The initial version of the Viterbi algorithm deals with binary inputs and outputs hard values of the information bits; it can however also be used with a probabilistic input and an Euclidean metric (this algorithm is referred to as Soft Viterbi in the rest of this document). Another version of the Viterbi algorithm is the Soft-Output Viterbi Algorithm (SOVA) [30], where *a priori* information on the input bits is taken into account.

The Viterbi algorithm is actually known to minimize the word error probability, but not the bit error probability. The optimal algorithm regarding this error probability is the trellis-based symbol-by-symbol MAP algorithm, also called the Bahl, Cocke, Jelinek and Raviv (BCJR) algorithm, proposed in 1974 [31]. This algorithm, detailed in Appendix C, computes forward and backward recursions in the trellis to evaluate the probabilities of the trellis states and transitions, to finally give an estimate of the APP of the information bits. When discovered, the authors admitted that the BCJR complexity was such that it could not be considered as an alternative to the Viterbi algorithm, especially since the bit error probability improvement is minimal. However, using the BCJR algorithm revealed itself crucial when considering iterative decoding methods.

1.3.4.5 Turbo Codes

The turbo principle was invented by Berrou, Glavieux and Thitimajshima in 1993 [8]. Their technique was rapidly shown to be able to closely approach the channel capacity, and is considered a major breakthrough in channel coding. The concept relies on the parallel concatenation of two RSC encoders separated by an interleaver, as presented in Figure 1.12 (a). The original proposition consisted in two rate $1/2$ RSC codes. With the use of the interleaver, both encoders operate on the same set of information bits, but have different input sequences, and thus different output sequences. As the two encoders are systematic, the input bits are only transmitted once and the data rate is $1/3$. The encoding process is called Parallel Concatenated Convolutional Code (PCCC). If the principle of code concatenation was proposed in [32] long before the invention of TC, the novelty of the principle was mainly in the decoding procedure, with the use of iterative decoding.

The architecture of the decoder is depicted in Figure 1.12 (b). It is composed of two decoders, one for each RSC code, and several interleavers. Each decoder uses the BCJR to estimate the APP of the information bits, or more precisely the log-APP ratios of the information bits, defined as

$$L\left(b_{n,t} \,\middle|\, \boldsymbol{R}_1^N\right) = \log \frac{\Pr\left(b_{n,t} = +1 \,\middle|\, \boldsymbol{R}_1^N\right)}{\Pr\left(b_{n,t} = -1 \,\middle|\, \boldsymbol{R}_1^N\right)}, \tag{1.71}$$

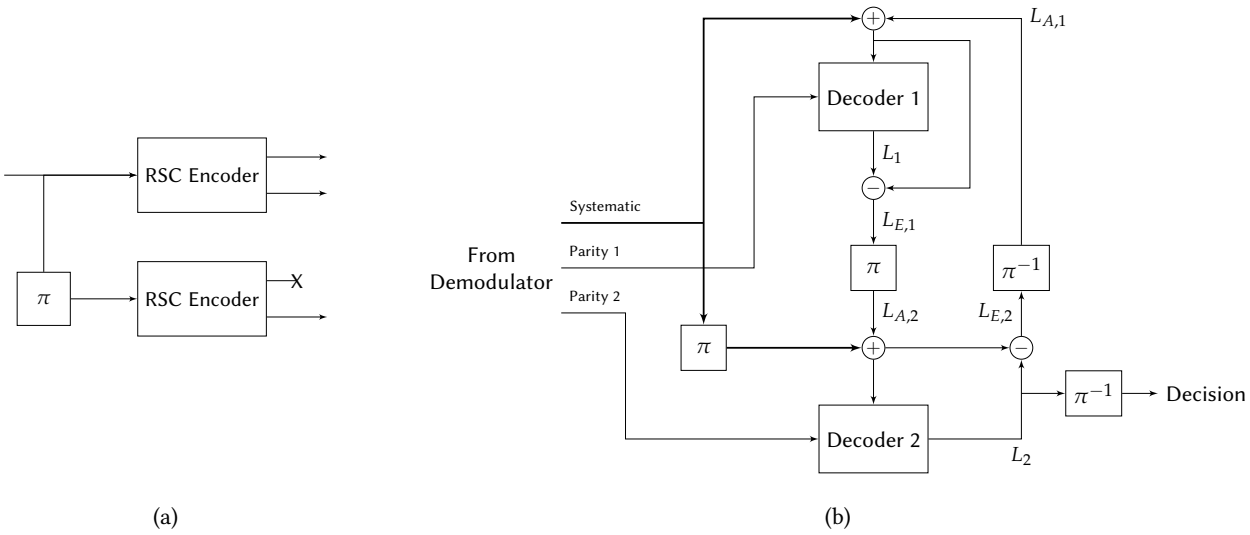

FIGURE 1.12 – *Principle of Turbo Code encoder (a) and decoder (b)*

where $\boldsymbol{R}_1^N = [\boldsymbol{r}_1, \boldsymbol{r}_2, \ldots, \boldsymbol{r}_N]$ is the received sequence of codewords and $b_{n,t}$ the information bit at index n of the t-th information word. In turbo decoding, unlike usual convolutional codes decoding, one decoder uses both the information from the channel and the output information generated by the other decoder. In the algorithm described in Appendix C, the likelihood of a codeword is now weighted by the *a priori* information of having that codeword, coming from the other decoder. Considering the noisy codeword received at instant t $\boldsymbol{r}_t$, a codeword $\boldsymbol{c}^i$ of the alphabet and its associated information word $\boldsymbol{b}^i$, with $i \in \{0, \ldots, M-1\}$, the receiver computes, as demonstrated in Section C.2.2, Equation (C.27)

$$p\left(\boldsymbol{r}_t \,\middle|\, \boldsymbol{c}_t^i\right) \Pr\left(\boldsymbol{c}_t^i\right) = C_{\text{st}} \exp\left\{\frac{1}{2}\sum_{k\in\mathcal{S}}\left((L(b_{k,t}) + L_A(b_{k,t}))b_{k,t}^i\right) + \frac{1}{2}\sum_{k\in\mathcal{P}} L(c_{k,t})c_{k,t}^i\right\}. \tag{1.72}$$

The sum over $\mathcal{S}$ (resp. $\mathcal{P}$) represents the sum over the indexes corresponding to the systematic positions (resp. the parity positions). There are $\log_2(M)$ systematic positions, and $N_c - \log_2(M)$ parity positions. $b_{k,t}$ refers to the bit at index k of the information word associated to the received codeword at instant t, and $c_{k,t}$ to the parity bit at index k. $L(b_{k,t})$ (resp. $L(c_{k,t})$) is the LLR of the bit $b_{k,t}$ (resp. $c_{k,t}$), and $L_A(b_{k,t})$ the *a priori* log ratio on the information bits, defined as

$$L_A(b_{k,t}) = \log\frac{\Pr\left(b_{k,t} = +1\right)}{\Pr\left(b_{k,t} = -1\right)}. \tag{1.73}$$

Finally, C_{st} is a constant independent of i, cancelled out in further computation in the BCJR algorithm. Equation (1.72) clearly shows how the *a priori* information is included to the LLR at the systematic bits positions.

When selecting the information bit with index $k = n$ at time index t, the log-APP of the information bits given the received sequence of codewords $\boldsymbol{r}_1^N$, can be factorized to, according to Equation (C.30),

$$L\left(b_{n,t} \,\middle|\, \boldsymbol{R}_1^N\right) = L\left(b_{n,t}\right) + L_A\left(b_{n,t}\right) + L_E. \tag{1.74}$$

This means that the log-APP contains three informations: the LLR of the information bit from the channel $L\left(b_{n,t}\right)$, the *a priori* LLR $L_A\left(b_{n,t}\right)$ from the other decoder and the extrinsic information generated by the algorithm L_E (which depends on all the other bits). Only the extrinsic information is sent to the other decoder as *a priori*, as this will be new information from its point of view. The turbo name comes from this re-injection of the information between decoders, and similar to the principle used in turbo charged car engines.

The general decoding procedure can be described in several steps:

1. The *a priori* LLR are initialized to 0 (i.e. no *a priori* information).
2. Decoder 1 sums the LLR of the systematic bits from the channel and the *a priori* LLR $L_{A,1}$, and uses the LLR of the parity bits to compute (1.72). The BCJR algorithm is applied to compute the log-APP of the information bits L_1;

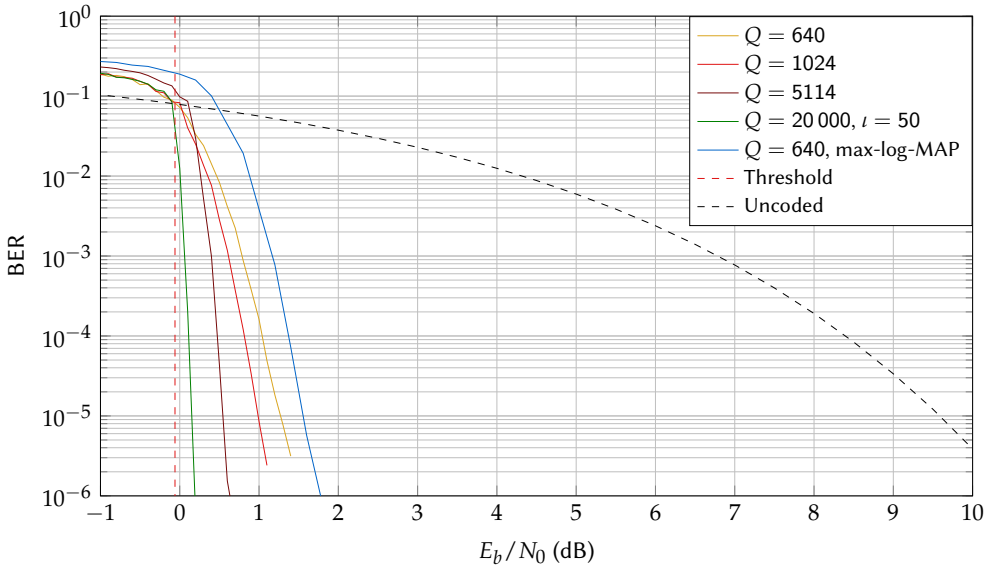

FIGURE 1.13 – *Performance of the* [13 15] *TC for various interleaver sizes* Q*, under the AWGN channel. A total of* $\iota = 10$ *iterations are performed unless stated otherwise.*

3. The extrinsic information of the first decoder $L_{E,1}$ is computed, interleaved and sent as the *a priori* LLR $L_{A,2}$ to the second decoder;
4. Decoder 1 sums the interleaved LLR of the systematic bits from the channel and the *a priori* LLR $L_{A,2}$, and uses the LLR of the parity bits to compute (1.72). The BCJR algorithm is applied to compute the log-APP of the information bits L_2;
5. The extrinsic information $L_{E,2}$ of the second decoder is computed and deinterleaved, and sent back to the first decoder, which will treat it as *a priori* information $L_{A,1}$.

The steps 2 to 5 correspond to one iteration. They can be repeated as many times as necessary. After a certain number of iterations, the APP of the information bits from the second decoder L_2 can be used to make a hard decision on the bits.

The typical performance of a TC using Monte Carlo simulations is depicted in Figure 1.13. The performance metric used is the Bit Error Rate (BER), defined as the ratio of erroneous bits over the total number of bits. The BER was computed for several values of E_b/N_0 and 4 values for the information block size Q (also equal to the interleaver size). The performance of uncoded BPSK is also depicted, demonstrating the gain offered by the TC. The BER performance of a TC is generally characterized by 3 regions:

- The *non-convergence region*, which corresponds to low values of E_b/N_0, where the BER stays high and does not evolve;
- The *waterfall region*, where the BER drops significantly. The starting E_b/N_0 value of the waterfall can be estimated by computing the threshold of the decoder (also called the turbo cliff position). It is the minimum level of E_b/N_0 required for the decoder to be able to correct all the erroneous bits, regardless of the interleaver size and the number of iterations performed. It represents the asymptotic behavior of the decoder. Evaluating the threshold can be done using the EXtrinsic Information Transfer (EXIT) chart tool [33], which is presented for the case of TC in Appendix D. The estimated threshold for the code considered is given in Figure 1.13;
- The *error floor region*, which is the region of E_b/N_0 where the BER performance flattens compared to the waterfall and decreases slowly with E_b/N_0.

Both the waterfall and the error floor regions depend on the interleaver size Q and the choice of constituent RSC codes. The error floor can be upper bounded using the distance spectrum of the code [34], and the bound can be approximated using only the low-weight codewords [35]. Concerning the waterfall, the dependence with Q corresponds to the loss of diversity when shortening the information block length [33]; this diversity is introduced thanks to both versions (one interleaved, the other not) of the same message.

The EXIT chart is a very useful tool when it comes to code or system design and analysis [36], and its interpretation gives indications on the number of iterations required to correct the maximum number of bits; during the waterfall, a large number of iterations are required when long interleaver sizes are considered, as a large number

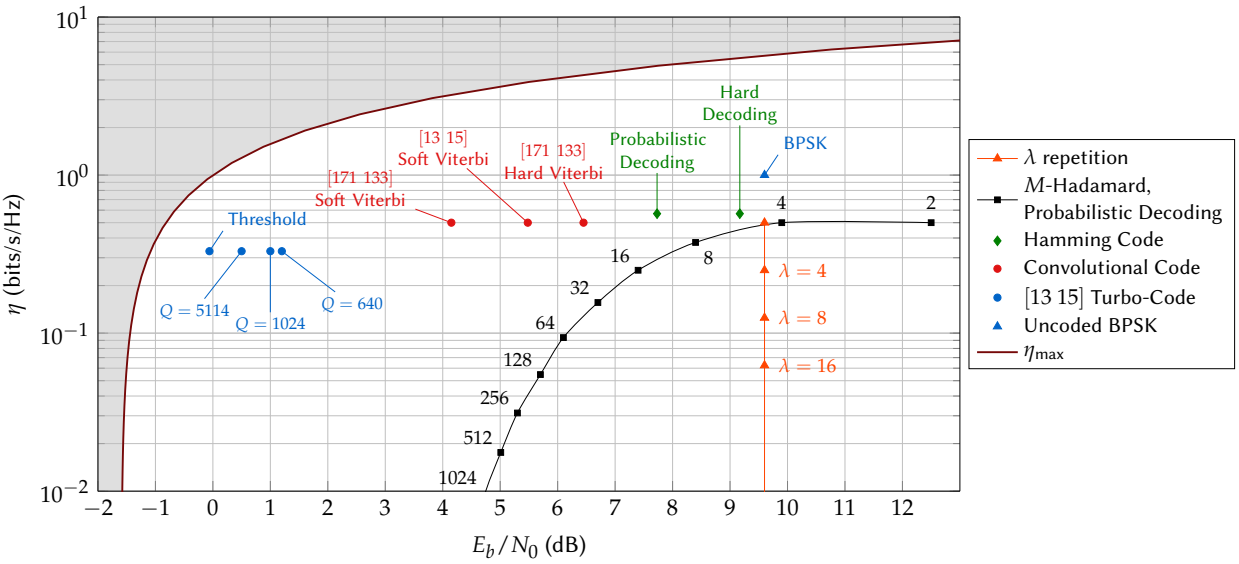

FIGURE 1.14 – *Comparison of the spectral efficiency and the required E_b/N_0 at BER $= 10^{-5}$ of various FEC schemes, under the AWGN channel. The maximum achievable spectral efficiency according to the channel capacity from* (1.15) *is also represented.*

of information exchanges are required for the decoder to correct erroneous bits. During the error floor, the decoder converges in only a few iterations, and the performance is dominated by the low-weight codewords.

In practical systems, the computation of the BCJR can reveal itself to be tricky because of the presence of exponential terms and multiplications. While the use of the SOVA algorithm to decode the trellis could be considered [37, 38], suboptimal MAP algorithm can be used such as the log-MAP and max-log-MAP algorithms [39]. The max-log-MAP algorithm relies on the simplification

$$\log\left(\sum_i e^{x_i}\right) \simeq \max_i(x_i), \tag{1.75}$$

and all computations can be done using only additions and max operations. In Figure 1.13, the BER performance of the decoder when using the suboptimal max-log-MAP is depicted, for the interleaver size $Q = 640$. The simplification is done at the expense of some performance loss, approximately 0.3dB for a BER of 10^{-5}, but this can be overcome with the use of weighting functions on the exchanges of extrinsic information inside the decoder [40].

1.3.4.6 PERFORMANCE

The performance of several schemes presented here are given in Figure 1.14. We represented the spectral efficiency versus the E_b/N_0 needed to achieve a BER of 10^{-5}, along with the maximum achievable spectral efficiency as given in Equation (1.16). As we used BPSK modulation for the simulations, the performance of the uncoded BPSK is also given.

The performance of three block codes are represented: the repetition code, the Hamming code and the Hadamard code. For the Hamming code, the performance of two decoders are given: a hard decoder, which searches for the codeword of the alphabet with minimum Hamming distance with the received codeword, and a probabilistic decoder which computes the ML decoding. The gain of using probabilistic decoding for block codes is 1.3dB, but requires a higher computing capacity. The Hadamard block code is an orthogonal code; under AWGN conditions, its performance with BPSK modulation is strictly equivalent to orthogonal modulation, as the computation of the error probability is similar. This code can reach the channel capacity for an infinite value of alphabet size M. The last block code presented here is the repetition code, with probabilistic decoding (i.e. recombination of the LLR, as given in Equation (1.68)). This code has no influence on the value of E_b/N_0 whatever the size of the repetition. It only reduces the spectral efficiency. However, one can notice with Equation (1.9) that using the code will reduce the level of SNR required for the scheme. This is the main reason why this code is used in a numerous amount of communication systems.

The figure 1.14 also depicts the performance of two convolutional codes: the [13 15] code previously presented and the [171 133] code, in their non-recursive form. This last code has a constraint length of 7, and is one of the rate 1/2 convolutional code with maximum free distance [41]. The higher this distance is, the better is the performance

of the code. Two decoders are used, one using the initial Viterbi algorithm [27], and the other using the Soft Viterbi algorithm. Using probabilistic decoding once more offers a gain, equal to 2.3dB. Using the convolutional code with maximum free distance allows for a gain of almost 1dB, showing the importance of the choice of the code.

The performance of the TC previously presented is also depicted, along with the threshold estimated with the EXIT analysis. This threshold is equal to -0.06dB, located only 1.02dB from the minimum achievable E_b/N_0, equal to $(E_b/N_0)_{\min} = -1.08$dB for $\eta = 1/3$. Decreasing the interleaver size introduces a loss of performance, but using TC allows for a gain of several dB compared to the classic convolutional codes.

After the TC breakthrough, some researchers rediscovered the so-called Low Density Parity Check (LDPC) codes, initially invented by Gallager [9]. This family of codes proved itself asymptotically more powerful than the TC, being able to approach the channel capacity very closely [42]. Recently, the polar codes [10] have been considered as promising for fifth generation (5G) [43], as they are the first codes to asymptotically achieve the capacity of some specific channels.

1.4 Existing Low Power Wide Area Industrial Solutions

As more and more solutions required LPWA connectivity, the industry went ahead and addressed the technical challenges with their own solution. More or less at the same time, the Institute of Electrical and Electronics Engineers (IEEE) 802.15 and the 3rd Generation Partnership Project (3GPP) working groups developed standards to address the same problem.

In this section, three majors industrial solutions from Sigfox, the LoRa alliance and Ingenu are reviewed, as well as the standards 802.15.4k and the Narrow-Band IoT (NB-IoT), part of a new release of the LTE standard.

1.4.1 Proprietary Technologies

Both proprietary solutions presented here are industrial solutions. Only few technical details are available, most of the documentation comes from marketing information. The European Telecommunications Standards Institute (ETSI) nonetheless set-up an Industry Specification Group within TG28 for low throughput networks [44], and some backward engineering of the LoRa physical layer has been performed [45].

1.4.1.1 Sigfox

Sigfox is a French company, created in 2010 and dedicated to IoT networks [46]. The company widely advertised that its technology relies on narrow band signaling. As presented in Section 1.2.2, Equation (1.12), reducing the data rate $R = \eta B$ lowers the sensitivity level, and this can be done by reducing either the spectral efficiency of the technique or the bandwidth. Narrow band signaling follows this second approach; a modulation with a relatively high spectral efficiency is used (without any channel coding), functioning at a high E_b/N_0, but the bandwidth B is low enough to ensure a satisfying sensitivity level.

Documentation suggests a bandwidth of 100Hz and Differential Binary Phase Shift Keying (DBPSK) modulation. This modulation is a memory modulation, the information is in the phase shifts. The modulation process can be represented by an encoder, given in Figure 1.15 (a). The output at time k, x_k, can be expressed using the two information bits b_k and b_{k-1} as $x_k = b_{k-1} \oplus b_k$, with $\oplus$ the binary sum operator. The modulation can be also represented by a trellis, given in Figure 1.15 (b). The input changes the state, and the output is the value of the state. In order to demodulate DBPSK and retrieve the Q information bits, the ML decoder would need to evaluate the likelihood of having each of the 2^Q possible sequences and search for the maximum, inducing an exponential complexity with Q. Instead, trellis decoding algorithm such as the algorithms used for convolutional codes can be used. The probabilities of transitions must be evaluated, while the probabilities of the states are observed. With $\boldsymbol{r}$ the received sequence of symbols, the LLR of the information bit at index k can be expressed with

$$L(b_k) = \log \frac{p(r_{k-1} \mid b_{k-1} = +1)\, p(r_k \mid b_k = +1) + p(r_{k-1} \mid b_{k-1} = -1)\, p(r_k \mid b_k = -1)}{p(r_{k-1} \mid b_{k-1} = +1)\, p(r_k \mid b_k = -1) + p(r_{k-1} \mid b_{k-1} = -1)\, p(r_k \mid b_k = +1)}. \tag{1.76}$$

The DBPSK modulation with probabilistic decoding reaches a BER of 10^{-5} for $E_b/N_0 \simeq 9.9$dB, and its spectral efficiency is 1 bits$\cdot$s$^{-1}\cdot$Hz^{-1}. According to Equation (1.12), with a bandwidth of 100Hz, the sensitivity is equal to $P_{\text{req}} = -143.7$dBm (without considering the noise factor of the receiver).

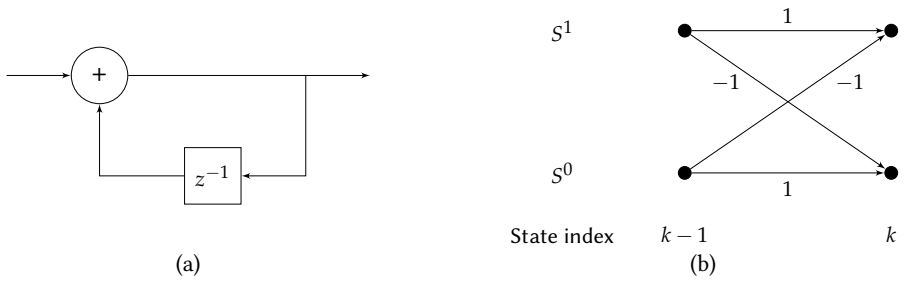

FIGURE 1.15 – *Encoder (a) and trellis (b) of the DBPSK modulation. On the trellis, the input bit is labeled on the transitions, and the output bit is the value of the state.*

1.4.1.2 LoRa

The LoRa Alliance [47] is an association of companies that collaborate to offer a LPWA connectivity solution. The physical layer is based on a technology patented by the former company Cycleo and acquired by Semtech since. The original patent [48] describes a technology based on the emission of orthogonal sequences, chosen as chirps, hence the denomination Chirp Spread Spectrum (CSS). The use of chirp signals for communication has been explored before [49], and CSS can be considered as an orthogonal modulation depending of the choice of the chirp sequence. The Zadoff-Chu sequences [50] are orthogonal as the circular autocorrelation of the sequence is zero for all nonzero delays. With a sequence of size M, a total of M delayed (or circularly shifted) sequences can be constructed, giving an alphabet of size M where each sequence is orthogonal to another thanks to the autocorrelation property. Alternatively, the process of chirp modulation can be seen as a form of FSK modulation (i.e. an alphabet of pure frequencies), and then multiplying the complex symbols by the base chirp. Spectrally, this spreads the power over all the carriers instead of exciting only one frequency. The Zadoff-Chu sequence is a Constant Amplitude Zero Auto-Correlation (CAZAC) sequence, and has interesting properties such as constant envelope.

The Transmitter (TX) and Receiver (RX) side of the LoRa modulation are given in Figure 1.16. While the TX is described in the patent [48], we chose the RX side that performs the dual operations of the TX, with ML detection and decoding, as suggested by their technical document [51]. The FEC used is the Hamming code where a parity bits are computed, with $a \in \{1,2,3,4\}$. The case $a = 3$ corresponds to the regular Hamming code, while $a = 4$ is the extended version. The parity bits can also be punctured, i.e. not sent, giving lower values for a. After encoding, bits are grouped into words of size SF (which stands for Spreading Factor (SF), even if it does not match the usual definition of the SF principle). Each group of bits is associated to one of the 2^{SF} orthogonal dimensions, and the result is multiplied by the base chirps in order to spread the signal on all frequencies.

At the RX side, the signal is despreaded by multiplying it with the conjugate of the base chirp. After this step, a classic orthogonal demodulation can be performed, in a coherent or non coherent way. Each codewords of length $4+a$ is then decoded, and the information bits are retrieved. The global spectral efficiency of the scheme is

$$\eta = \frac{4}{4+a}\frac{SF}{2^{SF}}, \tag{1.77}$$

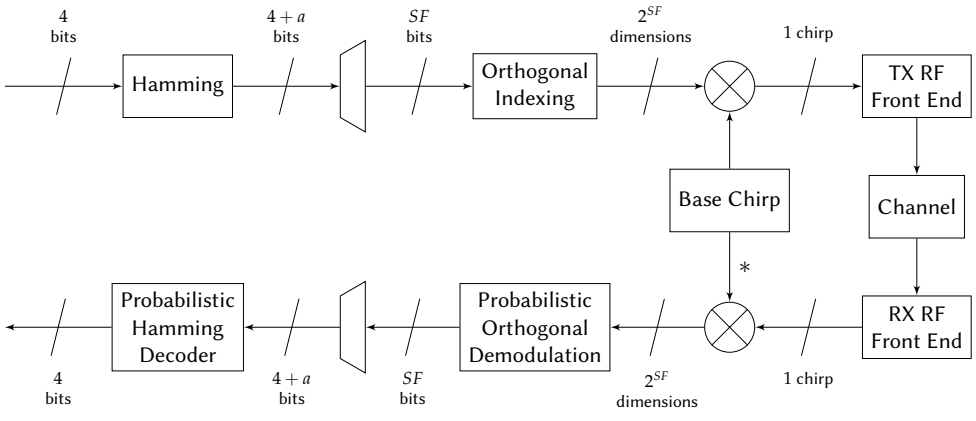

FIGURE 1.16 – *The LoRa CSSS transmitter and receiver.*

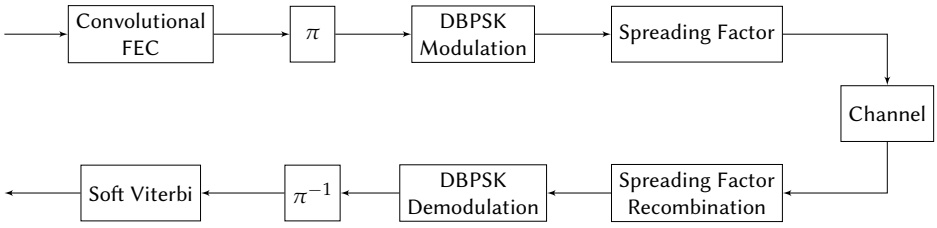

FIGURE 1.17 – *The 802.15.4k specifications transmitter and receiver.*

which is coherent with the use of an orthogonal modulation and the rate of the FEC scheme used.

The LoRa specifications indicate values of SF from 6 to 12, and a signal bandwidth $B = 125$kHZ, 250kHz or 500kHz.

1.4.2 Standardized Technologies

In telecommunications, standards are defined in order to allow for various systems and operators to coexist. Without some level of standardization, communication between devices would be impossible. The proprietary solutions respect the regulations concerning bandwidth and duty cycles, but need to transmit in the unlicensed frequency bands. These bands are used by numerous applications, thus interference with other users may be high. One of the benefits of using standardized solutions is the possible use of licensed bands, where interference level is contained.

While the technology used by proprietary solutions is kept secret to ensure the monopoly of the inventor company for this very technology, standards are open access and simply define rules to follow for the design of the communication system. Anybody can then create its own system, compliant with the standard, but using their own algorithms for signal detection, demodulation and decoding. In this section, the definition of the rules for the PHY layer of two standards are reviewed.

1.4.2.1 The IEEE 802.15.4k Standard

The IEEE 802.15.4k is a standard for local and metropolitan area networks, and is part of the Low-Rate Wireless Personal Area Networks (LR-WPAN) [52]. It aims at low energy critical infrastructure monitoring networks. This standard supports three PHY layer modes: Direct Sequence Spread Spectrum (DSSS) with DBPSK or Offset-QPSK, or FSK. DSSS with DBPSK modulation is adapted to more constrained situations, and will be presented here. Standard specifications allow the use of a SF value SF from 16 to 32768.

Block diagrams for transmitter and receiver are given in Figure 1.17. The transmitter is composed of a FEC block, defined to be the convolutional code of rate $1/2$, with generator polynomials [171 133] and constraint length $K = 7$. After encoding, interleaving is done to ensure diversity at the reception side. The data is modulated using DBPSK and is "repeated" by the use of a binary direct sequence of size SF. The spectral efficiency of the physical layer is

$$\eta = \frac{1}{2SF}. \tag{1.78}$$

The receiver executes the reverse operations of the transmitter side. After despreading the signal (executing the mean weighted by the elements of the binary direct sequence), we use a soft DBPSK decoder. Knowing how data was interleaved at the transmitter side, the deinterleaving operation is applied before the Soft Viterbi decoder, designed to retrieve the information bits.

While the standard has been considered as a LPWA solution [53], the Random Phase Multiple Access (RPMA) technique, developed by the US company Ingenu [54], is allegedly based on the IEEE 802.15.4k standard, i.e. its PHY layer is compliant with the standard. It uses the DSSS technique, and their specific access technique is described by the patent [55]. Regarding the physical layer, we will consider the exact same elements as the 802.15.4k standard, except the possible values for the SF, ranging from 64 to 8192.

1.4.2.2 Narrow Band LTE for IoT

The 3GPP consortium recently issued a standard for the NB-IoT [56]. This standard is actually a new release of the LTE standard [57], and includes 3 modes for IoT applications. Since it is an evolution of the LTE, it includes other elements of this standard, such as its channel coding procedure [58]. Some industrial group research teams

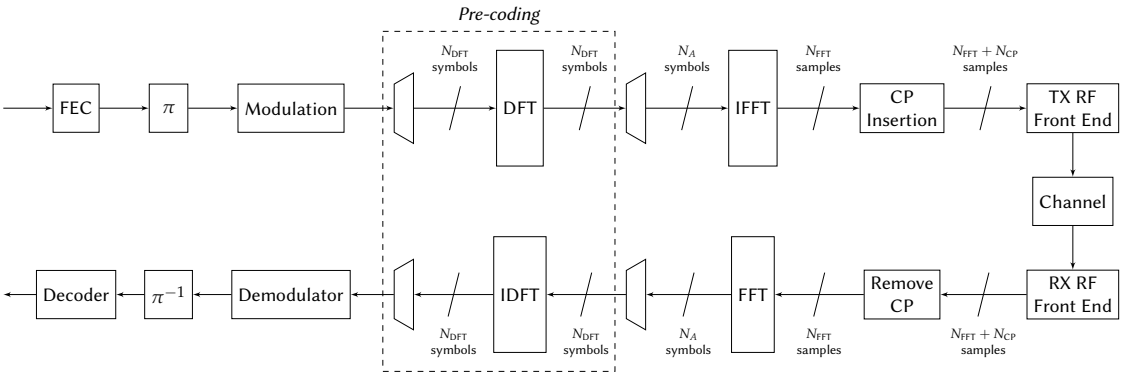

FIGURE 1.18 – *The OFDM/SC-FDMA transmitter and receiver.*

also unveiled more about the NB-IoT standard, such as Nokia [59] and Ericsson [60]. The NB-IoT has two main modes: the Downlink (DL) and Uplink (UL) modes.

For the UL mode, the modulation can be chosen between BPSK and QPSK, and the FEC used is the [13 15] TC from the LTE standard [58]. The parity bits of the TC can be punctured, giving two possible rates for the channel code: 1/3 and 1/2 (when punctured). The message can be repeated up to 128 times, giving a processing gain at the receiver side.

For the DL mode, i.e. the connection from the base-station to the device, data is modulated using QPSK. The channel code used is a Tail Biting Convolutional Code (TBCC), with generator polynomials [133 171 165] [58], giving a rate 1/3. The use of TBCC allows the receiver (the device) to use a low complexity Soft Viterbi decoder, and the tail biting property avoids the needs to send extra bits to close the trellis. A repetition up to 512 can be applied.

As part of the LTE standard, the data must be modulated using Orthogonal Frequency Division Multiplexing (OFDM) signaling. For the DL, classic OFDM is assumed, while for the UL, both Single Carrier Frequency Division Multiple Access (SC-FDMA) and single carrier transmission are considered. Compared to OFDM, both SC-FDMA and single carrier offer a lower PAPR [61], which is interesting at the device level as it lowers the energy consumption of the PA.

The architecture of a OFDM/SC-FDMA transceiver is given in Figure 1.18. Modulated symbols are grouped into blocks of size N_{DFT}, and a DFT of the same size is applied on each group. The symbols are then mapped to N_A carriers, and an Inverse Fast Fourier Transform (IFFT) of size N_{FFT} is applied. The mapping of the symbols is done in the frequency domain and the IFFT generates a signal in the time domain. After this step, a Cyclic Prefix (CP) is inserted, i.e. the last N_{CP} samples of a time symbol (which contains N_{FFT} samples) are added at the beginning of the symbol, giving a symbol of size $N_{\text{FFT}} + N_{\text{CP}}$. At the receiving side, after removing the CP, a Fast Fourier Transform (FFT) is applied to recover the mapped symbols from the transmitter. The Inverse Discrete Fourier Transform (IDFT) is then applied to the DFT blocks sent in the first place, in order to recover the modulated symbols. SC-FDMA is a multiplexing technique, as several symbols are transmitted at different frequencies during the same time symbol. The DFT step can be seen as a type of pre-coding, and is omitted when OFDM signaling is considered.

The value of N_A is usually equal to N_{DFT}, equal to 12, 6 or 3. With the carrier spacing in LTE being 15kHz, the bandwidth of 12 carriers is equal to 180kHz. When only a single carrier is used, the bandwidth can be chosen equal to 15kHz or 3.75kHz.

The spectral efficiency of the NB-IoT scheme is given by

$$\eta = R_c \cdot \frac{\eta_{\text{mod}}}{SF}, \tag{1.79}$$

where SF is the repetition factor, R_c the coding rate and η_{mod} the spectral efficiency of the modulation used.

1.4.3 PERFORMANCE

The parameters of the different technologies previously presented that minimize the sensitivity are summarized in Table 1.1. For Sigfox, only one mode is available, but for every other technique, the parameters of the configuration (size of modulation, number of repetitions, code rate) giving the lowest spectral efficiency are indicated. The bandwidths, data rate, sensitivity levels and the band used are also given. In order to obtain the estimated sensitivity levels, simulations of the different schemes under an AWGN channel were performed, and the E_b/N_0 required for a BER of 10^{-5} is integrated in the sensitivity formula (1.12) along with the data rate of the technique.

	Parameters	η	Bandwidth	R	Band	Sensitivity
Unit	N/A	$bits{\cdot}s^{-1}{\cdot}Hz^{-1}$	*Hz*	$bits{\cdot}s^{-1}$	*MHz*	*dBm*
Sigfox [44]	N/A	1	100	100	868 (ISM)	−144
LoRa [47]	$SF = 12,\ a = 4$	$1.4 \cdot 10^{-3}$	125 000	183	868 (ISM)	−147
RPMA [54]	$SF = 8192$	$6.1 \cdot 10^{-5}$	1 000 000	61	2400 (ISM)	−150
NB-IoT (DL) [56,59]	QPSK, $R_c = 1/3$, $SF = 512$	$1.3 \cdot 10^{-3}$	180 000	234	Licensed	−146
NB-IoT (UL) [56,59]	BPSK, $R_c = 1/3$, $SF = 128$	$2.6 \cdot 10^{-3}$	3750	9	Licensed	−163

TABLE 1.1 – *Parameters of the different modes which minimize the sensitivity level, for all the considered techniques.*

Whatever the technique used, extremely low levels of sensitivity can be reached, at the expense of a very low data rate. Naturally, these values do not include the possible implementation performance loss nor the noise factor of the receivers. Probabilistic demodulation and MAP decoding for the TC have been selected, while the max-log approximation may be chosen to reduce complexity. However, this comparison gives the limits of each technology concerning their reachable sensitivity.

In Figure 1.19, the spectral efficiency versus the E_b/N_0 required for a BER of 10^{-5} for each technology has been represented, along with the maximum achievable spectral efficiency as given with Equation (1.16). Along with the lowest possible spectral efficiencies, the performance characteristics for the highest spectral efficiencies are also given for each technology. It should be emphasized that this representation is normalized by the bandwidth. While Sigfox appears far from the maximum achievable energy efficiency (or minimum achievable E_b/N_0), this solution still reaches low levels of sensitivity because of its narrow band approach. For all other techniques, low sensitivity is reached by decreasing the spectral efficiency, and the E_b/N_0 performance varies from one technology to another. The NB-IoT approach, as it uses a TC, is the closest to the minimum achievable E_b/N_0, with a gap of approximately 2.6dB for its lowest spectral efficiency point (note that an interleaver size $Q = 1000$ was used for this performance), while the Sigfox technique is the farthest with a gap of $\sim$ 10dB. One should consider that complexity of the compared schemes are different, as the receiver needs to compute turbo decoding for the NB-IoT case. However, since this is the UL mode, the receiver in this case is a base station, which is considered to have a large computational capacity. The cost of increasing complexity due to the use of a more sophisticated FEC can be paid by the receiver side. The difference of performance in E_b/N_0 should not be interpreted directly as the difference in sensitivity, since the bandwidth and spectral efficiencies of Sigfox system versus NB-IoT are not similar. However, a data rate of 104bits·s^{-1}can be achieved by using the NB-IoT with parameters $SF = 12$, $R_c = 1/3$ and a bandwidth of 3.75kHz

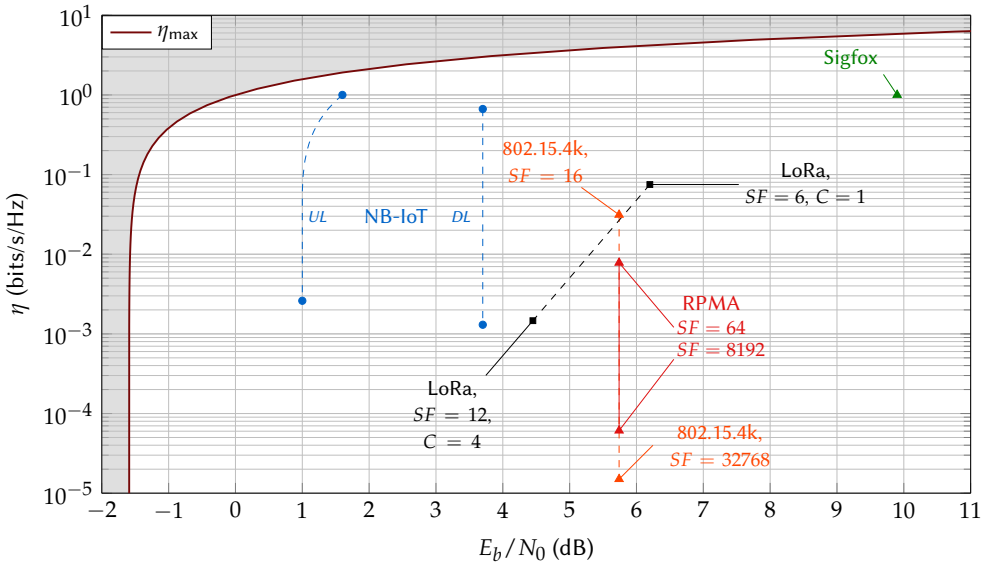

FIGURE 1.19 – *Comparison of the spectral efficiency and the required E_b/N_0 at BER $= 10^{-5}$ of various LPWA solutions, under the AWGN channel. The maximum achievable spectral efficiency according to the channel capacity from* (1.15) *is also represented.*

and BPSK modulation. The spectral efficiency for this case, given by Equation (1.79) is equal to $\eta = 2.7 \cdot 10^{-2}$ bits·s^{-1}·Hz^{-1}, and with a required E_b/N_0 of 1dB, the sensitivity for this case is -153dB. This means that for a same data rate, the NB-IoT with these parameters uses 37,5 more bandwidth and an increased complexity to achieve a gain of 9 dB in sensitivity versus the Sigfox solution. Other comparisons could be made, but the choice of one solution versus another is always a matter of compromise on the bandwidth, time duration of the signal, and complexity. However, it is straightforward that all solutions follow the same strategy, which is to reduce the data rate to improve the sensitivity level.

1.5 Conclusion

The design of a new LPWA PHY layer is a critical issue for the new generation of IoT networks, as a large amount of connected devices are expected to need this type of connectivity solution in the coming years. Industrial solutions exist and standardization is in the process. The main strategy to reach low sensitivity levels is clearly to reduce the data rate, either by reducing the bandwidth or the spectral efficiency of the technology used. When considering the minimum achievable E_b/N_0 according to the channel capacity as defined by Shannon versus the various LPWA solutions, an important gain in energy efficiency has not been yet achieved. The ultimate limit $(E_b/N_0)_{\text{lim}} = -1.59$dB can be approached only by solutions that have a relatively low spectral efficiency. However, lowering the spectral efficiency is not sufficient to getting closer to the limit, and most solutions are 5dB away from the $(E_b/N_0)_{\text{lim}}$. Only the TC solution provided by the UL NB-IoT standard is the closest to $(E_b/N_0)_{\text{lim}}$, at the expense of an increased complexity at the receiver side. The transmitter (i.e. the node) complexity is kept low to ensure low consumption. More sophisticated reception algorithms should be considered in order to achieve a gain in energy efficiency. The choice of waveform is also a critical matter as it impacts the energy efficiency and the PAPR of the technique, and a constant envelope technique is preferred in order to release some constraints on the transmitter's PA.

For the next part of this thesis, the study of how to approach the capacity at low spectral efficiencies is investigated. While repetition can be used to reduce the spectral efficiency and hence improve the sensitivity level, a more sophisticated reception algorithm is considered in order to achieve an energy efficiency gain. The study leads to a new PHY layer, so-called Turbo-FSK.

Chapter Summary

In this chapter, the general LPWA context has been presented, and the key system parameters that will be used throughout this document have been introduced, notably the sensitivity, a key metric to evaluating the long range capacity of a technique, and the well-known channel capacity introduced by Claude Shannon. The critical elements of a physical layer have been presented, and several modulation, demodulation and FEC techniques are detailed, including orthogonal modulations and the TC, a powerful channel code. Finally, some existing LPWA solutions are described, such as the NB-IoT and the LoRa technologies. Each technique have been implemented in a simulation chain in order to compare its performance. Its spectral efficiency and required E_b/N_0 are confronted with the limits of the information theory, in order to evaluate the achievable possible gain.

Bibliography of Chapter 1

[7] C. Shannon. "A Mathematical Theory of Communication". In: *The Bell System Technical Journal* 27.3 (1948), pp. 379–423.

[8] C. Berrou, A Glavieux, and P. Thitimajshima. "Near Shannon Limit Error-Correcting Coding and Decoding: Turbo-Codes". In: *IEEE International Conference on Communications (ICC). Geneva.* Vol. 2. 1993, pp. 1064–1070.

[9] R. G. Gallager. "Low-Density Parity-Check Codes". PhD thesis. 1963.

[10] E. Arikan. "Channel Polarization: A Method for Constructing Capacity-Achieving Codes for Symmetric Binary-Input Memoryless Channels". In: *IEEE Transactions on Information Theory* 55.7 (2009), pp. 3051–3073.

[11] Machina Research. *LPWA Technologies - Unlock New IoT Market Potential.* A White Paper prepared for the LoRa Alliance. 2014.

[12] H. T. Friis. "A Note on a Simple Transmission Formula". In: *Proceedings of the IRE* 34.5 (1946), pp. 254–256.

[13] M. Loy. *Understanding and Enhancing Sensitivity in Receivers for Wireless Applications.* Texas Instrument, Wireless Communication Business Unit, Technical Brief SWRA030. 1999.

[14] H. Kwon and T. Birdsall. "Channel Capacity in Bits per Joule". In: *IEEE Journal of Oceanic Engineering* 11.1 (1986), pp. 97–99.

[15] J. Proakis. *Digital Communications 3rd Edition.* Communications and signal processing. McGraw-Hill, 1995.

[16] F. H. Raab et al. "Power Amplifiers and Transmitters for RF and Microwave". In: *IEEE Transactions on Microwave Theory and Techniques* 50.3 (2002), pp. 814–826.

[17] S. C. Thompson. "Constant Envelope OFDM Phase Modulation". PhD thesis. University of California, San Diego, 2005.

[18] S. Cui, A. J. Goldsmith, and A. Bahai. "Energy-Constrained Modulation Optimization". In: *IEEE Transactions on Wireless Communications* 4.5 (2005), pp. 2349–2360.

[19] P. Bento et al. "Measuring the Magnitude of Envelope Fluctuations: Should We Use the PAPR?" In: *2014 IEEE 80th Vehicular Technology Conference (VTC2014-Fall).* 2014, pp. 1–5.

[20] S. Benedetto and E. Biglieri. *Principles of Digital Transmission: With Wireless Applications.* Norwell, MA, USA: Kluwer Academic Publishers, 1999.

[21] J. Hagenauer, E. Offer, and L. Papke. "Iterative Decoding of Binary Block and Convolutional Codes". In: *IEEE Transactions on Information Theory* 42.2 (1996), pp. 429–445.

[22] K. Cho and D. Yoon. "On the General BER Expression of one- and two-Dimensional Amplitude Modulations". In: *IEEE Transactions on Communications* 50.7 (2002), pp. 1074–1080.

[23] J. Costello D.J. and J. Forney G.D. "Channel Coding: The Road to Channel Capacity". In: *Proceedings of the IEEE* 95.6 (2007), pp. 1150–1177.

[24] R. W. Hamming. "Error Detecting and Error Correcting Codes". In: *The Bell System Technical Journal* 29.2 (1950), pp. 147–160.

[25] P. Elias. "Coding for Noisy Channels". In: *IRE Convention Record* 3.2 (1955), pp. 37–46.

[26] H. Ma and J. Wolf. "On Tail Biting Convolutional Codes". In: *IEEE Transactions on Communications* 34.2 (1986), pp. 104–111.

[27] A. Viterbi. "Error Bounds for Convolutional Codes and an Asymptotically Optimum Decoding Algorithm". In: *IEEE Transactions on Information Theory* 13.2 (1967), pp. 260–269.

[28] A. Viterbi. "Convolutional Codes and Their Performance in Communication Systems". In: *IEEE Transactions on Communication Technology* 19.5 (1971), pp. 751–772.

[29] J. Heller and I. Jacobs. "Viterbi Decoding for Satellite and Space Communication". In: *IEEE Transactions on Communication Technology* 19.5 (1971), pp. 835–848.

[30] J. Hagenauer and P. Hoeher. "A Viterbi Algorithm with Soft-Decision Outputs and its Applications". In: *Global Telecommunications Conference and Exhibition 'Communications Technology for the 1990s and Beyond' (GLOBECOM), 1989. IEEE.* 1989, 1680–1686 vol.3.

[31] L. Bahl, J. Cocke, F. Jelinek, and J. Raviv. "Optimal Decoding of Linear Codes for Minimizing Symbol Error Rate (Corresp.)" In: *IEEE Transactions on Information Theory* 20.2 (1974), pp. 284–287.

[32] G. D. Forney. *Concatenated Codes*. Cambridge, 1966.

[33] S. ten Brink. "Convergence Behavior of Iteratively Decoded Parallel Concatenated Codes". In: *IEEE Transactions on Communications* 49.10 (2001), pp. 1727–1737.

[34] S. Benedetto and G. Montorsi. "Average Performance of Parallel Concatenated Block Codes". In: *Electronics Letters* 31.3 (1995), pp. 156–158.

[35] L. C. Perez, J. Seghers, and D. J. Costello. "A Distance Spectrum Interpretation of Turbo Codes". In: *IEEE Transactions on Information Theory* 42.6 (1996), pp. 1698–1709.

[36] M. El-Hajjar and L. Hanzo. "EXIT Charts for System Design and Analysis". In: *IEEE Communications Surveys Tutorials* 16.1 (2014), pp. 127–153.

[37] J. Hagenauer and L. Papke. "Decoding "Turbo"-Codes with the Soft Output Viterbi Algorithm (SOVA)". In: *Proceedings of 1994 IEEE International Symposium on Information Theory*. 1994, pp. 164–.

[38] M. P. C. Fossorier, F. Burkert, S. Lin, and J. Hagenauer. "On the Equivalence Between SOVA and max-log-MAP Decodings". In: *IEEE Communications Letters* 2.5 (1998), pp. 137–139.

[39] P. Robertson, P. Hoeher, and E. Villebrun. "Optimal and Sub-Optimal Maximum a Posteriori Algorithms Suitable for Turbo Decoding". In: *European Transactions on Telecommunications* 8.2 (1997), pp. 119–125.

[40] J. Vogt and A. Finger. "Improving the max-log-MAP Turbo Decoder". In: *Electronics Letters* 36.23 (2000), pp. 1937–1939.

[41] P. Frenger, P. Orten, and T. Ottosson. "Convolutional Codes with Optimum Distance Spectrum". In: *IEEE Communications Letters* 3.11 (1999), pp. 317–319.

[42] S.-Y. Chung, G. D. Forney, T. J. Richardson, and R. Urbanke. "On the Design of Low-Density Parity-Check Codes Within 0.0045 dB of the Shannon Limit". In: *IEEE Communications Letters* 5.2 (2001), pp. 58–60.

[43] L. Liu and C. Zhang. "Circuits and Systems for 5G Network: Massive MIMO and Advanced Coding". In: *2015 IEEE 11th International Conference on ASIC (ASICON)*. 2015, pp. 1–4.

[44] *Low Throughput Networks (LTN): Protocol and Interfaces*. ETSI Group Specification GS LTN 003, V 1.1.1. 2014.

[45] A. Augustin, J. Yi, T. Clausen, and W. M. Townsley. "A Study of LoRa: Long Range & Low Power Networks for the Internet of Things". In: *Sensors* 16.9 (2016), p. 1466. URL: http://www.mdpi.com/1424-8220/16/9/1466.

[46] *SigFox website*. http://www.sigfox.com/. Accessed: July 26, 2017.

[47] *LoRa Alliance*. https://www.lora-alliance.org/. Accessed: July 26, 2017.

[48] O. Seller and N. Sornin. "Low Power Long Range Transmitter". Patent US 20140219329 A1. 2014.

[49] A. Springer et al. "Spread Spectrum Communications Using Chirp Signals". In: *IEEE/AFCEA EUROCOMM 2000. Information Systems for Enhanced Public Safety and Security (Cat. No.00EX405)*. 2000, pp. 166–170.

[50] D. Chu. "Polyphase Codes with Good Periodic Correlation Properties (Corresp.)" In: *IEEE Transactions on Information Theory* 18.4 (1972), pp. 531–532.

[51] *LoRa Modulation Theory*. Semtech Technical Brief. 2014.

[52] *802.15.4k: Low-Rate Wireless Personal Area Networks (LR-WPANs) Amendment 5: Physical Layer Specifications for Low Energy, Critical Infrastructure Monitoring Networks*. IEEE Standard for Local and metropolitan area networks. 2013.

[53] X. Xiong et al. "Low Power Wide Area Machine-to-Machine Networks: Key Techniques and Prototype". In: *IEEE Communications Magazine* 53.9 (2015), pp. 64–71.

[54] *How RPMA Works*. A White Paper by Ingenu. Retrieved from the Ingenu website.

[55] T. Myers. "Random Phase Multiple Access System With Meshing". Patent US 7,773,664 B2. 2010.

[56] *LTE Evolved Universal Terrestrial Radio Access (E-UTRA): Physical Channels and Modulation*. 3GPP TS 36.211, V13.2.0, Release 13. 2016.

[57] *Whitepaper Narrowband Internet of Things*. Rohde & Schwarz. 2016.

[58] *LTE Evolved Universal Terrestrial Radio Access (E-UTRA): Multiplexing and Channel Coding*. 3GPP TS 36.212, V12.6.0, Release 12. 2015.

[59] R. Ratasuk, B. Vejlgaard, N. Mangalvedhe, and A. Ghosh. "NB-IoT System for M2M Communication". In: *2016 IEEE Wireless Communications and Networking Conference*. 2016, pp. 1–5.

[60] Y. P. E. Wang et al. “A Primer on 3GPP Narrowband Internet of Things”. In: *IEEE Communications Magazine* 55.3 (2017), pp. 117–123.

[61] H. G. Myung, J. Lim, and D. J. Goodman. “Single Carrier FDMA for Uplink Wireless Transmission”. In: *IEEE Vehicular Technology Magazine* 1.3 (2006), pp. 30–38.

CHAPTER 2

TURBO-FSK

CHAPTER CONTENTS

Low sensitivity levels can be achieved using schemes with a low spectral efficiency. In this chapter, a new transmission scheme relying on this principle is proposed and analyzed: Turbo-FSK. After introducing the origins and the motivations of the scheme, the principle of Turbo-FSK is described. Optimization of the parameters using the EXtrinsic Information Transfer (EXIT) chart technique is also presented. The chapter concludes with the analysis of the scheme for short block sizes and its comparison versus channel capacity and the Low Power Wide Area (LPWA) solutions.

2.1 Origins of Turbo-FSK

As presented in the previous chapter, there are two main strategies for a specific scheme to reach low sensitivity levels: reduce the spectral efficiency or reduce the bandwidth. Each option has benefits and drawbacks; reducing the bandwidth imposes different constraints, and reducing the spectral efficiency is achieved by using a different modulation, a Forward Error Correction (FEC) with more redundancy or a higher Spreading Factor (SF). The latter approach is investigated. The channel capacity as expressed by Shannon is also considered. A system operating close to this limit would be highly efficient. In this section, some preliminary considerations as to how a potential solution could be designed are studied, and a low rate channel code is described.

2.1.1 Preliminary Considerations: Concatenated FSK

In the previous chapter, orthogonal modulations were introduced, and shown to reach the channel capacity for an infinite size of alphabet. The performance of orthogonal modulations is represented in Figure 1.8, along with the maximum achievable spectral efficiency. The energy efficiency of orthogonal modulations increases with the size of alphabet M. However large sizes of M are required to approach the theoretical limit for which the spectral efficiency is close to 0; this makes this approach inefficient for practical solutions. Orthogonal modulations with small sizes of alphabet ($M < 1024$) are nonetheless interesting, as they offer a good energy efficiency with low spectral efficiency, and could provide interesting levels of sensitivity in the LPWA context.

For low power modulation schemes, Frequency Shift Keying (FSK) orthogonal modulation is often selected. One of the main benefits of FSK modulation is its constant envelope. As presented in Section 1.2.4, working with this type of modulation releases constraints for the Power Amplifier (PA), increasing its efficiency and lowering its cost. Most of the existing solutions for LPWA networks indeed use constant envelope modulation. Furthermore, FSK is a well-known technology, and using a mainstream technology can be very attractive due to the availability of multiple off-the-shelf solutions [62]. Finally, FSK modulation can be implemented with an Orthogonal Frequency Division Multiplexing (OFDM) transceiver [63].

Repetition is a well-known technique to reduce the sensitivity level, but it does not improve the energy efficiency of the system. However, it is known that the association of random permutations between repetitions and a probabilistic iterative receiver (turbo process) allows for high energy efficiency gains [8]. Following this approach, an early consideration was the use of a parallel concatenations of two FSK modulations. The considered scheme, so-called Concatenated FSK, is represented in Figure 2.1 (dashed block omitted). If the receiver simply recombines both received sequences of symbols, the gain provided by the scheme is strictly equivalent to a repetition or spreading. The spectral efficiency of the initial FSK modulation is divided by a factor of 2. While the level of sensitivity of the modulation could be further reduced by increasing the amount of repetitions, this would not improve the energy efficiency of the scheme. In order to do so, a more sophisticated receiver should be used.

The dashed block π is now considered and corresponds to an interleaving step. Each FSK is considered as a code. One decoder can use the information generated by the other decoder (the extrinsic information) to perform its estimation of the information bits. This use of interleaved extrinsic information introduces diversity in the

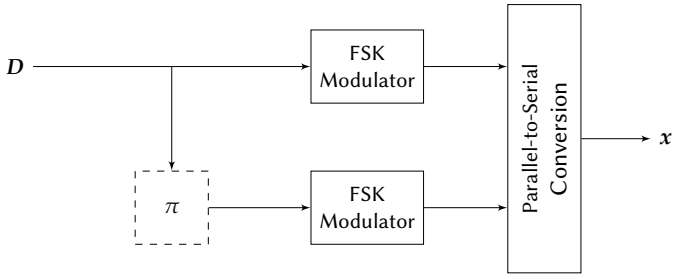

Figure 2.1 – *Parallel concatenation of two FSK modulations.*

decoder, which is used to increase the energy efficiency of the scheme. The structure is similar to the one used for the Turbo Codes (TCs) [8]. These codes are known to be highly energy efficient and to closely approach the Shannon capacity limit. With this type of scheme, the complexity at the transmitter side remains low, as the cost of complexity is paid at the receiver side. Using a TC can be seen as repeating the information and adding some redundancy on each repetition, which reduces the spectral efficiency. A sophisticated receiver then processes the received sequence and exploits the diversity of the repetitions to achieve an energy efficiency gain.

In order to study the performance of such a scheme, a different alphabet from the FSK, but which has the same orthogonal property, is considered: the Hadamard code. This code is convenient to study because it is a binary code. A channel code was proposed in the literature, using the same strategy and the Hadamard code, leading to the Turbo-Hadamard channel code

2.1.2 The Turbo-Hadamard Channel Code

The initial proposition of this code, developed by Li Ping in 1998, consisted in a parallel concatenation of Hadamard codes, associated with a turbo decoder [64]. More precisely, bi-orthogonal Hadamard codes were used. Following the definition of the Hadamard code given in Section 1.3.4.1, the bi-orthogonal Hadamard alphabet of size M $\widehat{\boldsymbol{H}_M}$ is given by

$$\widehat{\boldsymbol{H}_M} = \begin{bmatrix} \boldsymbol{H}_{M/2} \\ -\boldsymbol{H}_{M/2} \end{bmatrix}, \tag{2.1}$$

thus giving an alphabet with M codewords of length $N_c = M/2$ (equivalently, the size of the matrix $\widehat{\boldsymbol{H}_M}$ is $M \times (M/2)$). The performance of this code is equivalent to the performance of the orthogonal Hadamard code of size M (which matrix would be of size $M \times M$), but the spectral efficiency is increased by a factor 2. The bi-orthogonal Hadamard code is also a systematic code. For the rest of the document, the following notations are used: M is the alphabet size; N_c is the length of the codeword; q is the number of information bits in a codeword and m is the length of the binary word (which may include additional parity bits, or else $m = q$) mapped on a codeword.

The encoder of the Turbo-Hadamard code is given in Figure 2.3 and the dashed blocks are bypassed. The information bits are represented by a matrix $\boldsymbol{D}$. An information block of size Q is divided in N_q information words of size q bits. The segmentation of the information block is depicted in Figure 2.2. The first stage of the encoder is the systematic output of the Turbo-Hadamard encoder, while the other λ stages will only output the parity bits of the Hadamard codewords. Each stage uses an interleaved version of the input bits, and then applies the bi-orthogonal Hadamard code, which associates each information word of q bits to one of the M Hadamard codewords from the alphabet. Setting $m = \log_2(M)$, this imposes $m = q$, and as a bi-orthogonal alphabet is considered, the final codeword length is $N_c = M/2 = 2^{m-1}$ chips. Since only the parity bits are emitted, the output of each stage consists in a matrix with $M/2 - q$ parity bits, and $\boldsymbol{S}^{\ell}$ ($\ell \in \{0, \ldots, \lambda - 1\}$) is a matrix with $M/2 - q$ rows and N_q columns. With this representation, $m = q$ corresponds to the number of information bits per Hadamard codeword, and this implies that q is a multiple of Q (otherwise, some padding bits may be added). Considering the systematic bits and the λ stages, the code rate is equal to

$$R_c = \frac{q}{q + \lambda\left(2^{q-1} - q\right)}. \tag{2.2}$$

The receiver, not detailed here, is presented in [64]. The authors rapidly concluded that the scheme was not efficient due to a very high error floor. The performance of a code strongly depends on the Hamming distance between the codewords. The larger the distance is, the better is the performance. As the all-0 word is one of the

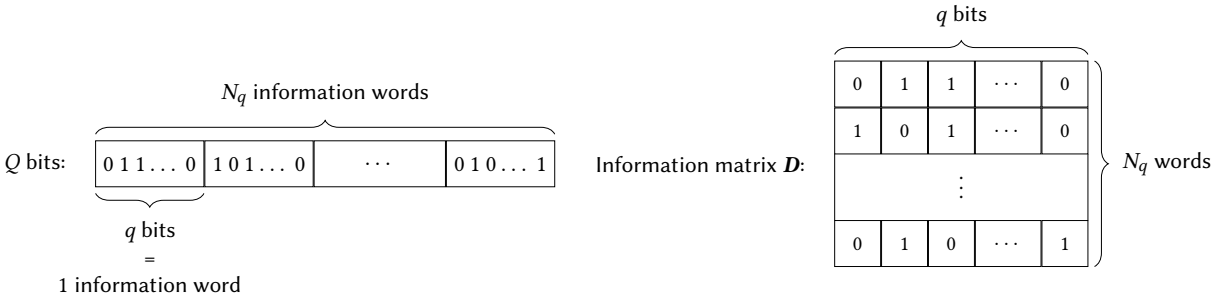

Figure 2.2 – *Segmentation of the information block of size Q in N_q words of size q, and construction of the matrix $\boldsymbol{D}$.*

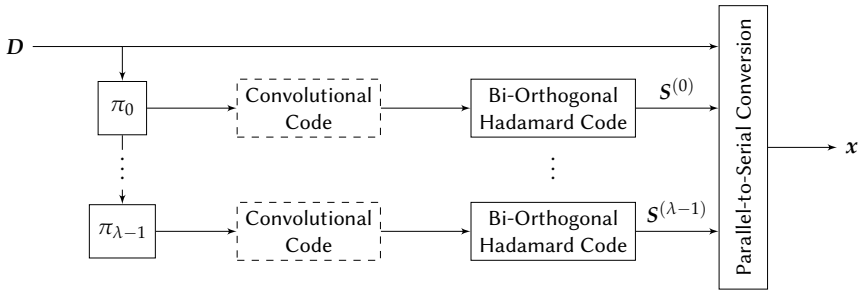

FIGURE 2.3 – *The Turbo-Hadamard encoding principle from [64] and its extension (in dashed) from [65].*

possible codewords, the Hamming weight of a word, defined as the Hamming distance between the word and the all-0 word, is the used metric. Finding the minimum distance is thus equivalent to finding the codeword with the lowest Hamming weight. The Hadamard code in its bi-orthogonal form has a minimum distance of $M/4$. Intuitively, the minimum output weight is obtained when the input information word has a weight of 1. The output of each stage will then consist in a single non-zero Hadamard code, the rest of the codes being all-0 codes. The output weight can then be roughly estimated to $\lambda \cdot M/4$, a slightly overestimated value since we considered a systematic form. But all the weight-1 input information words will have the same output weight, generating a large multiplicity for this weight, and a high error floor.

To overcome this problem, an extension of the initial principle was proposed [65], where a convolutional code is integrated. This extension corresponds to the dashed blocks in Figure 2.3. The convolutional code executes operations on each information word of q bits and adds a parity bits, to form a word of size $m = q + a$ bits. The bi-orthogonal Hadamard alphabet needs to have $M = 2^m$ elements, and the size of the Hadamard codewords is now equal to $N_c = M/2 = 2^{m-1} = 2^{q+a-1}$. The code rate is then

$$R_c = \frac{q}{q + \lambda\left(2^{q+a-1} - q\right)}, \tag{2.3}$$

thus lower than in the previous proposition. With the selected notations, the first scheme (without the convolutional code) is equivalent to the setting $a = 0$.

The use of the convolutional code will "break" the low-weight input words allowing for more than one Hadamard code to be different from 0. For example, using the exclusive OR (XOR) accumulator, an input word of the form $0 \ldots 00100 \ldots 0$ becomes $0 \ldots 00111 \ldots 1$. In order to illustrate the effect of the convolutional code, the output weights of every possible weight-1 input word have been represented in Figure 2.4, for an information block size of $Q = 498$ and the scheme with or without the convolutional code. The denomination "Concatenated Hadamard" corresponds to the initial proposition, without convolutional code. The accumulator was used in the Turbo-Hadamard case, adding only $a = 1$ parity bit. While in the case of Concatenated Hadamard every weight-1 input word gives the same low weight output, the accumulator increases significantly the possible output weights. However, it is not possible to conclude on the minimum distance of the code, since only weight-1 inputs are considered. The full spectrum of the possible outputs needs to be computed in order to estimate the minimum distance of the code.

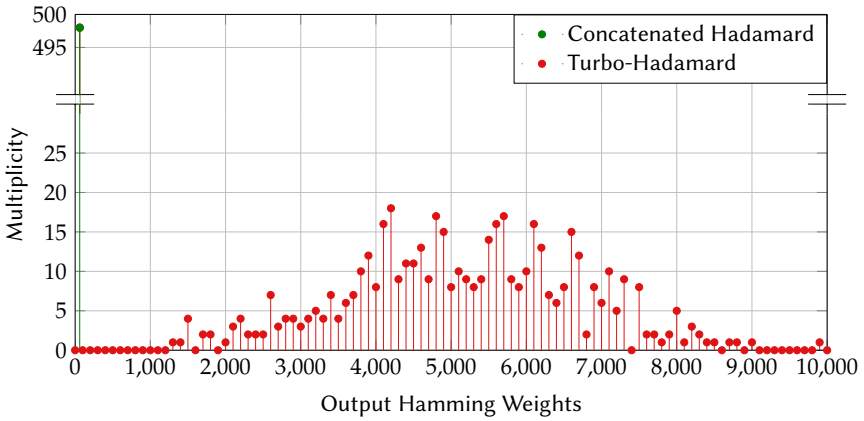

FIGURE 2.4 – *Influence of the convolutional code on the weights of the encoded words corresponding to every possible combination of length-498 weight-1 input information word. For both schemes, the parameters are $Q = 6$ and $\lambda = 4$. A random interleaver is used.*

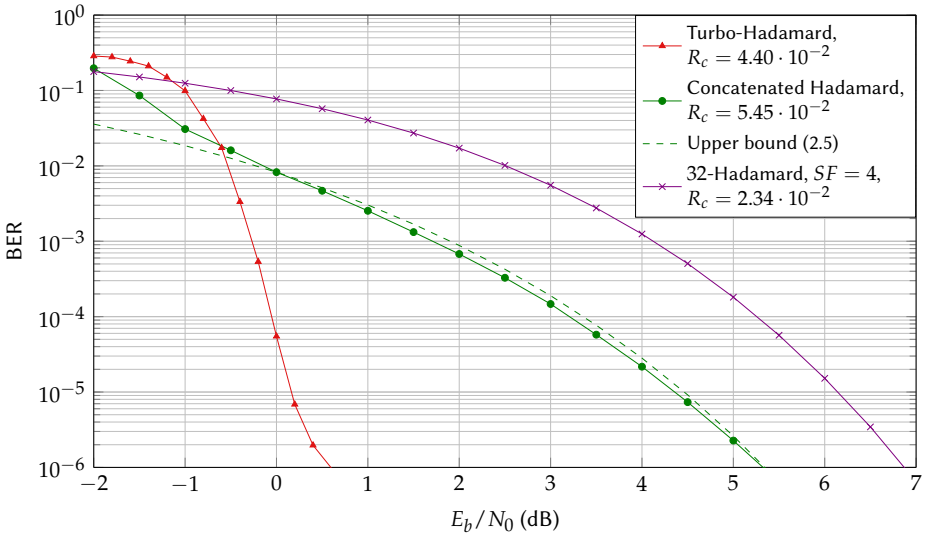

FIGURE 2.5 – *Turbo-Hadamard performance when considering the non-convolutive and the convolutive encoders (with the accumulator). The information block size is set to* $Q = 1024$ *bits, with parameters* $\lambda = 4$ *and Hadamard codewords of length* 32.

In the error floor region, i.e. at high E_b/N_0, an upper bound on the probability of bit error $\Pr(e)$ can be expressed by [65, 66]

$$\Pr(e) \leq \frac{1}{2} \sum_{y} \sum_{w} \frac{w}{Q} N_{w,y} \operatorname{erfc}\left(\sqrt{y R_c \frac{E_b}{N_0}}\right), \tag{2.4}$$

where R_c is the code rate, w is the Hamming weight of the information word leading to a codeword with weight y, $N_{w,y}$ is the number of codewords with weight y (or the multiplicity) and erfc is the function defined in (1.51). Because of the erfc function, codewords with small output weights (small y) will influence the upper bound more. A looser upper bound can be expressed by considering the contribution of the minimal distance only. This distance is known for the Concatenated Hadamard scheme and obtained for input words of weight 1. The bound can be expressed as

$$\Pr(e) \leq \frac{1}{2Q} N_{1,d_{min}} \operatorname{erfc}\left(\sqrt{d_{\min} R_c \frac{E_b}{N_0}}\right), \tag{2.5}$$

where $N_{w,d_{\min}} = Q$ and $d_{\min}$ depends on the parameters. The code rate R_c is given by Equation (2.2).

The performance in presence of Additive White Gaussian Noise (AWGN) and using a Binary Phase Shift Keying (BPSK) modulation for both schemes is depicted in Figure 2.5, along with the upper bound of the Concatenated Hadamard code computed with Equation (2.5) and the performance of a bi-orthogonal Hadamard code with a repetition factor of 4. An information block size $Q = 1042$ bits is selected, and $\lambda = 4$ stages are used. The parameter q is adjusted so that both schemes use Hadamard codewords of length $M/2 = 32$ ($M = 2^q$ for the Concatenated Hadamard and $M = 2^{q+1}$ for Turbo-Hadamard). Spectral efficiencies are slightly different but with the same order of magnitude.

The scheme 32-bi-orthogonal Hadamard with a repetition factor of 4 uses the classic Hadamard code. The receiver simply recombines the 4 repeated sequences and performs Maximum Likelihood (ML) decision (without any iterative process). The performance is not modified by the number of repetitions when considering the E_b/N_0, but the spectral efficiency is reduced. When considering the Concatenated Hadamard scheme, the use of a more sophisticated receiver which combines the different observations in the turbo process is implied. The result gives a gain of 2dB for a Bit Error Rate (BER) of 10^{-5}. However, as previously explained, this scheme has a poor minimal distance and a high error floor. It is rapidly reached and the waterfall region does not appear. To overcome this problem, the Turbo-Hadamard code adds some binary addition at the transmitter side to improve the minimal distance. The resulting scheme exhibits a much lower error floor, which only appears below 10^{-5} of BER. The gain at this BER is more than 4dB, or more than 6dB compared to the original scheme using the Hadamard code with repetition.

The Turbo-Hadamard scheme has been extensively studied, and its theoretical study using EXIT charts [67] shows that the scheme can approach the channel capacity as close as 0.3dB. Starting from an orthogonal code, the Turbo-Hadamard principle demonstrates the possibility that, using a parallel concatenation of orthogonal codes

with a convolutional step in each branch and a sophisticated receiver, the channel capacity can be closely approached. Extensions of the scheme have been proposed [68], but so far it has mostly been used for access procedures in coding spreading structure [69] and interference cancellation [70].

2.2 Principle of Turbo-FSK

In the previous section, key elements leading to the proposition of the Turbo-FSK scheme have been presented. FSK modulation demonstrates some interesting properties in the LPWA context (such as orthogonal modulation, constant envelope and convenient implementation). Also, the parallel concatenation of orthogonal codes associated with a convolutional code and a sophisticated receiver shows promising performance. In this section, the principle of the newly proposed Turbo-FSK transmission scheme is presented. A detailed explanation of its transmitter and receiver is given, and its typical performance is presented.

2.2.1 Transmitter

In order to present the transmitter for Turbo-FSK, the encoding and modulation procedures are described. The specific construction of the trellis is also reviewed.

Using similar notations as for the Turbo-Hadamard code and the segmentation depicted in Figure 2.2, the information block is composed of Q bits and is represented by the matrix $\boldsymbol{D}$, of size $q \times N_q$ (with $N_q = Q/q$, which is the number of binary words of length q in the information block). It is made from N_q row vectors $\boldsymbol{b} = \{b_n\}_{n\in\{0,\dots,q-1\}}$.

2.2.1.1 Architecture

The Turbo-FSK transmitter is depicted in Figure 2.6. The parallel structure is composed of λ stages, and the input of each one is an interleaved version of $\boldsymbol{D}$.

The Parity-Accumulator encoder used in each stage is depicted in Figure 2.7. Each rows $\boldsymbol{b}$ of the input are sequentially treated. The sum modulus 2 of the q bits and the memory is computed and the memory is updated with the result. The process can be interpreted as applying an accumulator on the parity of the q information bits. The encoder generates words of length $q+1$ bits ($a = 1$ with the Turbo-Hadamard notation), consisting in the q input bits and the output of the accumulator. The Parity-Accumulator is a Recursive Systematic Convolutional (RSC) code. By convention, the initiate state of the memory is set to 0, and the final state is forced to 0 by adding one extra information word. As the value of this word depends on the N_q previous words, it must be computed during the encoding process. At the end, the encoder generates $N_q + 1$ encoded words of size $m = q + 1$.

These $N_q + 1$ binary words are fed to the FSK Mapping block, which associates the m bits to one of the $M = 2^m$ codewords of the alphabet $\boldsymbol{\mathcal{A}}$. To perform FSK signaling, $\boldsymbol{\mathcal{A}}$ is constructed from the Hermitian transpose Discrete Fourier Transform (DFT) matrix (or the Inverse Discrete Fourier Transform (IDFT)) where $\boldsymbol{\mathcal{A}} = \boldsymbol{W}_M^H$ and

$$\boldsymbol{W}_M = \left\{\omega^{ki}\right\}_{\substack{k=0,1,\dots,M-1\\ i=0,1,\dots,M-1}}, \tag{2.6}$$

where $\omega = e^{-j\frac{2\pi}{M}}$ is the M-th root of unity. The output codeword is thus a row vector of M chips, where each element is a complex number. The output of the ℓ-th stage with $\ell \in \{0,\dots,\lambda-1\}$ is denoted by the matrix $\boldsymbol{S}^{(\ell)}$ of size $M \times (N_q + 1)$.

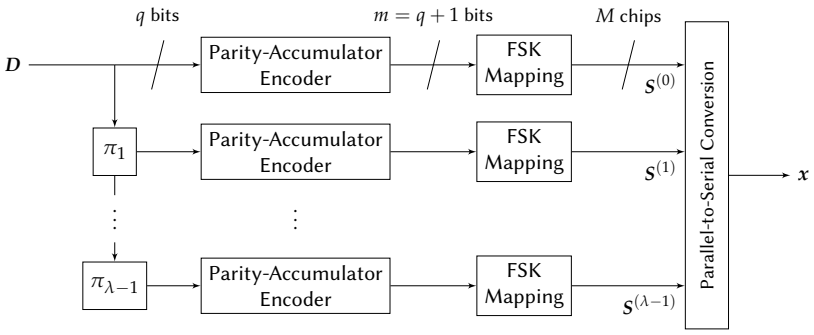

Figure 2.6 – *The Turbo-FSK transmitter architecture*

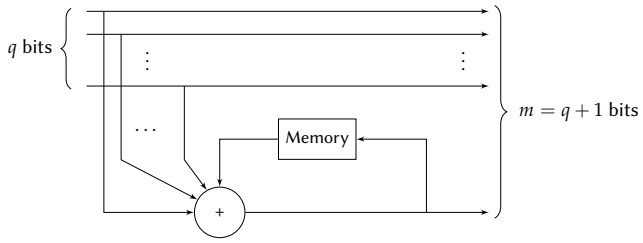

FIGURE 2.7 – *The Parity-Accumulator encoder*

The output of each stage is then concatenated into a signal $\boldsymbol{x}$, which contains $\lambda \times (N_q + 1)$ FSK codewords. As seen in Section 1.3.2, when considering a bandwidth B and a chip time equal to $T_c = 1/B$, the spectral efficiency is equal to the ratio between the number of information bits and the number of chips corresponding to the information block. The overall spectral efficiency of the scheme is thus given by

$$\eta = \frac{Q}{\lambda(N_q+1)M} \approx \frac{q}{\lambda M} = \frac{\log_2(M)-1}{\lambda M}. \tag{2.7}$$

where the approximation is valid when a large value of Q is considered. q corresponds to the number of information bits in one FSK codeword, with the relation $q = m - 1 = \log_2(M) - 1$.

2.2.1.2 TRELLIS

Since the Parity-Accumulator is a convolutional code, the encoding process can be represented with a trellis. However, because multiple information words of size q can have the same parity, several information words will lead to the same transition as there are parallel branches in the trellis. In Figure 2.8 (a), the t-th section of the trellis when $q = 2$ is represented. The output binary words are labeled on each branch. The underlined bits correspond to the input q bits, and the bold bit is the output of the accumulator (i.e. the content of the memory). The memory state is flipped when the parity of the input bits is equal to 1. There are 4 possible input words and 8 possible output words. The same input word is mapped to 2 different branches. This result can be generalized to every value of q, with 2^q possible input words and 2^{q+1} possible output words, for a total of 2^{q-1} branches per transition.

The output words of the Parity-Accumulator are then mapped to FSK codewords, as presented in Figure 2.6. The FSK codewords are denoted $\boldsymbol{c}^i$, with $i \in \{0, \ldots, M-1\}$. The trellis can now be represented with the codewords labeled on each branch, as represented in Figure 2.8 (b). This is one of the possible mappings. When considering the AWGN channel, all the mappings are equivalent due to the orthogonality property of the alphabet.

In Figure 2.9, the trellis of the Turbo-FSK with $M = 16$ is represented. For this case, each state transition has 4 different codewords.

When compared to the Turbo-Hadamard scheme, the main difference is the choice of alphabet. These two alphabets have the same orthogonal property, and thus the same performance on an AWGN channel. However, when the Hadamard code is systematic, the FSK alphabet is not. Each codeword is now a sequence of complex numbers

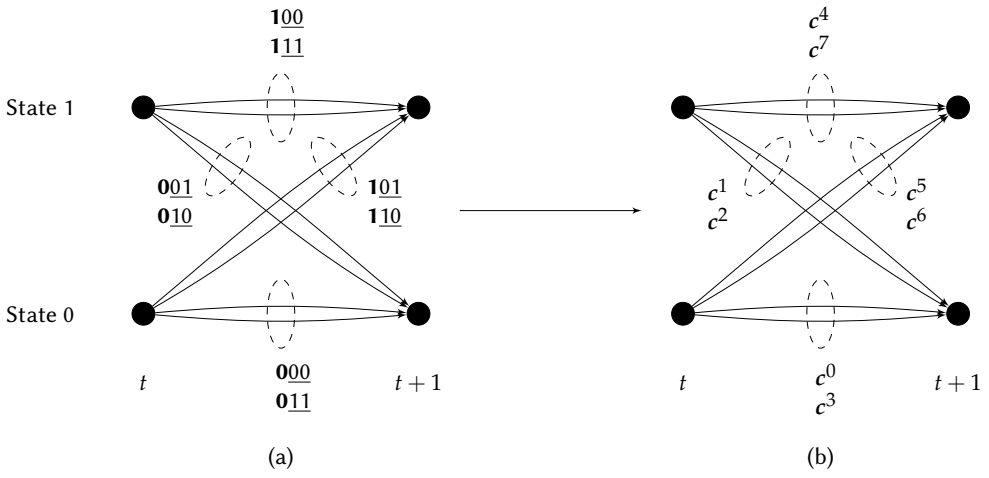

FIGURE 2.8 – *(a) Trellis of the Parity-Accumulator code with parameter $q = 2$. (b) Trellis of the Turbo-FSK with parameter $M = 8$.*

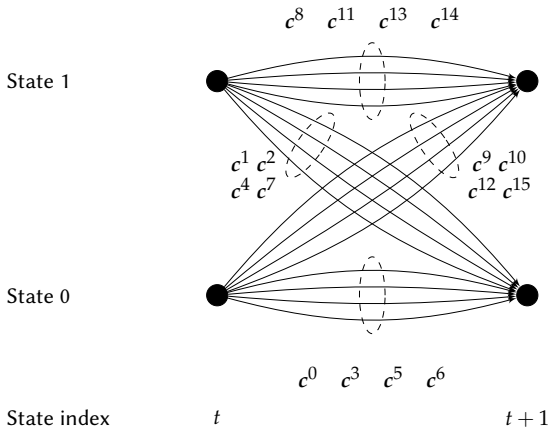

FIGURE 2.9 – *Trellis of the Turbo-FSK with parameter* $M = 16$.

directly associated to a physical waveform, as presented in Figure 1.7. This also means that the information bits are repeated λ times while they are only sent one time when using the Turbo-Hadamard scheme, thus the spectral efficiency is reduced. Due to these differences, the decoder of the Turbo-Hadamard channel code cannot be used for the Turbo-FSK scheme and a specific receiver must be derived.

2.2.2 RECEIVER

The receiver for Turbo-FSK relies on the fundamental principle of a turbo decoder. At the transmitter, λ versions of the same message have been encoded and sent. For each version, the receiver estimates the information bits given both the observation of the channel for this version and the *a priori* information coming from the decoding of the other versions. To do so, the Bahl, Cocke, Jelinek and Raviv (BCJR) is used on the code's trellis. The algorithm computes the *A Posteriori* Probability (APP) of the codewords given the observation and deduces the APP of information bits. One iteration of the receiver consists in doing this process for each version. Multiple iteration may be performed.

In order to represent the operations processed at the receiver for one version of the message, a simplified representation is depicted in Figure 2.10. As previously mentioned, there are two inputs: the channel observations consisting in noisy FSK waveforms, and the *a priori* information from the other $(\lambda - 1)$ decoders, represented as log-ratios of the information bits. The *a priori* information must be interleaved to correspond to the information for this version. One of the key features of the receiver that ensures good performance is to consider the orthogonal FSK codewords as the metric on the trellis when performing the BCJR. Using the example of $q = 2$, the trellis in Figure 2.8 (b) considers the likelihood of orthogonal codewords as the metric, as each branch is orthogonal to all the others. On the contrary, the trellis in Figure 2.8 (a) considers the binary words, which are not orthogonal to each other. This property of the scheme was considered in [65] (for the Turbo-Hadamard). The influence of this metric is studied in a later section. For the orthogonal codeword metric to be used, the likelihoods of the M possible codewords considering the observation from the channel are computed, and the *a priori* information is recombined and expressed as orthogonal codeword probabilities. These two values are multiplied. Intuitively, the likelihood of each codeword coming from the channel is weighted by the *a priori* probability of the codeword coming from the other decoders. The result is fed to the BCJR, which estimates the information bits. The *a priori* information is then removed in order to obtain the extrinsic information, which is de-interleaved and then used to estimate the

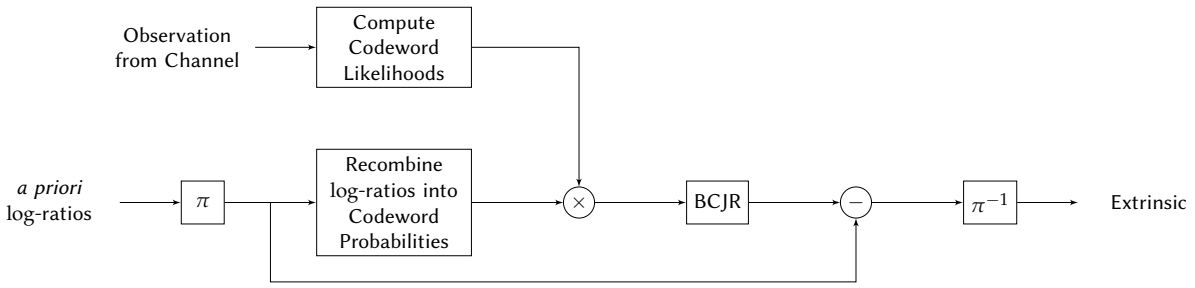

FIGURE 2.10 – *Schematic representation of the receiver's operations, when the orthogonal codewords metrics is used.*

information bits of another version.

The rest of this section consists of several technical descriptions of the receiver. First, the mathematical derivations of the BCJR are presented, i.e. the rigourous description of how the algorithm processes the orthogonal codewords metric (represented by likelihood of the codewords) to estimate the information bits. Second, the global architecture of the receiver is introduced, showing how the receiver can be split into a front-end that performs the detection of the FSK waveform (by computing the likelihoods) and an iterative decoder. Third, precisions on how the information is exchanged inside the iterative decoder are presented (notably correcting some approximations of the representation Figure 2.10). Finally, the max-log simplification of the decoding algorithm is presented.

2.2.2.1 Derivation of the BCJR Algorithm

The decoding of a parallel concatenated scheme with binary codewords [8] was treated in Chapter 1. The BCJR algorithm [31] is presented in Appendix C. This algorithm is used to compute the logarithmic ratio of the APP of the information bits, defined as log-APP with

$$L\left(b_{n,t} \,\middle|\, \boldsymbol{R}_1^{N_q+1}\right) = \log \frac{\Pr\left(b_{n,t} = +1 \,\middle|\, \boldsymbol{R}_1^{N_q+1}\right)}{\Pr\left(b_{n,t} = -1 \,\middle|\, \boldsymbol{R}_1^{N_q+1}\right)}, \tag{2.8}$$

where $\boldsymbol{R}_1^{N_q+1}$ is the received codeword sequence and $b_{n,t}$ is the bit at index n of the information word at time index t.

The BCJR algorithm itself actually computes the APP of the transitions $\Pr\left(S_{t-1} = s',\, S_t = s \,\middle|\, \boldsymbol{R}_1^{N_q+1}\right)$, with $\{s, s'\} \in \{0, \ldots, N_s - 1\}^2$, where N_s is the number of states and S_t (resp. S_{t-1}) is the state at time index t (resp. $t-1$), with $t \in \{1, \ldots, N_q + 1\}$. The derivation of this APP is done in Appendix C.1, and can be expressed using

$$\Pr\left(S_{t-1} = s',\, S_t = s \,\middle|\, \boldsymbol{R}_1^{N_q+1}\right) = \frac{\alpha_{t-1}(s') \cdot \gamma_t(s', s) \cdot \beta_t(s)}{p\left(\boldsymbol{R}_1^{N_q+1}\right)}, \tag{2.9}$$

where α and β are computed recursively with

$$\alpha_t(s) = \sum_{s'=0}^{N_s-1} \alpha_{t-1}(s')\gamma_t(s', s) \tag{2.10}$$

and

$$\beta_t(s) = \sum_{s'=0}^{N_s-1} \gamma_{t+1}(s, s')\beta_{t+1}(s'). \tag{2.11}$$

The value of $\gamma_t(s', s)$ is related to the likelihood of one transition to occur and the *a priori* probability of that transition. It is expressed

$$\gamma_t(s', s) = p\left(\boldsymbol{r}_t \,\middle|\, S_t = s,\, S_{t-1} = s'\right) \Pr\left(S_t = s \,\middle|\, S_{t-1} = s'\right). \tag{2.12}$$

In the Turbo-FSK case, a single transition from s' to s is represented by multiple codewords $\boldsymbol{c}^i$. If we denote $\mathcal{T}_{s' \to s}$ the group of codewords that maps the transition from s' to s, the previous term $\gamma_t(s', s)$ can be expressed with

$$\gamma_t(s', s) = \sum_{i \in \mathcal{T}_{s' \to s}} p\left(\boldsymbol{r}_t \,\middle|\, \boldsymbol{c}^i\right) \Pr\left(\boldsymbol{c}^i\right), \tag{2.13}$$

where $p\left(\boldsymbol{r}_t \,\middle|\, \boldsymbol{c}^i\right)$ is the likelihood of observing $\boldsymbol{r}_t$ given that $\boldsymbol{c}^i$ was sent, and $\Pr\left(\boldsymbol{c}^i\right)$ is the *a priori* probability of having the codeword $\boldsymbol{c}^i$.

The codeword $\boldsymbol{c}^i$ encodes an information word $\boldsymbol{b}^i$ of length q. The *a priori* probability of having the codeword $\boldsymbol{c}^i$ is expressed, as developed in Appendix C.2.2, as

$$\begin{aligned} \Pr\left(\boldsymbol{c}^i\right) &= \prod_{k=0}^{q-1} \Pr\left(b_k = b_k^i\right) \\ &= C_{\text{st}} \exp\left\{\frac{1}{2} \sum_{k=0}^{q-1} L_A(b_k) b_k^i\right\}, \end{aligned} \tag{2.14}$$

where b_k refers to the value of the bit at index k, C_{st} is a constant independent of i cancelled out in further computations and L_A the *a priori* log ratio defined in Section 1.3.4.5 and given by

$$L_A(b_k) = \log \frac{\Pr(b_k = +1)}{\Pr(b_k = -1)}. \tag{2.15}$$

The likelihood of the FSK codeword $p\left(\boldsymbol{r}_t \,\middle|\, \boldsymbol{c}^i\right)$ under an AWGN channel is given by (cf. Equation (1.40))

$$\begin{aligned} p\left(\boldsymbol{r}_t \,\middle|\, \boldsymbol{c}_t^i\right) &= \prod_{k=0}^{M-1} p\left(r_{k,t} \,\middle|\, c_{k,t}^i\right) \\ &= \left(\frac{1}{2\pi\sigma_{\text{ch}}^2}\right)^M \exp\left\{-\frac{\|\boldsymbol{r}_t\|^2}{2\sigma_{\text{ch}}^2}\right\} \exp\left\{-\frac{\|\boldsymbol{c}^i\|^2}{2\sigma_{\text{ch}}^2}\right\} \exp\left\{\frac{1}{\sigma_{\text{ch}}^2} \operatorname{Re}\left(\langle \boldsymbol{r}_t, \boldsymbol{c}^i \rangle\right)\right\}. \end{aligned} \tag{2.16}$$

If the FSK alphabet is assumed normalized, then the product of (2.14) and (2.16) gives

$$p\left(\boldsymbol{r}_t \,\middle|\, \boldsymbol{c}_t^i\right) \Pr\left(\boldsymbol{c}^i\right) = C_{\text{st}} \exp\left\{\frac{1}{\sigma_{\text{ch}}^2} \operatorname{Re}\left(\langle \boldsymbol{r}_t, \boldsymbol{c}^i \rangle\right) + \frac{1}{2} \sum_{k=0}^{q-1} L_A(b_k) b_k^i\right\}, \tag{2.17}$$

where C_{st} is a constant independent of i and cancelled out in further computations. At the transmitter, the codewords $\boldsymbol{c}^i$ are taken from the IDFT. Following the definition of the scalar product given in Equation (1.29), the term $\langle \boldsymbol{r}_t, \boldsymbol{c}^i \rangle$ is strictly equivalent to the i-th dimension of the DFT of $\boldsymbol{r}_t$. The likelihood can thus be computed using a front-end that executes a DFT on the received sequence.

Using the α and β of BCJR algorithm, the APP of the codeword $\boldsymbol{c}^i$ is given by

$$\Pr\left(\boldsymbol{c}^i \,\middle|\, \boldsymbol{R}_1^{N_q+1}\right) = \frac{\alpha_{t-1}(s_i') \cdot p\left(\boldsymbol{r}_t \,\middle|\, \boldsymbol{c}^i\right) \Pr\left(\boldsymbol{c}^i\right) \cdot \beta_t(s_i)}{p\left(\boldsymbol{R}_1^{N_q+1}\right)}, \tag{2.18}$$

where s_i' (resp. s_i) is the starting (resp. arriving) state of the transition mapped by the codeword $\boldsymbol{c}^i$.

$\mathcal{B}_u^n$ refers to the group of codewords which encode an information word for which the bit $b_n = u$. The APP of the information bit $b_{n,t}$ is given by

$$\Pr\left(b_{n,t} = u \,\middle|\, \boldsymbol{R}_1^{N_q+1}\right) = \sum_{i \in \mathcal{B}_u^n} \Pr\left(\boldsymbol{c}^i \,\middle|\, \boldsymbol{R}_1^{N_q+1}\right), \tag{2.19}$$

and using Equation (2.8), the log-APP can be computed with

$$L\left(b_{n,t} \,\middle|\, \boldsymbol{R}_1^{N_q+1}\right) = \log \frac{\sum_{i \in \mathcal{B}_{+1}^n} \alpha_{t-1}(s_i') \cdot p\left(\boldsymbol{r}_t \,\middle|\, \boldsymbol{c}^i\right) \Pr\left(\boldsymbol{c}^i\right) \cdot \beta_t(s_i)}{\sum_{i \in \mathcal{B}_{-1}^n} \alpha_{t-1}(s_i') \cdot p\left(\boldsymbol{r}_t \,\middle|\, \boldsymbol{c}^i\right) \Pr\left(\boldsymbol{c}^i\right) \cdot \beta_t(s_i)}. \tag{2.20}$$

2.2.2.2 Architecture of the Receiver

In the expression of the log-APP, the terms $p\left(\boldsymbol{r}_t \,\middle|\, \boldsymbol{c}^i\right)$ correspond to the likelihood of the codeword $\boldsymbol{c}^i$. It is related to the channel observation, and can be computed by a front-end performing a DFT on the received sequence. The likelihood needs to be computed only once, as its value is independent from the iterative process. The value $\Pr\left(\boldsymbol{c}^i\right)$ is the *a priori* probability, coming from the other decoders.

The receiver's architecture of the Turbo-FSK is depicted in Figure 2.11. The time observation $\boldsymbol{r}$ is reorganized into λ matrices $\boldsymbol{r}^{(\ell)}$, with $\ell \in \{0, \ldots, \lambda - 1\}$ and the channel observation of each stage is retrieved. The matrix $\boldsymbol{r}^{(\ell)}$ has a size of $(N_q + 1) \times M$, and corresponds to the received codewords matrix $\boldsymbol{R}_1^{N_q+1}$ previously considered for the BCJR computation. For each stage, the detector (or front-end) computes the likelihood of the codewords of the alphabet given in Equation (2.16), or simply the left term in the exponential in (2.17). As this step involves a DFT, it can be efficiently performed using the Fast Fourier Transform (FFT) algorithm [71] . The likelihood of each of the M codewords is sent to the decoder, which estimates the log-APP of the information bits in 4 steps:

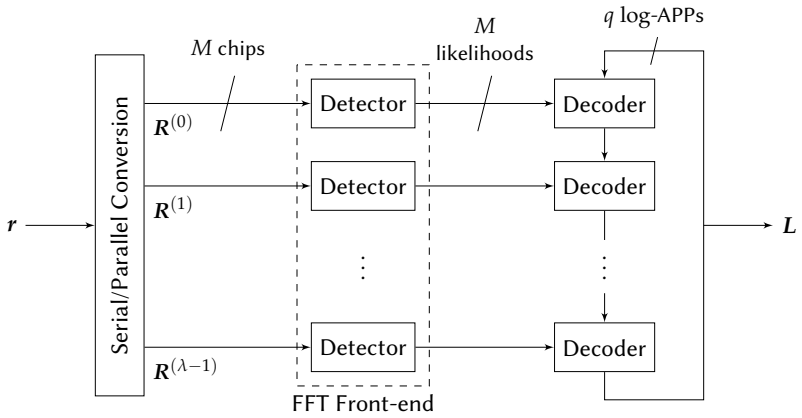

FIGURE 2.11 – *The Turbo-FSK receiver architecture.*

1. Using the likelihood from the detector and the *a priori* probability from the other decoders, the product of (2.17) is computed.
2. For each transition $s' \to s$, the value of $\gamma_t(s', s)$ is computed using Equation (2.13).
3. Under the initialization conditions $\alpha_0(0) = 1$ and $\beta_{N_q+1}(0) = 1$, the values of α and β for all t are computed.
4. The log-APP is computed with Equation (2.20).

Since an interleaver step separates each encoder, the *a priori* information needs to be properly de-interleaved when decoding. The same process is repeated for all decoders. One iteration refers to the execution of the 4 steps previously presented and iterations can be repeated. At the end of an iteration, the matrix $\boldsymbol{L}$ of size $a \times q$ contains the log-APP of all the decoders. A hard decision can be made from $\boldsymbol{L}$ by taking the sign of each log-APP of the q bits.

With this architecture, the detection of the FSK, i.e. the estimation of the likelihoods of the codewords of the alphabet, is done prior to turbo decoding. The demodulation is combined with decoding, as the Log Likelihood Ratio (LLR) of the encoded bits are never computed. This absence of actual demodulation makes the scheme very singular and very distinct from the Bit-Interleaved Coded Modulation (BICM) scheme [72] and its iterative form [73], where the demodulator and the decoder exchange their extrinsic information. The BICM scheme was extensively studied for the FSK case in [74, 75, 76].

2.2.2.3 Exchanges of Extrinsic Information

The extrinsic information generated by the BCJR algorithm can be expressed by the log-APP. The product depending on the codeword $\boldsymbol{c}^i$ in the log-APP can be factorized as

$$\begin{aligned} p\left(\boldsymbol{r}_t \,\middle|\, \boldsymbol{c}_t^i\right) \Pr\left(\boldsymbol{c}^i\right) &= \prod_{k=0}^{M-1} p\left(r_{k,t} \,\middle|\, c_{k,t} = c_{k,t}^i\right) \prod_{k=0}^{q-1} \Pr\left(b_{k,t} = b_{k,t}^i\right) \\ &= \Pr\left(b_{n,t} = b_{n,t}^i\right) \prod_{k=0}^{M-1} p\left(r_{k,t} \,\middle|\, c_{k,t} = c_{k,t}^i\right) \prod_{\substack{k=0 \\ k\neq n}}^{q-1} \Pr\left(b_{k,t} = b_{k,t}^i\right), \end{aligned} \tag{2.21}$$

and the log-APP is now expressed

$$\begin{aligned} L\left(b_{n,t} \,\middle|\, \boldsymbol{R}_1^{N_q+1}\right) &= \log \frac{\Pr\left(b_{n,t} = +1\right)}{\Pr\left(b_{n,t} = -1\right)} + \log \frac{\displaystyle\sum_{i \in \mathcal{B}_{+1}^n} \alpha_{t-1}(s_i') \cdot p\left(\boldsymbol{r}_t \,\middle|\, \boldsymbol{c}_t^i\right) \prod_{\substack{k=0 \\ k\neq n}}^{q-1} \Pr\left(b_{k,t} = b_{k,t}^i\right) \cdot \beta_t(s_i)}{\displaystyle\sum_{i \in \mathcal{B}_{-1}^n} \alpha_{t-1}(s_i') \cdot p\left(\boldsymbol{r}_t \,\middle|\, \boldsymbol{c}_t^i\right) \prod_{\substack{k=0 \\ k\neq n}}^{q-1} \Pr\left(b_{k,t} = b_{k,t}^i\right) \cdot \beta_t(s_i)} \\ &= L_A(b_{n,t}) + L_E, \end{aligned} \tag{2.22}$$

i.e. as the sum of the *a priori* log ratios L_A fed to the decoder and the extrinsic information L_E generated by the algorithm. However, the LLR of the considered bit has not been extracted, as it is usually done when considering

binary codewords. Here, the codewords are complex waveforms and the LLR of one specific bit cannot be computed without demodulating the waveform. The system requires the likelihoods of the codewords to estimate the APP. For the following, the denomination extrinsic information includes the channel observation that cannot be extracted.

The details of the input and output log ratios for one decoder ℓ at iteration ι are represented in Figure 2.12. In order to demonstrate that the output of this decoder contains the extrinsic information of all the other decoders as well as its own, we expressed the value of the output of each decoder. All matrices have a size of $q \times N_q$, and the log ratio $\boldsymbol{L}^{(\ell),\iota}$ refers to this log ratio for decoder ℓ at iteration ι. The *a priori* and extrinsic log ratios are initialized as

$$\begin{aligned} \boldsymbol{L}_A^{(0),1} &= \mathbf{0} \\ \boldsymbol{L}_E^{(\ell),0} &= \mathbf{0} \qquad \forall \ell. \end{aligned} \tag{2.23}$$

For the first iteration ($\iota = 1$) and using Equation (2.22), the consecutive log-APP matrices are given by

$$\begin{aligned} \boldsymbol{L}^{(0),1} &= \boldsymbol{L}_A^{(0),1} + \boldsymbol{L}_E^{(0),1} = \boldsymbol{L}_E^{(0),1} \\ \boldsymbol{L}^{(1),1} &= \boldsymbol{L}_A^{(1),1} + \boldsymbol{L}_E^{(1),1} = (\boldsymbol{L}^{(0),1} - \boldsymbol{L}_E^{(1),0}) + \boldsymbol{L}_E^{(1),1} = \boldsymbol{L}_E^{(0),1} + \boldsymbol{L}_E^{(1),1} \\ &\cdots \\ \boldsymbol{L}^{(\lambda-1),1} &= \sum_{\ell=0}^{\lambda-1} \boldsymbol{L}_E^{(\ell),1}, \end{aligned} \tag{2.24}$$

which confirms that at the end of the first iteration, the extrinsic value of all decoders is included in the log-APP matrix. When starting the second iteration ($\iota = 2$), the *a priori* log ratio of the first decoder is given by

$$\begin{aligned} \boldsymbol{L}_A^{(0),2} &= \boldsymbol{L}^{(\lambda-1),1} - \boldsymbol{L}_E^{(0),1} \\ &= \sum_{\ell=1}^{\lambda-1} \boldsymbol{L}_E^{(\ell),1}, \end{aligned} \tag{2.25}$$

and its log-APP is given by

$$\begin{aligned} \boldsymbol{L}^{(0),2} &= \boldsymbol{L}_A^{(0),2} + \boldsymbol{L}_E^{(0),2} \\ &= \sum_{\ell=1}^{\lambda-1} \boldsymbol{L}_E^{(\ell),1} + \boldsymbol{L}_E^{(0),2}. \end{aligned} \tag{2.26}$$

By generalizing at the iteration ι, the log-APP of the ℓ-th decoder is given by

$$\boldsymbol{L}^{(\ell),\iota} = \sum_{k=0}^{\ell} \boldsymbol{L}_E^{(k),\iota} + \sum_{k=\ell+1}^{\lambda-1} \boldsymbol{L}_E^{(k),\iota-1}, \tag{2.27}$$

confirming that the log-APP contains the extrinsic information of all the previous decoders and the extrinsic information of all the next decoders, for this iteration. Additionally, Equation (2.25) shows how one decoder only uses the extrinsic information from all the other decoders as *a priori*, and does not reuse information it generated in previous iterations.

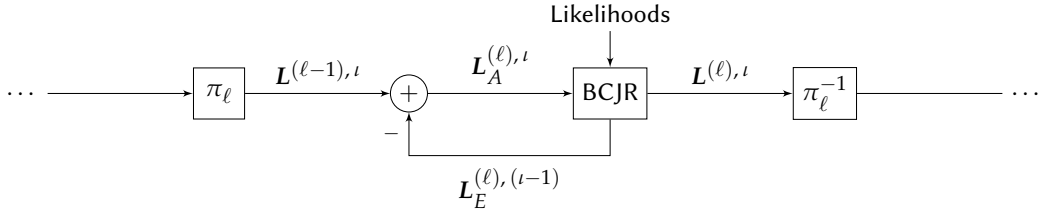

FIGURE 2.12 – *The exchanges of* log *ratios around one decoder* ℓ *at iteration* ι.

2.2.2.4 Sub-optimal Algorithm

The algorithm previously described performs the Maximum *A Posteriori* (MAP). It is optimal as it minimizes the probability of bit error, but requires the computation of numerous multiplication and exponential functions. This is hardly feasible in a practical implementation thus a simplification should be considered. The most common technique for turbo receivers is to work with the log of all the term of the MAP receiver. The max-log approximation can then be used. It is given by

$$\log\left(\sum_i e^{x_i}\right) \simeq \max_i(x_i). \tag{2.28}$$

Following this simplification, the product of (2.9) is given by

$$\log\left(\alpha_{t-1}(s')\cdot\gamma_t(s',s)\cdot\beta_t(s)\right) = \log\alpha_{t-1}(s') + \Gamma_t(s',s) + \log\beta_t(s), \tag{2.29}$$

where $\log\alpha_t$ is expressed from (2.10) as

$$\log\alpha_t(s) = \max_{s'}\left[\log\alpha_{t-1}(s') + \Gamma_t(s',s)\right] \tag{2.30}$$

and $\log\beta_t$ is expressed from (2.11) as

$$\log\beta_t(s) = \max_{s'}\left[\Gamma_{t+1}(s,s') + \log\beta_{t+1}(s')\right]. \tag{2.31}$$

The term Γ_t is obtained by using the max-log operator on Equation (2.13) combined with (2.17), and is expressed

$$\Gamma_t(s',s) = \max_{i\in\mathcal{T}_{s'\to s}}\left[\frac{1}{\sigma^2_{\text{ch}}}\text{Re}\left(\langle \boldsymbol{r}_t, \boldsymbol{c}^i\rangle\right) + \frac{1}{2}\sum_{k=0}^{q-1} L_A(b_k)b_k^i\right]. \tag{2.32}$$

Finally, the log-APP of the bit is given by

$$\begin{aligned} L\left(b_{n,t}\,\middle|\,\boldsymbol{R}_1^{N_q+1}\right) = &\max_{i\in\mathcal{B}^n_{+1}}\left[\log\alpha_{t-1}(s'_i) + \frac{1}{\sigma^2_{\text{ch}}}\text{Re}\left(\langle \boldsymbol{r}_t, \boldsymbol{c}^i\rangle\right) + \frac{1}{2}\sum_{k=0}^{q-1} L_A(b_k)b_k^i + \log\beta_t(s_i)\right] \\ &- \max_{i\in\mathcal{B}^n_{-1}}\left[\log\alpha_{t-1}(s'_i) + \frac{1}{\sigma^2_{\text{ch}}}\text{Re}\left(\langle \boldsymbol{r}_t, \boldsymbol{c}^i\rangle\right) + \frac{1}{2}\sum_{k=0}^{q-1} L_A(b_k)b_k^i + \log\beta_t(s_i)\right]. \end{aligned} \tag{2.33}$$

The algorithm using this max-log approximation is referred to as the max-log-MAP algorithm. The performance loss of the max-log-MAP algorithm can be reduced by weighting the extrinsic information exchanged in the decoder [40].

2.2.3 Typical Performance

To illustrate the performance of the Turbo-FSK scheme, simulations are performed for the AWGN channel, with coherent reception. Because the processing gain after 10 iterations is small, our simulations are restricted to this number of iterations. For this study, only random interleavers are considered, but performance improvements could be achieved by using optimized interleaving functions. First, the performance versus the Turbo-Hadamard scheme presented in Section 2.1.2 is considered, and the difference between the two schemes are studied. Then, the architecture of the proposed receiver is questionned and compared to another possible option. Finally, the influence of the different parameters (size of FSK, number of stages and size of interleaver) is investigated.

2.2.3.1 Performance versus Turbo-Hadamard

The two main differences between the Turbo-Hadamard channel code and the Turbo-FSK are the alphabet of codewords and the transmission of the systematic bits. In the Turbo-FSK case, codewords are no longer binary, and the systematic bits of each stage are transmitted. In order to quantify the performance loss of repeating the information bits, we consider an alternative to the initial Turbo-Hadamard, where all the systematic bits are sent λ times. This scheme will be referred to as Turbo-Hadamard Repeat. The accumulator is considered, leading to

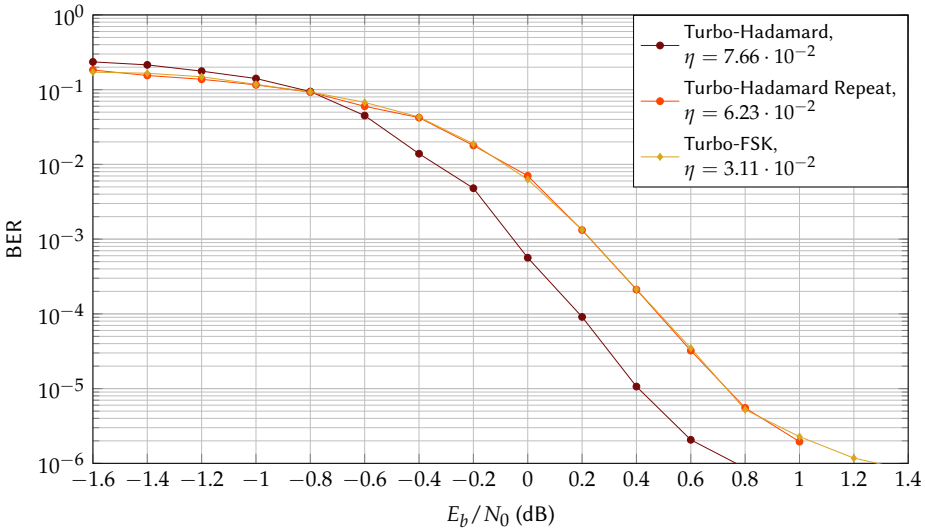

FIGURE 2.13 – *Performance of the Turbo-FSK scheme versus Turbo-Hadamard and Turbo-Hadamard Repeat for the case* $q = 4$, $\lambda = 4$ *and* $Q = 1024$. 10 *iterations are performed, and the MAP algorithm is used.*

$a = 1$ in Section 2.1.2. Compared to the rate of Turbo-Hadamard given in Equation (2.3), the code rate of the Turbo-Hadamard Repeat is reduced, and can be expressed

$$R_c = \frac{q}{\lambda \cdot 2^q}. \tag{2.34}$$

A BPSK modulation is considered, and since this modulation has a spectral efficiency of 1 bits·s^{-1}·Hz^{-1}, the spectral efficiencies of the Turbo-Hadamard schemes are equal to their rate. Compared to the spectral efficiency of Turbo-FSK given Equation (2.7) and where $M = 2^{q+1}$, there is a factor 2. This is due to the use of a bi-orthogonal alphabet which is twice more efficient, while the Turbo-FSK scheme uses an orthogonal alphabet.

In order to compare the schemes, we choose the parameters $q = 4$ and $\lambda = 4$. For the Turbo-FSK scheme, this implies the use of FSK codewords of length 32, while the bi-orthogonal Hadamard codewords in the other schemes have a length of 16 bits. For an interleaver size $Q = 1024$, the BER performance of the three considered schemes are depicted in Figure 2.13. The difference of performance between the Turbo-Hadamard and the Turbo-Hadamard Repeat shows the impact of the repetition of the systematic bits. The repetition actually induces a loss of performance of approximately 0.3dB. The BER performance of the Turbo-FSK and the Turbo-Hadamard Repeat is similar because the modulations used (respectively FSK and bi-orthogonal Hadamard) have the same performance under AWGN channel. Apart from the modulation, both schemes are similar. The comparison of performance of both the Turbo-Hadamard and the Turbo-FSK versus the Turbo-Hadamard Repeat shows that the difference of performance of the Turbo-FSK versus the initial Turbo-Hadamard scheme is only due to the repetition of the systematic bits. Due to the fact that the Turbo-FSK uses non-binary codewords, it is non-systematic. This performance is shown for an arbitrary (but equal) value of q for all schemes. Optimization of the parameters is investigated in a following section.

The differences in performance and in spectral efficiency do not consider the specificities of the waveform used, which, for example, may have an influence on frequency selective channels.

2.2.3.2 Alternative Receiver Based on Binary Codewords Metric

In the introduction of Section 2.2.2, concerning the description of the receiver, it was emphasized how the receiver needs to consider the orthogonal codewords as the metric for the computation of the BCJR. The derivation of the receiver was made in that perspective. However, another metric that can be used for the BCJR is the use of the binary word, as labeled in Figure 2.8 (a). The schematic view of the operation to estimate the information bits of one version is then depicted in Figure 2.14. Unlike the conventional Turbo-FSK receiver, the observation from the channel is converted into LLR, i.e. the FSK is demodulated. For each FSK codewords, $q + 1$ LLRs are obtained: q systematic bits and 1 extra bit from the encoder. The systematic LLRs from the channel are then added to the *a priori* interleaved log-ratios, and the BCJR uses the log-ratios of the binary words as the metric. Branches in the trellis are not orthogonal to each other. Extrinsic information is then computed by substracting the log-ratios of the information bits fed to the BCJR. Using this receiver, the front-end (i.e. the FSK demodulator) no longer feeds

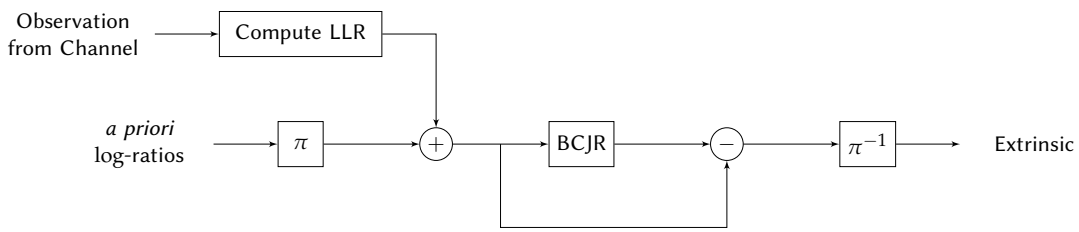

FIGURE 2.14 – *Alternative receiver for Turbo-FSK, using binary codewords metric.*

likelihoods to the decoder but LLR of the encoded bits. The whole system can thus be seen as the concatenation of a TC (which uses the Parity-Accumulator RSC encoder) and an FSK modulation.

2.2.3.3 PERFORMANCE OF THE RECEIVER

Three possible receivers are compared: the Turbo-FSK receiver proposed in Section 2.2.2.2 (referred to as Proposed Receiver) with the MAP, the same Turbo-FSK receiver but using the max-log approximation, and the Alternative Receiver previously presented and depicted in Figure 2.14, with the MAP algorithm. The Turbo-FSK with parameters $M = 32$, $\lambda = 4$ and $Q = 1024$ is chosen, and for the three possible receivers simulations are performed under AWGN channel. The BER performance using each possible receiver is depicted in Figure 2.15, along with the performance of the uncoded 32-FSK modulation, repeated 4 times. For the Proposed Receiver, the figure shows the performance loss with the use of the max-log approximation to be around 0.4dB. However, only max and sums operations are required instead of the exact probabilities and complexity of the algorithm is significantly reduced.

When considering the MAP algorithm only, the Proposed Receiver outperforms the Alternative Receiver with a gap of 4.2dB for a BER of 10^{-5}. Since the difference between the two receivers is the metric used by the BCJR algorithm, we can conclude that using the orthogonal codewords metric on the trellis (instead of the binary codewords metric when using the alternative receiver) is vital for the receiver to achieve good performance. The exchange of channel observations between the front-end (i.e. the detector) and the iterative receiver must be done through the use of likelihoods of the codewords, instead of LLR of the encoded bits as it is conventionally done.

The $(E_b/N_0)_{\min}$ for this spectral efficiency (equal to -1.544dB), computed with Equation (1.16), is represented as well. The Proposed Receiver with the MAP algorithm reaches a BER of 10^{-5} at 0.8dB, only 2.4dB away from the minimum reachable E_b/N_0.

2.2.3.4 INFLUENCE OF THE PARAMETERS

Turbo-FSK is characterized by three parameters: the interleaver size q, the number of stages λ, and the size of the FSK codewords M. The influence of each parameter on the performance is studied through BER simulations.

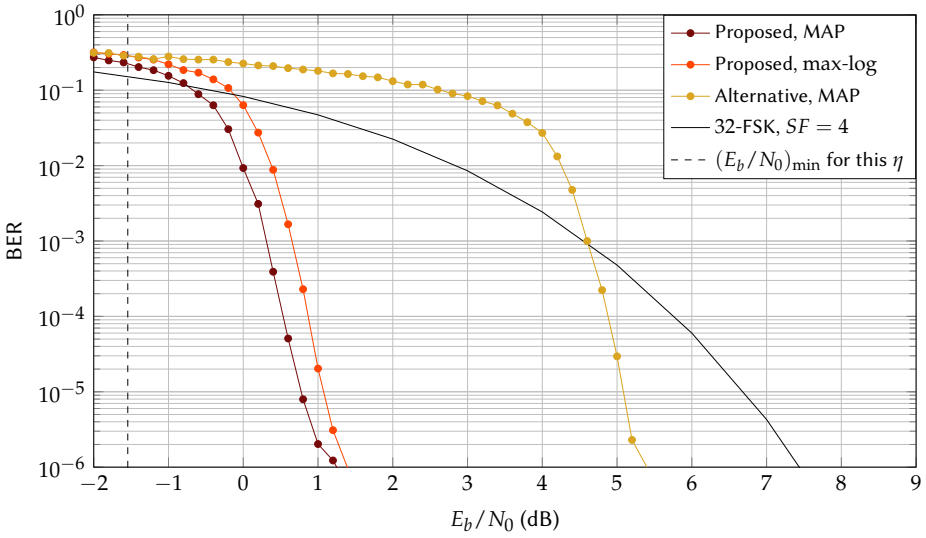

FIGURE 2.15 – *Performance of the Turbo-FSK scheme with parameters $M = 32$, $\lambda = 4$ and $Q = 1024$, for the three possible receivers. The spectral efficiency is equal to $\eta = 3.11 \cdot 10^{-2}$ bits·s^{-1}·Hz^{-1}. 10 iterations are performed, and the MAP algorithm is used.*

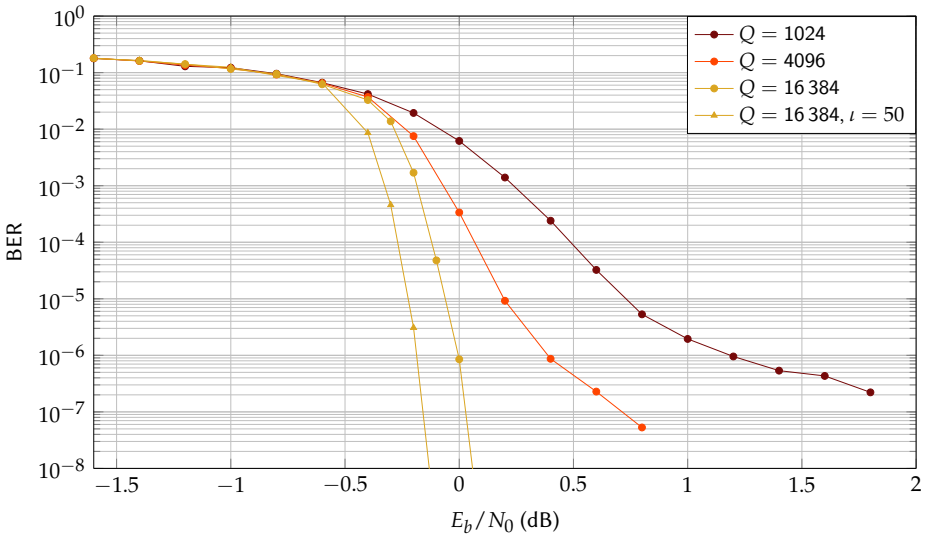

FIGURE 2.16 – *Performance of the Turbo-FSK scheme with parameters $M = 32$, $\lambda = 4$, for various values of interleaver size Q and under the AWGN channel. The spectral efficiency is equal to $\eta = 3.11 \cdot 10^{-2}$ bits·s^{-1}·Hz^{-1}. 10 iterations are performed, and the MAP algorithm is used.*

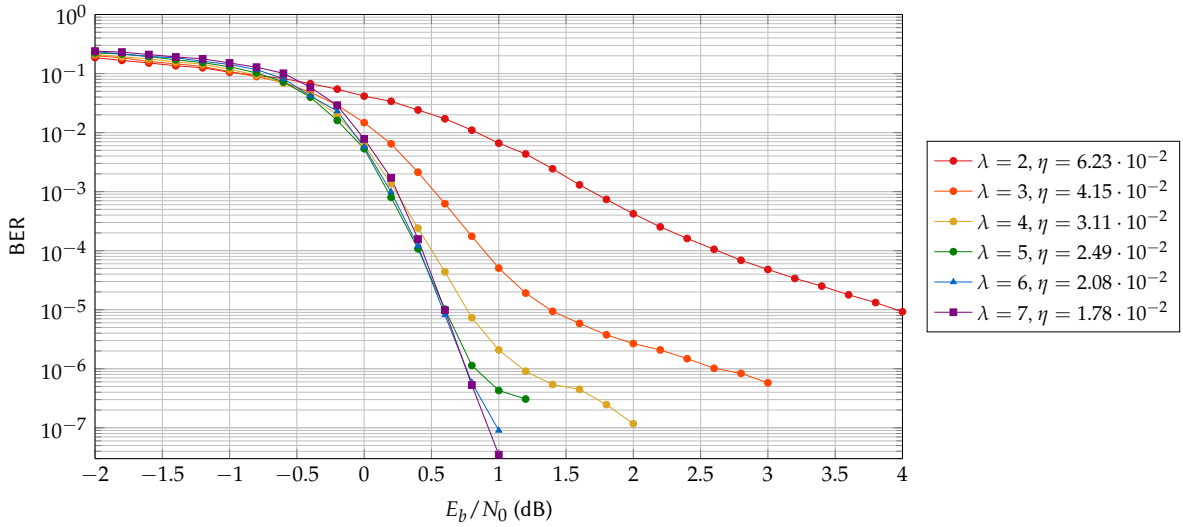

FIGURE 2.17 – *Performance of the Turbo-FSK scheme with parameters $M = 32$, $Q = 1024$, for various values of λ and under the AWGN channel. 10 iterations are performed, and the MAP algorithm is used.*

For an FSK alphabet size of 32 and $\lambda = 4$ stages, the BER performance of the Turbo-FSK scheme for various sizes of interleaver $Q = 1024$, 4096 and 16 384 are computed. The measured BER is depicted in Figure 2.16, along with the performance after 50 iterations for $Q = 16\,384$. The interleaver size clearly impacts on the level of the error floor, a known effect of turbo codes. It also impacts the complexity, as the trellis that needs to be decoded becomes significantly bigger. For this size of alphabet $M = 32$, there are $Q + 1 = 1024/4 + 1 = 257$ sections when $Q = 1024$ versus $Q + 1 = 16384/4 + 1 = 4097$ sections for $Q = 16\,384$. For larger sizes of Q, performance can be improved by computing more iterations, as observed when 50 iterations are performed for $Q = 16\,384$. However, increasing the number of iterations performed may increase the decoding latency, as significantly more operations need to be computed.

The BER performance of the Turbo-FSK scheme for various values of the parameter λ with an alphabet size $M = 32$ and an interleaver size $Q = 1000$ is depicted in Figure 2.17. Increasing the value of λ from 2 to 5 improves the performance; after $\lambda = 5$, the increase has a very low impact on the waterfall, but reduces the error floor level. Increasing λ has also the effect of reducing the spectral efficiency, given by Equation (2.7), as it represents the number of interleaved versions of the information bits that are encoded.

For a fixed number of stages $\lambda = 4$ and interleaver size $Q = 1000$, the BER performance of the Turbo-FSK scheme

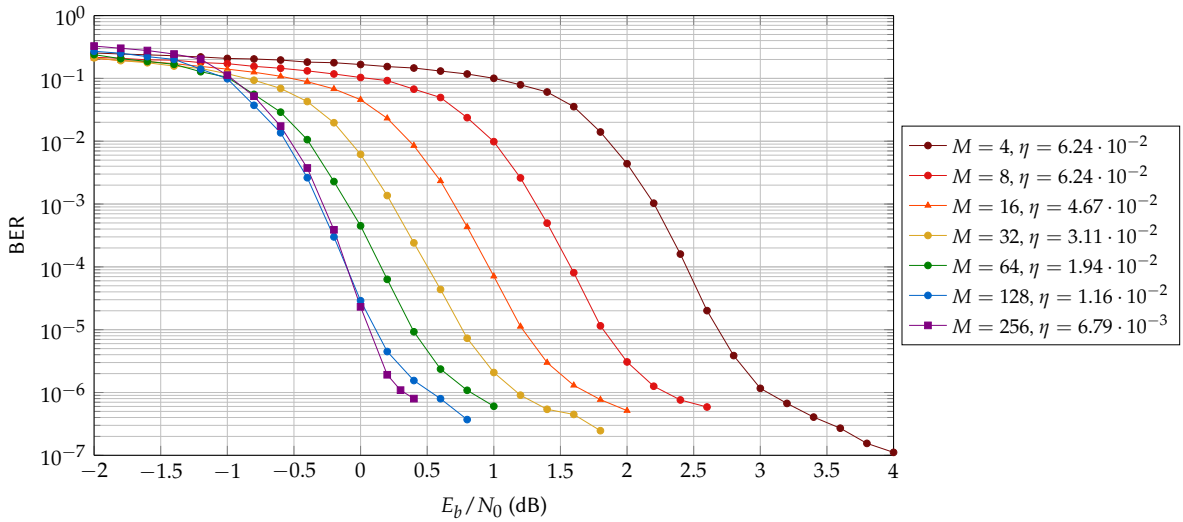

FIGURE 2.18 – *Performance of the Turbo-FSK scheme with parameters $\lambda = 4$, $Q = 1024$, for various size of FSK alphabet M and under the AWGN channel.* 10 *iterations are performed, and the MAP algorithm is used.*

with sizes of FSK alphabet from $M = 4$ to 256 is given in Figure 2.18. Increasing the alphabet size reduces the spectral efficiency, but also has an impact on the waterfall and the error floor regions. Up to the value $M = 128$, the waterfall position is improved with the alphabet size. The improvement is negligible when using the value $M = 256$. The error floor clearly seems to be related to the value of M, and is always decreased when M is increased. Considering this tendency, it can be expected that for a specific λ and interleaver size, a value of M minimizes the E_b/N_0 required to reach a BER of 10^{-5}.

From the observation of the BER performance, it is clear that the parameters strongly impact the behavior of the scheme. The evolution of the performance with λ and M shows that finding the parameter couple that minimizes the E_b/N_0 required for a specific level of error is a non-trivial matter. While orthogonal modulations are known to reach the channel capacity, increasing the size of M over a certain value starts to have little influence on the performance. In order to optimize the parameters regarding the required E_b/N_0, a theoretical tool used in turbo receivers, the EXIT chart, is studied for the case of Turbo-FSK.

2.3 Optimization of the Parameters

The three parameters of Turbo-FSK strongly influence the performance of the scheme, i.e. the E_b/N_0 required for a specific BER. From the analysis done in Chapter 1, the energy efficiency of a system is maximized when the required E_b/N_0 is minimized and the information theory expresses the minimum achievable E_b/N_0, denoted $(E_b/N_0)_{\min}$ (see Equation (1.16)). In order to optimize the system regarding the required E_b/N_0, the asymptotic performance of the scheme (i.e. for large sizes of interleaver q) for the possible values of the parameters M and λ are evaluated. An exhaustive search versus the parameters will then give the minimum reachable E_b/N_0 for the system. The asymptotic performance is estimated with the EXIT chart tool.

The EXIT chart applied to Turbo-FSK is first presented along with the theoretical background, its computation and interpretation. The asymptotic performance is then evaluated and the M and λ couple giving the lowest E_b/N_0 is derived.

2.3.1 EXIT Charts for Turbo-FSK

The EXIT chart is a common tool to analyze iterative processes and predict the behavior of the decoder. An introduction to the theory and its interpretation is presented in Appendix D, for the case of TC. The EXIT chart is specific to a receiver and represents the extrinsic response of the receiver for a given *a priori* input. In his original proposal [33], Stefan ten Brink suggested the use of Mutual Information (MI) to represent the quantity of information. The MI is a measure of the statistical dependency between two random variables. When considering the equally probable random binary variable X and the random variable Y, the MI can be expressed (see Appendix D)

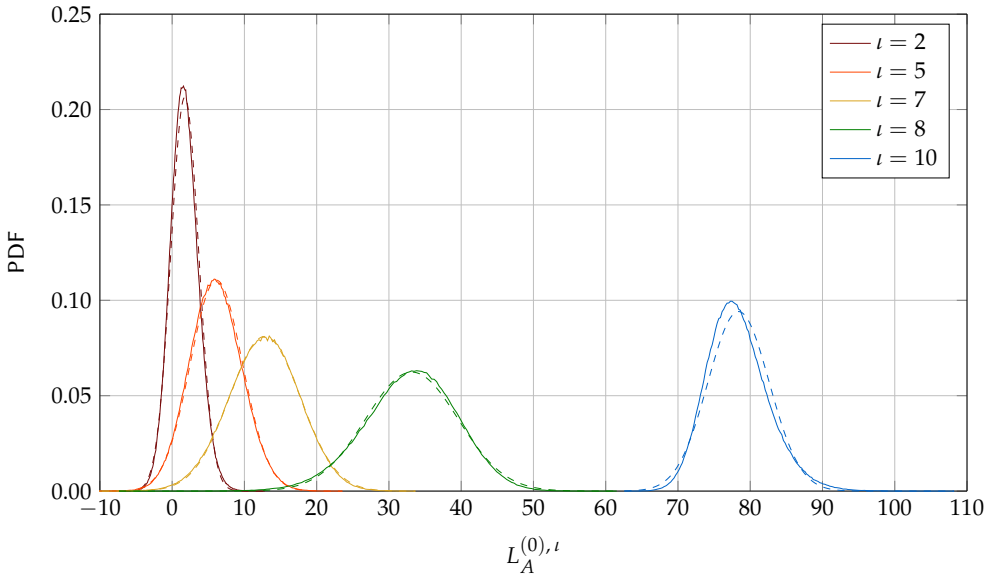

FIGURE 2.19 – *The PDF of the a priori log ratio of the first decoder $L_A^{(0),\iota}$, for various iterations ι. The all-zero information word is sent and $E_b/N_0 = 0$dB. The Gaussian approximations, obtained by measuring the mean and the variance of the distributions, are represented by the dashed curves. The parameters for the Turbo-FSK are $M = 32$, $\lambda = 4$, $Q = 10^6$, and the MAP algorithm is used.*

as

$$I(X, Y) = \frac{1}{2} \sum_{u \in \{-1,+1\}} \int_y p(y \mid x = u) \log_2 \frac{2p(y \mid x = u)}{p(y \mid x = -1) + p(y \mid x = +1)} dy. \tag{2.35}$$

$p(y \mid x = u)$ is the likelihood of observing y when $x = u$ was transmitted. The value of the MI ranges from 0 to 1, with $I(X, Y) = 0$ when X and Y are independent. The value $I(X, Y) = 1$ shows complete correlation between the two variables. For the EXIT analysis, the source X is the information bits and two MI are considered: the *a priori* MI, where Y is the *a priori* log ratios L_A, and the extrinsic MI, where Y is the extrinsic log ratios L_E.

2.3.1.1 *A PRIORI* MODEL

In order to model the *a priori* input of one decoder, a Gaussian model is suggested in [33]. The Gaussian distribution of the log ratios in turbo decoders is studied in [77, 78]. For the Turbo-FSK, this assumption is verified by performing a simulation where the all-zero information word $(00\ldots0)$ is sent. This observation is legitimate considering the symmetry of the distributions, and the fact that the orthogonality of the Turbo-FSK protects all the bits of an information word equally. The Probability Density Function (PDF) of the *a priori* input of the first decoder after some iterations ι is computed ($L_A^{(0),\iota}$ following the definition in Section 2.2.2.3). The case $M = 32$, $\lambda = 4$ is considered. The interleaver size is set to $Q = 10^6$ for a sufficient statistic on the PDF. An AWGN channel is used, with $E_b/N_0 = 0$dB. The obtained PDFs are depicted in Figure 2.19. The Gaussian approximations are represented by the dashed curves and computed with the measured mean and variance of the distribution of the log ratios. They match accurately the distributions, demonstrating that the *a priori* information can be modelled by a normal law.

The *a priori* model is given by $\mathcal{N}(\mu_A, \sigma_A)$, with $\mu_A = \sigma_A^2/2$, as shown in Appendix D. The *a priori* log ratios are expressed

$$L_A(x) = \mu_A \cdot x + n_A. \tag{2.36}$$

The model relies only on the parameter σ_A, and denoting $L_A(x) = y$, the conditional PDF can be expressed

$$p(y \mid x) = \frac{1}{\sqrt{2\pi}\sigma_A} \exp\left\{ -\frac{1}{2\sigma_A^2} \left(z - \frac{\sigma_A^2}{2} x \right)^2 \right\}. \tag{2.37}$$

Using this expression, the computation of the *a priori* MI simplifies to the calculation of the function J for the considered σ_A (see Section D.1.3), with

$$I_A = J(\sigma_A) = 1 - \int_{-\infty}^{+\infty} \frac{1}{\sqrt{2\pi}\sigma_A} \exp\left\{ -\frac{1}{2\sigma_A^2} \left(z - \frac{\sigma_A^2}{2} \right)^2 \right\} \log_2 (1 + e^{-z}) dz. \tag{2.38}$$

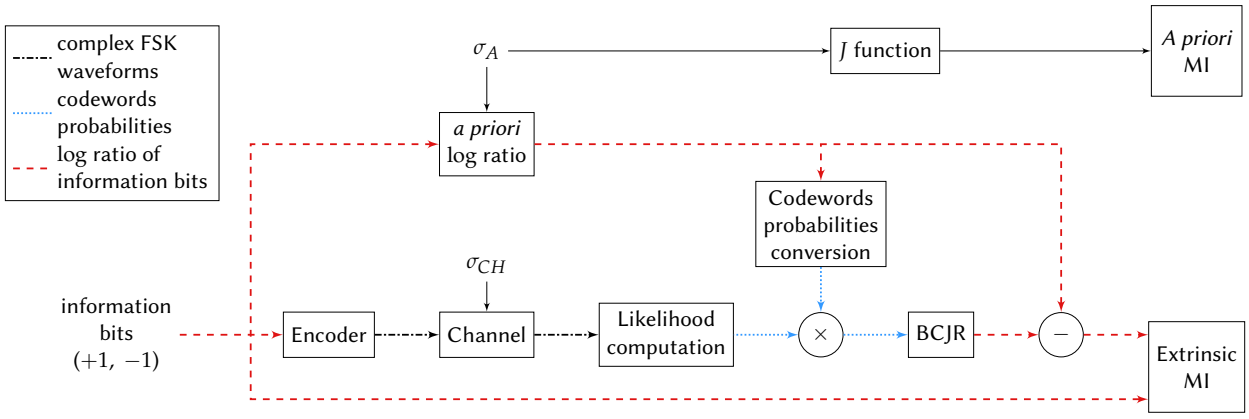

FIGURE 2.20 – *The EXIT Chart computation for the Turbo-FSK*

2.3.1.2 MULTI-DIMENSIONAL EXIT CHART

Multidimensional structures including more than two codes have been suggested prior to this work for the Turbo-Hadamard [79], and EXIT computation for these codes was studied in [80]. When two decoders are used, the exchange of information between the decoders during the successive iterations can be represented in a two dimension plot. If λ decoders are considered, the representation of the exchanges needs to be done in λ dimensions. Graphical interpretation becomes impossible for $\lambda > 3$, except when all decoders are the same (which is the case for the Turbo-FSK). A two-dimensional projection can then be computed. If this projection does not intersect with the diagonal line going from $(0,0)$ to $(1,1)$, convergence toward the maximum of MI is possible. The formula of the *a priori* MI must be changed (see Section D.3 and [80]) to

$$I_A = J\left(\sqrt{\lambda - 1} \cdot \sigma_A\right). \tag{2.39}$$

This formula can be interpreted as the fact that each decoder receives information from the other $\lambda - 1$ decoders.

2.3.1.3 EXIT CHART COMPUTATION

The process to compute the EXIT chart for the Turbo-FSK is depicted in Figure 2.20. From the information bits and the given σ_A, the top part computes the *a priori* log ratios with Equation (2.36). With the σ_A considered and the number of stages λ, the J function is applied with the correction (2.39), to obtain the MI associated to the σ_A. Since J is an function increasing with σ_A, the higher the value of σ_A, the higher the MI (i.e. the more correlated are the log ratio to the information bits).

The bottom part consists in computing the channel observations of the encoded information bits. After encoding, the AWGN noise with variance σ^2_{ch} is added. The likelihoods of the codewords are then computed, and the *a priori* log ratios generated by the top level are used to compute the *a priori* probabilities of the codewords. The product of Equation (2.17) is then computed and fed to the BCJR algorithm, which estimates the log-APP of the information bits. As pointed out previously, the system does not only compute log ratios, but also uses values related to the probabilities of the codewords. In the figure, links between blocks may refer to different physical quantities.

As presented in Section 2.2.2.3, the log-APP computed with the BCJR algorithm can be expressed

$$L = L_A + L_E, \tag{2.40}$$

where L_E is called the extrinsic log ratio, but actually contains both the extrinsic information and the channel likelihood. The later cannot be extracted in the case of the Turbo-FSK as the code is not systematic. When L_A is removed from L, the extrinsic log ratios are obtained and can be used to compute the sum of integration of (2.35) to get the MI.

The EXIT Chart computation does not depend on the interleaving function, which implies statistical independence between the different stages of the decoder. Also, the computations need to be done using very large block sizes q, in order to ensure a sufficient statistic for the PDF estimations.

2.3.1.4 INTERPRETATION

The EXIT can be used to track how the information is exchanged between the decoders (see Appendix D). For a given level of noise (expressed in E_b/N_0), it can also predict the convergence of the decoder, after an arbitrary

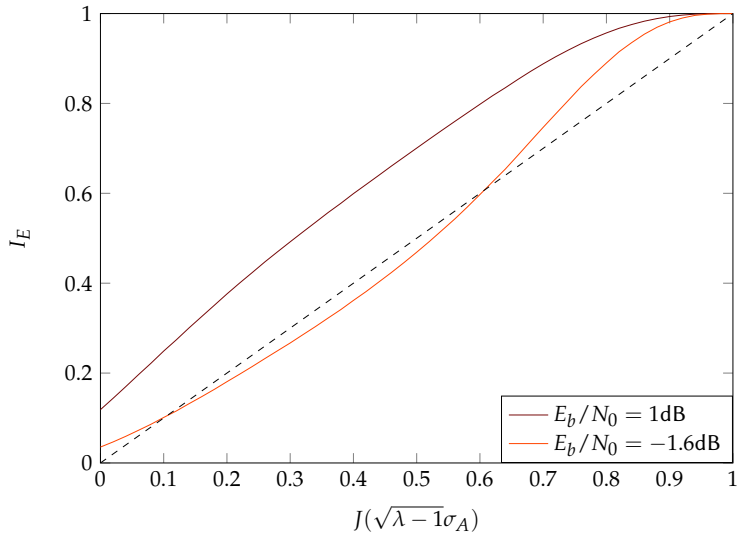

FIGURE 2.21 – *EXIT Charts of the Turbo-FSK decoder with parameters* $M = 128$, $\lambda = 4$, *for various values of* E_b/N_0. *The information block size was set to* $Q = 100\,000$.

number of iterations, toward the error-free information word (i.e. $I_E = 1$, the maximum MI). The EXIT chart computations result for two values of E_b/N_0 are depicted in Figure 2.21, along with the diagonal $(0,0) \rightarrow (1,1)$. The Turbo-FSK scheme with parameters $M = 128$, $\lambda = 4$ is selected, with an information block size of $Q = 100\,000$. The MAP algorithm is used.

For $E_b/N_0 = 1$dB, the EXIT chart goes up to $I_E = 1$ without intersecting the diagonal. The decoder will then, after a certain number of iterations, successfully retrieve the exact information word. However, for $E_b/N_0 = -1.6$dB, the EXIT chart intersects the diagonal around $I_A \simeq 0.1$. Whatever the number of iterations, the decoding process cannot converge towards the error-free information word for this E_b/N_0 value.

2.3.1.5 INFLUENCE OF THE FSK CODEWORDS

The Turbo-Hadamard EXIT chart analysis was done in [67]. In order to evaluate the influence of the non-binary non-sytematic codewords on the decoder's behavior, we compare the EXIT of the Turbo-FSK versus the Turbo-Hadamard and the Turbo-Hadamard Repeat presented in Section 2.2.3.1. For all schemes, the parameters $M = 3$ and $\lambda = 3$ are selected, with an information block size $Q = 100\,000$. The MAP algorithm is used. The EXIT charts are depicted in Figure 2.22. The influence of the systematic bits is observed when comparing the schemes Turbo-

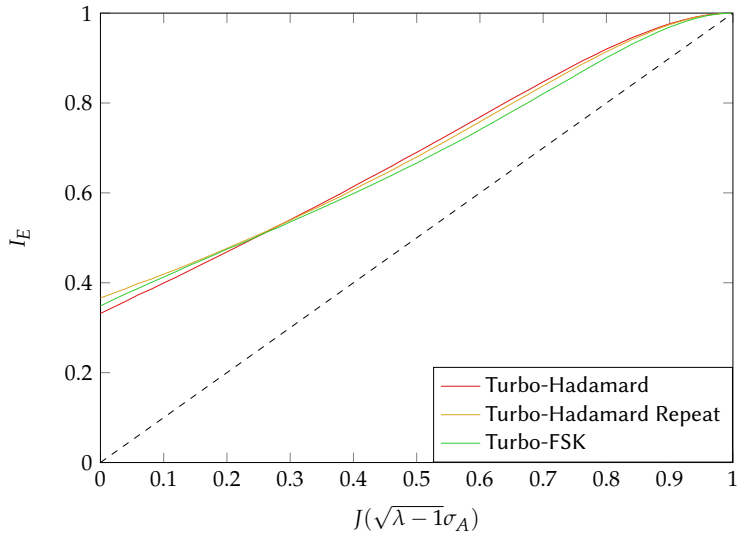

FIGURE 2.22 – *Comparison of the EXIT chart for different schemes with the same parameters* $M = 3$, $\lambda = 3$, *under an AWGN channel with* $E_b/N_0 = 2$*dB. The information block size is set to* $Q = 100\,000$.

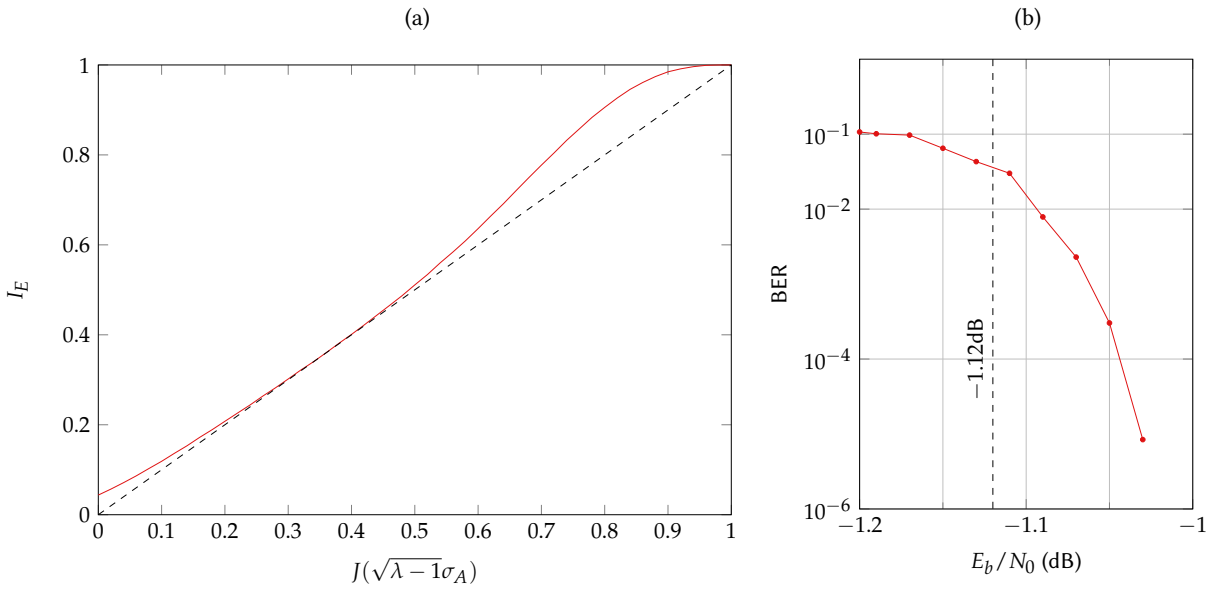

FIGURE 2.23 – *(a) EXIT Chart and (b) BER performance of the Turbo-FSK scheme with parameters* $M = 128$, $\lambda = 4$. *The EXIT Chart is computed for* $E_b/N_0 = -1.12$*dB and the information block size was set to* $Q = 100\,000$. *BER performance is computed using* $Q = 100\,000$, 100 *iterations and the MAP algorithm.*

Hadamard Repeat and Turbo-Hadamard. The influence of the non-binary codewords (and the computations with an extrinsic information that includes the channel information) is observed when comparing the Turbo-Hadamard Repeat and the Turbo-FSK. The EXIT charts are very close, but these non-similarities will induce small differences in the receiver's behavior.

2.3.2 Evaluation of the Asymptotic Performance

The EXIT chart interpretation gives the information on the convergence of the decoder for a specific E_b/N_0. It is then possible to search for the lowest E_b/N_0 for which the decoder converges toward $I_E = 1$ (i.e. no intersection with the diagonal line). This value represents the threshold (also called the turbo cliff position), the point at which the decoder can start to successfully retrieve the correct information word. This can be seen as the asymptotic performance of the code, since it considers a very large sizes of information block and perfect decorrelation between the λ observations.

Using an exhaustive search, the threshold of the Turbo-FSK for the case $M = 128$ and $\lambda = 4$ has been estimated equal to $E_b/N_0 = -1.12$dB. The EXIT chart for this case and with $Q = 100\,000$ is given in Figure 2.23 (a). The curve approaches the diagonal very closely, but there is no intersection. We can conclude that the decoder can, for this value of E_b/N_0, converge after an arbitrary number of iterations. In order to confirm the estimation, the BER performance for the same scheme with 100 decoding iterations is simulated. The results is depicted in Figure 2.23 (b). As predicted, the BER starts to drop significantly after $E_b/N_0 \simeq -1.12$dB, to reach a value of 10^{-5} at $E_b/N_0 = -1.03$dB. Using the EXIT chart, the threshold of the decoder was accurately estimated.

Following the same approach, an exhaustive search of the parameters of the Turbo-FSK is used to find the parameter couple of M and λ that has the lowest threshold. For values spanning from $M = 16$ to $M = 2048$ and $\lambda = 2$ to $\lambda = 6$, the estimated threshold in E_b/N_0 of each case is given in Table 2.1. In the table, the lowest threshold regarding λ for a specific M is denoted with a * symbol, while the lowest threshold is in bold. A graphic representation of the threshold in E_b/N_0 versus the alphabet size M for the different values of λ is also depicted in Figure 2.24. The parameter couple corresponding to the lowest threshold is $M = 512$ and $\lambda = 3$. This parameter couple is optimum regarding the required E_b/N_0. This result was hardly predictable considering the performance of BER only. Despite the difference between the Turbo-FSK and the Turbo-Hadamard, an equivalent result was obtained for the latter in [67].

The spectral efficiency of the configuration $M = 512$ and $\lambda = 3$ is equal to (using Equation (2.7)) $\eta = 5.21 \cdot 10^{-3}$ bits$\cdot$s$^{-1}\cdot$Hz^{-1}. The value of $(E_b/N_0)_{\min}$ for this η is given by Equation (1.16) and is equal to -1.584dB. The Turbo-FSK scheme with this configuration is only located at 0.284dB from the minimum achievable E_b/N_0.

Using the EXIT chart, the optimum parameter couple regarding the required E_b/N_0 was found. These results also show the ability of the Turbo-FSK to perform at ultra low levels of E_b/N_0, and thus ultra high energy efficien-

λ	M							
	16	32	64	128	256	512	1024	2048
2	2.23	1.61	1.15	0.86	0.53	0.30	−0.13	−0.61
3	0.33	−0.17	−0.59	−0.94	−1.23*	**−1.30***	−1.19*	−1.07*
4	0.02	−0.46	−0.84	−1.12*	−1.20	−1.04	−0.83	−0.59
5	−0.06*	−0.51*	−0.86*	−1.09	−1.03	−0.77	−0.47	−0.18
6	−0.06*	−0.51*	−0.84	−1.02	−0.84	−0.52	−0.14	0.19

TABLE 2.1 – *Threshold values in E_b/N_0 for every tested M and λ.*

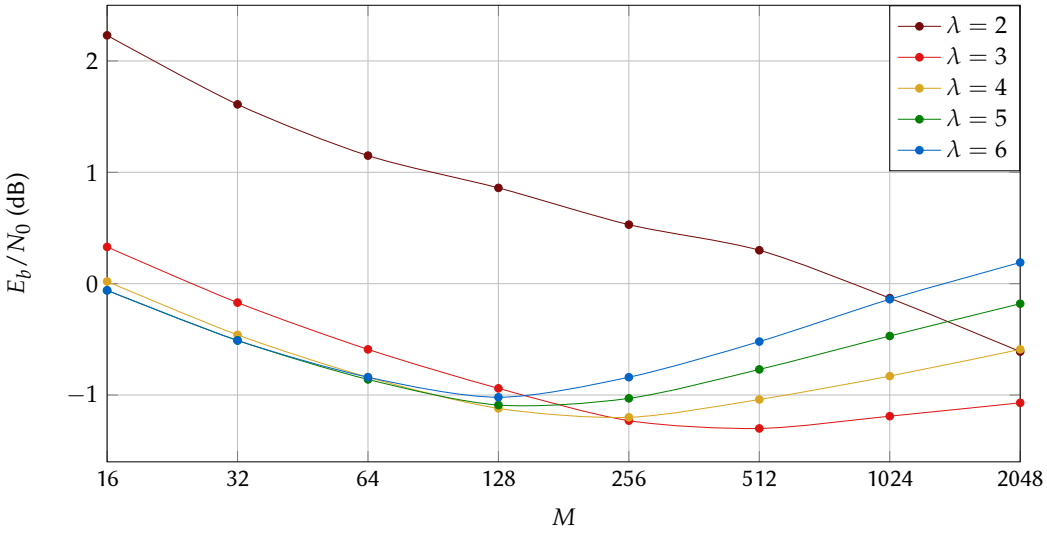

FIGURE 2.24 – *Threshold values in E_b/N_0 versus the alphabet size M, for the various tested λ.*

cies. However, this performance should be confronted against more reasonable interleaver sizes, and the spectral efficiency of each configuration should be considered.

2.4 Analysis

In this section, several aspects related to the performance of the Turbo-FSK are discussed. The previous section demonstrated the very promising asymptotic performance of the Turbo-FSK scheme. When considering the LPWA context introduced in the first chapter, small block sizes are usually expected. The analysis will thus concern three aspects: the optimization of the parameters when short block sizes are considered, the confrontation of the E_b/N_0 performance against the spectral efficiency, and finally the comparison of the Turbo-FSK versus previously introduced LPWA solutions.

2.4.1 Performance for Short Block Sizes

The EXIT tool is useful to estimate the asymptotic performance of an iterative decoder. However, it assumes perfect independence between the different interleaved information messages of the decoder. A large size of information block must be considered to guarantee this property. For this reason, the EXIT chart does not permit the prediction of the performance of a system with short block sizes. Other tools may be considered [36, 81, 82], but standard and extensive BER simulations can also give satisfactory results.

Following this approach, the required E_b/N_0 to reach a BER of 10^{-4} is estimated using a dichotomy algorithm, for various values of M and λ and with an interleaver size of $Q = 1000$. Random interleavers and the MAP algorithm were used. The results are summarized in Table 2.2. Here again, the lowest threshold regarding λ for a specific M is denoted with a $*$ symbol, while the lowest threshold is in bold. The optimum set of parameters regarding the required E_b/N_0 for this size of interleaver is $M = 1024$ and $\lambda = 3$. With this configuration, the spectral efficiency is equal to $\eta = 2.92 \cdot 10^{-3}$ bits·s^{-1}·Hz^{-1}. For this spectral efficiency the value of $(E_b/N_0)_{\min}$ is −1.587dB. The best set of parameters gives a performance that is 1.35dB away from the minimum achievable E_b/N_0.

λ	M							
	16	32	64	128	256	512	1024	2048
2	3.00	2.62	2.09	1.64	1.25	0.91	0.57	0.31
3	1.40	0.89	0.48	0.14	−0.13	−0.22*	**−0.24***	0.00*
4	0.95	0.49	0.13	−0.10*	−0.17*	0.02	0.35	0.52
5	0.84	0.40	0.08*	−0.04	0.08	0.35	0.78	1.07
6	0.74*	0.37*	0.13	0.04	0.35	0.73	1.10	1.46

TABLE 2.2 – *E_b/N_0 values to reach a BER of 10^{-4} for every M and λ tested, with $Q = 1000$ bits.*

The best set is different from the one obtained with the EXIT chart optimization of Section 2.3.2. However, the latter is only 0.02dB away from the best set found. Compared to the asymptotic performance, the loss incured by the use of this size of interleaver is 1dB on average (included between 0.8 and 1.25dB).

2.4.2 Performance versus Channel Capacity

Asymptotic and finite-length performance of the Turbo-FSK are achieved with a different spectral efficiency for every configuration, which can be computed with Equation (2.7). In order to confront the performance with the limit from the information theory, the spectral efficiency of each configuration is represented versus the asymptotic and finite-length required E_b/N_0 in Figure 2.25, along with the maximum achievable spectral efficiency given by Equation (1.15) and the performance of the M-ary orthogonal modulations. For the Turbo-FSK, the E_b/N_0 value are taken from Tables 2.1 and 2.2. To make the figure easily readable, only the values of λ from 3 to 6 are considered, as the performance when $\lambda = 2$ is less interesting. As λ is increased, the spectral efficiency is lowered; for each value of M, the point with the higher spectral efficiency corresponds to $\lambda = 3$, the second to $\lambda = 4$ and so on.

Results highlight the general trend of the performance of the Turbo-FSK and its proximity to the minimum achievable $(E_b/N_0)_{\min}$, for all the configurations. As previously mentioned, the Turbo-FSK with parameters $M = 512$ and $\lambda = 3$ is at 0.284dB of the $(E_b/N_0)_{\min}$ for the asymptotic performance and 1.35dB when the interleaver size is set to $Q = 1000$. The performance of the uncoded 512-orthogonal modulation with a repetition factor of 3 is also represented in the figure. The gain of the Turbo-FSK versus the orthogonal modulation with repetition code is considerable, up to 6.2dB, and their spectral efficiencies only differ by a ratio of 8/9.

It should be remembered that the original strategy of the Turbo-FSK is to use the repetition to lower the spectral efficiency and to employ a sophisticated receiver to approach the $(E_b/N_0)_{\min}$. These results clearly demonstrate that the Turbo-FSK fulfils its original purpose and exhibits promising performance for the LPWA context.

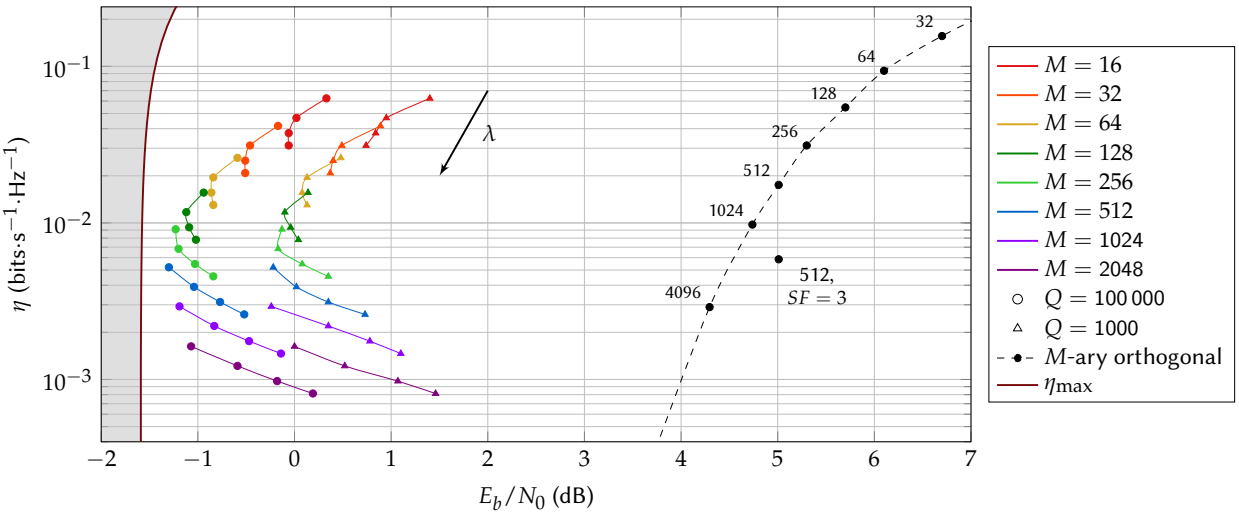

FIGURE 2.25 – *Performance of the Turbo-FSK versus the maximum achievable spectral efficiency, for various values of parameters M and λ (from 3 to 6). The E_b/N_0 values are taken from Table 2.1 and Table 2.2, and the spectral efficiency is computed with (2.7). The maximum achievable spectral efficiency according to the channel capacity is computed using (1.15).*

2.4.3 Comparison to Existing LPWA Solutions

As the optimum set of parameters has been found for the Turbo-FSK scheme, its performance should be compared to the existing LPWA solutions presented in Chapter 1. In order to do so, we select 3 different schemes, in addition to the Turbo-FSK. For all the schemes, the parameters λ is defined and used to modulate the spectral efficiency of the scheme. This way, by selecting the appropriated λ, a fair comparison between the different schemes can be made. All the comparisons are done under the AWGN channel.

The first selected scheme is the Institute of Electrical and Electronics Engineers (IEEE) 802.15.4k standard presented in Section 1.4.2.1. This scheme combines a convolutional code of rate $1/2$ with generators [171 133] and a constraint length of 7. A Differential Binary Phase Shift Keying (DBPSK) modulation is used, and a SF of value λ is applied. The spectral efficiency is thus

$$\eta = \frac{1}{2\lambda}. \tag{2.41}$$

Probabilistic DBPSK demodulation and probabilistic Viterbi decoding are used on the receiver side. A random interleaver is used between the FEC and modulation schemes.

The second scheme is based on the LoRa technology, which was presented in Section 1.4.1.2 and combines an orthogonal modulation and a Hamming code. The parameter λ sets the size of the orthogonal alphabet, equal to 2^λ. The number of parity bits of the Hamming code is a, and the binary code rate is equal to $4/(4+a)$. The spectral efficiency is given by

$$\eta = \frac{\lambda}{2^\lambda} \cdot \frac{4}{4+a}. \tag{2.42}$$

The receiver performs the probabilistic coherent demodulation of the orthogonal alphabet, and the probabilistic decoding of the Hamming code.

The third selected scheme is the Uplink (UL) Narrow-Band IoT (NB-IoT) as described is Section 1.4.2.2. This scheme employs a highly efficient FEC, the rate $1/3$ [13 15] TC. It also uses BPSK modulation with OFDM signaling, but the specific signaling can be omitted when considering the AWGN channel. A SF of value λ is applied to reduce the spectral efficiency, which can be expressed

$$\eta = \frac{1}{3\lambda}. \tag{2.43}$$

The receiver performs the turbo decoding using the MAP algorithm, and 10 iterations are performed.

The Turbo-FSK with the optimum set of parameters $M = 512$ and $\lambda = 3$ is selected for the comparison. The spectral efficiency for this case is equal to $5.17 \cdot 10^{-3}$ bits·s^{-1}·Hz^{-1}. The value of the parameter λ defined for every technique is adjusted for all the schemes to have the same spectral efficiency. The parameters of all the compared solutions are summarized in Table 2.3. All interleavers are random, except for the internal interleaver of the TC [13 15], where the interleaver defined by the third generation (3G) standard [58] was used.

The Packet Error Rate (PER) performance with an information block size $Q = 1024$ (or 128 bytes) is depicted in Figure 2.26. The PER is the ratio of the decoded packets with at least one bit-error over the total number of transmitted packets. The x axis is expressed in Signal-to-Noise Ratio (SNR), which can be obtained from the E_b/N_0 and the spectral efficiency using the relation of Equation (1.5). As the spectral efficiencies are almost all equals, the difference between the performance of each scheme would be approximately the same in E_b/N_0. Regarding the required SNR, the IEEE 802.15.4k standard is the least efficient as a SNR of -17.5dB is required to reach a PER of 10^{-2}. The LoRa based technique offers an improvement of 1dB for the same PER. As expected, the schemes including a turbo receiver show significant gains. The NB-IoT UL technique requires 3.5dB less of SNR for the same PER. The best is the Turbo-FSK with parameters $M = 512$ and $\lambda = 3$, which requires a SNR of -23.1dB (1dB less than the NB-IoT) for that same PER.

PHY-layer	**802.15.4k**	**LoRa based**	**NB-IoT UL**	**Turbo-FSK**
Modulation	DBPSK	1024-Orthog	BPSK	512-FSK
FEC	CC [171 133]	Hamming	TC [13 15]	Turbo-FSK
Binary code-rate	1/2	4/8	1/3	-
λ	97	10	64	3
η $(\cdot 10^{-3})$	5.16	4.88	5.19	5.17

Table 2.3 – *Parameters of the* 4 *different techniques compared.*

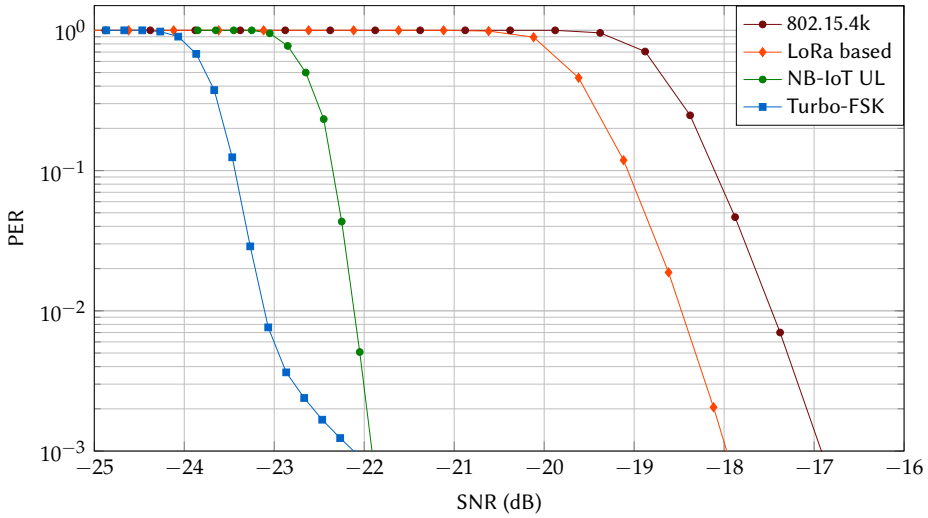

FIGURE 2.26 – *PER performance of the compared solutions presented in Table 2.3, under the AWGN channel.*

All the considered solutions have a low required SNR. Following the definition of the sensitivity Equation (1.8), a low level of sensitivity (or alternatively, a long range) is achieved with a low level of required SNR. The same spectral efficiency was considered for all the different techniques, so the gain in SNR can be interpreted directly as the gain in sensitivity. For example, the Turbo-FSK scheme with the considered parameters has a sensitivity level 4.6dB lower than the sensitivity level of the LoRa scheme. For a same spectral efficiency, the Turbo-FSK has a longer range. Using the Friis equation given in Equation (1.1) and by only allowing the received power and the distance d to vary, the distance gain between two techniques is given by (under free path loss)

$$\frac{d_2}{d_1} = \sqrt{\frac{P^1_{\text{req}}}{P^2_{\text{req}}}}. \tag{2.44}$$

P^1_{req} (resp. P^2_{req}) is the sensitivity of the first technique (resp. the second) expressed in linear and D_1 (resp. D_2) is the distance between the transmitter and the receiver required to attain the sensitivity under free path loss of the first technique (resp. the second technique). The 4.6dB gain between the Turbo-FSK and the LoRa technique can thus be interpreted as a gain of 1.7 in the range of the communication. Alternatively, for the same range, the transmit power in the Turbo-FSK case can be reduced by 4.6dB, i.e. by a factor of 2.9. More than demonstrating once again the high efficiency of the Turbo-FSK scheme for the LPWA context, these results also emphasize the capacity of turbo processed systems to achieve very high performance at low levels of SNR.

The spectral efficiency of the schemes versus the required E_b/N_0 for a BER of 10^{-5} is depicted in Figure 2.27, along with the performance of the M-ary orthogonal modulations and the maximum achievable spectral efficiency given by Equation (1.15). As the spectral efficiency is almost the same for every scheme, the performance of the 4 different schemes are on the same horizontal line. The gain in BER approximately follows the gain observed in PER. Again, the Turbo-FSK offers a gain of 1dB on the required E_b/N_0 versus the NB-IoT scheme. The required E_b/N_0 for the LoRa scheme and the IEEE 802.15.4k is respectively 4.9 and 5.8dB higher than for the Turbo-FSK. As observed in the previous section, the Turbo-FSK with these parameters is close to the minimum achievable E_b/N_0; only at 1.61dB for this value of η, while the NB-IoT solution is at 2.6dB. The performance of the NB-IoT scheme when $\lambda = 1$ (i.e. no SF is applied) is also depicted in Figure 2.27. For this specific case, the spectral efficiency is much higher (close to 1/3), and the required E_b/N_0 is the same (since the value of the SF does not impact the required E_b/N_0). The gap to the minimum achievable E_b/N_0 is now only 2.08dB. The flexibility of the NB-IoT system allows a large variety of spectral efficiencies which could be necessary depending on the selected application. Naturally, having a higher spectral efficiency impacts the sensitivity level required (see Equation (1.12)). Compared to the case where $\lambda = 64$, the NB-IoT with $\lambda = 1$ has a spectral efficiency multiplied by $\lambda = 64$. For the same bandwidth, the rate is also multiplied by $\lambda = 64$, and the sensitivity level is amplified by a factor of $10 \cdot \log_{10}(64) \simeq 18$dB. If however the data rate is kept constant, the sensitivity level stays the same but the bandwidth needs to be divided by a factor of $\lambda = 64$, which may lead to a narrow band system.

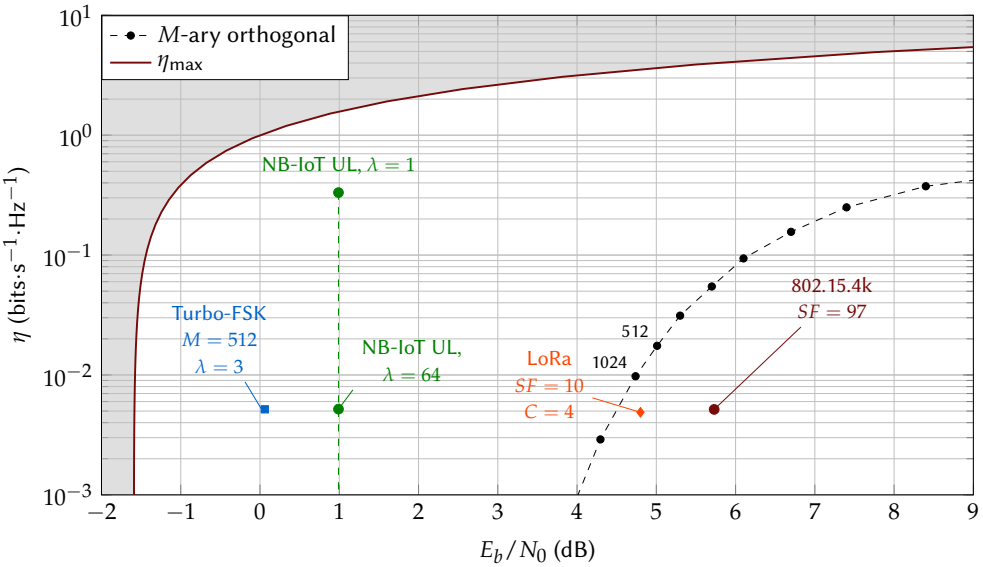

FIGURE 2.27 – *Comparison of the spectral efficiency and the required E_b/N_0 at BER $= 10^{-5}$ of the compared solutions, under the AWGN channel. The maximum achievable spectral efficiency according to the channel capacity from* (1.15) *is also represented.*

2.5 CONCLUSION

One of the main strategies for LPWA systems is to exchange data at low spectral efficiencies. Following this approach, a system was proposed based on the mix of orthogonal modulation, repetition and a turbo receiver: Turbo-FSK. The performance depending on the parameters seems rather unpredictable considering BER performance only. The use of the EXIT chart tool designed for iterative processes enables the optimization of the parameters. The threshold of the decoder for a large set of parameters was estimated, and the configuration having the closest threshold from the minimum achievable E_b/N_0 was found to be $M = 512$ and $\lambda = 3$. This configuration approaches the ultimate E_b/N_0 by 0.284dB, or 1.35dB (for a BER of 10^{-4}) when the interleaver size is set to $Q = 1000$, a more adequate size for the LPWA context. Compared to the existing LPWA solutions, the Turbo-FSK with its optimized parameters offers very low levels of sensitivity, and interesting gains in term of range or transmit power reduction.

The maximum value of the spectral efficiency of the Turbo-FSK scheme is $1/8$ (considering the smallest parameters $M = 4$ and $\lambda = 2$). Even if a small spectral efficiency is appropriate in the LPWA context, existing solutions such as the NB-IoT approach generally offer wider ranges of spectral efficiencies. A larger amount of applications can be covered, including those requiring higher data rates. The flexibility of the system is also increased, which may be interesting when the range of the communication is reduced.

The results presented in this chapter led to an article in the journal entitled *Elsevier Comptes Rendus Physique* [83], and were presented in several international conferences: the proposed Turbo-FSK scheme was presented at the SPAWC'15 conference [84], the comparison with the existing LPWA solutions was introduced at CROWNCOM'16 [85] and the parameters optimization using the EXIT chart tool was presented at ISTC'16 [86].

CHAPTER SUMMARY

In this chapter, the origins and motivations that lead to our design of the Turbo-FSK scheme have first been introduced. The scheme differs from the Turbo-Hadamard channel code, as it combines modulation and coding in the same process. The scheme was then extensively detailed, from the transmitter design to the derivation of the BCJR algorithm used in the turbo receiver. Performances for various parameters were simulated and compared to the initial Turbo-Hadamard scheme or alternative receivers. We optimized the parameters using the EXIT chart tool, which we first derived for the specific multi-dimensional case. Finally, we evaluated the performance for short block sizes and confronted the Turbo-FSK scheme with existing LPWA solutions.

Bibliography of Chapter 2

[8] C. Berrou, A Glavieux, and P. Thitimajshima. "Near Shannon Limit Error-Correcting Coding and Decoding: Turbo-Codes". In: *IEEE International Conference on Communications (ICC). Geneva.* Vol. 2. 1993, pp. 1064–1070.

[31] L. Bahl, J. Cocke, F. Jelinek, and J. Raviv. "Optimal Decoding of Linear Codes for Minimizing Symbol Error Rate (Corresp.)" In: *IEEE Transactions on Information Theory* 20.2 (1974), pp. 284–287.

[33] S. ten Brink. "Convergence Behavior of Iteratively Decoded Parallel Concatenated Codes". In: *IEEE Transactions on Communications* 49.10 (2001), pp. 1727–1737.

[36] M. El-Hajjar and L. Hanzo. "EXIT Charts for System Design and Analysis". In: *IEEE Communications Surveys Tutorials* 16.1 (2014), pp. 127–153.

[40] J. Vogt and A. Finger. "Improving the max-log-MAP Turbo Decoder". In: *Electronics Letters* 36.23 (2000), pp. 1937–1939.

[58] *LTE Evolved Universal Terrestrial Radio Access (E-UTRA): Multiplexing and Channel Coding*. 3GPP TS 36.212, V12.6.0, Release 12. 2015.

[62] *SX1272 from Semtech, datasheet*. http://www.semtech.com/wireless-rf/rf-transceivers/sx1272/. Accessed: July 26, 2017.

[63] K. Kikuchi and M. Osaki. "Highly-Sensitive Coherent Optical Detection of M-ary Frequency-Shift Keying Signal". In: *Optics Express* 19.26 (2011), B32–B39.

[64] L. Ping and S. Chan. "Iterative Decoding of Concatenated Hadamard Codes". In: *IEEE International Conference on Communications (ICC).* Vol. 1. 1998, 136–140 vol.1.

[65] L. Ping, W. Leung, and K. Y. Wu. "Low-Rate Turbo-Hadamard Codes". In: *IEEE Transactions on Information Theory* 49.12 (2003), pp. 3213–3224.

[66] S. Benedetto and G. Montorsi. "Unveiling Turbo Codes: Some Results on Parallel Concatenated Coding Schemes". In: *IEEE Transactions on Information Theory* 42.2 (1996), pp. 409–428.

[67] Y.-J. Wu and L. Ping. "On the Limiting Performance of Turbo-Hadamard Codes". In: *IEEE Communications Letters* 8.7 (2004), pp. 449–451.

[68] N. Shimanuki, B. M. Kurkoski, K. Yamaguchi, and K. Kobayashi. "Improvements and Extensions of Low-Rate Turbo-Hadamard Codes". In: 2006.

[69] L. Ping, L. Liu, K. Y. Wu, and W. K. Leung. "Approaching the Capacity of Multiple Access Channels Using Interleaved Low-Rate Codes". In: *IEEE Communications Letters* 8.1 (2004), pp. 4–6.

[70] X. Wu, Z. Yang, J. Yan, and J. Cui. "Low-Rate Turbo-Hadamard Coding Approach for Narrow-Band Interference Suppression". In: *2014 IEEE International Conference on Communications (ICC).* 2014, pp. 2130–2134.

[71] J. W. Cooley, P. A. W. Lewis, and P. D. Welch. "The Fast Fourier Transform and its Applications". In: *IEEE Transactions on Education* 12.1 (1969), pp. 27–34.

[72] G. Caire, G. Taricco, and E. Biglieri. "Bit-Interleaved Coded Modulation". In: *IEEE Transactions on Information Theory* 44.3 (1998), pp. 927–946.

[73] X. Li and J. A. Ritcey. "Bit-Interleaved Coded Modulation with Iterative Decoding". In: *IEEE Communications Letters* 1.6 (1997), pp. 169–171.

[74] S. Cheng and M. C. Valenti. "Bit-Interleaved Turbo-Coded Noncoherent Orthogonal Modulation with Iterative Demodulation and Decoding: Capacity Limits and Convergence Analysis". In: *Conference Record of the Thirty-Eighth Asilomar Conference on Signals, Systems and Computers, 2004.* Vol. 2. 2004, 2020–2024 Vol.2.

[75] M. C. Valenti, E. Hueffmeier, B. Bogusch, and J. Fryer. "Towards the Capacity of Noncoherent Orthogonal Modulation: BICM-ID for Turbo Coded NFSK". In: *IEEE MILCOM 2004. Military Communications Conference, 2004.* Vol. 3. 2004, 1549–1555 Vol. 3.

[76] J. Panaro. "Simple Iterative Decoding for Bit-Interleaved Coded Orthogonal Modulation". In: *Joint IST Workshop on Mobile Future. SympoTIC '06.* 2006, pp. 16–19.

[77] M. Fu. "Stochastic Analysis of Turbo Decoding". In: *IEEE Transactions on Information Theory* 51.1 (2005), pp. 81–100.

[78] H. E. Gamal and A. R. Hammons. "Analyzing the Turbo Decoder Using the Gaussian Approximation". In: *IEEE Transactions on Information Theory* 47.2 (2001), pp. 671–686.

[79] C. Berrou, M. Jezequel, and C. Douillard. "Multidimensional Turbo Codes". In: *1999 Information Theory and Networking Workshop (Cat. No.99EX371)*. 1999, pp. 27–.

[80] S. ten Brink. "Convergence of Multidimensional Iterative Decoding Schemes". In: *Conference Record of the Thirty-Fifth Asilomar Conference on Signals, Systems and Computers*. Vol. 1. 2001, 270–274 vol.1.

[81] J. W. Lee and R. E. Blahut. "Convergence Analysis and BER Performance of Finite-Length Turbo Codes". In: *IEEE Transactions on Communications* 55.5 (2007), pp. 1033–1043.

[82] Y. Polyanskiy, H. V. Poor, and S. Verdu. "Channel Coding Rate in the Finite Blocklength Regime". In: *IEEE Transactions on Information Theory* 56.5 (2010), pp. 2307–2359.

[83] Y. Roth, J.-B. Doré, L. Ros, and V. Berg. "Turbo-FSK, a Physical Layer for Low-Power Wide-Area Networks: Analysis and Optimization". In: *Elsevier Comptes Rendus Physique* 18.2 (2017). Energy and radiosciences, pp. 178 –188. URL: //www.sciencedirect.com/science/article/pii/S163107051630158X.

[84] Y. Roth, J.-B. Doré, L. Ros, and V. Berg. "Turbo-FSK: A New Uplink Scheme for Low Power Wide Area Networks". In: *2015 IEEE 16th International Workshop on Signal Processing Advances in Wireless Communications (SPAWC)*. Stockholm, Sweden, 2015, pp. 81–85.

[85] Y. Roth, J.-B. Doré, L. Ros, and V. Berg. "A Comparison of Physical Layers for Low Power Wide Area Networks". In: *11th EAI International Conference on Cognitive Radio Oriented Wireless Networks (Crowncom)*. Grenoble, France, 2016.

[86] Y. Roth, J.-B. Doré, L. Ros, and V. Berg. "EXIT Chart Optimization of Turbo-FSK: Application to Low Power Wide Area Networks". In: *9th International Symposium on Turbo Codes & Iterative Information Processing 2016 (ISTC'16)*. Brest, France, Sept. 2016.

CHAPTER 3

Towards Spectral Efficiency Flexibility

Chapter contents

Orthogonal modulations combined with a sophisticated receiver were proven highly energy efficient in the previous chapter, with performance close to the minimum achievable E_b/N_0. In this chapter, the solution is extended to higher spectral efficiencies using an alphabet that combines orthogonal and linear modulations. A puncturing procedure is also introduced. Performance and influence of the various parameters are evaluated, along with the gain in spectral efficiency.

3.1 Motivations

In the previous chapter, a design with low spectral efficiency and high energy efficiency was presented. The technology matches the requirements for Low Power Wide Area (LPWA) networks, with a maximum spectral efficiency of 1/8. Having a low spectral efficiency is a common approach, as it can give a low data rate $R = \eta B$ depending on the bandwidth B, thus leading to a low level of sensitivity P_{req} with (1.12). However, the Narrow-Band IoT (NB-IoT) solution, which reaches promising performance in terms of E_b/N_0 (see Section 1.4.3), also includes configurations with relatively high spectral efficiency (up to 1 bits$\cdot$s$^{-1}\cdot$Hz^{-1}). With these configurations, constraints on the bandwidth may be relaxed (as it can be reduced while keeping the same data rate and level of sensitivity), or a higher data rate can be achieved at the expense of a higher level of sensitivity (if the bandwidth is kept constant). In other words, a flexible scheme holds a particular interest for Internet-of-Things (IoT) applications.

A system may require flexibility as the need for ultra low levels of sensitivity may not be consistent for the entire network. For example, when considering two nodes at two different distances from the base station, one very close and one very far, both need different levels of sensitivity in order to communicate. The farthest node may need a received power equal to the sensitivity, but as the other node is closer, the sensitivity level offered by the technique used may lead to an excess power link budget. For this node, the power at the transmitter side can be adjusted to have a received power equal to the sensitivity, or if the technique is flexible, the configuration can be changed to a higher level of sensitivity, which may come with a higher data rate, and thus a shorter time over-the-air for the data packet. From a more simple perspective, flexibility of the configurations can also lead to the cohabitation of various applications (with various requirements in terms of data rate for example) in the same network.

In conventional techniques, one of the most-used techniques to increase the spectral efficiency is to increase the order of the linear modulation used. For example, if Quadrature Amplitude Modulation (QAM) modulation is used, then using a 16-QAM instead of a 4-QAM doubles the spectral efficiency of the modulation. However, changing the modulation implies a change in the required E_b/N_0 (see Section 1.3.3.3), as it increases with the size of the alphabet when considering a linear modulation. Also, 16-QAM modulation does not have a constant envelope. Information is carried by the amplitude of the waveform. This may lead to higher levels of Peak to Average Power Ratio (PAPR), a situation not convenient for the transmitter of low consumption devices. As conventional techniques usually consist in a modulation associated with a Forward Error Correction (FEC), changing the spectral efficiency can be done by changing the code rate of the FEC. This is commonly performed by puncturing (i.e. not transmitting) some of the bits generated by the encoder. At the receiver side, the Log Likelihood Ratio (LLR) of these bits is set to 0 (i.e. the two possible values of the bits are considered equally probable). By doing this, the performance of the code is reduced, and the rate of the code is increased. To some extent, the performance loss is acceptable considering the gain in spectral efficiency of the technique. A typical example is the Turbo Code (TC) used in Long Term Evolution (LTE) [58] which can be punctured to offer a rate of 1/2 instead of the regular 1/3 rate, thus increasing the spectral efficiency by a factor 1.5 (which is also referred to as the puncturing rate).

The Turbo-FSK scheme only considers Frequency Shift Keying (FSK) orthogonal waveforms, and the parameters are M, the size of the orthogonal alphabet and λ the number of stages. In the next section, a new type of modulation is introduced, that combines linear and orthogonal modulations in order to reach higher spectral efficiencies.

3.2 Orthogonal with Coplanar Subsets Modulation

In order to describe the modulation, the alphabet of modulation is introduced and its construction detailed. After some examples, performance is presented. This section should be regarded as an introduction to a new modulation scheme and not as an extensive study of it.

3.2.1 Definition of the Alphabet

The definitions of the orthogonal and linear alphabet are given in Section 1.3.2. With the purpose to increase the spectral efficiency of the modulation, a specific kind of alphabet $\boldsymbol{\mathcal{A}}$ is presented. In order to build the alphabet, a total of $N_\perp$ orthogonal dimensions are considered. Each dimension can be considered as a complex plane. It is then

possible to select N_L points in each complex plane, i.e. coplanar points. The alphabet is built using $N_\perp$ orthogonal subsets, denoted $\mathcal{A}_\delta$ with $\delta \in \{0, \ldots, N_\perp - 1\}$. Each subset consists in N_L coplanar vectors, each constructed from the N_L coplanar point of the complex plane. The total size of the alphabet is $M = N_\perp \times N_L$. Considering two symbols $\boldsymbol{s}^i$ and $\boldsymbol{s}^{i'}$ from the alphabet (with $\{i, i'\} \in \{0, \ldots, M-1\}^2$), they must respect

$$\langle \boldsymbol{s}^i, \boldsymbol{s}^{i'} \rangle = \begin{cases} A_{i-i'} & \text{if } \exists\, \delta \in \{0, \ldots, M-1\}, \text{ such that } \boldsymbol{s}^i, \boldsymbol{s}^{i'} \in \mathcal{A}_\delta \\ 0 & \text{otherwise} \end{cases}, \tag{3.1}$$

where $A_{i-i'}$ is a complex number proportional to the coplanarity relation between two symbols from the same subset. This constraint means that some symbols of the alphabet may not be orthogonal between each other, but two symbols taken from two distinct subsets are orthogonal between each other. Two symbols of the same subset are coplanar vectors. Each subset is thus equivalent to a linear modulation with N_L elements. The $N_\perp$ orthogonal subsets offer a certain degree of orthogonality in the alphabet. The process can be seen as a combination of both orthogonal and linear modulation, and is denominated Orthogonal with Coplanar Subsets (OCS) modulation.

Considering the baseband model, the $N_\perp$ orthogonal dimensions require the symbols to be represented with $N_\perp$ chips, while the linear dimension corresponds to a multiplicative term equal to one of the N_L different values from the complex plane. The symbols from the alphabet can be expressed

$$\boldsymbol{s}^i = \boldsymbol{f}^\delta z_p, \tag{3.2}$$

with i a function of δ and p depending on the mapping and where $\boldsymbol{f}^\delta = \left[f_0^\delta, f_1^\delta, \ldots, f_{N_\perp-1}^\delta\right]$ is one of the $N_\perp$ vectors composing the orthogonal dimensions of the alphabet. The coefficient $z_p \in \mathbb{C}$, with $p \in \{0, \ldots, N_L - 1\}$, is taken from the complex plane and represents the linear modulation.

The overall M dimensions of the modulation can represent a total of $m = \log_2(M) = \log_2(N_\perp) + \log_2(N_L)$ bits. Each symbol of the alphabet consists of $N_\perp$ chips. The spectral efficiency is given by the ratio between the number of information bits contained in one symbol and the number of chips per symbols, with

$$\eta = \frac{\log_2(N_\perp) + \log_2(N_L)}{N_\perp} = \frac{\log_2(N_\perp)}{N_\perp} + \frac{\log_2(N_L)}{N_\perp}, \tag{3.3}$$

which includes the spectral efficiency of the orthogonal modulation $\log_2(N_\perp)/N_\perp$ and the gain from the introduction of the linear modulation, equal to $\log_2(N_L)/N_\perp$.

3.2.2 Examples of Modulations

In practice, common modulations can be chosen to represent both orthogonal and linear parts of the OCS modulation. An example of OCS modulation is given in Figure 3.1. For the orthogonal modulation, the $N_\perp = 4$ Pulse Position Modulation (PPM) was used, and the $N_L = 4$ Pulse Amplitude Modulation (PAM) was used as linear modulation. A set of $M = 16$ waveforms is constructed, and each line of the figure corresponds to one of the 4 orthogonal subsets $\mathcal{A}_\delta$. The vectors $\boldsymbol{f}^\delta$ can be picked as lines or columns from the identity matrix of size 4. The coplanar coefficients z_p are real, simplifying the coplanarity in collinearity. The spectral efficiency of this modulation is equal to

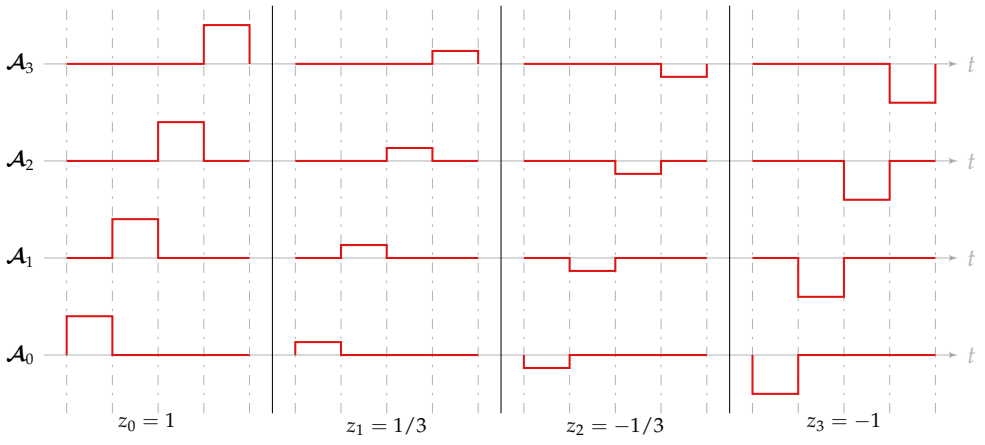

Figure 3.1 – *Example of an OCS modulation: the 4-PPM 4-PAM modulation, with $M = 16$.*

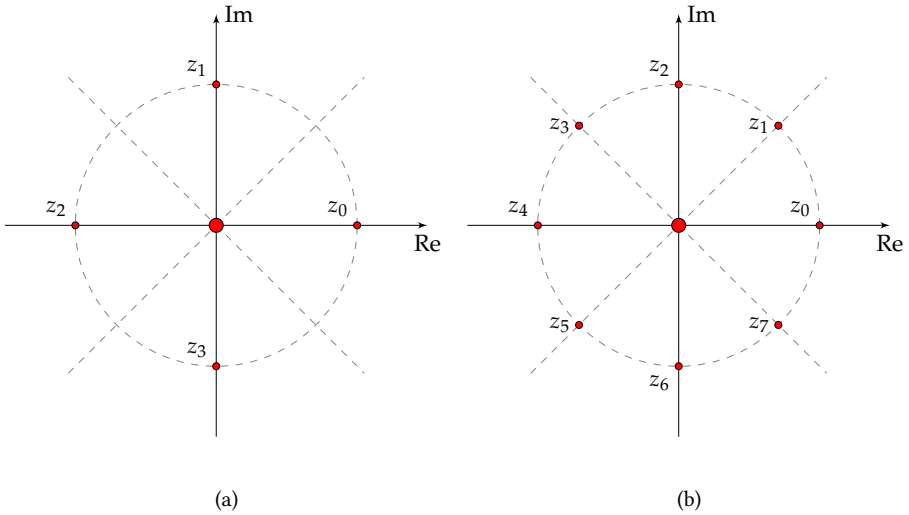

FIGURE 3.2 – *Projection on the δ-th orthogonal dimension: the $N_\perp$-FSK 4-PSK modulation (a) and $N_\perp$-FSK 8-PSK modulation (b).*

1, higher than the 4-PPM alone (which has a spectral efficiency of $1/2$) and lower than the 4-PAM by itself since it has a spectral efficiency of 2.

Another example of modulation is the $N_\perp$ FSK with N_L Phase Shift Keying (PSK). Each of the frequency carriers can have N_L phase, exactly like PSK modulation. The vectors $\boldsymbol{f}^\delta$ can be picked as lines or columns from the Discrete Fourier Transform (DFT) matrix of size $N_\perp$, and the coplanar coefficients are taken as roots of unity, with $z_p = \exp\left\{j\frac{2\pi}{N_L}p\right\}$. An interesting representation is the projection of all the symbols of the alphabet $\boldsymbol{\mathcal{A}}$ on one of the orthogonal dimensions, δ, i.e. the representation of the complex plane associated to the dimension. If $N_L = 4$ (4-PSK), one of the $N_\perp$ possible projections is depicted in Figure 3.2 (a). The 4 phase shifts of the subset appear, giving a constellation quite similar to the regular 4-PSK constellation. However, since all the other subsets are orthogonal, the projection on this specific dimension gives 0. In addition to the 4 elements of the subset, the constellation also shows a possible point in 0, corresponding to the $4 \times (N_\perp - 1)$ symbols outside this subset. The projection on one of the orthogonal dimensions for $N_L = 8$ (8-PSK) is depicted in Figure 3.2 (b). If 4-FSK ($N_\perp = 4$) is considered, the alphabet contains 32 elements, and the spectral efficiency is equal to $5/4$. There is no constraint on the choice of linear modulation, but the presence of the point 0 in the constellation could be considered for optimizing the Euclidean distances in the constellation. It should be noted that the choice of FSK has no influence on the representation, but it can impact other factors such as the robustness when considering selective frequency channels or the PAPR. This example of modulation has a constant envelope, while this is not the case for the example depicted in Figure 3.1.

3.2.3 Maximum Likelihood Receiver

In order to derive an expression for the Maximum Likelihood (ML) receiver, the likelihood of the symbols from the alphabet must be evaluated. The Additive White Gaussian Noise (AWGN) channel is considered, with noise variance σ^2_{ch}. With $\boldsymbol{r}$ the received symbols and assuming that $\boldsymbol{s}^i$ was transmitted, the likelihood of the symbol is given by

$$\begin{aligned} p\left(\boldsymbol{r}\,\middle|\,\boldsymbol{s}^i\right) &= \prod_{k=0}^{N_\perp-1} p\left(r_k\,\middle|\,s_k^i\right) \\ &= \left(\frac{1}{2\pi\sigma^2_{\text{ch}}}\right)^{N_\perp} \exp\left\{-\frac{1}{2\sigma^2_{\text{ch}}}\sum_{k=0}^{N_\perp-1}\|r_k - s_k^i\|^2\right\} \\ &= \left(\frac{1}{2\pi\sigma^2_{\text{ch}}}\right)^{N_\perp} \exp\left\{-\frac{1}{2\sigma^2_{\text{ch}}}\sum_{k=0}^{N_\perp-1}\|r_k\|^2\right\} \exp\left\{-\frac{1}{2\sigma^2_{\text{ch}}}\sum_{k=0}^{N_\perp-1}\left\|s_k^i\right\|^2 + \frac{1}{\sigma^2_{\text{ch}}}\sum_{k=0}^{N_\perp-1}\langle r_k, s_k^i\rangle\right\}. \end{aligned} \tag{3.4}$$

The first two terms are independent of the index i, and can thus be substituted by a constant C_{st}. Following the definition of the vector $\boldsymbol{s}$ given in Equation (3.2), the scalar product can be expressed

$$\langle r_k, s_k^i\rangle = \text{Re}\left(r_k \cdot \overline{s_k^i}\right) = \text{Re}\left(r_k \cdot \overline{f_k^\delta \cdot z_p}\right) = \text{Re}\left(r_k \cdot \overline{f_k^\delta} \cdot \overline{z_p}\right), \tag{3.5}$$

and the summation over k is expressed

$$\begin{aligned}\sum_{k=0}^{N_\perp-1}\langle r_k, s_k^i\rangle &= \sum_{k=0}^{N_\perp-1}\mathrm{Re}\left(r_k\cdot\overline{f_k^\delta}\cdot\overline{z_p}\right)\\ &= \mathrm{Re}\left(\overline{z_p}\cdot\sum_{k=0}^{N_\perp-1} r_k\cdot\overline{f_k^\delta}\right)\\ &= \mathrm{Re}\left(\overline{z_p}\cdot\langle \boldsymbol{r}, \boldsymbol{f}^\delta\rangle\right),\end{aligned} \tag{3.6}$$

where $\langle \boldsymbol{r}, \boldsymbol{f}^\delta\rangle$ represents the projection of the received vector $\boldsymbol{r}$ on the subset $\boldsymbol{\mathcal{A}}_\delta$ which includes $\boldsymbol{s}^i$.

Also, the definition of the symbols yields

$$\begin{aligned}\sum_{k=0}^{N_\perp-1}\left\|s_k^i\right\|^2 &= \sum_{k=0}^{N_\perp-1}\left\|f_k^\delta\cdot z_p\right\|^2\\ &= \|z_p\|^2\cdot\sum_{k=0}^{N_\perp-1}\left\|f_k^\delta\right\|^2\\ &= \|z_p\|^2\cdot\left\|\boldsymbol{f}^\delta\right\|^2.\end{aligned} \tag{3.7}$$

Using (3.6) and (3.7) in (3.4), the likelihood is expressed

$$p\left(\boldsymbol{r}\,\middle|\,\boldsymbol{s}^i\right) = C_{\mathrm{st}}\exp\left\{-\frac{\|z_p\|^2}{2\sigma_{\mathrm{ch}}^2}\cdot\left\|\boldsymbol{f}^\delta\right\|^2+\frac{1}{\sigma_{\mathrm{ch}}^2}\mathrm{Re}\left(\overline{z_p}\cdot\langle \boldsymbol{r}, \boldsymbol{f}^\delta\rangle\right)\right\}. \tag{3.8}$$

The likelihood of classic orthogonal modulations, given in Equation (1.40), can be retrieved from this result by setting $N_L = 1$ and $z_p = 1$.

From the expression of the likelihood, the ML receiver can be realized by computing

$$\hat{s} = \left\{\boldsymbol{s}^i\,\middle|\,\max_{\substack{\delta\in\{0,\ldots,N_\perp-1\}\\ p\in\{0,\ldots,N_L-1\}}} -\frac{1}{2}\|z_p\|^2\cdot\left\|\boldsymbol{f}^\delta\right\|^2+\mathrm{Re}\left(\overline{z_p}\cdot\langle \boldsymbol{r}, \boldsymbol{f}^\delta\rangle\right)\right\}. \tag{3.9}$$

3.2.4 Performances

In order to illustrate the performance of the modulation, Bit Error Rate (BER) performance is computed under the AWGN channel. The 4-FSK 8-PSK is used, associated with the ML receiver derived in the previous section. This modulation has an alphabet size equal to $M = 32$ and 4 orthogonal subsets. Its spectral efficiency is equal to $5/4$.

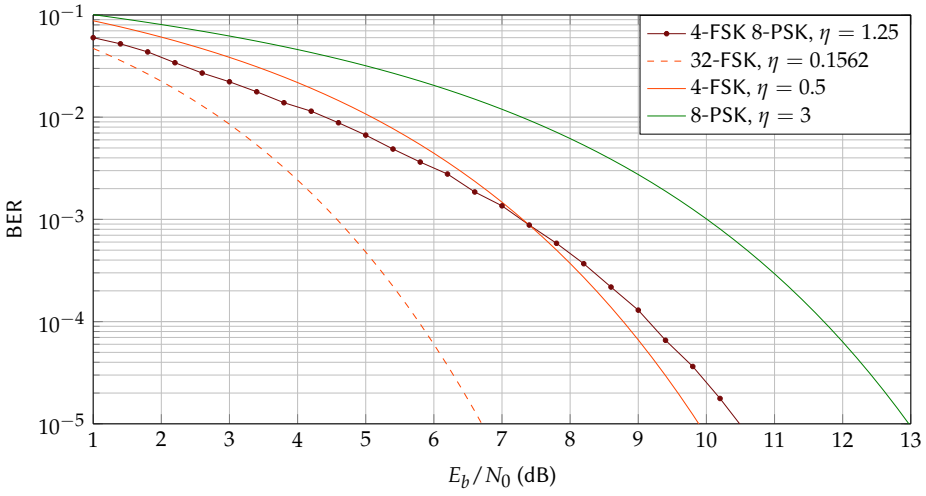

Figure 3.3 – *BER performance of the* 4*-FSK* 8*-PSK OCS modulation, along with the performance of some classic modulation schemes.*

The performance is depicted in Figure 3.3, along with the performance of the 8-PSK, the 4-FSK, and the 32-FSK (which has the size of alphabet, but is orthogonal).

The performance of the modulation with these parameters is close to the performance of the 4-FSK, but with a spectral efficiency increased by a factor of 2.5. The 8-PSK modulation has a better spectral efficiency but needs 3 more dB to reach a BER of 10^{-4}. In comparison, the 32-FSK offers much better performance but at a lower spectral efficiency. The difference with the 32-FSK illustrates the impact of the reduction of orthogonality of the alphabet, due to the introduction of the linear modulation. The performance loss is non-negligible and is done for the benefit of an increased spectral efficiency. Overall, the modulation offers a better compromise in terms of performance and spectral efficiency than the other schemes.

The modulation has two parameters that influence both the spectral efficiency and the performance. Further studies should be realized in order to have a better comprehension of the scheme. This study will focus on its use with the turbo process presented in the previous chapter.

3.3 Coplanar Turbo-FSK

Having a scheme with a flexible spectral efficiency is interesting for situations where the requirements in sensitivity or data rate change frequently. In the previous chapter, the Turbo-FSK scheme was presented and optimized. Its comparison with existing LPWA solutions showed a real potential for the solution, but its design induced ultra low levels of spectral efficiency. With the purpose to increase the spectral efficiency of the Turbo-FSK scheme, two new features are introduced: the use of OCS modulation with FSK modulation previously presented, and the integration of a puncturing procedure. This new scheme, so-called Coplanar Turbo-FSK, is described in this section. Both the transmitter and the receiver are reviewed.

3.3.1 Transmitter

In order to describe the transmitter for the Coplanar Turbo-FSK scheme, its architecture is reviewed. The encoding procedure, close to the one used for Turbo-FSK, is first explained. Two specific features of the Coplanar Turbo-FSK are then introduced: the puncturing procedure and the use of OCS modulation. Finally, the trellis generated by the encoding process is presented.

3.3.1.1 Encoder

The architecture of the transmitter is presented in Figure 3.4. For consistency in this paper, the notations of Chapter 2 and the segmentation depicted in Figure 2.2 are used: Q is the information block size, and it is divided into N_q binary words of size q (thus $Q = N_q \cdot q$). The transmitter is composed of λ similar stages and the stage $\ell \in \{0, \ldots, \lambda - 1\}$ is considered. The information block is interleaved with the function π_ℓ^{int}, where int stands for internal, as this interleaver corresponds to the interleaver used for the turbo process. The N_q words of length q are then encoded using the encoder presented in Figure 2.7. The encoder adds 1 parity bit for each information word and an extra word to force the memory state back to 0. The rate of the code is

$$R_c = \frac{Q}{(N_q + 1)(q + 1)} \approx \frac{q}{q + 1}, \tag{3.10}$$

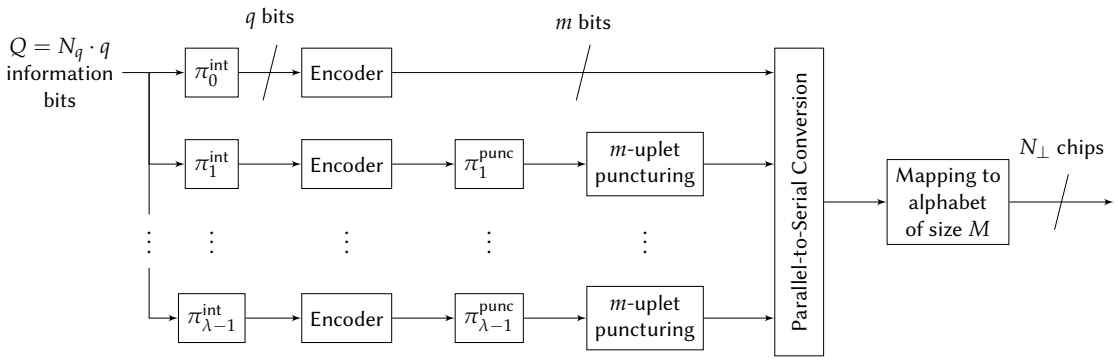

Figure 3.4 – *The Coplanar Turbo-FSK transmitter architecture.*

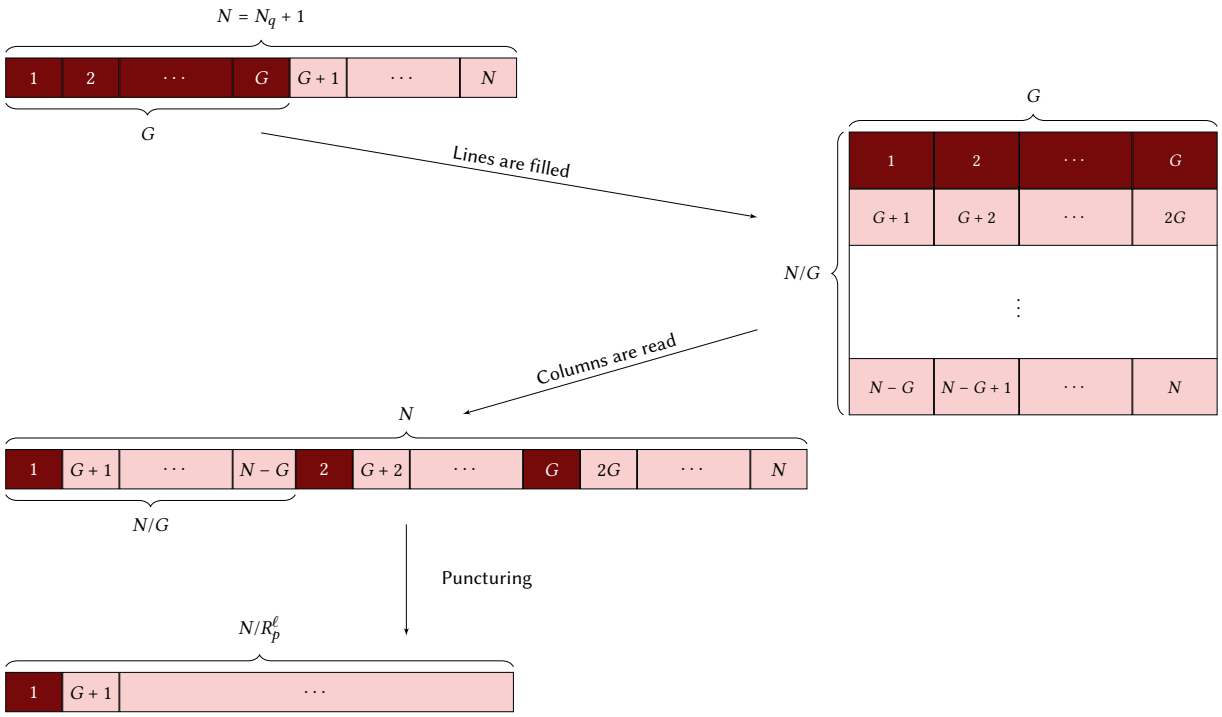

FIGURE 3.5 – *Puncturing procedure using a block interleaver of size G.*

where the approximation is valid for large sizes of Q (i.e. $N_q + 1 \approx N_q$). The size of the encoded words is denoted m, with $m = q + 1$. For each stage, the sequence of $N_q + 1$ binary words of length m is to be modulated. Each binary word of size m will be associated with one of the elements of the alphabet of modulation $\mathcal{A}$, referred to as codewords. In order to increase the spectral efficiency of the scheme, a puncturing step is also considered.

3.3.1.2 PUNCTURING

Puncturing consists commonly of removing some parity bits of the encoded sequence. Only the systematic bits and a reduced number of parity bits are sent. For the considered scheme, removing some parity bits would involve changing the size m to q for some specific words. However, the size of the words to be modulated should be kept to a constant value, equal to m. In order to fulfill this condition, entire words of size m (or alternatively, codewords) are punctured. If the first stage is not punctured, then every systematic bit is sent at least once. Every other stage is punctured at a rate $R_p^\ell \geq 1$. This rate may differ depending on the stage. The overall puncturing rate is denoted by R_p, and is equal to

$$R_p = \frac{\lambda(N_q+1)}{(N_q+1) + \sum_{\ell=1}^{\lambda-1} \frac{(N_q+1)}{R_p^\ell}} = \frac{\lambda}{1 + \sum_{\ell=1}^{\lambda-1} \frac{1}{R_p^\ell}}, \tag{3.11}$$

with $R_p \geq 1$.

In order to avoid puncturing too many consecutive codewords and induce holes in the trellis, a block interleaver π_ℓ^{punc} of size G is used. An example of the procedure to organize the puncturing is depicted in Figure 3.5. Alternative procedures could be considered. The block is interleaved by filling a matrix of size $G \times (N_q + 1)$ row by row, and the same matrix is read column by column to form the interleaved output. Considering the puncturing rate of stage ℓ to be R_p^ℓ, the actual step of puncturing consists in selecting only the first $(N_q + 1)/R_p^\ell$ binary words. The use of the block interleaver scatters the punctured binary words over the whole sequence.

An example of a puncturing pattern is depicted in Figure 3.6. For this particular example, the puncturing rate of every stage is equal to $R_p^\ell = 3/2$, and there are $\lambda = 4$ stages. The overall puncturing rate, given by (3.11), is equal to $R_p = 4/3$. The matrix interleaver parameter G was set to 3, and the input sequence is circularly shifted for the first two stages.

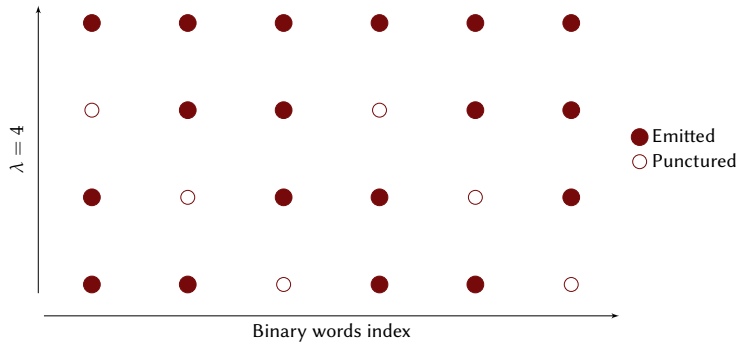

FIGURE 3.6 – *A specific puncturing pattern for* $R_p = 4/3$. *The puncturing rate of every stage except the first one is equal to* $R_p^{\ell} = 3/2$. *The block interleaver parameter is* $G = 3$

3.3.1.3 MODULATION

After puncturing, the overall sequence consists of $\lambda(N_q+1)/R_p$ binary words of size m. These words are mapped to the alphabet of codewords $\mathcal{A}$ of size M. The alphabet is chosen as the OCS alphabet, described in Section 3.2, with FSK as orthogonal modulation. The parameters are the number of orthogonal subsets $N_\perp$ (i.e. the number of possible frequencies) and the number of elements in each subset N_L. The alphabet size is given by $M = N_\perp \times N_L$. The two parameters are related to the size of the binary word with $m = \log_2(M) = \log_2(N_\perp) + \log_2(N_L)$. With the spectral efficiency of the modulation as defined by Equation (3.3), the overall spectral efficiency of the scheme is given by

$$\eta = \frac{Q}{\lambda(N_q+1)m} \cdot R_p \cdot \frac{m}{N_\perp} = \frac{N_q \cdot q}{\lambda(N_q+1)N_\perp} \cdot R_p. \tag{3.12}$$

Following the relation $m = q+1$ and the relation between m and the parameters of the modulation $2^m = N_\perp N_L$, the number of information bits per codeword is given by

$$q = \log_2(N_\perp) + \log_2(N_L) - 1. \tag{3.13}$$

The spectral efficiency can be approximated, for large sizes of information block Q, with

$$\eta \approx \frac{\log_2(N_\perp) + \log_2(N_L) - 1}{\lambda N_\perp} \cdot R_p. \tag{3.14}$$

This expression includes the 4 main parameters which define the scheme: the number of stages λ, the number of orthogonal subsets in the alphabet $N_\perp$, the number of elements in each subset N_L and the puncturing rate R_p (the size of the alphabet is obtained with the product $M = N_\perp N_L$). The rate of the Turbo-FSK defined in Chapter 2,

N_L \ $N_\perp$	256	128	64	32	16	8	4	2	
1	0.10	0.18	0.31	0.52	0.83	1.25	1.67	1.67	M
2	0.12	0.21	0.36	0.62	1.04	1.67	2.50	3.33	2
4	0.13	0.23	0.42	0.73	1.25	2.08	3.33	5.00	4
8	0.14	0.26	0.47	0.83	1.46	2.50	4.17	6.67	8
16	0.16	0.29	0.52	0.94	1.67	2.92	5.00	8.33	16
32	0.17	0.31	0.57	1.04	1.88	3.33	5.83	10.00	32
M	8192	4096	2048	1024	512	256	128	64	

TABLE 3.1 – *Spectral efficiency (expressed in* 10^{-1} *bits·s*$^{-1}$*·Hz*$^{-1}$*) for various values of* $N_\perp$ *(number of orthogonal subsets) and* N_L *(size of the linear modulation). The other parameters are taken equal to* $\lambda = 3$ *and* $R_p = 1$, *and the spectral efficiency is computed using* (3.14). *The size of alphabet* M *is constant along each diagonal, and indicated at the end of the diagonal.*

Equation (2.7), can be obtained by setting $N_L = 1$ and $R_p = 1$. The orthogonal modulation is then the FSK and there is no linear modulation. The introduction of these two new parameters allows for higher ranges of spectral efficiency. Increasing the size N_L or the puncturing rate R_p clearly increases the spectral efficiency. In Table 3.1, values of spectral efficiency (expressed in 10^{-1} bits·s^{-1}·Hz^{-1}) for sizes of linear modulation N_L spanning from 1 to 32 and number of orthogonal subsets from 2 to 256 are presented. The other parameters are chosen equal to $\lambda = 3$ and $R_p = 1$. As the product $M = N_\perp N_L$ is constant over a diagonal, the value of M is given at the end of each diagonal. This table clearly shows that using the considered modulation, the alphabet size M can be kept constant while multiplying the spectral efficiency by a power of 2. It can be noted that the first line (i.e. $N_L = 1$) is equivalent to the Turbo-FSK scheme, presented in Chapter 2.

3.3.1.4 Trellis

With the use of the accumulator in the encoding process, a trellis is established, which associates each input information word to one of the 4 possible transitions. Each information is associated to a branch in the trellis; as there are $M = 2^m$ possible information words, each transition has $M/4$ branches. The mapping performed between the binary words of length m and the codewords from the alphabet can be represented on the trellis.

For the Turbo-FSK case, an example of mapping for the alphabet of size $M = 8$ is represented in Figure 2.8. As all the codewords are orthogonal to each other, the choice of mapping has no influence on the distance between the branches in the trellis. All branches are in different orthogonal dimensions. However, when considering the OCS modulation, this is no longer the case. Codewords belonging to a same subset are not orthogonal between each other. Examples of OCS alphabet were presented in Section 3.2.2, and the conclusion was that the distance between the various symbols of the alphabet is modified by the introduction of a linear component. When mapping the binary words to the codewords, consideration must be taken on the orthogonality of the trellis, i.e. on the distances between the symbols associated to the transitions.

An example of trellis for the case $N_\perp = 4$ and $N_L = 8$ is depicted in Figure 3.7. For this configuration, there are $M = 32$ branches. The mapping is then done so that each transition corresponds to a unique orthogonal subset. All the parallel branches are mapped by codewords belonging to the same subset. Since FSK is considered for the orthogonal modulation, the vectors f are lines of the DFT matrix of size $N_\perp = 4$. When PSK is considered as the linear modulation, the projection of all the codewords of the alphabet $\mathcal{A}$ on one of the orthogonal dimension δ is given in Figure 3.2. Using this mapping, the transitions in the trellis are ensured to be further apart, as the distance between the orthogonal subsets is larger than the minimum distance in each subset. This may not be the case for other mappings or for other values of the parameters $N_\perp$ and N_L. The influence of the choice of mapping on the performance is studied later.

3.3.2 Receiver

Since the Coplanar Turbo-FSK scheme is an extension of Turbo-FSK, its receiver has a lot of similarities. The Turbo-FSK receiver is presented in Section 2.2.2. In this section, the derivations adapted to the Maximum *A Posteriori* (MAP) Coplanar Turbo-FSK receiver are presented, along with the architecture of the receiver.

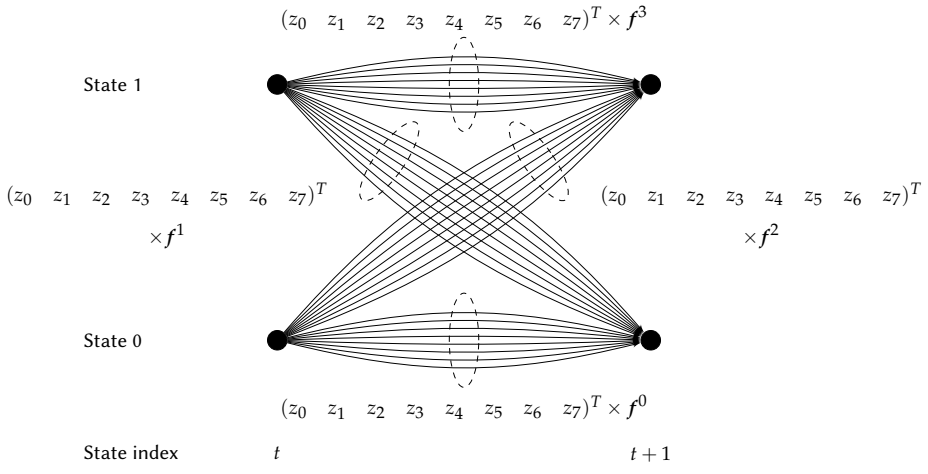

Figure 3.7 – *A section of the trellis for the configuration $N_\perp = 4$ and $N_L = 8$, with one possible mapping .*

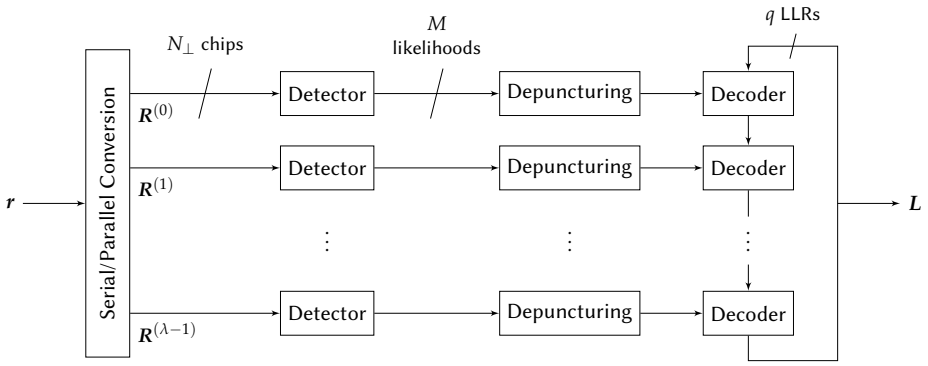

FIGURE 3.8 – *The Coplanar Turbo-FSK receiver architecture.*

3.3.2.1 Derivation of the Receiver

In the Turbo-FSK receiver, the Bahl, Cocke, Jelinek and Raviv (BCJR) algorithm is used in order to compute the log-*A Posteriori* Probabilities (APP) ratios of the information bits. The log-APP are given by

$$L\left(b_{n,t} \,\middle|\, \boldsymbol{R}_1^{N_q+1}\right) = \log \frac{\Pr\left(b_{n,t} = +1 \,\middle|\, \boldsymbol{R}_1^{N_q+1}\right)}{\Pr\left(b_{n,t} = -1 \,\middle|\, \boldsymbol{R}_1^{N_q+1}\right)}, \tag{3.15}$$

where $\boldsymbol{R}_1^{N_q+1}$ is the received codewords sequence and $b_{n,t}$ the bit at index n of the information word at time index t. The derivations of the receiver are similar to the Turbo-FSK, and the use of the BCJR introduces the same terms α (Equation (2.10)), β (Equation (2.11)) and γ (Equation (2.13)). The final expression of the log-APP is

$$L\left(b_{n,t} \,\middle|\, \boldsymbol{R}_1^{N_q+1}\right) = \log \frac{\sum_{i \in \mathcal{B}_{+1}^n} \alpha_{t-1}(s_i') \cdot p\left(\boldsymbol{r}_t \,\middle|\, \boldsymbol{c}^i\right) \Pr\left(\boldsymbol{c}^i\right) \cdot \beta_t(s_i)}{\sum_{i \in \mathcal{B}_{-1}^n} \alpha_{t-1}(s_i') \cdot p\left(\boldsymbol{r}_t \,\middle|\, \boldsymbol{c}^i\right) \Pr\left(\boldsymbol{c}^i\right) \cdot \beta_t(s_i)}, \tag{3.16}$$

where $\mathcal{B}_{+1}^n$ (resp. $\mathcal{B}_{-1}^n$) is the group of codewords that encodes information words for which the bit b_n is equal to $+1$ (resp. -1). $p\left(\boldsymbol{r}_t \,\middle|\, \boldsymbol{c}^i\right)$ is the likelihood of the codeword $\boldsymbol{c}^i$ and $\Pr\left(\boldsymbol{c}^i\right)$ its *a priori* probability, given by the other decoders and expressed using the *a priori* log ratios with Equation (2.14). Considering the chosen OCS alphabet, for which the symbols likelihood was developed in Section 3.2.3, Equation (3.8), and with $\boldsymbol{c}^i = z_p \boldsymbol{f}^\delta$, the product can be expressed

$$p\left(\boldsymbol{r}_t \,\middle|\, \boldsymbol{c}^i\right) \Pr\left(\boldsymbol{c}^i\right) = C_{\text{st}} \exp\left\{ -\frac{\|z_p\|^2}{2\sigma_{\text{ch}}^2} \cdot \left\|\boldsymbol{f}^\delta\right\|^2 + \frac{1}{\sigma_{\text{ch}}^2} \operatorname{Re}\left(\overline{z_p} \cdot \langle \boldsymbol{r}_t, \boldsymbol{f}^\delta \rangle\right) + \frac{1}{2} \sum_{k=0}^{q-1} L_A(b_k) b_k^i \right\}. \tag{3.17}$$

In this expression, both the orthogonal and linear components of the codeword $\boldsymbol{c}^i$ appear.

3.3.2.2 Architecture

The architecture of the receiver is depicted in Figure 3.8. The λ stage observations are first retrieved. For each stage, the observation consists in $(N_q+1)/R_p^\ell$ codewords of length $N_\perp$. The detail of one stage is depicted in Figure 3.9. The detector computes both the correlation on the orthogonal dimensions and the first term of (3.17) in order to estimate a quantity related to the likelihood of the M codewords. The result is a matrix of size $(N_q+1)/R_p^\ell \times M$. Then, the depuncturing block appends $(N_q+1)(1-1/R_p^\ell)$ extra lines, corresponding to the same number of punctured codewords at the transmitter side. For these lines, the M likelihoods are equal, i.e. the receiver considers each codeword to be equally probable. Interleaving is then applied and scatters the appended lines over the whole sequence. This step requires the receiver to use the same interleaver used for puncturing as the one used at the transmitter side. The receiver also needs to know the puncturing rate for each stage. When considering the trellis representation, puncturing consists in not transmitting some sections of the trellis. The receiver then considers every branch of the punctured sections to be equally probable.

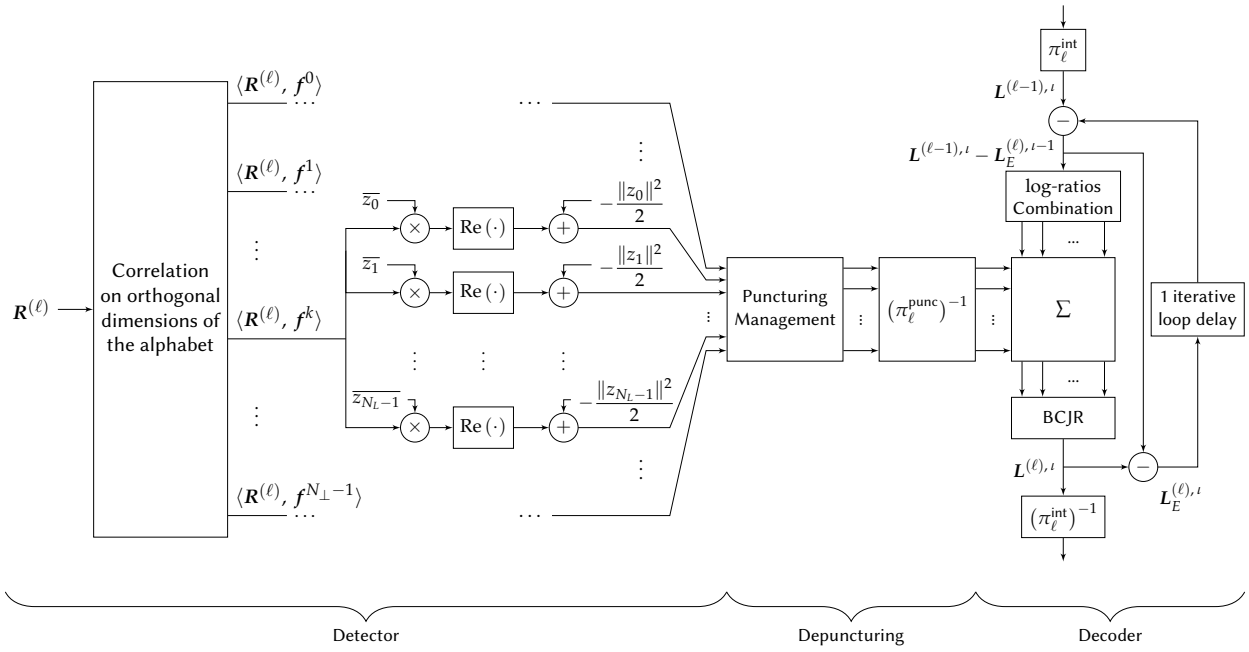

FIGURE 3.9 – *The Coplanar Turbo-FSK one stage receiver's architecture.*

The detector and the puncturing management provide the log of the likelihood part of (3.17). It is fed to the decoder, which first computes the log of the *a priori* part (the third term) of (3.17) by combining the *a priori* log ratios. After summation, the log of (3.17) is fed to the BCJR algorithm, which estimates the log-APP of the information bits using Equation (3.16). The extrinsic log ratio is then computed and stored for use at the following iteration. The process is similar to the one presented in Section 2.2.2.3. After interleaving, the log-APP are fed to the next decoder. Complexity of the BCJR algorithm can be reduced by using the max-log approximation as described in Section 2.2.2.4. Using the approximation avoids the computation of exponential functions, required when computing the MAP algorithm. For the case where the FSK orthogonal alphabet is selected, the correlation on the orthogonal dimensions may be done using the Fast Fourier Transform (FFT) algorithm.

The initial motivation for Coplanar Turbo-FSK was to introduce flexibility in terms of spectral efficiency. Starting from the initial Turbo-FSK scheme, a specific puncturing procedure is introduced in order to reduce the number of transmitted codewords by a factor R_p, the puncturing rate. The alphabet of codewords is also modified by introducting N_L linear components, so that the size of the codewords is reduced to $N_\perp$, while the number of elements of the alphabet stays equal to M, with $M = N_L N_\perp$. The introduction of these linear components may also be interpreted as a reduction in the orthogonality of the alphabet, and may have a strong impact on the performance of the scheme.

3.4 Analysis

The design of the scheme gives 5 parameters to study: the number of orthogonal subsets $N_\perp$, the size of the linear modulation N_L (the two are related to the alphabet size with $M = N_\perp N_L$), the number of stages λ, the puncturing rate R_p and the choice of mapping on the trellis. In this section, each parameter is studied and the performance of the scheme according to this parameter is assessed. The EXtrinsic Information Transfer (EXIT) chart for Turbo-FSK, presented in Section 2.3.1, was demonstrated to be able to predict the behavior of the decoder. Its use for the analysis of the Coplanar Turbo-FSK is considered.

The impact of the choice of how to map codewords on the trellis is first studied. The second aspect studied is the choice of linear modulation and how it can influence the performances. For the case $N_L = 8$, the use of Amplitude Phase-Shift Keying (APSK) with various shapes is examined. The asymptotic performance of the scheme is evaluated, and the linear modulation is optimized according to the threshold in E_b/N_0. The puncturing mechanism, introduced for the Coplanar Turbo-FSK scheme is then studied. It allows for gains in spectral efficiency, at the expense of some performance loss, which is evaluated for some use cases. Finally, some configurations of the scheme are compared to the maximum achievable spectral efficiency, and the flexibility in terms of spectral efficiency of the Coplanar Turbo-FSK is demonstrated.

Section	Study	Changing Parameter(s)	Constant Parameter(s)
3.4.1	Influence of the Choice of Trellis Mapping	M, λ, Mapping	R_p
3.4.2	Influence of the Parameter of APSK Modulation	$N_\perp$	N_L, λ, R_p, Mapping
3.4.3	Effects of Puncturing	R_p	$N_\perp$, N_L, λ, Mapping
3.4.3	Impact on Spectral Efficiency	$N_\perp$, N_L, λ	R_p, Mapping

TABLE 3.2 – *Organization of the section concerning the analysis of the parameters. $N_\perp$ is the number of orthogonal subsets and N_L the size of the linear modulation with $M = N_\perp N_L$. R_p is the puncturing rate and λ is the number of stages. Three mappings are considered, denoted $\perp$, L and X.*

Table 3.2 summarizes the content of the section and mentions what are the changing or constant parameters for each subsection. For all simulations, FSK is used as orthogonal modulation and PSK as linear modulation (except for the subsection 3.4.2, where APSK is used). When BER performance is computed, a random interleaving function is selected.

3.4.1 Loss of Orthogonality in the Trellis

As presented when describing the trellis, the introduction of linearities in the alphabet can also be interpreted as a loss of orthogonality. For the initial case of the Turbo-FSK, the M codewords of the alphabet are orthogonal to each other. When using the OCS modulation, only the $N_\perp$ subsets (each containing N_L codewords) are orthogonal to each other. The choice of the mapping of the binary words of length m on the alphabet of size M can be expected to have an impact on the performance. In order to quantify that impact, various trellis and mappings are compared. The thresholds are estimated using the EXIT chart technique. No puncturing is applied (i.e. $R_p = 1$) and PSK is chosen as the linear modulation (the values z_p are taken as roots of the unity).

3.4.1.1 Trellis Classification

Since the alphabet has M elements and there are M branches in the trellis ($M/4$ branches per transition), the total number of possible mapping is equal to $M!$. As this value increases exponentially (for example, $16! \simeq 2.09 \cdot 10^{13}$), we consider three types of mapping.

The first type, denominated $\perp$ mapping, is characterized by the group of orthogonal vectors $\mathcal{F}_{s'\to s}$, and

$$\boldsymbol{c}^i \in \mathcal{T}_{s'\to s} \quad \text{iff} \quad \boldsymbol{f}^\delta \in \mathcal{F}_{s'\to s}, \tag{3.18}$$

where $\boldsymbol{c}^i = z_p \boldsymbol{f}^\delta$ and $\mathcal{T}_{s'\to s}$ is the group of branches corresponding to the transition from s' to s. This means that two different transitions are mapped by codewords from different subsets. This mapping ensures orthogonality

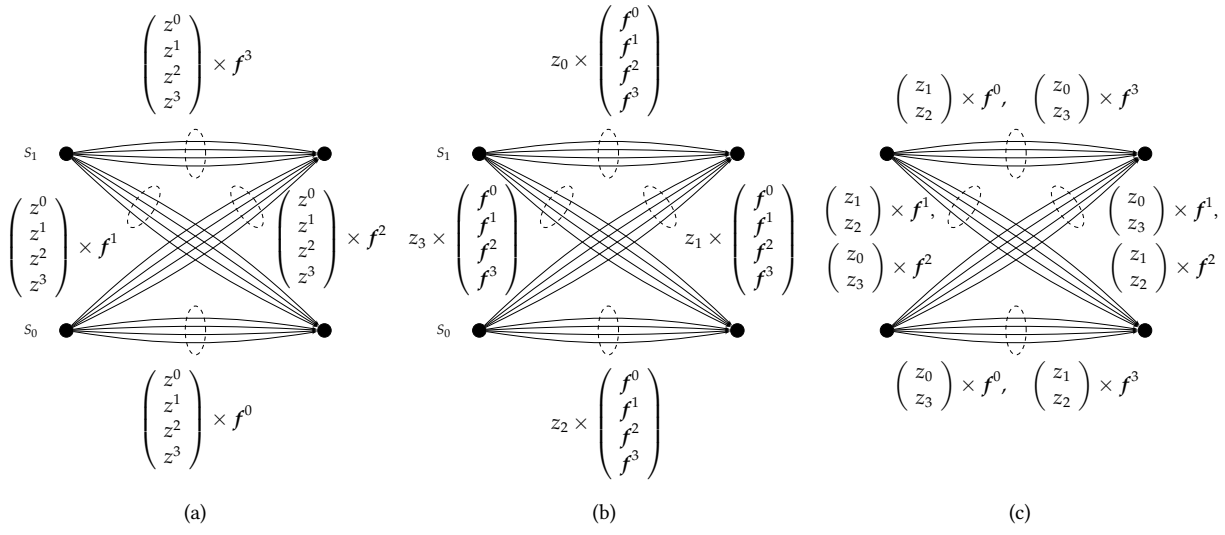

FIGURE 3.10 – *Example of $\perp$ mapping (a), L mapping (b) and X mapping (c) for the case $N_\perp = 4$ and $N_L = 4$ (i.e. $M = 16$).*

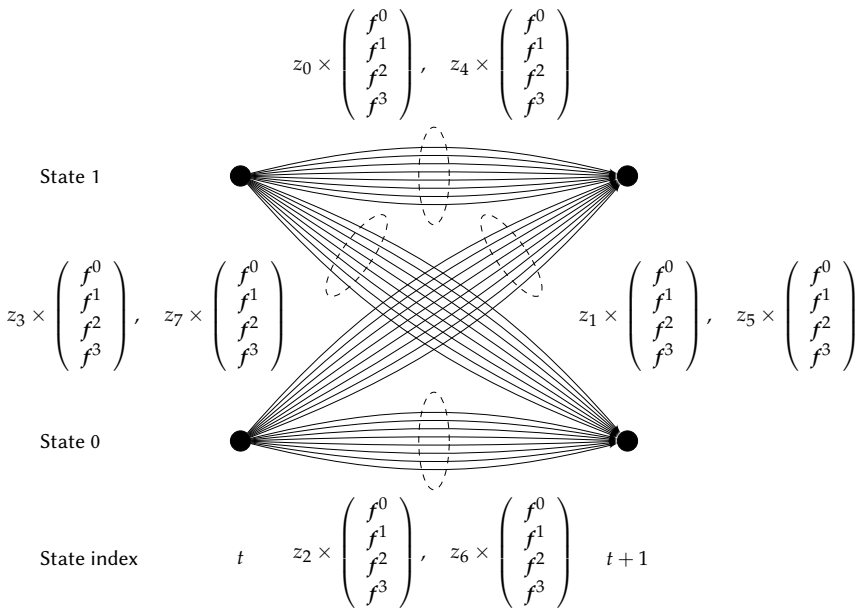

FIGURE 3.11 – *A section of the trellis with L mapping for the configuration* $N_\perp = 4$ *and* $N_L = 8$.

between the transitions, a property of the Turbo-FSK. The example of mapping for $N_\perp = 4$ and $N_L = 8$ given in Figure 3.7 belongs to the $\perp$ mapping, with *e.g* $\mathcal{F}_{1\to 1} = \{f^3\}$. In Figure 3.10 (a), the case $N_\perp = 4$ and $N_L = 4$ is represented for a $\perp$ mapping.

The second type of mapping considered is the L mapping. It is characterized by the group $\mathcal{Z}_{s'\to s}$ with

$$\boldsymbol{c}^i \in \mathcal{T}_{s'\to s} \quad \text{iff} \quad z_p \in \mathcal{Z}_{s'\to s}. \tag{3.19}$$

With this mapping, two different transitions are mapped by codewords with different z_p, but that may belong to the same subset. There is no orthogonality between the transitions, but there is orthogonality between the branches of a transition. A L mapping for the case $N_\perp = 4$ and $N_L = 8$ is depicted in Figure 3.11, with for example $\mathcal{Z}_{1\to 1} = \{z^0, z^4\}$. In Figure 3.10 (b), the case $N_\perp = 4$ and $N_L = 4$ is represented for a L mapping.

The third mapping, denominated X mapping, is a hybrid mapping. For each transitions, the $M/4$ branches are mapped in $N_\perp/2$ of the orthogonal dimensions, and each orthogonal dimension can be modulated by $N_L/2$ of the linear values. The mapping is selected so that pairs of orthogonal dimensions are modulated by the N_L linear values.

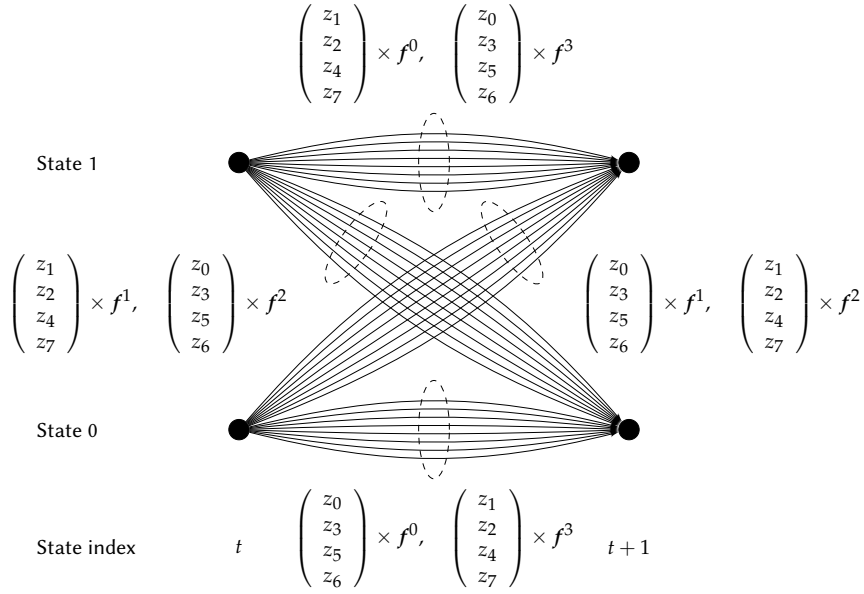

FIGURE 3.12 – *A section of the trellis with X mapping for the configuration* $N_\perp = 4$ *and* $N_L = 8$.

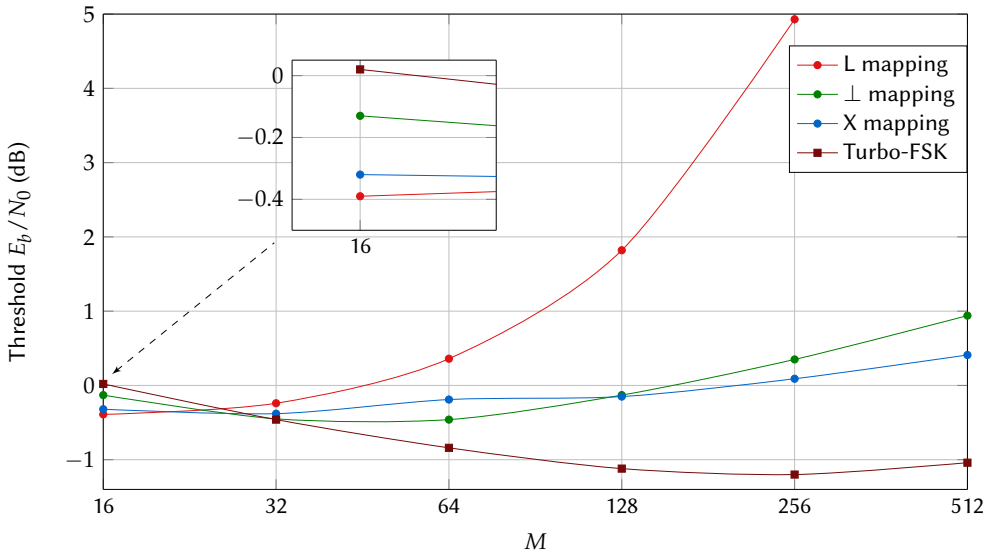

FIGURE 3.13 – *Thresholds for various size of alphabet M and mappings, with $N_\perp = 4$ (4-FSK) and $\lambda = 4$.*

A X mapping for the case $N_\perp = 4$ and $N_L = 4$ is depicted in Figure 3.10 (c), and another for the case $N_\perp = 4$ and $N_L = 8$ is depicted in Figure 3.12. This mapping somehow mixes the two mappings $\perp$ and L. The pair of transitions $1 \to 1$ and $0 \to 0$ is orthogonal to the pair $1 \to 0$ and $0 \to 1$, but the two transitions $1 \to 1$ and $0 \to 0$ are mapped by codewords in the same orthogonal subsets.

The three mapping types correspond to several of the $M!$ possible mappings, and two different mappings of the same type may lead to variation in performance. However, each mapping defines a general structure for the trellis, and the study will help evaluate the impact of the mapping on the performance.

3.4.1.2 Threshold Comparisons

In order to estimate the asymptotic performance, thresholds of the Coplanar Turbo-FSK with various parameters and mappings are computed. For each size of alphabet M, four trellis mappings are considered: the three mappings previously introduced and the fully orthogonal mapping, where each branch is orthogonal to all the other branches. This mapping is strictly equivalent to the Turbo-FSK.

For the first comparison, we consider the Coplanar Turbo-FSK where the number of orthogonal subsets is kept constant and equal to $N_\perp = 4$. The number of elements in the subsets increases with M as $N_L = M/N_\perp = M/4$. The estimated thresholds for values of M spanning from 16 to 512 and with the parameter $\lambda = 4$ are depicted in Figure 3.13. The trellis depicted and presented previously actually corresponds to some of the mappings used for these simulations: the case $M = 16$ with $\perp$ mapping is depicted in Figure 3.10 (a); the case $M = 32$ with $\perp$ mapping is depicted in Figure 3.7, the case $M = 16$ with L mapping is depicted in Figure 3.10 (b), the case $M = 32$ with L mapping is depicted in Figure 3.11 and the case $M = 32$ with X mapping is depicted in Figure 3.12.

Since one of the properties of the linear modulations is to have an energy efficiency decreasing with the order of the modulation, a loss in performance is expected when increasing the value of N_L. For all cases but $M = 16$, the thresholds of the Coplanar Turbo-FSK is indeed higher than the threshold of the Turbo-FSK, for all types of mappings. However, the loss varies depending on the selected mapping. More particularly, the L mapping (which totally gives up orthogonality between the transitions) has a threshold more than 6dB higher that the orthogonal case for $M = 256$, while using the X mapping reduces this gap to 1dB. This mapping performs better than the $\perp$ mapping for larger sizes of alphabet, with a gain of 0.5dB for $M = 512$. This figure emphasizes the importance of choosing mappings that maintain a certain degree of orthogonality between the transition in the trellis. However, preserving complete orthogonality (i.e. $\perp$ mapping) reveals itself less interesting than introducing linearities between some transitions (i.e. X mapping).

The case $M = 16$ shows interesting results. Indeed, for this size of alphabet, the Coplanar Turbo-FSK performs better than the Turbo-FSK. Also, the L mapping outperforms the two other mappings, and offers 0.4dB of gain versus the Turbo-FSK. The trellis for this mapping and configuration is depicted in Figure 3.10 (b). As the PSK modulation was selected as linear modulation, the projection on one of the orthogonal subsets is depicted Figure 3.2 (a). This representation also gives an indication of the distances between the various codewords. With a normalized constellation, the distance between *e.g* z_0 and 0 (i.e. all the other codewords in the other subsets) is 1. But the

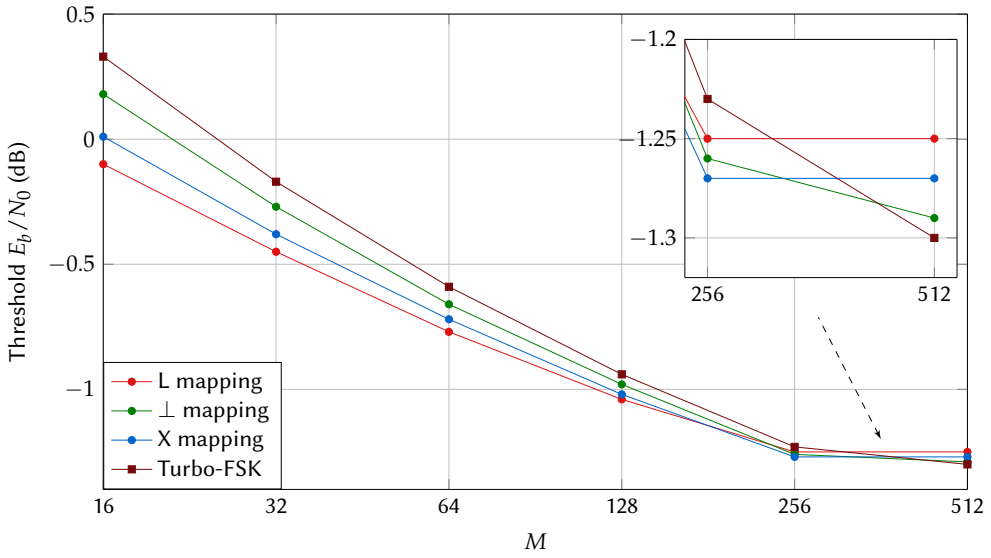

FIGURE 3.14 – *Thresholds for various size of alphabet M and mappings, with $N_L = 4$ (QPSK) and $\lambda = 3$.*

distance between z_0 and z_1 is $\sqrt{2} \simeq 1.41$ and the distance between z_0 and z_2 is 2. Since the L mapping with $N_L = 4$ associates each transition to one of the four possible z_p, transitions are further apart than when simple orthogonality is considered. The distance in the projection also explains why the L mapping performs significantly worse for larger sizes of M: the transitions get closer as N_L increases.

With these considerations on the 4-PSK modulation, and its potential gain versus the Turbo-FSK scheme, we wish to study this size of linear modulation versus various values of $N_\perp$. The parameter $\lambda = 3$ is selected, and alphabet sizes spanning from 16 to 512 are chosen (equivalent to sizes of FSK spanning from 4 to 128). The same 4 mappings are considered, and the estimated thresholds are depicted in Figure 3.14. Up to an alphabet size equal to $M = 128$, the L mapping outperforms the other mappings, with a gain of 0.42dB versus the Turbo-FSK for $M = 16$. For $M = 256$ (or $N_\perp = 64$), the Coplanar Turbo-FSK with every mapping has a lower threshold than the Turbo-FSK, but the difference is much less significant. For $M = 512$, the thresholds of the Coplanar Turbo-FSK are no longer lower than the Turbo-FSK. The impact of having larger distances due to the choice of linear modulation is reduced when large numbers of orthogonal subsets are considered. Considering the L mapping, the distance between the transitions is the same when $M = 16$ and when $M = 512$, but each transition has 4 orthogonal branches per transition in the first case and 128 in the second case.

As expected when first considering the use of a linear component, some performance loss is observed for large sizes of N_L. Nonetheless, the loss, due to the reduction of orthogonality in the trellis, can be reduced by selecting an appropriate mapping that maintains some orthogonal properties between the transitions. Also, the use of the 4-PSK modulation can reveal itself beneficial for the performance when a relatively small number of orthogonal subsets are considered (up to $N_\perp = 64$).

In addition to the three parameters that are $N_\perp$, N_L and λ, the selected mapping must be considered for the Coplanar Turbo-FSK, and there are $M!$ possible mappings. This makes the scheme arduous to study, and only a small proportion of the parameters have been explored. It is possible for another configuration to exceed the initial Turbo-FSK, but this configuration has not been found yet. For the rest of the study, the X mapping is considered, as it offers a compromise in terms of performance.

3.4.2 Use of the APSK Modulation

Various linear modulations can be selected when designing the OCS alphabet. In this section, the Coplanar Turbo-FSK is studied for the specific value of $N_L = 8$ and with the use of APSK modulation. 8-PSK, a form of 8-APSK, was considered for the previous simulations. The use of APSK allows for changes in the distances of the coplanar points in each subset. 2 amplitude levels are considered, scattering the 8 points of the constellation on two distinct rings. The goal is to study the influence of the distance between the elements of the same subset. After describing the parameters of the modulation, its usage in the Coplanar Turbo-FSK is reviewed. The parameters of the Coplanar Turbo-FSK are set to $R_p = 1$ and $\lambda = 3$, and X mapping is selected.

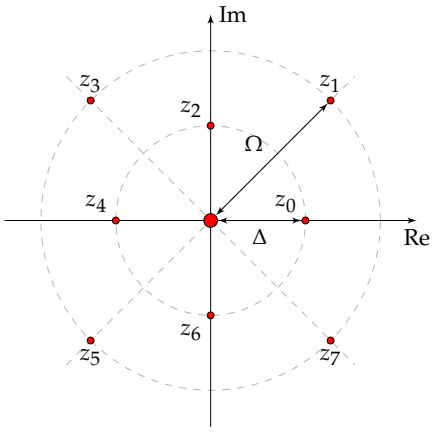

FIGURE 3.15 – *Projection on the δ-th orthogonal dimension with $N_L = 8$ and APSK modulation.*

3.4.2.1 PARAMETRIZATION OF THE PROJECTION

As presented when describing the OCS modulation in Section 3.2, a useful representation is the projection of all the codewords on one of the orthogonal components (i.e. on one of the complex planes). Using the APSK modulation, the projection is depicted in Figure 3.15. The 8 points are distributed into 2 circles of radius Δ and Ω. The elements of the subsets are given by

$$z_p = \begin{cases} \Delta \exp\left\{-j\frac{\pi}{4}p\right\} & \text{if } p \text{ even} \\ \Omega \exp\left\{-j\frac{\pi}{4}p\right\} & \text{if } p \text{ odd} \end{cases}. \tag{3.20}$$

The parameter Ω can be expressed as a function of Δ using the normalization condition

$$\begin{aligned} & \frac{\Delta^2 + \Omega^2}{2} = 1 \\ \Leftrightarrow \quad & \Omega = \sqrt{2 - \Delta^2}. \end{aligned} \tag{3.21}$$

Changing the value of Δ thus modifies the position of the 8 points. The value $\Delta = 1$ (which gives $\Omega = 1$) corresponds to the standard 8-PSK modulation. Unlike the PSK modulation, the APSK is not a constant envelope modulation due to the possible variations in amplitude. The PAPR of the modulation is given by

$$\text{PAPR}(\Delta) = \max(\Delta, \Omega) = \max_{\Delta}\left(\Delta, \sqrt{2 - \Delta^2}\right). \tag{3.22}$$

The evolution of both Ω and the PAPR with the value of Δ is depicted in Figure 3.16. This representation illustrates the loss in PAPR induced by the modification of the modulation's parameter Δ.

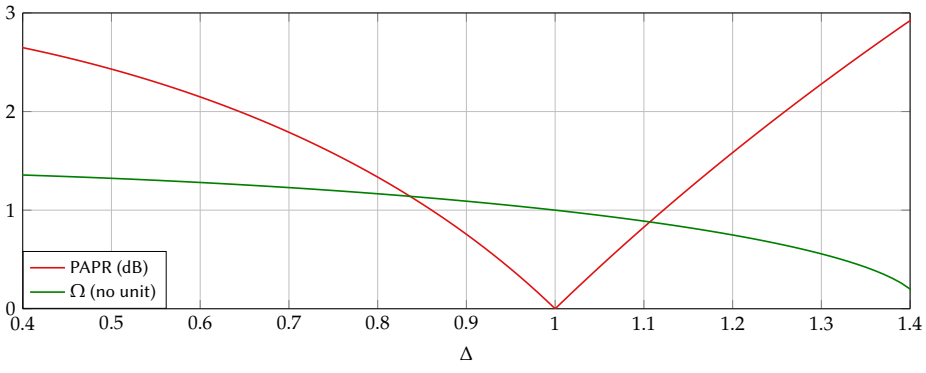

FIGURE 3.16 – *PAPR (in dB) and Ω depending on the value of Δ for the APSK modulation as parametrized in Figure 3.15.*

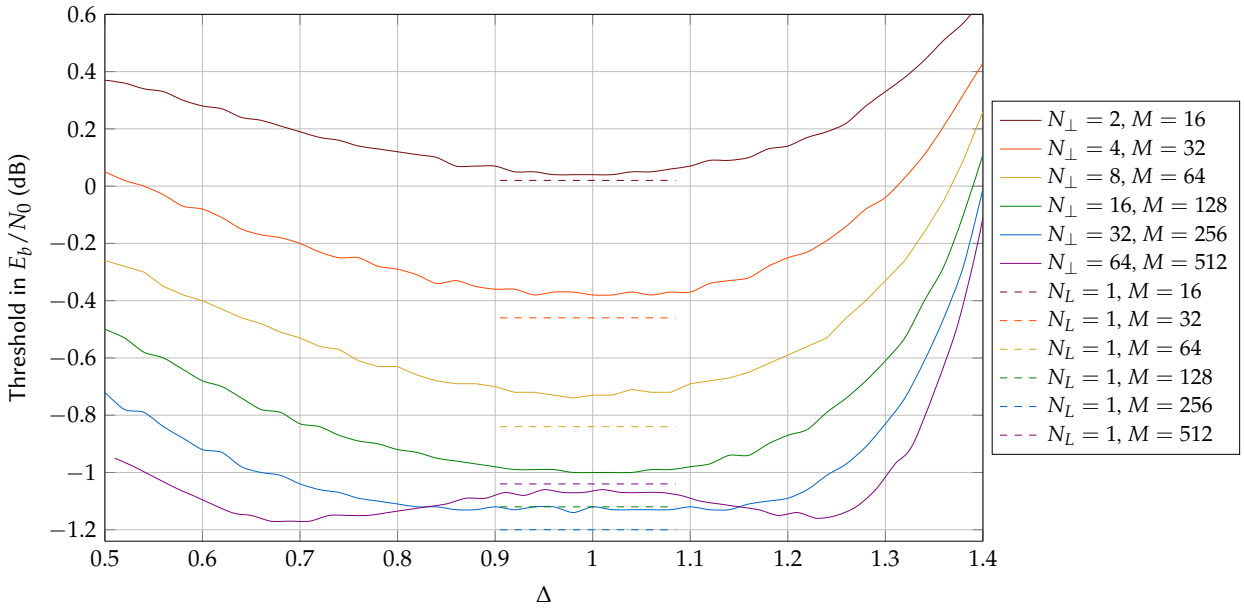

FIGURE 3.17 – *Thresholds for various values of the constellation parameter* Δ*, using different sizes of alphabet* M *(always with* $N_L = 8$*) and* $\lambda = 4$*. X mapping is used and no puncturing is applied.*

3.4.2.2 Optimization of the Modulation Parameter

The way the linear modulation was designed, distances in the alphabet are modified according to the value of Δ. In order to evaluate the influence of this parameter when considering Coplanar Turbo-FSK, the thresholds of the scheme using various parameters are estimated using the EXIT chart tool. The Coplanar Turbo-FSK scheme with parameter $\lambda = 4$ is selected. Values of Δ spanning from 0.5 to 1.4 and alphabet sizes from $M = 16$ to 512 are tested, and the thresholds are depicted on Figure 3.17. The thresholds for the orthogonal Turbo-FSK (equivalent to $N_L = 1$) are also depicted in dashed lines. As expected, modifying the value of Δ changes the threshold of the system. It appears that the value $\Delta = 1$ (i.e. the 8-PSK) shows the lowest threshold for the majority of alphabet sizes, from 16 to 256. However, for $M = 512$, setting the parameter to $\Delta = 0.69$ gives a threshold equal to −1.17dB, i.e. 0.13dB lower than the threshold of the Turbo-FSK for the same size of alphabet. The optimum form for the modulation is no longer the 8-PSK. The projection on one of the orthogonal components for the value $\Delta = 0.69$ is represented in Figure 3.15.

In order to validate these results, BER simulations are performed under AWGN channel, with an interleaver size $Q = 100\,000$ and 100 decoding iterations. Three cases are considered: Turbo-FSK with $M = 512$, and Coplanar

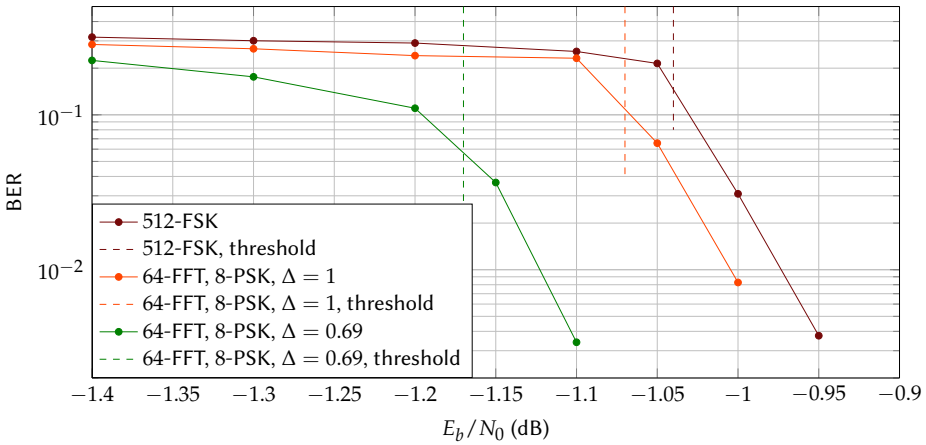

FIGURE 3.18 – *BER performance under the AWGN channel versus* E_b/N_0 *for the configuration* $M = 512$*,* $\lambda = 4$*,* $R_p = 1$ *and X mapping. Two configurations of* N_L *and* N_L *are compared:* $N_\perp = 512$ *and* $N_L = 1$ *(i.e. Turbo-FSK) and* $N_\perp = 16$ *and* $N_L = 8$*. For this last configuration, the constellation parameter is set to* $\Delta = 1$ *or* $\Delta = 0.69$*. The information block size is set to* $Q = 100\,000$ *and* 100 *decoding iterations are performed.*

Turbo-FSK with $N_\perp = 64$, $N_L = 8$ and $\Delta = 1$ (i.e. 8-PSK) or $\Delta = 0.69$. The result is depicted in Figure 3.18, along with the estimated thresholds. As we wish to validate the prediction of the thresholds, the simulation are performed for moderately high BER levels. The BER curve converges towards the value predicted by the EXIT charts. Compared to the threshold analysis, an equivalent gain is achieved in BER, demonstrating once again that Coplanar Turbo-FSK with APSK and the indicated parameters has the potential to outperform the Turbo-FSK scheme.

If some performance improvement is observed when using 8-APSK with parameter $\Delta = 0.69$ in the Coplanar Turbo-FSK for the configuration $N_\perp = 64$ and $\lambda = 4$, this effect is not present for other values of $N_\perp$. Moreover, it should be considered that the constant envelope property is lost when selecting a value of Δ different from 1. For example, setting $\Delta = 0.69$ induces a PAPR equal to 1.83dB according to Equation (3.22).

3.4.3 Influence of Puncturing

When proposing the Coplanar Turbo-FSK, a puncturing mechanism has been introduced to fulfill the flexibility required by wireless systems. Unlike classical coding schemes where puncturing is done at the bit level, we have demonstrated that in the case of Coplanar Turbo-FSK, puncturing has to be performed on binary words, as they are associated to a non-binary non-systematic waveform in the modulation process. Overall, the puncturing mechanism reduces the number of transmitted symbols. At the receiver, these punctured codewords are considered unknown and the likelihood of all the codewords from the alphabet is equal. Entire sections of the trellis are unknown. While a gain in spectral efficiency is achieved, the receiver has less information from the channel to work with. Using puncturing usually has a negative impact on the performance. The case $N_\perp = 16$ and $N_L = 8$ is selected. Using the parameter $\lambda = 4$ and a X mapping, 5 different puncturing patterns are simulated, for which the parameters are given

R_p	R_p^0	R_p^1	R_p^2	R_p^3	G	η $(\cdot 10^{-1})$
1	1	1	1	1	N/A	0.932
4/3	1	3/2	3/2	3/2	3	1.24
3/2	1	3/2	3/2	3	3	1.40
8/5	1	2	2	2	2	1.49
12/7	1	3/2	3	3	3	1.60
2	1	3	3	3	3	1.86

Table 3.3 – *Parameters of the different puncturing patterns tested. R_p is the global puncturing rate and R_p^ℓ, with $\ell \in \{0, \ldots, \lambda - 1\}$, the puncturing rate of stage ℓ. G is the parameter of the interleaver matrix, and η is the spectral efficiency, expressed in bits$\cdot s^{-1} \cdot Hz^{-1}$. The other parameters are set to $N_\perp = 16$, $N_L = 8$ and $\lambda = 4$.*

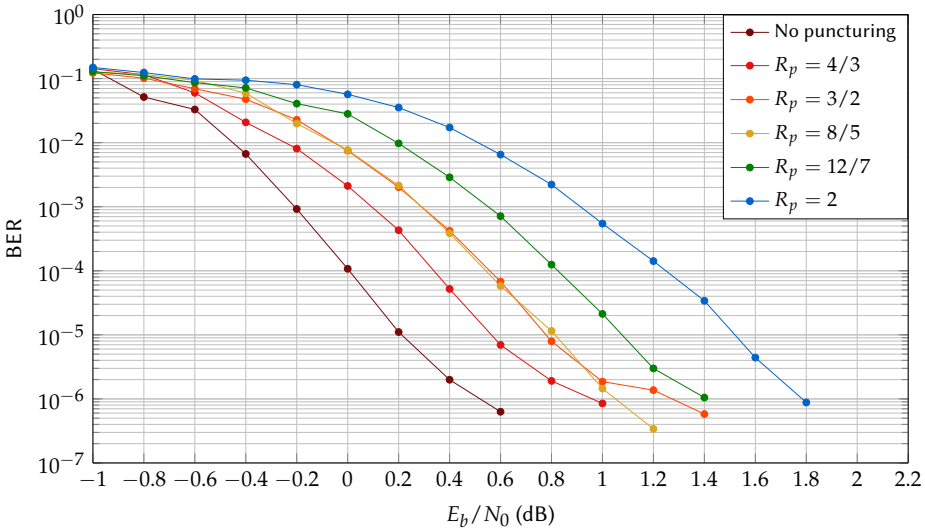

Figure 3.19 – *BER performance under the AWGN channel versus E_b/N_0 of Coplanar Turbo-FSK with the configuration $N_\perp = 16$, $N_L = 8$, $\lambda = 4$, X mapping and various puncturing rates. The spectral efficiency without puncturing is equal to $9.32 \cdot 10^{-2}$, and for punctured cases the spectral efficiencies are given in Table 3.3. The interleaver size is set to $Q = 1000$ and 10 decoder iterations are performed.*

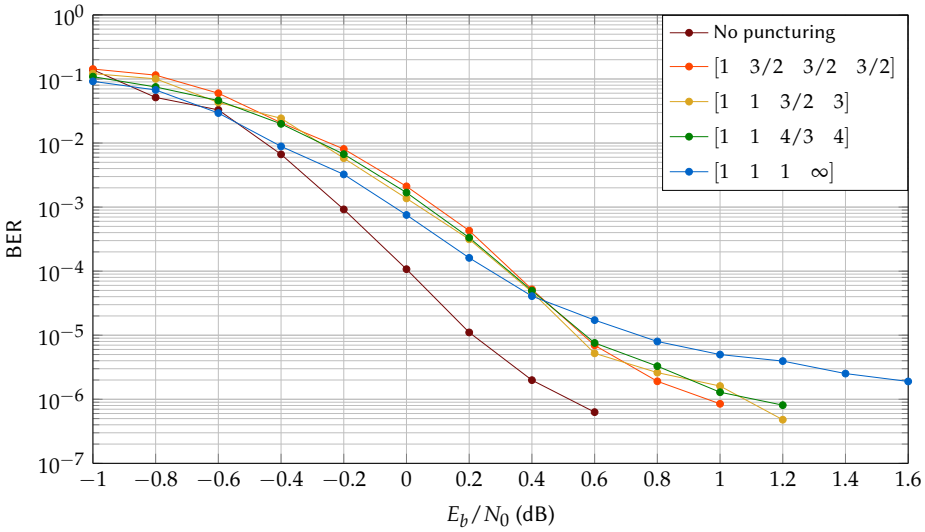

FIGURE 3.20 – *BER performance under the AWGN channel versus E_b/N_0 of Coplanar Turbo-FSK with the configuration $N_\perp = 16$, $N_L = 8$, $\lambda = 4$, X mapping and a puncturing rate of $R_p = 4/3$. The spectral efficiency without puncturing is equal to $9.32 \cdot 10^{-2}$ while the spectral efficiency with puncturing is equal to $1.24 \cdot 10^{-1}$. The interleaver size is set to $Q = 1000$ and 10 decoder iterations are performed.*

in Table 3.3. Puncturing rates spanning from 4/3 to 2 are considered, as well as cases where the puncturing rate of the different branches is equal or varies. The BER performance with $Q = 1000$ is depicted in Figure 3.19. As expected, increasing the puncturing rate induces a loss in performance, at the benefit of a gain in spectral efficiency (which is given, for each case, in Table 3.3). For the case $R_p = 2$ and $Q = 1000$, only 334 codewords are transmitted instead of 668 for the case without puncturing. The spectral efficiency is multiplied by 2 at the expense of a performance loss of 1.3dB for a BER of 10^{-5}. The cases $R_p = 3/2$ and $R_p = 8/5$ give the same performance, even though the puncturing rates are different. For the case $R_p = 8/5$, branches puncturing rates are all equal while the $R_p = 3/2$ uses two different puncturing rates on the branches.

In order to study the influence of the choice of puncturing rate on each branch, we select the case $R_p = 4/3$. Four combinations of branches puncturing rates are selected, and the BER performance is depicted in Figure 3.20. The combinations are given in the form $[R_p^0\ R_p^1\ R_p^2\ R_p^3]$. $G = 3$ for all cases except the case [1 1 4/3 4] where $G = 4$. For the case [1 1 1 ∞], the last branch is not sent. This case corresponds to $\lambda = 3$, as the last branch does not give any information. The other cases with various puncturing rates give rather similar performance, only a small performance gain is achieved when selecting irregular puncturing. However, these cases benefit from the error floor of the case $\lambda = 4$, which is lower than the error floor of the case $\lambda = 3$. This means that only by adding some codewords of one branch, the error floor can be reduced.

In order to emphasize this effect, the Packet Error Rate (PER) performance for the case $\lambda = 3$ without puncturing and the case $\lambda = 4$ with $R_p = 4/3$ is depicted in Figure 3.21. These two configurations have the same spectral efficiency and are thus comparable in Signal-to-Noise Ratio (SNR). The PER performance of the case $\lambda = 4$ without puncturing and the case $\lambda = 5$ with $R_p = 5/4$ (with $R_p^\ell = 4/3$ and $G = 4$) are also represented in the figure. These two configurations also have the same spectral efficiency, equal to $\eta = 9.319 \cdot 10^{-2}$. For both cases, using a value of λ with puncturing gives performance close to the case $\lambda - 1$ without puncturing, but the error floor is significantly reduced. When considering the error floor, it is thus more interesting to use puncturing than reducing the value of λ to achieve higher levels of spectral efficiencies. However, complexity is increased; when considering a receiver with λ instead of $\lambda - 1$ branches, this implies the execution an additional trellis decoding.

Puncturing is very often used to increase the spectral efficiency or the coding rate. For the Coplanar Turbo-FSK scheme, the puncturing procedure introduced has the expected effect. The spectral efficiency is increased, at the expense of some performance loss. However, this loss can be acceptable depending on the requirements of spectral efficiency versus energy efficiency. Monte Carlo simulations on particular configurations have highlighted that a lower error floor is achieved by puncturing a scheme with $\lambda + 1$ stages instead of considering a scheme with λ stages and without puncturing. Both schemes have the same spectral efficiency but have different error floor. This is nonetheless done at the expense of the complexity increase, as the receiver needs to compute the BCJR algorithm for the λ branches.

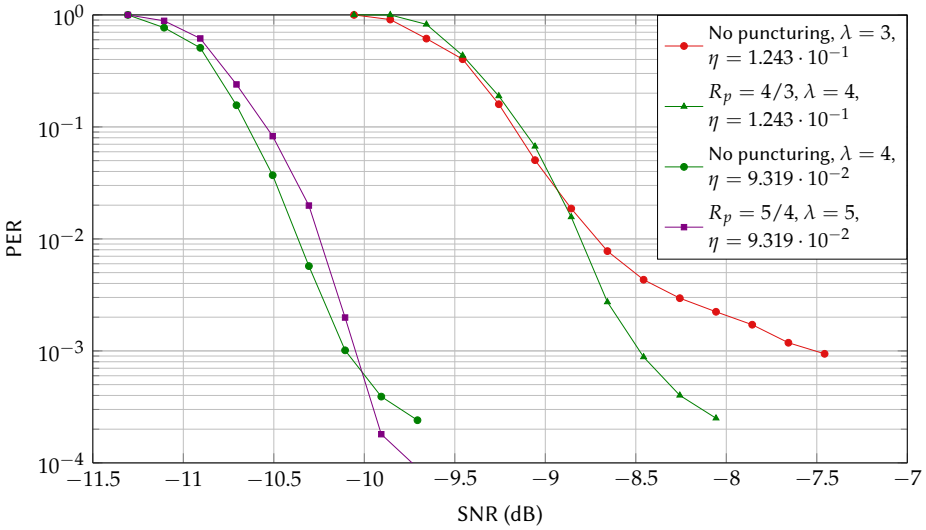

FIGURE 3.21 – *PER performance under the AWGN channel versus the SNR of Coplanar Turbo-FSK with the configuration* $N_\perp = 16$, $N_L = 8$ *and X mapping with two different values for* λ*, with and without puncturing. The interleaver size is set to* $Q = 1000$ *and* 10 *decoder iterations are performed.*

3.4.4 PERFORMANCE VERSUS THE CHANNEL CAPACITY

In the previous chapter, the various configurations of the Turbo-FSK have been compared to the maximum achievable spectral efficiency, as defined by Shannon's limit. As the number of configurations for Coplanar Turbo-FSK is very large, the same representation would be difficult to read. In order to confront the scheme with the information theory's limit, only two sizes of alphabet M are considered: 128 and 512. For each size, the parameter λ that leads to the best threshold for the Turbo-FSK case (the thresholds are given in the Table 2.1) is selected. Then, starting from $N_\perp = M$ and $N_L = 1$, the thresholds for all the possible values for $N_\perp$ and N_L are evaluated. Each configuration has a different spectral efficiency, which is computed using Equation (3.12). No puncturing is considered (i.e. $R_p = 1$). The N_L-PSK linear modulation is used, FSK modulation is selected for orthogonal modulation and X mapping is chosen. The value of the thresholds in E_b/N_0 versus the configurations' spectral efficiencies are depicted in Figure 3.22, along with the maximum achievable spectral efficiency according to the channel capacity, computed using (1.15), and the threshold of the [13 15] TC with Binary Phase Shift Keying (BPSK) modulation. For each point, the parameter couple $(N_\perp, N_L)$ is labeled. For example, the point labeled $(8, 64)$ for the curve $M = 512$ and $\lambda = 3$ corresponds to $N_\perp = 8$ and $N_L = 64$.

For both sizes of alphabet, the effect of increasing the size of the linear modulation (i.e. decreasing the number

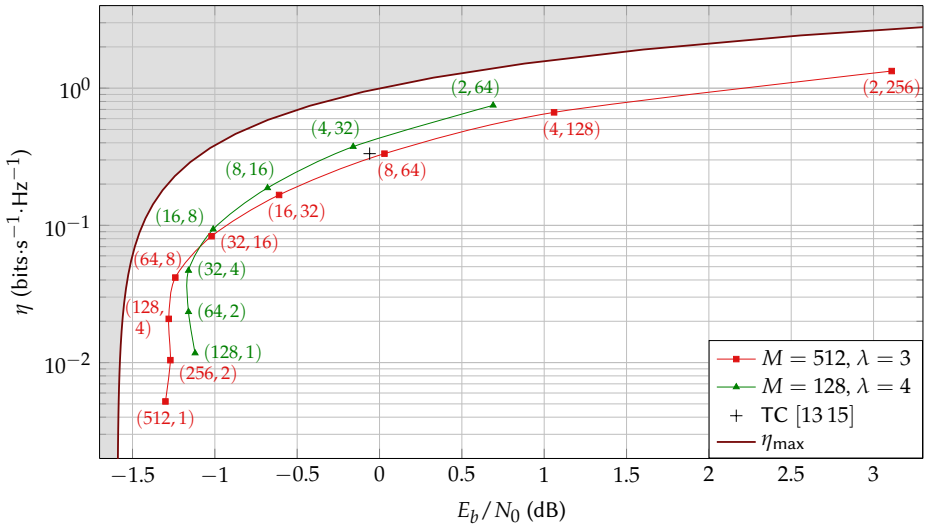

FIGURE 3.22 – *Spectral efficiency versus threshold for various sizes of alphabet* M *and parameter* λ*, using various combinations of* $(N_\perp, N_L)$*. The spectral efficiency is computed with* (3.12)*. The maximum achievable spectral efficiency according to the channel capacity is computed using* (1.15)*. A X mapping was selected, without any puncturing (i.e.* $R_p = 1$*).*

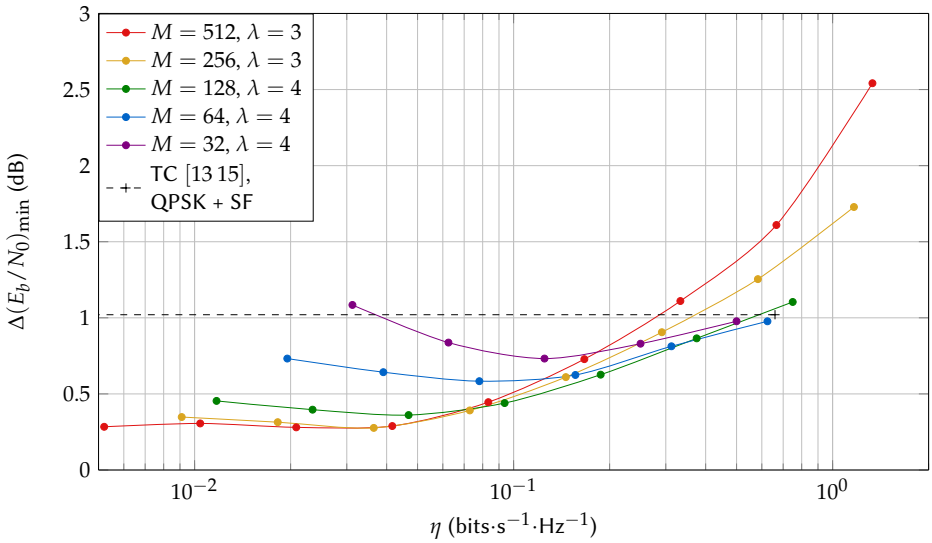

FIGURE 3.23 – *Difference between the threshold in E_b/N_0 and the $(E_b/N_0)_{\min}$ for the configuration's spectral efficiency computed with* (1.16)*, versus the spectral efficiency, for various sizes of alphabet M and values of λ. No puncturing is applied and a X mapping is selected. For each curve, the left-most point corresponds to $N_\perp = M$, $N_L = 1$ and the right-most point corresponds to $N_\perp = 2$, $N_L = M/2$.*

of orthogonal subsets) also increases the spectral efficiency. Up to a certain value, the impact on the threshold is very limited, an effect previously observed. The minimum distance in the trellis is maintained, and the performance depends on the choice of mapping (for all configurations, the X mapping described in Section 3.4.1 is selected). When $N_L \geq 8$, this minimum distance starts to decrease, with a negative effect on the threshold level.

The threshold of the [13 15] TC is depicted in Figure 3.22. This is the channel code used in the NB-IoT approach for LPWA solutions. With BPSK modulation, this scheme has a threshold of -0.06dB for a spectral efficiency of $1/3$. As shown in the figure, the performance of the TC can be closely approached using different configurations. Also, in the case of the NB-IoT approach, a Spreading Factor (SF) is used to reduce the spectral efficiency. While using the Coplanar Turbo-FSK scheme, spectral efficiency can be reduced by selecting a different configuration, which will additionally lead to a gain in energy efficiency, unlike using a SF which does not allow for an energy efficiency gain.

These results clearly demonstrate how the Coplanar Turbo-FSK scheme allows for a gain in spectral efficiency while having thresholds close to the minimum achievable E_b/N_0. Thanks to the introduction of a linear modulation, spectral efficiencies up to $4/3$ ($N_\perp = 2$, $N_L = 256$ and $\lambda = 3$) can be achieved. However, this comes with a significant performance loss compared to the Turbo-FSK with the same size of alphabet (4.41dB for the same configuration). Spectral efficiency can also be increased by using puncturing (at the expense of more performance loss).

In order to observe the difference between the performance and the $(E_b/N_0)_{\min}$ given by the information theory, the value

$$\Delta(E_b/N_0)_{\min} = \frac{E_b}{N_0} - \left(\frac{E_b}{N_0}\right)_{\min} \tag{3.23}$$

is computed for each configuration, where E_b/N_0 is the threshold and $(E_b/N_0)_{\min}$ the minimum achievable E_b/N_0 for the spectral efficiency of the considered configuration. All three values expressed in dB. 5 sizes of alphabet are selected, from 512 to 32, and the parameter λ is equal to 3 or 4. The difference between the minimum achievable E_b/N_0 is depicted versus the spectral efficiency in Figure 3.23, along with the performance of the TC [13 15] using Quadrature Phase Shift Keying (QPSK) modulation and a SF. For each curve, the left-most point corresponds to the configuration $N_\perp = M$ while the right-most point corresponds to $N_\perp = 2$. Large sizes of alphabet are required for the scheme to be close to the minimum achievable E_b/N_0 (as it was observed for the Turbo-FSK case). However, when increasing the spectral efficiency, having a large alphabet increases the gap to the $(E_b/N_0)_{\min}$. This is because the size of the non-energy efficient linear modulation becomes large. For higher spectral efficiencies, lower orders of alphabet sizes must be considered, as they can even outperform the TC chosen here. For example, the configuration $N_\perp = 4$, $N_L = 32$, $\lambda = 4$ (hence $M = 128$, depicted in green in the figure) has a spectral efficiency equal to $3/8 = 0.375$ and is 0.16dB closer to the minimum E_b/N_0 compared to the TC.

These results demonstrate once more how the introduction of a linear component in the alphabet allows for a high flexibility in spectral efficiency, with a reasonable loss in E_b/N_0.

3.5 Conclusion

The Turbo-FSK scheme shows promising performance for LPWA network applications. However, the existing solutions (notably the NB-IoT) usually allow for a large spectral efficiency flexibility, which can be useful in adapting the data rate of the Physical (PHY) layer to the rate required for the considered application. With this perspective, two main features have been considered for the design of Coplanar Turbo-FSK: the use of puncturing, a common technique in channel coding which enables higher coding rate, and the introduction of a linear component in the alphabet's design. The puncturing allows for a gain in spectral efficiency at the expense of some performance loss. Puncturing can also be used to lower the error floor, with an increase in complexity at the receiver side. The introduction of linear modulations can be interpreted as a loss of orthogonality in the trellis. The choice of mapping impacts the performance, as the distances between codewords and transitions are modified. With these two new technical features, the Coplanar Turbo-FSK scheme can reach two decades of spectral efficiency while staying close to the minimum achievable E_b/N_0. The study of the 5 main parameters of the scheme consisted in evaluating the performance regarding the variations of one or several of the parameters. A joint optimization with all the parameters could be considered, but would require an inconceivable amount of processing power because of the very large amount of configurations to be tested. Optimization of the interleaving function could also be considered and may lead to some performance improvement. Also, while FSK modulation was selected to construct the orthogonal part of the alphabet of Coplanar Turbo-FSK, any other orthogonal modulation could be selected (such as PPM, Hadamard codes, etc).

Both Turbo-FSK and Coplanar Turbo-FSK have been extensively studied, but mostly from a theoretical approach. Only the AWGN channel was considered. For a more practical approach, performance has to be assessed using more realistic channel models. Also, parametrization of the waveform has to be discussed with regard to various criteria such as the available bandwidth, the propagation channel coherence bandwidth, robustness to Radio Frequency (RF) impairments like Carrier Frequency Offset (CFO), etc. The goal of the last chapter will be to give some directions in the design of a realistic system, while taking into account practical constraints.

The results presented in this chapter led to the preparation of an article to be submitted [87], and the Coplanar Turbo-FSK technology has been patented [88].

Chapter Summary

In this chapter, Turbo-FSK has been extended to the Coplanar Turbo-FSK scheme. The alphabet construction using OCS modulation, which combines orthogonal and linear modulations, was described and examples were presented. The Coplanar Turbo-FSK scheme was then detailed, including the specific puncturing procedure used at the transmitter side and the architecture of the receiver. Performance of the scheme was then assessed. The impact of the mapping on the trellis was studied, the shape of the linear modulation was optimized, the performance loss due to puncturing was estimated and the various configurations of the scheme were compared to the maximum achievable spectral efficiency computed from the Shannon's limit.

Bibliography of Chapter 3

[58] *LTE Evolved Universal Terrestrial Radio Access (E-UTRA): Multiplexing and Channel Coding*. 3GPP TS 36.212, V12.6.0, Release 12. 2015.

[87] Y. Roth, J.-B. Doré, L. Ros, and V. Berg. "Coplanar Turbo-FSK: A Flexible and Power Efficient Modulation for the Internet-of-Thing". In: *To be submitted* (2017).

[88] Y. Roth, J.-B. Doré, L. Ros, and V. Berg. "Transmission/Reception System Based on the Use of a Joint Orthogonal and Linear Modulation". Patent EUR. 2017.

CHAPTER 4

Application to Low Power Wide Area Networks

Chapter contents

The comparison of the Coplanar Turbo-FSK scheme considering multiple scenarios is investigated. A Fast Fourier Transform (FFT)-based system is designed, and commonly used waveforms are compared. Complexity and Peak to Average Power Ratio (PAPR) at the transmitter side are considered, as these aspects are critical for Low Power Wide Area (LPWA) systems. Performance under frequency-selective channels, with static or mobility conditions, is assessed.

4.1 Motivations

In the previous chapters, the Turbo-FSK scheme has been designed to address the issues related to the LPWA context. The scheme was optimized regarding its performance. As the context includes various applications with different requirements and since higher levels of sensitivity may be tolerated, flexibility in spectral efficiency has been introduced. The Coplanar Turbo-FSK enables large ranges of spectral efficiencies, and offers performance in E_b/N_0 close to Shannon's limit. The studies have been done following a theoretical approach. First, Maximum *A Posteriori* (MAP) receivers without approximation were derived. This assumption implies the use of multiple computations of exponential functions and products, which are cumbersome features in practical systems. Second, only the Additive White Gaussian Noise (AWGN) channel was considered.

When transiting through the transmission channel, a signal may be reflected off various elements. Delayed copies of the transmitted signal are received, each of which experience various effects in phase and amplitude. This multipath propagation model is very often considered for wireless communications, and induces Inter-Symbol Interference (ISI). It also leads to fading effects. The recombination of the various paths may lead to severe losses or high gains depending on the frequency. This type of channel is said to be frequency selective, and its effects are overcome with the use of a well-known technology, Orthogonal Frequency Division Multiplexing (OFDM) [89, 90, 91]. In addition to the introduction of a Cyclic Prefix (CP) to avoid ISI, frequency multiplexing simplifies the equalization procedure required to compensate the channel impact [92]. The system allows for better practical performance than single carrier modulation under this type of channel. The modulation is very sensitive to Carrier Frequency Offset (CFO), as it deteriorates the orthogonality between the carriers and induces Inter-Carrier Interference (ICI) [93]. However, the main drawback of OFDM is that the signal exhibits a high PAPR [94, 95]. Multiplexing is done by performing a summation of several modulated symbols. The resultant power might be equal to the sum of the powers of all transmitted symbols. The output power may exhibit large variations.

In this chapter, a more practical approach is considered for the Turbo-FSK scheme. In this perspective, we wish to study the performance of the scheme under frequency selective channels, and to evaluate other indicators, such as the complexity and the impact of the modulation on the PAPR. These aspects have not been studied yet and represent critical elements for low power devices. In order to develop a more practical implementation of the scheme, approximations of the MAP algorithm will be used and a FFT-based system is considered. The architecture is very close to typical OFDM systems and allows for comparisons with state of the art techniques such as Single Carrier Frequency Division Multiple Access (SC-FDMA). Moreover, the Narrow-Band IoT (NB-IoT) solution presented in Chapter 1, designed to be compatible with the Long Term Evolution (LTE) network, relies on the use of an OFDM architecture [56]. Comparisons with this potential LPWA solution will be straightforward.

4.2 System Model

This section is dedicated to the presentation of all the schemes that will be used for comparison versus the previously introduced Turbo-FSK scheme (in its flexible version). Three schemes are considered: OFDM modulation, where Quadrature Phase Shift Keying (QPSK) symbols are mapped on the used carriers, SC-FDMA, where a precoding is applied and Frequency Shift Keying (FSK) modulation. The use of the Turbo Code (TC) [13 15] as channel coding is considered. Each scheme is integrated into the FFT-based system, in order to fit the context of OFDM waveform framework. Frequency selective channels are considered. The computation of the Log Likelihood Ratio (LLR) from the channel is presented.

Two schemes based on the Turbo-FSK principle are considered. The first scheme is standard Turbo-FSK, or Coplanar Turbo-FSK when a linear modulation is introduced. For the second scheme, a different orthogonal alphabet is selected. We choose an alphabet based on Zadoff-Chu (ZC) sequences, a type of Constant Amplitude Zero Auto-Correlation (CAZAC) sequence. Constructed in the frequency domain, the sequence keeps its property of zero-autocorrelation, but unlike FSK signaling, energy is sent at every frequency. This is thus a type of spread spectrum modulation, and its use associated with the Turbo-FSK principle is referred to as the Coplanar Turbo-ZC. Both schemes Turbo-FSK and Turbo-ZC require the likelihood of the codewords to be used as the metric for the Bahl,

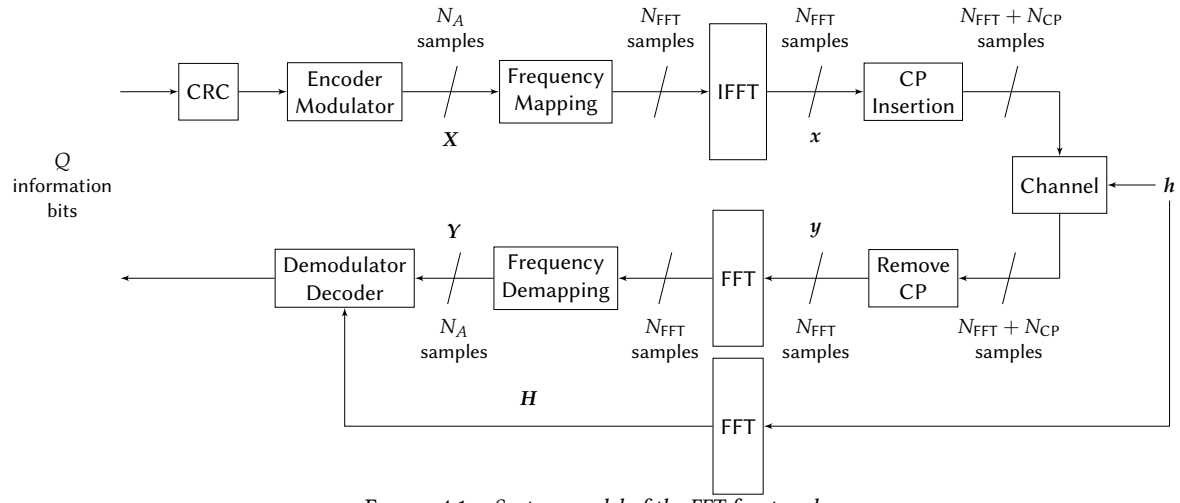

FIGURE 4.1 – *System model of the FFT front-end.*

Cocke, Jelinek and Raviv (BCJR) algorithm. For these schemes, there is no need to compute the LLR, only the likelihood of the codewords needs to be fed to the decoder.

After introducing the FFT-based system, each technique is described. For each one, the structure of the transmitter and the receiver is reviewed and the computation of the LLR (or the likelihood) is derived.

4.2.1 FFT-based System

In this FFT-based system, the signal is constructed in the frequency domain in order to map the N_{FFT} available carrier frequencies (with potentially 0 on specific frequencies). The transmitter is described, and without any consideration of the technique used, the likelihood of a sequence is computed. The result will be used in further sections to derive the LLR computation of the considered schemes. The receiver is also presented, along with the values of the parameters considered for the simulations.

4.2.1.1 Transmitter

The FFT-based system is depicted in Figure 4.1. From the information packet of size Q, a Cyclic Redundancy Check (CRC) of length 16 bits is computed and appended to the information block, so that the receiver can detect errors in the packet. Encoding and modulation steps are then performed; these steps depend on the choice of the technique, which are further presented. The output of this block is represented by a matrix of size $N_A \times N_s$, where N_A is the number of active frequencies and N_s the number of time slots (or OFDM symbols). This is the time-frequency allocation which is then included in the FFT grid of size $N_{FFT} \times N_s$. Inverse Discrete Fourier Transform (IDFT) of size N_{FFT} is then applied to convert the frequency signal into a time signal consisting of $N_{FFT} \times N_s$ samples (or chips). The efficient Inverse Fast Fourier Transform (IFFT) algorithm is used to perform the IDFT. Considering the vector $\boldsymbol{X}$ of length N_{FFT}, the signal $\boldsymbol{x}$ is given by

$$x(k) = \frac{1}{N_{FFT}} \sum_{n=0}^{N_{FFT}-1} X(n) e^{j2\pi \frac{kn}{N_{FFT}}}, \tag{4.1}$$

which is the IDFT of the vector $\boldsymbol{X}$. A CP of length N_{CP} consisting of the last N_{CP} samples of each OFDM symbol is then appended at the beginning of each symbol.

4.2.1.2 Channel

The signal then transits through the channel as depicted in Figure 1.5. The use of a CP avoids ISI between two successive symbols and allows the effect of the channel to be expressed by a circular convolution when the size of the CP is greater than the channel delay spread. The multi-path channel is modelled by a discrete-time domain representation i.e. a Finite Impulse Response (FIR) filter applied at chip-time. The useful signal (without CP) at index k is given by

$$y(k) = \sum_{l=0}^{L_{ch}-1} h(l) x(k-l) + \nu(k), \tag{4.2}$$

where $\boldsymbol{h}$ is the channel impulse response, a complex vector with L_{ch} elements, representing the gain of each possible paths. The elements ν_k of the noise vector $\boldsymbol{\nu}$ follow a circularly-symmetric and zero mean complex normal distribution. The circular convolution assumption can only be considered if $N_{\text{CP}} \geq L_{\text{ch}}$, i.e. if the delays of the previous OFDM symbols only affect the CP of the current symbol and not its useful part.

4.2.1.3 Likelihood of a Sequence

In order to compute the LLR of the transmitted bits for each technique, we wish to derive the likelihood of observing a sequence $\boldsymbol{y}$ given that a sequence $\boldsymbol{x}$ was transmitted. A generic form for the sequence transmitted is considered, and simplifications will occur further when considering specific modulation techniques. The likelihood of observing a sequence $\boldsymbol{y}$ given that a sequence $\boldsymbol{x}$ was transmitted is given by

$$p\left(\boldsymbol{y} \mid \boldsymbol{x}\right) = \prod_{k=0}^{N_{\text{FFT}}-1} p\left(y(k) \mid x(k)\right). \tag{4.3}$$

Assuming a normal distribution with variance σ_{ch}^2 for the noise, elements of the product are expressed as

$$\begin{aligned} p\left(y(k) \mid x(k)\right) &= \frac{1}{2\pi\sigma_{\text{ch}}^2} \exp\left\{ -\frac{1}{2\sigma_{\text{ch}}^2} \left\| y(k) - \sum_{l=0}^{L_{\text{ch}}-1} h(l)x(k-l) \right\|^2 \right\} \\ &= \frac{1}{2\pi\sigma_{\text{ch}}^2} \exp\left\{ -\frac{\|y(k)\|^2}{2\sigma_{\text{ch}}^2} - \frac{1}{2\sigma_{\text{ch}}^2} \left\| \sum_{l=0}^{L_{\text{ch}}-1} h(l)x(k-l) \right\|^2 + \frac{1}{\sigma_{\text{ch}}^2} \left\langle y(k), \sum_{l=0}^{L_{\text{ch}}-1} h(l)x(k-l) \right\rangle \right\}, \end{aligned} \tag{4.4}$$

hence

$$\begin{aligned} p\left(\boldsymbol{y} \mid \boldsymbol{x}\right) = \left(\frac{1}{2\pi\sigma_{\text{ch}}^2}\right)^{N_{\text{FFT}}} \exp\left\{ -\sum_{k=0}^{N_{\text{FFT}}-1} \frac{\|y(k)\|^2}{2\sigma_{\text{ch}}^2} - \frac{1}{2\sigma_{\text{ch}}^2} \sum_{k=0}^{N_{\text{FFT}}-1} \left\| \sum_{l=0}^{L_{\text{ch}}-1} h(l)x(k-l) \right\|^2 \right. \\ \left. + \frac{1}{\sigma_{\text{ch}}^2} \sum_{k=0}^{N_{\text{FFT}}-1} \left\langle y(k), \sum_{l=0}^{L_{\text{ch}}-1} h(l)x(k-l) \right\rangle \right\}. \end{aligned} \tag{4.5}$$

The first term in the exponential is independent of $\boldsymbol{x}$ and can be considered as a constant. In order to simplify the expression of the likelihood, we derive the expression of the other two sums. The second sum can be expressed as

$$\begin{aligned} \sum_{k=0}^{N_{\text{FFT}}-1} \left\| \sum_{l=0}^{L_{\text{ch}}-1} h(l)x(k-l) \right\|^2 &= \sum_{k=0}^{N_{\text{FFT}}-1} \left\| \sum_{l=0}^{L_{\text{ch}}-1} h(l) \cdot \frac{1}{N_{\text{FFT}}} \sum_{n=0}^{N_{\text{FFT}}-1} X(n) e^{j2\pi \frac{n}{N_{\text{FFT}}}(k-l)} \right\|^2 \\ &= \frac{1}{N_{\text{FFT}}^2} \sum_{k=0}^{N_{\text{FFT}}-1} \left\| \sum_{n=0}^{N_{\text{FFT}}-1} X(n) \left(\sum_{l=0}^{L_{\text{ch}}-1} h(l) e^{-j2\pi \frac{ln}{N_{\text{FFT}}}} \right) e^{j2\pi \frac{nk}{N_{\text{FFT}}}} \right\|^2 \\ &= \frac{1}{N_{\text{FFT}}^2} \sum_{k=0}^{N_{\text{FFT}}-1} \left\| \sum_{n=0}^{N_{\text{FFT}}-1} X(n)H(n) e^{j2\pi \frac{nk}{N_{\text{FFT}}}} \right\|^2, \end{aligned} \tag{4.6}$$

where $H(n)$ is the n-th dimension of the Discrete Fourier Transform (DFT) of size N_{FFT} of the channel coefficients vector $\boldsymbol{h}$.

The third sum of Equation (4.5) can be expressed as

$$\begin{aligned}\sum_{k=0}^{N_{\text{FFT}}-1}\left\langle y(k),\sum_{l=0}^{L_{\text{ch}}-1}h(l)x(k-l)\right\rangle &= \text{Re}\left(\sum_{k=0}^{N_{\text{FFT}}-1}y(k)\sum_{l=0}^{L_{\text{ch}}-1}\overline{h(l)x(k-l)}\right)\\ &= \text{Re}\left(\sum_{k=0}^{N_{\text{FFT}}-1}y(k)\sum_{l=0}^{L_{\text{ch}}-1}\overline{h(l)}\cdot\frac{1}{N_{\text{FFT}}}\sum_{n=0}^{N_{\text{FFT}}-1}\overline{X(n)}e^{-j2\pi\frac{n}{N_{\text{FFT}}}(k-l)}\right)\\ &= \frac{1}{N_{\text{FFT}}}\text{Re}\left(\sum_{n=0}^{N_{\text{FFT}}-1}\overline{X(n)}\sum_{l=0}^{L_{\text{ch}}-1}\overline{h(l)}e^{j2\pi\frac{ln}{N_{\text{FFT}}}}\sum_{k=0}^{N_{\text{FFT}}-1}y(k)e^{-j2\pi\frac{kn}{N_{\text{FFT}}}}\right)\\ &= \frac{1}{N_{\text{FFT}}}\text{Re}\left(\sum_{n=0}^{N_{\text{FFT}}-1}\overline{X(n)H(n)}Y(n)\right),\end{aligned} \tag{4.7}$$

where $Y(n)$ is the n-th dimension of the DFT of size N_{FFT} of the vector $\boldsymbol{y}$. Combining Equation (4.5) with (4.6) and (4.7), the likelihood of the sequence is expressed

$$p\left(\boldsymbol{y}\mid\boldsymbol{x}\right)=C_{\text{st}}\exp\left\{-\frac{1}{2\sigma_{\text{ch}}^2}\frac{1}{N_{\text{FFT}}^2}\sum_{k=0}^{N_{\text{FFT}}-1}\left\|\sum_{n=0}^{N_{\text{FFT}}-1}X(n)H(n)e^{j2\pi\frac{nk}{N_{\text{FFT}}}}\right\|^2+\frac{1}{\sigma_{\text{ch}}^2}\frac{1}{N_{\text{FFT}}}\text{Re}\left(\sum_{n=0}^{N_{\text{FFT}}-1}\overline{X(n)H(n)}Y(n)\right)\right\}. \tag{4.8}$$

This expression as it is does not allow for LLR computation or Maximum Likelihood (ML) decoding, as the form of $\boldsymbol{x}$ was purposely kept general. However, the expression demonstrates the necessity for the receiver to compute the DFT of the received time-vector $\boldsymbol{y}$ denoted by $\boldsymbol{Y}$, and to have knowledge of $\boldsymbol{H}$, the DFT of the channel coefficients.

The LLR expression of each technique will be derived starting from this last equation. The LLR of the bit b_m is given by

$$L(b_m)=\log\frac{p\left(\boldsymbol{y}\mid b_m=+1\right)}{p\left(\boldsymbol{y}\mid b_m=-1\right)}, \tag{4.9}$$

with $\boldsymbol{y}$ the received noisy sequence as expressed with Equation (4.2). The likelihood of the observation given that the bit b_m has a value equal to $u=\pm1$ is expressed

$$p\left(\boldsymbol{y}\mid b_m=u\right)=\sum_{i\in\mathcal{X}_u^m}p\left(\boldsymbol{y}\,\middle|\,\boldsymbol{x}^i\right), \tag{4.10}$$

where $\mathcal{X}_u^m$ the group of sequences $\boldsymbol{x}$ which encode an information word for which the bit b_m is equal to u. Depending on the choice of modulation, the number of elements of $\mathcal{X}_u^m$ will differ along with the expression of the sequence $\boldsymbol{x}$, and thus the expression of the likelihood (4.8).

4.2.1.4 Receiver

In order to retrieve the information that was mapped in the frequency domain at the transmitter side, a DFT of size N_{FFT} is applied on each OFDM symbol, using the FFT algorithm. The result is the vector $\boldsymbol{Y}$, the channel observation. By selecting only the N_A used frequencies, the N_s vectors of size N_A transmitted at the first place are retrieved. This signal is fed to the demodulator/decoder along with the DFT of the channel coefficients vector $\boldsymbol{h}$, denoted with $\boldsymbol{H}$. This vector can also be interpreted as the complex gain on each frequency. Using the channel observation and the vector $\boldsymbol{H}$, the block demodulator uses a simplified formulation of (4.8) to compute the LLR of the transmitted bits. The information bits are finally estimated by the decoder and the CRC is computed to evaluate if the packet contains any error.

4.2.1.5 Parameters

Various parameters' values can be selected for the size of the FFT, the length of the CP, etc. The typical values defined for the LTE standard are selected. The 6 available modes corresponding to 6 different sets of parameters are presented in Table 4.1. Considering the inter-carrier spacing to be equal to 15kHz, the value of N_A gives the bandwidth used by the signal as $B = N_A \times 15 \cdot 10^3$Hz. The size N_A must be less than the number of available carriers.

Bandwidth	20 MHz	15 MHz	10 MHz	5 MHz	3 MHz	1.4 MHz
Sampling Frequency (MHz)	30.72	23.04	15.36	7.68	3.84	1.92
FFT Size N_{FFT}	2048	1536	1024	512	256	128
Number of Available Sub-carriers	1200	900	600	300	180	72
Cyclic Prefix Size N_{CP}	144	108	72	36	18	9
Guard Band on Each Side (kHz)	1000	750	500	250	150	160

TABLE 4.1 – *Parameters of the various LTE modes. For all configurations, the sub-carriers spacing is equal to* 15*kHz, and the CP duration is equal to* 4.6875μs.

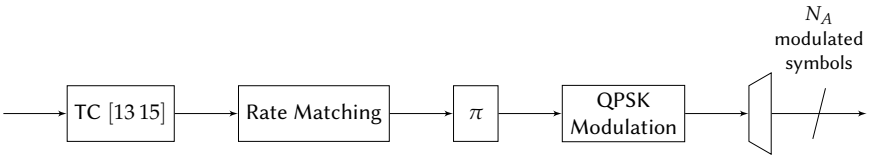

FIGURE 4.2 – *Encoder/Modulator for the TC-OFDM scheme.*

The spectral efficiency of the scheme depends on the use of the time and frequency resource and is expressed using

$$\eta = \frac{Q}{(N_{\text{FFT}} + N_{\text{CP}}) \cdot N_s}. \tag{4.11}$$

This expression takes into account all the spectral losses due to the introduction of the CRC and the CP.

4.2.2 TC-OFDM

The first scheme considered, the Turbo Coded Orthogonal Frequency Division Multiplexing (TC-OFDM), uses the classic OFDM associated with the [13 15] TC. It is a multiplexing technique, i.e. on each carrier is mapped a symbol obtained from a linear modulation. After introducing the system model for the transmitted, the computation of the LLR is presented. The receiver is finally described.

4.2.2.1 TRANSMITTER

The Encoder/Modulator block is depicted in Figure 4.2. The TC [13 15], presented in Section 1.3.4.5, is used associated with a rate matching mechanism. This last block punctures or repeats the encoded bits so that the final matrix fits the given size $N_A \times N_s$. The rate R_m corresponds to the ratio between the number of input bits of the rate matcher and the number of output bits. The TC output consists in $3Q + 12$ bits. As QPSK modulation is used, where each symbol contains two bits, and since $N_A \times N_s$ symbols are available, the matching rate is given by

$$R_m = \frac{3Q + 12}{2N_A N_s}. \tag{4.12}$$

If $R_m > 1$, then bits are punctured (with interleaving to ensure a correct repartition of the punctured bits), and if $R_m < 1$, bits are repeated. The output of the rate matcher is then interleaved and fed to the modulator which perform QPSK modulation. Each couple of bits is thus associated to one of the 4 symbols of the modulation alphabet. The constellation is depicted in Figure 1.6 (b). Eventually, thanks to the use of the rate matcher, a total of $N_A \times N_s$ QPSK modulated symbols are generated. A serial to parallel conversion is then performed to obtain the final matrix of size $N_A \times N_s$.

4.2.2.2 LLR COMPUTATION

Due to the use of QPSK modulation, the group $\mathcal{X}_u^m$ from (4.10) contains 2 elements: the value of one bit b_m with $m \in \{0, 1\}$ is represented by two distinct symbols. As the modulated symbol was associated to the carrier v with $v \in \{0, \ldots, N_A - 1\}$, the sequence $\boldsymbol{x}^i$ is expressed

$$x^i(k) = \frac{1}{N_{\text{FFT}}} s^i \exp\left\{ j2\pi \frac{kv}{N_{\text{FFT}}} \right\}, \tag{4.13}$$

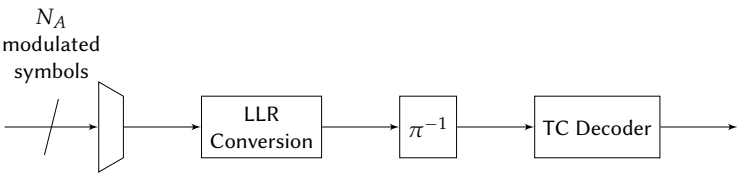

FIGURE 4.3 – *Demodulator/Decoder for the TC-OFDM scheme.*

where s^i with $i \in \{0, \ldots, 3\}$ is the complex coefficient taken from the QPSK alphabet of size 4. The DFT of the sequence $\boldsymbol{x}^i$ is equal to

$$\begin{aligned} X^i(n) &= \sum_{k=0}^{N_{\text{FFT}}-1} x^i(k) e^{-j2\pi \frac{kn}{N_{\text{FFT}}}} \\ &= s^i \cdot \frac{1}{N_{\text{FFT}}} \sum_{k=0}^{N_{\text{FFT}}-1} \exp\left\{ j2\pi \frac{k(v-n)}{N_{\text{FFT}}} \right\} \\ &= \begin{cases} s^i & \text{if } n = v \\ 0 & \text{otherwise} \end{cases} . \end{aligned} \tag{4.14}$$

Using the expression of the DFT of $\boldsymbol{x}^i$ and the expression (4.8), the likelihood of the observation given that the sequence $\boldsymbol{x}^i$ was sent is given by

$$p\left(\boldsymbol{y} \,\middle|\, \boldsymbol{x}^i\right) = C_{\text{st}} \exp\left\{ -\frac{1}{2\sigma_{\text{ch}}^2} \frac{1}{N_{\text{FFT}}} \left\| s^i \right\|^2 \|H(v)\|^2 + \frac{1}{\sigma_{\text{ch}}^2} \frac{1}{N_{\text{FFT}}} \text{Re}\left(\overline{s^i} \overline{H(v)} Y(v) \right) \right\}. \tag{4.15}$$

As the modulus of all the symbols of the QPSK alphabet is constant, the first term of the sum is independent of i and can be factorized. Using (4.9) and (4.10), the LLR of the bit b_m is thus given by

$$L(b_m) = \log \frac{\sum_{i \in \mathcal{X}_1^m} \exp\left\{ \frac{1}{N_{\text{FFT}}\sigma_{\text{ch}}^2} \text{Re}\left(\overline{s^i} \overline{H(v)} Y(v) \right) \right\}}{\sum_{i \in \mathcal{X}_{-1}^m} \exp\left\{ \frac{1}{N_{\text{FFT}}\sigma_{\text{ch}}^2} \text{Re}\left(\overline{s^i} \overline{H(v)} Y(v) \right) \right\}}. \tag{4.16}$$

In order to retrieve the whole binary stream which was modulated, the LLR of the bits for each carrier are computed, i.e. for $v \in \{0, \ldots, N_A - 1\}$.

Due to the particular symmetry of the QPSK constellation (i.e. the values of the symbols s^i, depicted in Figure 1.6) the expression of the LLR can be further simplified. Denoting $[b_1\, b_0]$ the information word mapped by one symbol on the carrier v, their LLR is expressed by

$$\begin{aligned} L(b_0) &= \frac{\sqrt{2}}{N_{\text{FFT}}\sigma_{\text{ch}}^2} \text{Re}\left(\overline{H(v)} Y(v) \right) \\ L(b_1) &= \frac{\sqrt{2}}{N_{\text{FFT}}\sigma_{\text{ch}}^2} \text{Im}\left(\overline{H(v)} Y(v) \right) \end{aligned} , \tag{4.17}$$

which reflects how b_0 is mapped on the real part of the symbol, and b_1 is mapped on the imaginary part. To obtain this result, we made no assumption on the operations of the receiver, and thus demonstrated that the optimum receiver for OFDM modulation is the v-th dimension of the DFT of the received sequence combined with the v-th dimension of the DFT of the channel coefficients. As the max-log algorithm is used for in the TC decoder, the coefficient $\sqrt{2}/(N_{\text{FFT}}\sigma_{\text{ch}}^2)$ can be dropped, which allows for the system to operate without any knowledge about the noise variance.

4.2.2.3 RECEIVER

The Demodulator/Decoder block of TC-OFDM is depicted in Figure 4.3. The stream of symbols is retrieved by performing parallel to serial conversion. The $N_A \times N_s$ modulated symbols are fed to the LLR computation block,

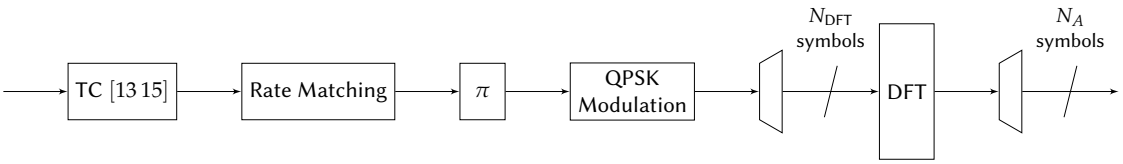

FIGURE 4.4 – *Encoder/Modulator for the TC-SC-FDMA scheme.*

which computes the LLR of the encoded bits using (4.17) (without the coefficients). After de-interleaving, the LLR are fed to the TC decoder. The first step is to recombine the repeated LLR or add zeros at the punctured positions. The turbo decoding as presented in Section 1.3.4.5 is performed. At the end of each iteration, the CRC is computed in order to detect errors in the packet. If there are no errors, iterations stop, but if the CRC is not verified, the decoder performs the next iteration. A limit of 10 iterations is set, and the max-log algorithm is used.

4.2.3 TC-SC-FDMA

The Turbo Coded Single Carrier Frequency Division Multiple Access (TC-SC-FDMA) uses the [13 15] TC in combination with SC-FDMA. The scheme differs from TC-OFDM as pre-coding is applied before mapping the carriers. After introducing the transmitter, the derivations of the LLR are presented. The operations done by the receiver are then detailed.

4.2.3.1 TRANSMITTER

The Demodulator/Decoder block for the TC-SC-FDMA is depicted in Figure 4.4. Like the TC-OFDM technique presented previously, the TC [13 15] is used along with a rate matching procedure, which repeats or punctures some of the encoded bits at a rate R_m given by Equation (4.12). QPSK modulation is then applied. Groups of 2 bits are mapped on one symbol of the QPSK constellation as depicted in Figure 1.6. Finally, a DFT of size N_{DFT} is applied, whose output is given by

$$X(n) = \sum_{w=0}^{N_{\text{DFT}}-1} s_w e^{-j2\pi \frac{wn}{N_{\text{DFT}}}}, \tag{4.18}$$

where s_w corresponds to a modulated symbol, with $w \in \{0, \ldots, N_{\text{DFT}} - 1\}$. In the LTE standard, the size N_{DFT} is chosen as equal to 12. For our study, we consider $N_{\text{DFT}} = N_A$ which is chosen as a power of 2. The result of the DFT is mapped on the N_A possible frequencies, so that the output consists of the expected matrix of size $N_A \times N_s$.

4.2.3.2 LLR COMPUTATION

Since QPSK modulation is considered, there are two bits per symbol. We compute the LLR of the bit b_m with $m \in \{0, 1\}$. From the expression (4.18), the sequence $\boldsymbol{x}$ is given by

$$x(k) = \frac{1}{N_{\text{FFT}}} \sum_{k=0}^{N_{\text{FFT}}-1} \sum_{w=0}^{N_{\text{DFT}}-1} s_w e^{-j2\pi \frac{wn}{N_{\text{DFT}}}} e^{j2\pi \frac{kn}{N_{\text{FFT}}}}. \tag{4.19}$$

Now considering the the symbol s_v modulating the bit b_m, the sequence can be expressed

$$x(k) = \frac{1}{N_{\text{FFT}}} \sum_{k=0}^{N_{\text{FFT}}-1} \left[s_v e^{-j2\pi \frac{vn}{N_{\text{DFT}}}} + \sum_{\substack{w=0 \\ w \neq v}}^{N_{\text{DFT}}-1} s_w e^{-j2\pi \frac{wn}{N_{\text{DFT}}}} \right] e^{j2\pi \frac{kn}{N_{\text{FFT}}}}. \tag{4.20}$$

Due to the use of QPSK modulation, there are 4 possibilities for s_v. However, the sequence $\boldsymbol{x}$ also depends on the $N_{\text{DFT}} - 1$ other symbols s_w, hence a total of $4^{N_{\text{DFT}}-1}$ possible combinations for the sum in Equation (4.20). For a given value of s_v, there are as many possible $\boldsymbol{x}$ sequences. Since a value of b_m is represented by two symbols, the group $\mathcal{X}_u^m$ of Equation (4.10) is composed of $2 \times 4^{N_{\text{DFT}}-1}$ sequences. The summation thus must be done over as many number of sequences, i.e. the complexity of the operation is exponential with N_{DFT} [96].

A suboptimal receiver is thus considered, based on a Zero-Forcing (ZF) algorithm. The output of the FFT (i.e. the observation) is expressed as [97]

$$Y(n) = H(n)X(n) + V(n), \tag{4.21}$$

with $H(n)$ the n-th dimension of the DFT of the channel coefficients, and $V(n)$ a noise term with variance $\sigma_V^2 = N_{\text{FFT}}\sigma_{\text{ch}}^2$ and zero-mean. Using the ZF approach consists of estimating $\widehat{X(n)}$ by computing

$$\widehat{X(n)} = \frac{\overline{H(n)}Y(n)}{\|H(n)\|^2} = X(n) + \frac{\overline{H(n)}}{\|H(n)\|^2}V(n). \tag{4.22}$$

The estimated symbol $\widehat{s_v}$ is thus given by

$$\begin{aligned}\widehat{s_v} &= \frac{1}{N_{\text{DFT}}}\sum_{n=0}^{N_{\text{DFT}}-1}\widehat{X(n)}e^{j2\pi\frac{vn}{N_{\text{DFT}}}} \\ &= s_v + V'(v),\end{aligned} \tag{4.23}$$

with

$$V'(v) = \frac{1}{N_{\text{DFT}}}\sum_{n=0}^{N_{\text{DFT}}-1}\frac{\overline{H(n)}}{\|H(n)\|^2}V(n)e^{j2\pi\frac{vn}{N_{\text{DFT}}}}. \tag{4.24}$$

As the noise term $V'(n)$ can also be considered zero-mean, its variance $\sigma_{V'}^2$ is given by

$$\sigma_{V'}^2 = E\left[V'(v)\overline{V'(v)}\right] = \frac{1}{N_{\text{DFT}}^2}E\left[\sum_{n=0}^{N_{\text{DFT}}-1}\frac{\overline{H(n)}}{\|H(n)\|^2}V(n)e^{j2\pi\frac{vn}{N_{\text{DFT}}}} \times \sum_{n=0}^{N_{\text{DFT}}-1}\frac{H(n)}{\|H(n)\|^2}\overline{V(n)}e^{-j2\pi\frac{vn}{N_{\text{DFT}}}}\right]. \tag{4.25}$$

The cross-terms are cancelled out due to the independence of the noise terms, and the variance can be expressed

$$\begin{aligned}\sigma_{V'}^2 &= \frac{1}{N_{\text{DFT}}^2}\sum_{n=0}^{N_{\text{DFT}}-1}E\left[\frac{\overline{H(n)}H(n)}{\|H(n)\|^4}\right]E\left[\overline{V(n)}V(n)\right]E\left[\left\|e^{j2\pi\frac{vn}{N_{\text{DFT}}}}\right\|^2\right] \\ &= \frac{\sigma_V^2}{N_{\text{DFT}}^2}\sum_{n=0}^{N_{\text{DFT}}-1}\frac{1}{\|H(n)\|^2} \\ &= \frac{N_{\text{FFT}}\sigma_{\text{ch}}^2}{N_{\text{DFT}}^2}\sum_{n=0}^{N_{\text{DFT}}-1}\frac{1}{\|H(n)\|^2}.\end{aligned} \tag{4.26}$$

The LLR is computed using

$$L(b_m) = \frac{\sum_{i\in\mathcal{X}_1^m}p\left(\widehat{s_v}\,\middle|\,s^i\right)}{\sum_{i\in\mathcal{X}_{-1}^m}p\left(\widehat{s_v}\,\middle|\,s^i\right)} \tag{4.27}$$

with

$$p\left(\widehat{s_v}\,\middle|\,s^i\right) = \mathrm{C_{st}}\exp\left\{\frac{1}{\sigma_{V'}}\langle\widehat{s_v}, s^i\rangle\right\}. \tag{4.28}$$

Similarly to the OFDM modulation and due to the symmetry of the QPSK constellation, the LLR of the information bits of the modulated symbol s_v is expressed, using (4.26)

$$\begin{aligned}L(b_0) &= \frac{\sqrt{2}N_{\text{DFT}}^2}{N_{\text{FFT}}\sigma_{\text{ch}}^2}\frac{1}{\sum_{n=0}^{N_{\text{DFT}}-1}\frac{1}{\|H(n)\|^2}}\,\text{Re}\left(\widehat{s_v}\right) \\ L(b_1) &= \frac{\sqrt{2}N_{\text{DFT}}^2}{N_{\text{FFT}}\sigma_{\text{ch}}^2}\frac{1}{\sum_{n=0}^{N_{\text{DFT}}-1}\frac{1}{\|H(n)\|^2}}\,\text{Im}\left(\widehat{s_v}\right)\end{aligned}. \tag{4.29}$$

As we consider the max-log approximation for further computations, the first coefficient can be ignored. The second coefficient, depending on $H(n)$ must be considered except if the channel coefficients vector $\boldsymbol{h}$ is constant for all the duration of the signal; in this situation, the second coefficient can be ignored too. Note that some other equalization techniques, such as the Minimum Mean Square Error (MMSE) equalizer, may have better performance. However, the benefit of the ZF equalizer is its capacity to operate without any knowledge on the noise variance σ_{ch}^2.

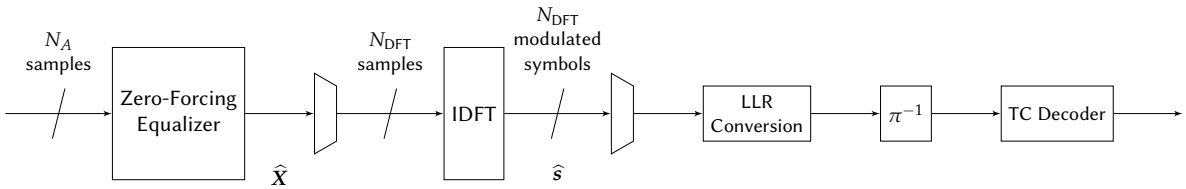

FIGURE 4.5 – *Demodulator/Decoder for the TC-SC-FDMA scheme.*

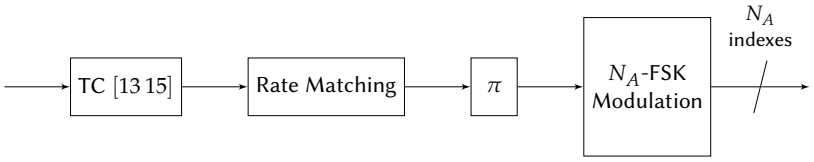

FIGURE 4.6 – *Encoder/Modulator for the TC-FSK scheme.*

4.2.3.3 RECEIVER

The Demodulator/Decoder block is depicted in Figure 4.5. The first step is to equalize the output of the FFT to compute (4.22). DFT is then applied to obtain the estimate of the modulated symbols as expressed with Equation (4.23), and then the LLR of the encoded bits are computed with Equation (4.29). After de-interleaving, the TC decoder block recombines the repeated bits or adds null LLR at the punctured positions, and performs iterative decoding. As in the TC-OFDM case, the CRC is used as stop criterion for the iterative decoding.

4.2.4 TC-FSK

The FSK is a common orthogonal modulation. Based on an alphabet of orthogonal waveforms equivalent to pure frequencies, it can be implemented thanks to the FFT-based system previously introduced. We consider its use associated with the TC [13 15] previously considered, in a scheme so-called Turbo Coded Frequency Shift Keying (TC-FSK).

4.2.4.1 TRANSMITTER

The TC-FSK modulation of size N_A associates groups of bits of size $\log_2(N_A)$ to one of the N_A possible frequencies. The Encoder/Modulator block is depicted in Figure 4.6. After TC encoding, rate matching is applied. The output of the encoder consists in $3Q+12$ bits, and N_s FSK symbols are available, or $\log_2(N_A) \times N_s$ bits. The matching rate is thus given by

$$R_m = \frac{3Q+12}{\log_2(N_A) \times N_s}. \tag{4.30}$$

Again, if $R_m > 1$, then bits are punctured (with interleaving to ensure a correct repartition of the punctured bits), and if $R_m < 1$, bits are repeated. Interleaving is then applied on the output of the rate matching block, and FSK modulation is performed. Each binary word $\boldsymbol{b}$ of size $\log_2(N_A)$ is associated to one of the N_A possible frequencies. If the binary word $\boldsymbol{b}$ is associated to the frequency i, then the output of the FSK modulator is

$$X(n) = \begin{cases} 1 & \text{if } n = i \\ 0 & \text{otherwise} \end{cases}. \tag{4.31}$$

The output matrix of size $N_A \times N_s$ is thus a sparse binary matrix containing N_s ones. The further use of the FFT in the transmitter's operations will generate a FSK signal, to be transmitted through the channel.

4.2.4.2 LLR COMPUTATION

After performing the IFFT, the sequence $\boldsymbol{x}^i$ is given by

$$x^i(k) = \frac{1}{N_{\text{FFT}}} \exp\left\{ j2\pi \frac{ki}{N_{\text{FFT}}} \right\}, \tag{4.32}$$

traducing the FSK principle where symbols consist in pure frequencies. Each of the N_A possible binary words are represented by a symbol; the value of one bit b_m of a binary word, with $m \in \{0, \ldots, \log_2(N_A) - 1\}$, is represented by

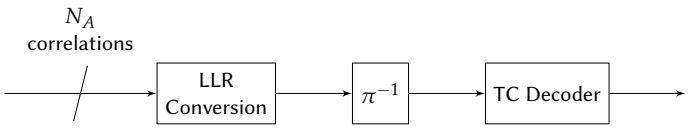

FIGURE 4.7 – *Demodulator/Decoder for the FSK scheme.*

$N_A/2$ frequencies. The group $\mathcal{X}_u^m$, over which the summation of Equation (4.10) is done, contains $N_A/2$ elements. Following the definition of a transmitted symbol, the likelihood of the observation given that the sequence $\boldsymbol{x}^i$ was transmitted is, using Equation (4.8)

$$p\left(\boldsymbol{y}\,\middle|\,\boldsymbol{x}^i\right) = C_{\text{st}} \exp\left\{\frac{1}{\sigma_{\text{ch}}^2 N_{\text{FFT}}}\left(\text{Re}\left(\overline{H(i)}Y(i)\right) - \frac{1}{2}\left\|H(i)\right\|^2\right)\right\}. \tag{4.33}$$

Using (4.9) and (4.10), the LLR of the bit b_m is thus given by

$$L(b_m) = \log \frac{\sum\limits_{i\in\mathcal{X}_1^m} \exp\left\{\frac{1}{\sigma_{\text{ch}}^2 N_{\text{FFT}}}\left(\text{Re}\left(\overline{H(i)}Y(i)\right) - \frac{1}{2}\left\|H(i)\right\|^2\right)\right\}}{\sum\limits_{i\in\mathcal{X}_{-1}^m} \exp\left\{\frac{1}{\sigma_{\text{ch}}^2 N_{\text{FFT}}}\left(\text{Re}\left(\overline{H(i)}Y(i)\right) - \frac{1}{2}\left\|H(i)\right\|^2\right)\right\}}. \tag{4.34}$$

As this expression requires the computation of multiple exponential functions, the max-log approximation is used to compute the LLR, with

$$L(b_m) = \max_{i\in\mathcal{X}_1^m}\left[\text{Re}\left(\overline{H(i)}Y(i)\right) - \frac{1}{2}\left\|H(i)\right\|^2\right] - \max_{i\in\mathcal{X}_{-1}^m}\left[\text{Re}\left(\overline{H(i)}Y(i)\right) - \frac{1}{2}\left\|H(i)\right\|^2\right]. \tag{4.35}$$

4.2.4.3 Receiver

The Demodulator/Decoder block is depicted in Figure 4.7. The use of the FFT algorithm is equivalent to a correlator. Since the transmitter sends pure frequencies, the N_A outputs corresponding to the N_A possible frequencies are used to estimate the LLR using Equation (4.35). De-interleaving is applied and the TC decoder block reconstructs the encoded stream by combining bits or adding extra LLRs. As in the other cases using an iterative receiver, the CRC is used as stop criterion.

4.2.5 Coplanar Turbo-FSK and Coplanar Turbo-ZC

Two schemes relying on the technique presented Chapter 3 are considered for comparisons. The first scheme concerns the use of Coplanar Turbo-FSK with Phase Shift Keying (PSK) modulation, which was considered in Chapter 3 and offers a constant envelope. The second scheme relies on the use of a CAZAC sequence to construct the orthogonal alphabet: the ZC sequence [50]. This scheme is referred to as Coplanar Turbo-ZC. The transmitter is described, and the alphabets and outputs of both considered schemes are presented. The likelihood is derived for each scheme, and the receiver is reviewed.

4.2.5.1 Transmitter

The Encoder/Modulator block for the Coplanar Turbo-FSK is depicted in Figure 4.8. Similarly to the transmitter presented in Section 3.3.1, the encoder consists in λ stages where each stage encodes an interleaved version of the Q information bits. The information block is divided into N_q information words of q bits. Eventually, a total of $\lambda \times (N_q + 1)$ binary words of length $q+1$ are generated. Each binary word is to be mapped on one of the codewords of the alphabet. In order to fit the N_s available symbols, the rate matcher punctures or repeats some binary words so that

$$R_m = \frac{\lambda \cdot (N_q + 1)}{N_s}. \tag{4.36}$$

Unlike the other scheme, the rate matcher operates at the word level, while it operated at the bit level previously. This is because entire words of size $q+1$ are to be mapped on the alphabet which contains $M = 2^{q+1}$ symbols.

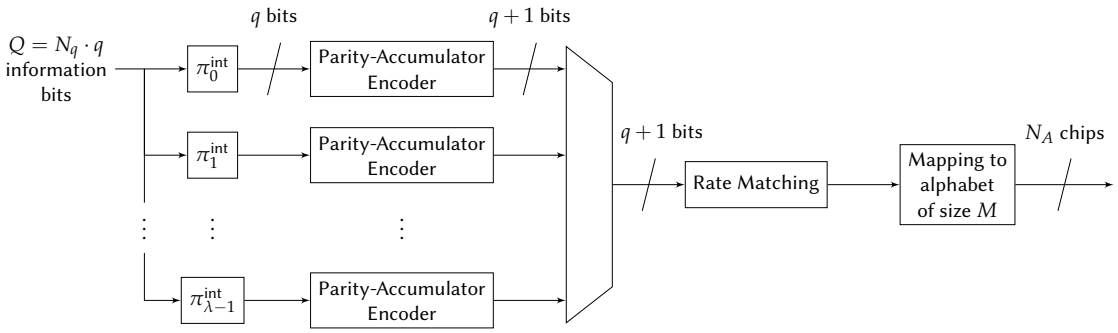

FIGURE 4.8 – *Encoder/Modulator for the Coplanar Turbo-FSK and Turbo-ZC schemes.*

The alphabet is constructed using N_A subsets $\boldsymbol{\mathcal{A}}^\delta$ with $\delta \in \{0, \ldots, N_A - 1\}$ (i.e. $N_\perp = N_A$ with the notation of Chapter 3) and N_L linear shifts given by the complex number z_p with $p \in \{0, \ldots, N_L - 1\}$. A symbol $\boldsymbol{s}^i$ is defined as

$$\boldsymbol{s}^i = \boldsymbol{f}^\delta z_p, \tag{4.37}$$

where $\boldsymbol{f}^\delta$ is one of the N_A vectors composing the orthogonal subsets. The alphabet size is given by

$$M = N_A N_L. \tag{4.38}$$

Also, the size of the alphabet defines the size q of the information words, with $q = \log_2(M) - 1$. The number of information words is thus given by

$$N_q = \frac{Q}{q} = \frac{Q}{\log_2(N_A N_L) - 1}. \tag{4.39}$$

4.2.5.2 Output for Coplanar Turbo-FSK

For the Coplanar Turbo-FSK scheme, FSK is used as orthogonal modulation and PSK as linear modulation. The complex coefficients are given by $z_p = e^{j2\pi p/N_L}$, and the vectors $\boldsymbol{f}^\delta$ are taken from the DFT matrix (i.e. as pure frequencies). The symbol $\boldsymbol{s}^i$ is expressed in time. When considering the FFT-based system, the transmitted sequence is constructed in frequency. The output of the mapper, assuming that the binary word $\boldsymbol{b}$ is associated to the symbol $\boldsymbol{s}^i$, is thus expressed by

$$X^i(n) = \begin{cases} z_p & \text{if } n = \delta \\ 0 & \text{otherwise} \end{cases}. \tag{4.40}$$

The output is, like the FSK modulation case, a sparse matrix of size $N_A \times N_s$, where only N_s elements are different from zero (one in each column). Similarly to the FSK modulation case, the use of the FFT algorithm afterward will generate a FSK signal.

4.2.5.3 Output for Coplanar Turbo-ZC

For the Coplanar Turbo-ZC scheme, the orthogonal part of the alphabet is constructed using ZC sequences, and PSK is used as linear modulation. The symbols of the alphabet are given by $\boldsymbol{s}^i = z_p \boldsymbol{f}^\delta$. Like for Coplanar Turbo-FSK, the complex coefficients are given by $z_p = e^{j2\pi p/N_L}$. The vectors $\boldsymbol{f}^\delta$ are constructed using a ZC sequence, which is denoted $\boldsymbol{g}_\mu$ and has two parameters, the length of the sequence N_{ZC} and its index μ, a positive integer. The sequence is given by

$$g_\mu(n) = \exp\left\{ j\pi \frac{\mu}{N_{\text{ZC}}} n \left(n + \text{mod}(N_{\text{ZC}}, 2)\right) \right\}, \tag{4.41}$$

where $\text{mod}(\cdot, 2)$ is the modulo two operator, and with $n \in \{0, \ldots, N_{\text{ZC}} - 1\}$. The zero-autocorrelation property of the ZC sequence allows for the construction of an orthogonal alphabet using circularly shifted versions of a base sequence. The vectors $\boldsymbol{f}^\delta$ are constructed from vector of the DFT matrix multiplied by the base sequence $\boldsymbol{g}_\mu$ with parameters $N_{\text{ZC}} = N_A$ and $\mu = 1$. It is given by

$$f^\delta(n) = g_1(n) \exp\left\{ j2\pi \frac{\delta n}{N_A} \right\} = \exp\left\{ j\pi \frac{n^2 + 2\delta n}{N_A} \right\}, \tag{4.42}$$

as N_A is defined as a power of 2.

Unlike the Coplanar Turbo-FSK, where symbols of the alphabet are expressed in time, we wish to express the symbols of the Coplanar Turbo-ZC alphabet in frequency. Assuming that the binary word $\boldsymbol{b}$ is associated to the sequence $\boldsymbol{s}^i$, the output of the mapping block is given by, using Equation (4.41)

$$X^i(n) = \exp\left\{j\pi\left(\frac{n^2+2\delta n}{N_A} + \frac{2p}{N_L}\right)\right\}. \tag{4.43}$$

with $n \in \{0, \ldots, N_A - 1\}$. The output matrix is thus again of size $N_A \times N_s$, but it is no longer sparse. Each column consists of a delayed ZC sequence.

4.2.5.4 Likelihood Computation

The specific decoding procedure of the Coplanar Turbo-FSK and the Coplanar Turbo-ZC requires only the computation of the likelihood of the symbols from the alphabet. From the general expression of the likelihood of a sequence given Equation (4.8), the likelihood for both schemes is obtained by considering the expression of the output of the Encoder/Modulator block.

For the Coplanar Turbo-FSK, the likelihood is expressed, using Equation (4.40) in Equation (4.8), by

$$p\left(\boldsymbol{y}\,\middle|\,\boldsymbol{x}^i\right) = C_{\text{st}} \exp\left\{\frac{1}{\sigma_{\text{ch}}^2 N_{\text{FFT}}}\left(\text{Re}\left(\overline{z_p}\,\overline{H(\delta)}Y(\delta)\right) - \frac{1}{2}\left\|H(\delta)\right\|^2\left\|z_p\right\|^2\right)\right\}. \tag{4.44}$$

For the Coplanar Turbo-ZC, the likelihood can be computed using Equation (4.43) in Equation (4.8) and is expressed

$$p\left(\boldsymbol{y}\,\middle|\,\boldsymbol{x}^i\right) = C_{\text{st}} \exp\left\{-\frac{1}{2\sigma_{\text{ch}}^2}\frac{1}{N_{\text{FFT}}^2}\sum_{k=0}^{N_{\text{FFT}}-1}\left\|\sum_{n=0}^{N_A-1} X^i(n)H(n)e^{j2\pi\frac{nk}{N_{\text{FFT}}}}\right\|^2 + \frac{1}{\sigma_{\text{ch}}^2}\frac{1}{N_{\text{FFT}}}\text{Re}\left(\sum_{n=0}^{N_A-1}\overline{X^i(n)}\,\overline{H(n)}Y(n)\right)\right\}. \tag{4.45}$$

Using the definition of the sequence $\boldsymbol{X}^i$ given in Equation (4.43), the following expression simplifies to

$$\begin{aligned}
\sum_{k=0}^{N_{\text{FFT}}-1}\left\|\sum_{n=0}^{N_A-1} X^i(n)H(n)e^{j2\pi\frac{nk}{N_{\text{FFT}}}}\right\|^2 &= \sum_{k=0}^{N_{\text{FFT}}-1}\left\|\sum_{n=0}^{N_A-1} H(n)\exp\left\{j\pi\frac{n^2+2n\delta}{N_A} + \frac{2p}{N_L} + j2\pi\frac{nk}{N_{\text{FFT}}}\right\}\right\|^2 \\
&= \sum_{k=0}^{N_{\text{FFT}}-1}\left\|\sum_{n=0}^{N_A-1} H(n)\exp\left\{j\pi\frac{n^2}{N_A} + j2\pi n\left(\frac{k}{N_{\text{FFT}}} - \frac{\delta}{N_A}\right)\right\}\right\|^2 \\
&= \sum_{k=0}^{N_{\text{FFT}}-1}\left\|\sum_{n=0}^{N_A-1} H(n)g_1(n)\exp\left\{j2\pi\frac{n}{N_{\text{FFT}}}\left(k - \delta\frac{N_{\text{FFT}}}{N_A}\right)\right\}\right\|^2 \qquad (4.46) \\
&= \sum_{k=0}^{N_{\text{FFT}}-1}\left\|\sum_{n=0}^{N_A-1} H(n)g_1(n)\exp\left\{j2\pi\frac{nk}{N_{\text{FFT}}}\right\}\right\|^2, \qquad (4.47)
\end{aligned}$$

where the simplification from (4.46) to (4.47) requires the ratio N_{FFT}/N_A to be an integer and comes from the periodicity of the element of the DFT. This demonstrates that the term for sequence i is equal to the term for sequence 0. This term is thus independent of i and can be considered as a constant. The likelihood for the case of Coplanar Turbo-ZC given in Equation (4.45) simplifies to

$$\begin{aligned}
p\left(\boldsymbol{y}\,\middle|\,\boldsymbol{x}^i\right) &= C_{\text{st}} \exp\left\{\frac{1}{\sigma_{\text{ch}}^2}\frac{1}{N_{\text{FFT}}}\text{Re}\left(\sum_{n=0}^{N_A-1}\overline{X^i(n)}\,\overline{H(n)}Y(n)\right)\right\} \\
&= C_{\text{st}} \exp\left\{\frac{1}{\sigma_{\text{ch}}^2}\frac{1}{N_{\text{FFT}}}\text{Re}\left(\overline{z_p}\sum_{n=0}^{N_A-1}\overline{g_1(n)H(n)}Y(n)e^{-j2\pi n\delta/N_A}\right)\right\}. \qquad (4.48)
\end{aligned}$$

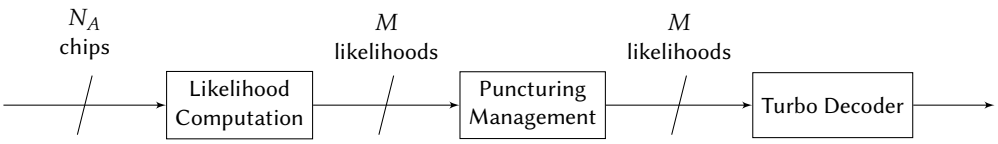

FIGURE 4.9 – *Demodulator/Decoderfor the Coplanar Turbo-FSK and Turbo-ZC schemes.*

In order to compute the likelihood, the received sequence of size N_A is multiplied by the conjugate of the channel coefficients and by the conjugate of the base sequence g_1 used to build the alphabet. A FFT of size N_A is then applied. The likelihood of the codeword i is finally obtained by multiplying the δ-th output of the FFT by the linear coefficient p and retrieving the real part. Compared to the Coplanar Turbo-FSK, the computation of the likelihood for the Coplanar Turbo-ZC requires two additional steps: the multiplication by the base sequence and the FFT of the size N_A.

4.2.5.5 RECEIVER

The Demodulator/Decoder block is depicted in Figure 4.9. After computing the likelihood of each sequence (using Equation (4.44) for Coplanar Turbo-FSK and Equation (4.48) for Coplanar Turbo-ZC), a matrix of size $M \times N_s$ is obtained, containing the likelihoods of all the possible symbols from the alphabet. In case of repetition, the puncturing management block recombines the repeated columns by adding them. If puncturing was performed at the transmitter, extra columns containing the same value for the M likelihood are appended. A matrix of size $M \times \lambda(N_q + 1)$ is eventually recovered. The turbo decoder then uses the observation of the λ stages to perform the iterative decoding presented in Section 2.2.2. The CRC is also used as a stop criterion, as it is computed at the end of each iteration.

4.2.6 SUMMARY

The system requires numerous parameters. Concerning the FFT-based encapsulation, the parameters are chosen as those corresponding to specific configurations of the LTE, as presented in Table 4.1. The number of information

Waveform	N_A	R_m	Receiver's metric	Time-Frequency Allocation
TC-OFDM	Number of multiplexed symbols	$\frac{3Q+12}{2N_A N_s}$	LLR, (4.17)	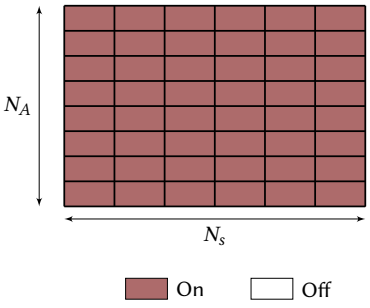
TC-SC-FDMA	Number of multiplexed symbols + size of DFT ($N_{\text{DFT}} = N_A$)	$\frac{3Q+12}{2N_A N_s}$	LLR, (4.29)	
Coplanar Turbo-ZC	Size of the ZC sequence	$\lambda \cdot \frac{\frac{Q}{\log_2(N_A N_L)-1}+1}{N_s}$	Likelihood, (4.48)	
TC-FSK	Number of possible frequencies	$\frac{3Q+12}{\log_2(N_A)N_s}$	LLR, (4.35)	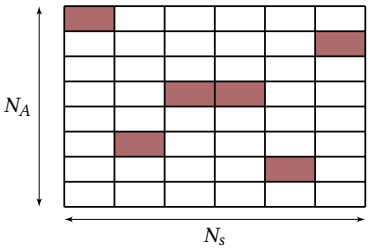
Coplanar Turbo-FSK	Number of possible frequencies	$\lambda \cdot \frac{\frac{Q}{\log_2(N_A N_L)-1}+1}{N_s}$	Likelihood, (4.44)	

TABLE 4.2 – *Summary of the various waveforms and their parameters: interpretation of the number of active carriers N_A, value of the rate matching R_m, metric of the receiver and the typical form of the Time-Frequency allocation.*

bits Q, the number of time sequences N_s (or also called OFDM symbols) and the number of active carriers N_A can be chosen arbitrarily. For simplicity, the case $N_{\text{DFT}} = N_A$ is always considered for the TC-SC-FDMA scheme. The Coplanar Turbo-FSK and Coplanar Turbo-ZC depend both on the parameter λ, the number of stages of the encoder, and the size of the PSK associated to the Turbo-FSK scheme can also be tuned with N_L.

Table 4.2 summarizes 3 different parameters of the waveforms: the interpretation of the number of active carriers N_A, the value of the rate matching R_m, and the metric of the receiver associated to the decisive equation to obtain it. An example of the output matrix of the Encoder/Modulator block is also depicted. It represents the spectral occupation over the active carriers for the duration of the signal, i.e. the Time-Frequency allocation over the active carriers. This view emphasizes how the FSK schemes (TC-FSK and Coplanar Turbo-FSK) do not use all the active carriers for one symbol, while for the other schemes, information is spread over all the available spectrum. However, due to the FSK signaling, the inactive carriers still carry information as the receiver needs to estimate which carrier is active. For the other schemes, the receiver knows that all carriers are active. The TC-OFDM and TC-SC-FDMA multiplex symbols over the N_A carriers, while the Coplanar Turbo-ZC simply uses these N_A carriers to transmit one orthogonal sequence.

4.3 Performance Comparison

In this section, the 5 schemes previously presented are compared. The comparisons concern practical aspects commonly used to describe a system. Three aspects are considered: the variation of the envelope of the signal at the output of the transmitter; the performance of the system under various channels and the complexity of the receiver algorithm. For each aspect, the performance of every techniques is assessed using specific parameters. For a fair comparison, the schemes are always compared with the same spectral efficiency. The same number of information bits is sent over the same Time-Frequency allocation. The rate matcher of each scheme will then puncture or repeat some bits/codewords.

There are many possible configurations for the 5 schemes. In order to restrict the study, some parameters are kept constant for all the schemes. As all the schemes were presented associated with the same FFT architecture, the parameters for this architecture can be taken equal for all the schemes. The parameters are chosen as corresponding to the mode 1.4MHz of LTE, given in Table 4.1. For all simulations, we consider the value $N_A = 16$ of active carriers, leading to a bandwidth equal to $B = 240$kHz. The packet size (or information block size) is set to $Q = 1000$. For the rest of the parameters, two scenarios are considered: a low throughput and a high throughput.

The parameters for the low throughput scenario are given in Table 4.3. The spectral efficiency is computed using Equation (4.11). For this scenario, the Turbo-FSK and the Turbo-ZC are used in the fully orthogonal mode, where codewords are orthogonal to each other. The value of the number of stages λ is taken from Table 2.1 as the one minimizing the threshold of the receiver for this size of alphabet, i.e. $\lambda = 5$. The TC-OFDM and the TC-SC-FDMA use QPSK modulation and the rate matcher corresponds to a repetition of factor 17.76.

For the high throughput scenario, the TC-FSK is no longer considered, because the considered number of symbols would require too many bits to be punctured and would significantly reduce the performance of the TC. The parameters for this scenario are given in Table 4.4. For the Coplanar Turbo-FSK and the Coplanar Turbo-ZC, some codewords are punctured and the linear parameter is set to $N_L = 32$. The value of the number of stages λ is taken from Table 2.1 as the one minimizing the threshold of the receiver for this size of alphabet, i.e. $\lambda = 3$. The TC-OFDM and the TC-SC-FDMA once more use QPSK modulation and the rate matcher corresponds to a repetition of factor 3.14. The effective data rate R can be computed with

$$R = \eta \cdot 128 \times 15 \cdot 10^3, \tag{4.49}$$

which gives a data rate of 8.24 kbps for the low throughput scenario and 46.68 kbps for the high throughput scenario.

Common parameters					
N_A	16	N_s	1700	η	$4.29 \cdot 10^{-3}$
Waveforms	**TC-OFDM**	**TC-SC-FDMA**	**TC-FSK**	**Turbo-ZC**	**Turbo-FSK**
Modulation	QPSK	QPSK	FSK	$N_L = 1, \lambda = 5$	$N_L = 1, \lambda = 5$
Matching Rate R_m	0.0563	0.0563	0.45	1	1

Table 4.3 – *Parameters of all the schemes for the low throughput scenario, using the configuration* 1.4*MHz of the LTE. The data rate is equal to* 8.24 *kbps.*

Common parameters					
N_A	16	N_s	300	η	$2.43 \cdot 10^{-2}$

Waveforms	TC-OFDM	TC-SC-FDMA	Coplanar Turbo-ZC	Coplanar Turbo-FSK
Modulation	QPSK	QPSK	$N_L = 32, \lambda = 3$	$N_L = 32, \lambda = 3$
Matching Rate R_m	0.3187	0.3187	1.28	1.28

TABLE 4.4 – *Parameters of all the schemes for the high throughput scenario, using the configuration* 1.4*MHz of the LTE. The data rate is equal to* 46.68 *kbps.*

In addition to the restriction of the choice of parameters in two scenarios, several assumptions are made. The first assumption is the ideal synchronization. There is no carrier or clock frequency offset, and no phase noise or timing offset. Also, we assume that the estimation of the channel coefficient matrix $\boldsymbol{H}$ is realized without error. This assumption is often referred to as the perfect Channel State Information (CSI) assumption and neglects all the loss of spectral efficiency due to the insertion of pilots or the estimation error on the CSI. The last assumption concerns the computation of the Signal-to-Noise Ratio (SNR). By convention, we choose to compute the SNR on the whole bandwidth of the FFT instead of only the active carriers. This means that we consider the noise directly at the input of Analog-to-Digital Converter (ADC) of the receiver.

The section is organized as follows. First, the Instantaneous-to-Average Power Ratio (IAPR) of all the scheme is evaluated. Then, performances are assessed under 3 different types of channel: the AWGN channel, a multi-path channel and the same channel but where mobility conditions are considered. The complexity of each scheme is then computed. Finally, the results are summarized in a graphical representation.

4.3.1 Instantaneous-to-Average Power Ratio

The variations of the envelope of a signal can be measured through the computation of the IAPR, as presented in Chapter 1, Section 1.2.4. This measure is very useful for evaluating the constraints for the Power Amplifier (PA). It is more relevant than the measure of the PAPR as it considers all the samples of the signal (and potentially, the samples that could reach the non-linear region of the PA) [19]. Having large variations will result in the necessity of having a highly linear PA, i.e. expensive and energy inefficient. The IAPR is measured from the time signal which is sent through the channel, after the addition of the CP in Figure 4.1. For all schemes or scenarios, this always corresponds to 16 active carriers on a FFT of size 128. For a sufficient statistic, 1000 packets are simulated.

The Complementary Cumulative Distribution Function (CCDF) of the IAPR's 5 schemes is depicted in Figure 4.10. The TC-OFDM has the largest variations and exhibits a probability of 10^{-3} to have an IAPR larger than 8dB. The TC-SC-FDMA shows a 2dB improvement in its variations, thanks to the use of pre-coding. The TC-FSK and the Turbo-FSK have the same performance i.e. an IAPR of 0dB, as both of these technique use the FSK modulation

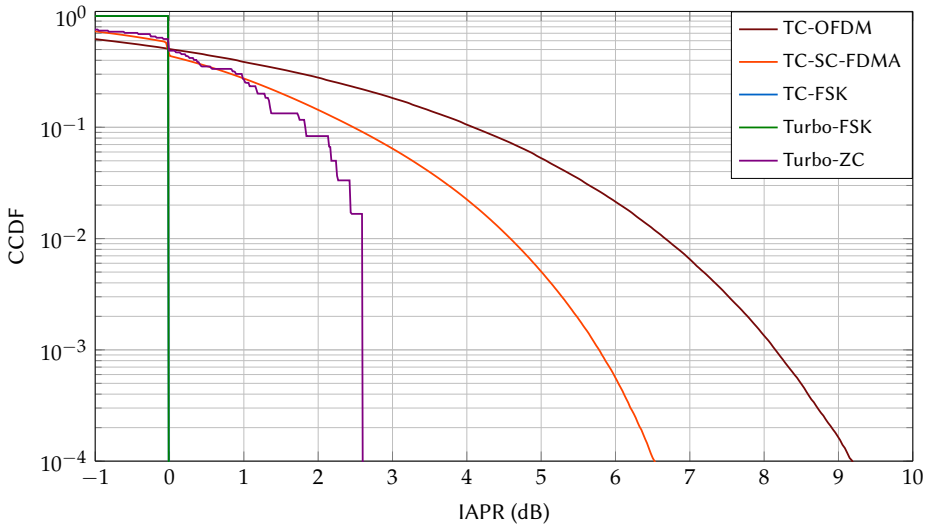

FIGURE 4.10 – *IAPR of the* 5 *schemes with the parameter* $N_A = 16$.

which has a constant envelope. Even though the Turbo-ZC was constructed using CAZAC sequences, its does not show a constant envelope. This is because the sequence was mapped in the frequency domain. The use of the IFFT oversampled the sequence to give a time signal that does not have a constant envelope. Moreover, the number of possible sequences is equal to 16, i.e. the variations of a given signal will correspond (on average) to the variations of the 16 possible sequences. When the ratio N_{FFT}/N_A is an integer, all the sequences have the same distribution of the IAPR (using a development similar to Equation (4.47)). The IAPR consists in a finite number of values (hence the discrete CCDF) and could be evaluated simply by considering the base sequence. The maximum IAPR of the Turbo-ZC appears to be around 2.6dB, a value that depends on the value of N_A and the choice of the base sequence.

The measure of the IAPR clearly emphasizes the major benefit of FSK signaling, its constant amplitude property. It guarantees an IAPR equal to 0dB for all samples. On the opposite, the IAPR of OFDM exhibits large variations, a well-known drawback of the technique.

4.3.2 AWGN Channel

The performance of all the schemes for both scenarios (low and high throughputs) are evaluated under the AWGN channel. In order to use the receivers for the AWGN channel, the channel coefficients $\boldsymbol{H}$ must be set to 1 for every value. The performance is assessed for both scenarios.

The performance for the low throughput scenario is depicted in Figure 4.11. Because of the choice of AWGN, TC-OFDM and TC-SC-FDMA are strictly equivalent, and so are the Turbo-FSK and the Turbo-ZC. The Turbo-FSK has less interesting performance compared to TC-OFDM, with a loss of 0.2dB. This is due to the choice of the parameters for the Turbo-FSK scheme, which are not the optimum parameters as obtained in Chapter 2. The TC-FSK is the least performant technique, with a 2.9dB loss of SNR for a Packet Error Rate (PER) of 10^{-2}, compared to TC-OFDM. This was expected, as unlike the Turbo-FSK the scheme does not use orthogonal metric for the decoding. This effect was studied in Chapter 2. Overall, all the schemes achieve low levels of PER at low levels of SNR and will hence exhibit low sensitivity levels.

The performance for the high throughput scenario is depicted in Figure 4.12. The TC-OFDM and TC-SC-FDMA are equivalent and so are the Turbo-FSK and the Turbo-ZC due to the choice of the AWGN channel. The Turbo-FSK is used in its optimum mode for this size of alphabet (512). If this configuration was shown to overcome the TC in Chapter 2, the scheme is not as effective as the TC-OFDM. The loss of performance is due to the use of the linear modulation of size 32 associated with the puncturing of more than 20% of the codewords. Despite the loss, the Turbo-FSK scheme is less than 0.4dB away from the TC-OFDM for a PER equal to 10^{-2}.

These simulations include the loss in spectral efficiency incurred by the introduction of the CP and the use of the CRC. The first is necessary to avoid ISI when considering multi-path channels. The latter is used to detect errors in the decoded packet and to compute the PER. Since this two elements correspond to a loss in spectral efficiency,

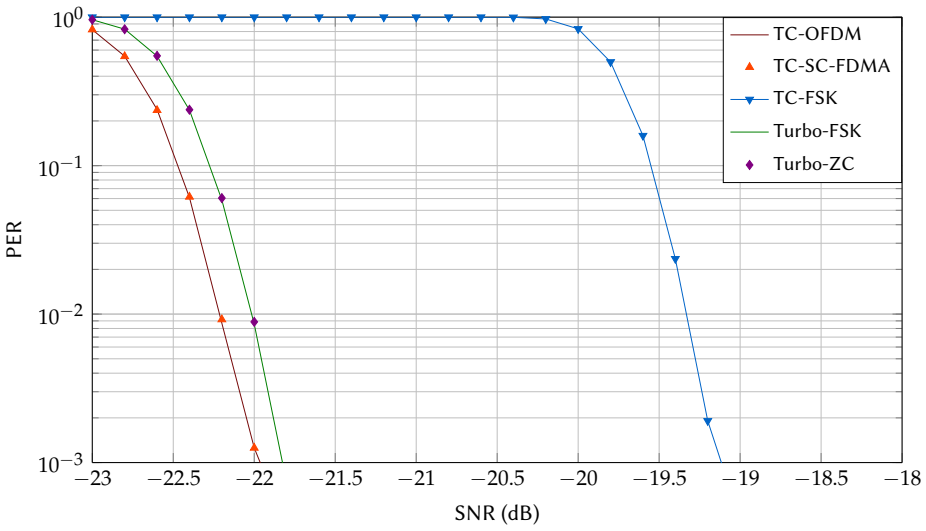

Figure 4.11 – *Performance of the* 5 *schemes for the low throughput scenario with parameters from Table 4.3, under the AWGN channel.*

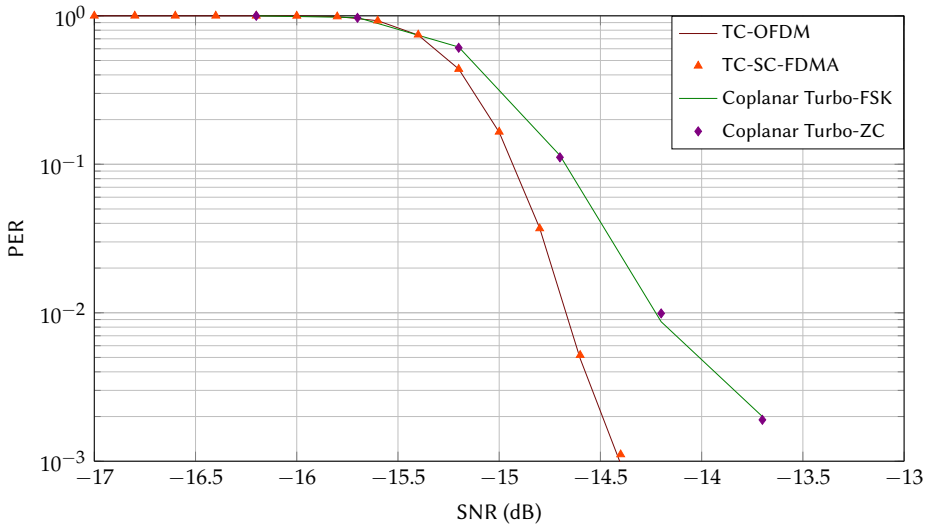

FIGURE 4.12 – *Performance of the schemes for the high throughput scenario with parameters from Table 4.4, under the AWGN channel.*

they can be interpreted as a loss in E_b/N_0. Using a CRC of size 16, the loss is expressed in dB as

$$10\log_{10}\frac{N_{\text{FFT}}}{N_{\text{FFT}}+N_{\text{CP}}}+10\log_{10}\frac{Q}{Q+16}. \tag{4.50}$$

With the considered parameters, this loss is equal to -0.37dB.

4.3.3 Frequency Selective Channels

When considering frequency selective channels, multiple models can be selected. For our study, Rayleigh fading is considered, i.e. the complex gains of the various paths follow a circular complex Gaussian distribution, and the modulus of the complex gain is Rayleigh distributed. The 3rd Generation Partnership Project (3GPP) organization defines several fading profiles [98, p.191]. For our study, the Extended Typical Urban (ETU) fading profile is considered. A profile is defined by the delays and the average attenuation of the different paths. The delays and average path powers for the ETU fading profile are given in Table 4.5. Generating the channel consists in generating a FIR filter, i.e. the coefficients h of Equation (4.2). The physical multi-path channel with analog delays must be interpolated to correspond to the considered sampling frequency. When considering a 1.92MHz sampling frequency, the 9 physical paths of the channel give a total of 14 samples for the channel coefficients h.

The delay spread τ of the channel is the maximum delay incurred by the channel. For the ETU profile, this delay spread is equal to $\tau = 5\mu$s. The coherence bandwidth B_{coh} of the channel is the bandwidth over which the channel is correlated. The channel can be considered frequency flat over a bandwith small compared to B_{coh}. The value of the coherence bandwidth can be approximated using the delay spread with

$$B_{\text{coh}} \approx \frac{1}{\tau}. \tag{4.51}$$

For the ETU profile, the coherence bandwidth is equal to $B_{\text{coh}} = 200$kHz. Since we considered the LTE parameters with a bandwidth of 1.4MHz, there is frequency selectivity (as the channel cannot be considered flat over the whole bandwidth). A representation of the frequency response of a channel using an ETU profile is depicted in Figure 4.13. A FFT of size 128 was used with a sampling frequency of 1.92MHz (parameters of the LTE 1.4MHz, as given in Table 4.1). The 16 allocated carriers are represented in blue. The frequency selectivity of the channel induces severe losses for some of the carriers, but also significant gains for other allocated carriers. As additive noise is also considered, the compensation of the channel may lead to the amplification of the noise.

Path delays (ns)	0	50	120	200	230	500	1600	2300	5000
Average path powers (dB)	−1.0	−1.0	−1.0	0.0	0.0	0.0	−3.0	−5.0	−7.0

TABLE 4.5 – *Delays and relative powers of the various paths for the ETU fading profile.*

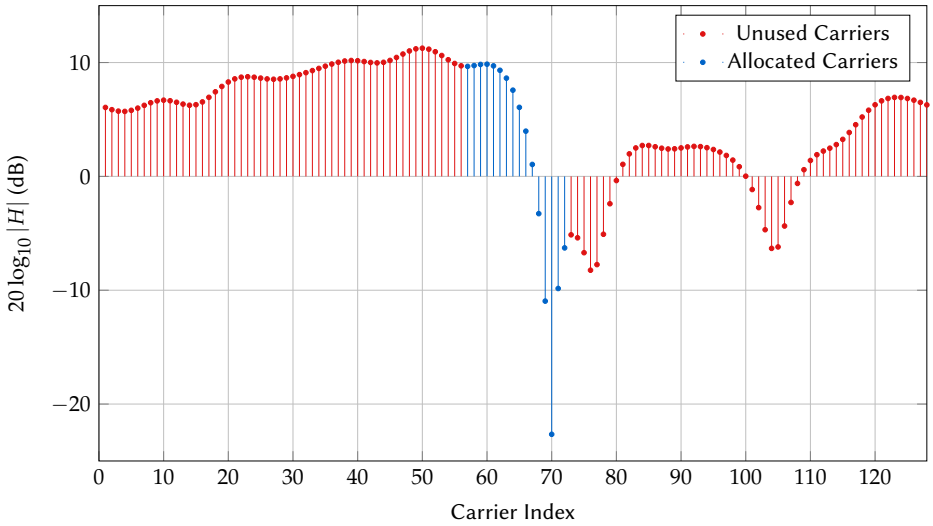

FIGURE 4.13 – *One realization of a Rayleigh fading channel with ETU fading profile.* 16 *allocated carriers.*

For this study, two cases of frequency selective channels are considered: the static case, where the channel does not evolve during time, and the mobility case, where the transmitter or the receiver move relative to one another.

4.3.3.1 STATIC RAYLEIGH FADING WITH ETU PROFILE

For the static case, the channel is considered constant over the whole duration of the transmitted signal. In order to compare the schemes, the performance over a fixed number of channel realizations is computed. Each realization having its own gain, the SNR is estimated at the input of the receiver. In the presented figures, the average SNR over all the realizations is presented on the horizontal axis. All the compared techniques experience the same realizations of channel. A large number of realizations is computed and perfect CSI is considered.

The performance of the 5 schemes for the low throughput scenario is depicted in Figure 4.14. For this scenario, the performance of TC-OFDM, Turbo-FSK and Turbo-ZC are almost similar. The TC-OFDM performs 0.2dB better than Turbo-FSK for a PER of 10^{-2}. The TC-FSK performs 3.1dB worse than TC-OFDM for the same PER, a value comparable to the loss observed in the AWGN case in Figure 4.11. The performance loss compared to Turbo-FSK can be incurred to the use of a different decoder, as the signaling technique is identical. The TC-SC-FDMA shows the worst performance. This can be attributed to the ZF equalizer, which is known to perform poorly under frequency selective channels. Overall, all the schemes demonstrate a frequency diversity which allows them to perform well

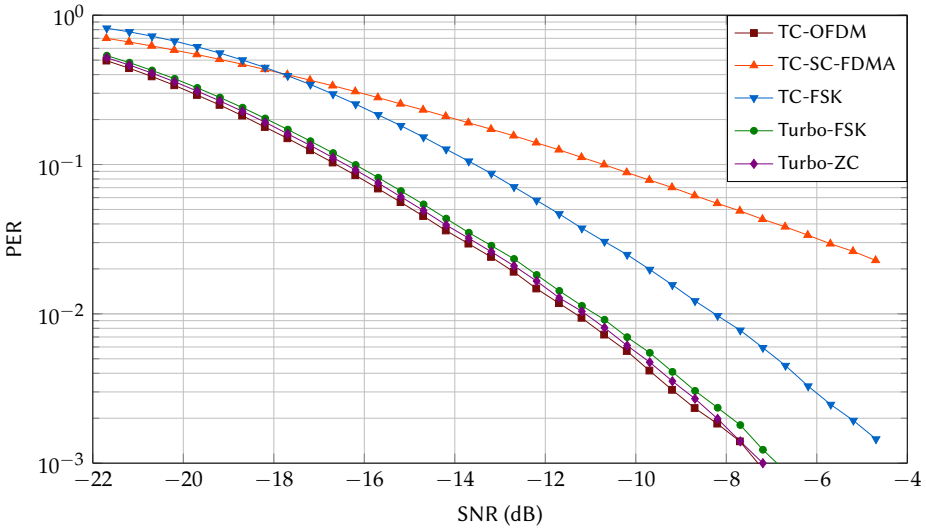

FIGURE 4.14 – *Performance of the* 5 *schemes for the low throughput scenario with parameters from Table 4.3, under the static Rayleigh fading channel with an ETU fading profile.*

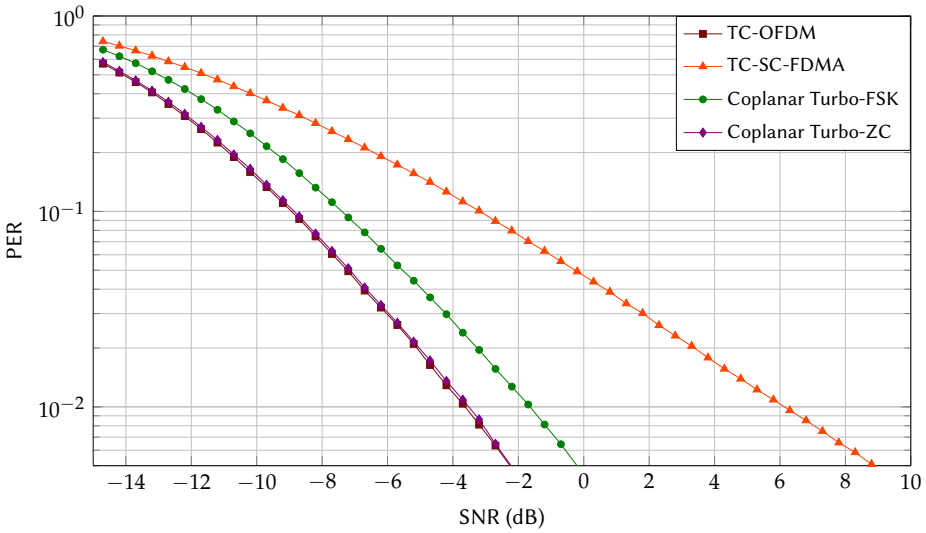

FIGURE 4.15 – *Performance of the 4 schemes for the high throughput scenario with parameters from Table 4.4, under the static Rayleigh fading channel with an ETU fading profile.*

under this type of channel. The 3 best systems can achieve a PER of 10^{-2} at a SNR around -11dB.

The performance when considering the high throughput scenario is depicted in Figure 4.15. As in the other scenario, the TC-SC-FDMA shows poor performance due to the use of the ZF equalizer. TC-OFDM and Turbo-ZC exhibits similar performance, reaching a PER of 10^{-2} at a SNR of -3.8dB. Unlike the low throughput scenario, the Turbo-FSK shows a 1.8dB loss compared to TC-OFDM and Turbo-ZC for the same PER. Both Turbo-FSK and Turbo-ZC use the exact same parameters. The difference in performance can thus be attributed to the use of different signaling techniques. However, this effect is not observed in the low throughput scenario, which may suggest that the use of a higher order of linear modulation ($N_L = 32$ for the high throughput scenario) magnified the difference between the use of ZC signaling and FSK signaling.

The degradation of the performance of the Turbo-FSK with the order of the linear modulation is investigated. Simulations under the Rayleigh fading with the ETU fading profile are performed. The number of active carriers is kept to a constant value equal to $N_A = 16$. An information block size equal to $Q = 1000$ is considered. Both the Turbo-FSK and the Turbo-ZC schemes are considered, with orders of linear modulation equal to $N_L = 1$, 4, 8, 16 and 32 with parameter $\lambda = 5$, 4, 4, 3 and 3 (respectively). Each configuration corresponds to a different value for the spectral efficiency. The performance of all the configurations is depicted in Figure 4.16. The gap between the two schemes remains around 0.2dB for values of N_L up to 8. However, the gap increases to 0.7dB for $N_L = 16$

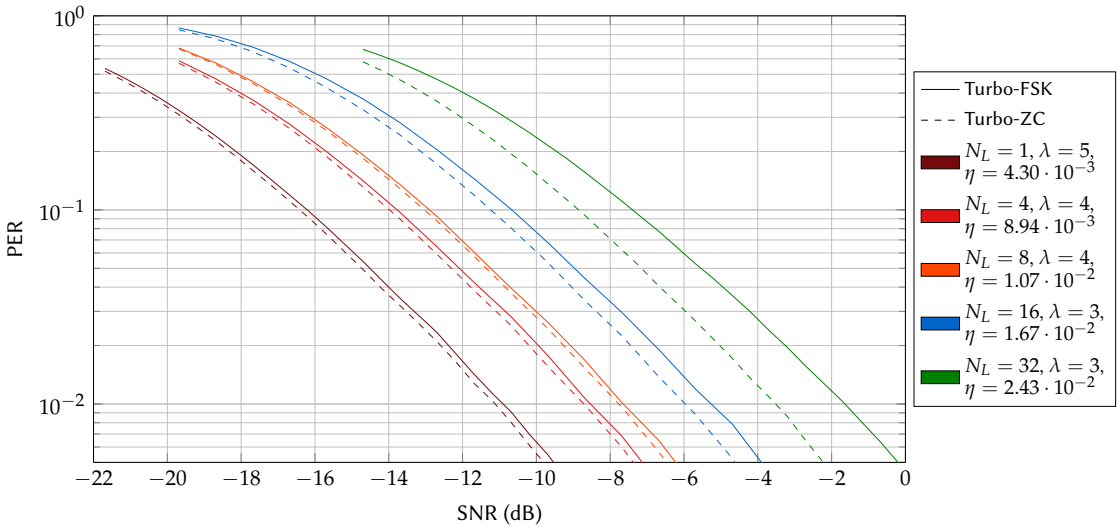

FIGURE 4.16 – *Performance of Turbo-FSK and Turbo-ZC for various sizes of N_L, under the static Rayleigh fading channel with an ETU fading profile.*

and is equal to 1.8dB for $N_L = 32$. The two signaling techniques use frequency diversity in different ways. For the ZC, the use of the sequence can be interpreted as spreading the spectrum on the N_A available carriers. At the receiver, the despreading operation (i.e. the multiplication by the conjugate of the base sequence used) recombines the gains of all of the N_A carriers. This process makes the Turbo-ZC scheme more resilient when the size of the linear modulation is increased. It also requires the use of an additional FFT operation on the N_A carriers which increases the complexity of the receiver.

The Turbo-FSK and Turbo-ZC schemes offer a frequency diversity comparable to the TC-OFDM. However, the frequency spreading used in the Turbo-ZC case is beneficial versus the Turbo-FSK, especially for large orders of linear modulation N_L. The TC-FSK suffers from the same performance loss as in the AWGN case, and the TC-SC-FDMA is disadvantaged because of the use of the inefficient ZF equalizer.

4.3.3.2 Rayleigh Fading with ETU Profile and Mobility

When mobility is considered, the complex gains of the paths evolve with time. This evolution is characterized by the maximum Doppler frequency, given by

$$f_d = \frac{v}{c} \cdot f_c, \tag{4.52}$$

where v is the velocity of the receiver relative to the transmitter, expressed in $\mathrm{m{\cdot}s^{-1}}$, f_c is the carrier frequency, expressed in Hz and c is the speed of light, equal to 299 792 458 $\mathrm{m{\cdot}s^{-1}}$. The Doppler frequency can also be used to estimate the coherence time T_{coh} of the channel, i.e. the time duration for which the channel can be considered correlated. The channel can thus be considered static over a duration short compared to T_{coh}. The coherence time T_{coh} is approximated by

$$T_{\text{coh}} \approx \frac{1}{f_d}. \tag{4.53}$$

In order to generate such channels, Jake's model [99] is considered. Using this model, the coefficients h of Equation (4.2) evolve in time (depending on the value of f_d) for each consecutive sample x. For the static case, the frequency response of the channel was the same for the N_s symbols and estimated by computing a FFT of the coefficients h. When mobility is considered, it is not possible to obtain exact knowledge of the frequency response of the channel, as the $N_{\text{FFT}} + N_{\text{CP}}$ samples of one symbol are affected by varying coefficients h. An average frequency response is thus computed. This average measure can be considered acceptable given that the channel variations are negligible during the symbol time T_s, i.e. $T_s \ll T_{\text{coh}}$. The symbol time given by

$$T_s = \frac{N_{\text{FFT}}}{f_s}, \tag{4.54}$$

where f_s is the sampling frequency (given in Table 4.1 for the different configurations of the LTE). For all the configurations of the LTE, the symbol time is equal to $T_s = 66.6\mu$s.

To illustrate the performance of the scheme considering the different scenarios, simulations are performed using a carrier frequency of $f_c = 2.4$GHz and a velocity equal to $v = 50$ $\mathrm{km{\cdot}h^{-1}}$. Using these parameters, the Doppler frequency is equal to $f_d = 111.2$Hz, giving a coherence time of $T_{\text{coh}} = 8.99$ms. The coherence time is thus 134 times greater than the symbol time. The channel estimation is considered constant for the duration of the multicarrier symbol.

The performance of the 5 schemes under mobility conditions for the low throughput scenario is depicted in Figure 4.17. When compared to the case of the static ETU depicted in Figure 4.14, mobility significantly improves the performance of all the schemes. The schemes benefit from a large redundancy (for example, the TC-OFDM and TC-SC-FDMA encoded bits are repeated more than 17 times, and the TC itself offers redundancy). In the mobility case, the same bit (or symbols) and its repetitions experience different channels gains. Far enough appart repetitions experience gains are partially uncorellated, and the fading effect of the channel is averaged over time. This is a form of time diversity and performance tends toward the AWGN case [15]. While the TC-SC-FDMA exhibited poor performance in the static ETU case, the high number of repetitions overcomes the negative impact of equalization and the scheme is less than 1dB away from TC-OFDM. The TC-FSK scheme is 3.5dB away from the TC-OFDM technique. The difference of performance in the static ETU case was in the same order of magnitude. Thanks to the use of repetition and a low spectral efficiency modulation technique, the TC-FSK scheme also benefits from diversity. The Turbo-FSK and the Turbo-ZC, which had a performance gap of 0.2dB for a PER of 10^{-2} in the static ETU case, now exhibits a 0.6dB gap. Both schemes use $\lambda = 5$ repetitions, which offers a diversity comparable to the other techniques.

The performance under mobility conditions for the high throughput scenario is depicted in Figure 4.18. Both the TC-OFDM and TC-SC-FDMA schemes benefit from diversity due to the redundancy, but at a smaller extent as

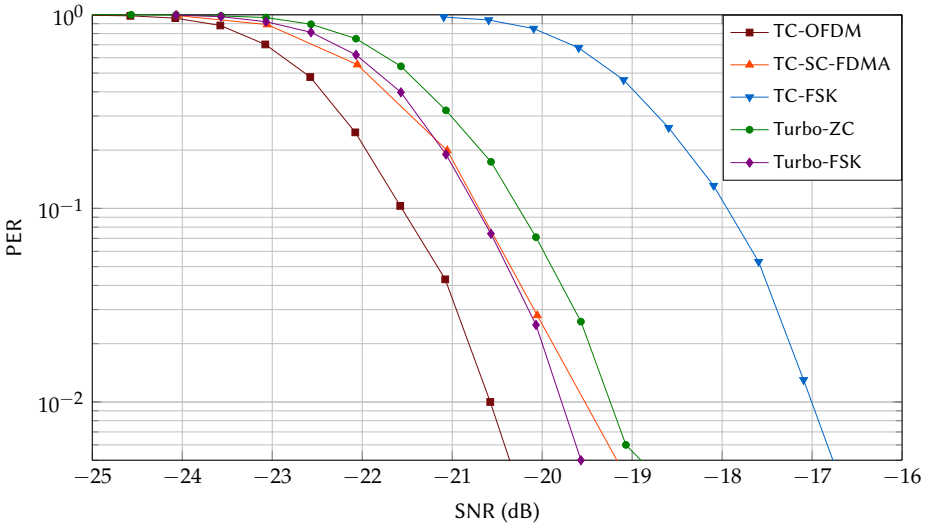

FIGURE 4.17 – *Performance of the* 5 *schemes for the low throughput scenario with parameters from Table 4.3, under the Rayleigh fading channel with an ETU fading profile and mobility. The carrier frequency is set to* 2.4*GHz and the speed is* 50 $km{\cdot}h^{-1}$.

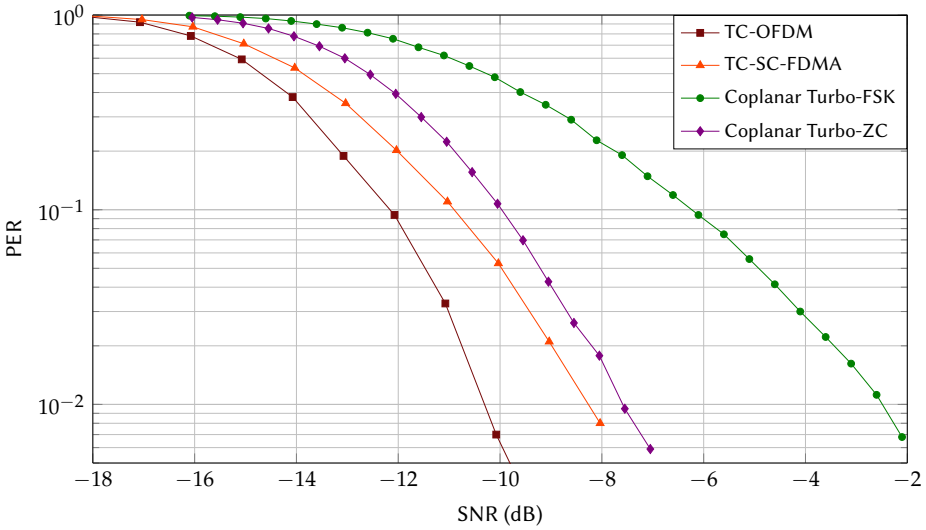

FIGURE 4.18 – *Performance of the* 4 *schemes for the high throughput scenario with parameters from Table 4.4, under the Rayleigh fading channel with an ETU fading profile and mobility. The carrier frequency is set to* 2.4*GHz and the speed is* 50 $km{\cdot}h^{-1}$.

there are only 3 repetitions. The curves tend less towards the AWGN case. While the Coplanar Turbo-ZC reached the performance of TC-OFDM for the static ETU case and was 0.5dB away at a PER of 10^{-2} in the AWGN case, the gap with TC-OFDM is now equal to 2.4dB. The Coplanar Turbo-FSK shows even worse performance and the gap between Coplanar Turbo-FSK and Coplanar Turbo-ZC is now equal to 5.4dB. For the Coplanar Turbo-FSK and the Coplanar Turbo-ZC, this lack of diversity gain could be explained by the combination of two aspects: the value of the parameter λ reduced to 3 and the number of orthogonal codewords drastically reduced. More information is mapped on the linear dimensions. This combination has a strong negative effect for the Coplanar Turbo-FSK, but it has less effects for the Coplanar Turbo-ZC. The spread spectrum feature of the ZC signaling seems again beneficial and the Coplanar Turbo-ZC outperforms the Coplanar Turbo-FSK.

The gains of performance in dB due to mobility at 50 $km{\cdot}h^{-1}$ versus the static ETU case for a PER of 10^{-2} are given in Table 4.6. As previously observed, gains in the low throughput scenarios are higher due to the large number of repetitions and the high redundancy of each scheme. The FSK, Turbo-FSK and Turbo-ZC show rather similar gains. However, in the high throughput scenario, gains are lower. Schemes benefit from less diversity due to the reduced redundancy. The Turbo-FSK shows a small gain, only 0.9dB.

The performance demonstrates that the various levels of redundancy for each scheme are beneficial in mobility conditions. Also, the Coplanar Turbo-ZC scheme outperforms the Coplanar Turbo-FSK, which can be explained

Waveforms	TC-OFDM	TC-SC-FDMA	TC-FSK	Turbo-FSK	Turbo-ZC
Low Throughput Scenario	9.3	18.1	8.7	8.3	8.7
High Throughput Scenario	6.7	14.4	N/A	0.9	4.4

TABLE 4.6 – *Gain of performance in dB due to mobility at* 50 $km{\cdot}h^{-1}$ *versus the static ETU case, for all the schemes and scenarios and for a PER of* 10^{-2}.

by its use of a spread spectrum technology. Nonetheless, only one configuration was studied, and perfect CSI was assumed. When larger values of Doppler frequency f_d are considered (i.e. larger velocity or carrier frequency, or both), the channel estimation can reveal itself cumbersome.

4.3.4 Complexity

In order to evaluate the complexity of the different receivers, we only consider the operations computed by the Demodulator/Decoder of Figure 4.1, as the rest of the operations are common to all schemes. All the receivers use a turbo decoder, but there are two distinct decoders: the decoder of the TC [13 15] and the Turbo-FSK decoder (which is common to both Turbo-FSK and Turbo-ZC). The computations of each receiver can be decomposed into 6 procedures, given as follow:

Procedure 1 Compute the channel metric (LLR or codewords likelihood). This procedure is computed for each scheme using the equations summarized in Table 4.2.

Procedure 2 Perform depuncturing or combine repetitions.

Procedure 3 Compute transition metrics for the BCJR algorithm. For Turbo-FSK, this is done using Equation (2.13) using the max-log approximation and the log of Equation (3.17). For the TC, the log of Equation (C.27) is used.

Procedure 4 Execute the Forward-Backward steps of the BCJR algorithm. This is done computing Equation (2.30) and Equation (2.31).

Procedure 5 Extract the log-APP from the probabilities generated by the BCJR algorithm. This is computed using Equation (3.16) and the max-log approximation.

Procedure 6 Compute extrinsic information to be fed to the other(s) decoder(s). This is done by removing the *a priori* log-ratios from the log-APP computed.

Procedures 1 and 2 are computed once as they consist of computing the channel observations for the turbo decoder. Procedures 3 to 6 perform the turbo decoding and are repeated as many times as there are iterations. The number of iterations is denoted ι.

Using the various equations previously introduced, the complexity of each procedure is estimated. Procedure 1 is specific to each scheme as it is the computation of the LLR or the likelihood of the codewords. The complexity in number of addition (ADD), max operation (MAX), multiplication (MULT) and division (DIV) for procedure 1 is given in Table 4.7. To obtain these values, we considered that a MAX operation on N elements can be done using $(N/2-1)$ MAX operations on 2 elements. We also considered the use of the FFT algorithm of size N to be done using $N\log_2(N)$ complex MULT (where 1 complex MULT is equivalent to 4 MULT and 2 ADD) and $N\log_2(N)$ complex ADD (where 1 complex ADD is equivalent to 2 ADD). Overall, 3 parameters influence the complexity: the number of symbols N_s, the number of active carriers N_A and for the Turbo-FSK and the Turbo-ZC, the size of the linear modulation N_L. For this last parameter, the use of the PSK modulation leads to simplifications. The expression inside the real part of the likelihood when the elements z_p are pure real (i.e. 1 or -1) or pure imaginary (i.e. j or $-j$) can be computed without multiplications. Since only the real part is considered, the complex multiplication can be simplified to 2 MULT and 1 ADD (the same simplification is done for the FSK).

The complexity of the other procedures when using the two possible decoders is estimated and given in Table 4.8. Due to the use of the max-log approximation, only MAX and ADD operations are computed. Procedure 2 implies operations only if the rate R_m is below 1, as it signifies that bits or codewords were repeated at the transmitter and would need to be recombined. The other procedures are repeated as many times as the number of iterations ι. They are also repeated 2 times for the TC (corresponding to the 2 Recursive Systematic Convolutional (RSC) decoders) and λ for the Turbo-FSK decoder. The complexity also depends on the length of the trellis, equal to $(Q+3)$ for the TC and to (N_q+1) for the Turbo-FSK. For the Turbo-FSK decoder, the size of the alphabet M (with $M = N_\perp N_L$) also appears to have an influence.

Waveform	Operation			
	MAX	ADD	MULT	DIV
OFDM	0	$2N_AN_s$	$4N_AN_s$	0
SC-FDMA	0	$(4N_A - 1 + 4N_A\log_2(N_A)) \times N_s$	$(3 + 2\log 2(N_A)) \times 2N_AN_s$	$(1 + 4N_A) \times N_s$
FSK	$2\left(\frac{N_A}{2} - 1\right)\log_2(N_A) \times N_s$	$(3N_A + \log_2(N_A)) \times N_s$	$4N_AN_s$	0
Turbo-FSK ($N_L \leq 4$)	0	$(2 + N_L) \times N_AN_s$	$4N_AN_s$	0
Turbo-FSK ($N_L > 4$)	0	$(2N_L - 1) \times N_AN_s$	$(N_L - 1) \times 2N_AN_s$	0
Turbo-ZC ($N_L \leq 4$)	0	$(2 + 2\log_2(N_A)) \times 2N_AN_s$	$(2 + \log_2(N_A)) \times 4N_AN_s$	0
Turbo-ZC ($N_L > 4$)	0	$(N_L + 4\log_2(N_A)) \times N_AN_s$	$(N_L + 2\log_2(N_A)) \times 2N_AN_s$	0

TABLE 4.7 – *Complexity of procedure* 1 *for the* 5 *different schemes.*

FEC	TC [13 15]		Turbo-FSK	
Operation	ADD	MAX	ADD	MAX
Procedure 2 (if $R_m < 1$)	$(3Q + 12)/R_m$	0	$(N_q + 1) \times \frac{\lambda M}{R_m}$	0
Procedure 3	$(5(Q + 3) + Q) \times 2\iota$	0	$(M\log_2(M) + 1) \times (N_q + 1)\lambda\iota$	$\left(\frac{M}{4} - 1\right)(N_q + 1) \times \lambda\iota$
Procedure 4	$32(Q + 3) \times 2\iota$	$16(Q + 3) \times 2\iota$	$8(N_q + 1) \times \lambda\iota$	$4(N_q + 1) \times \lambda\iota$
Procedure 5	$33Q \times 2\iota$	$14Q \times 2\iota$	$(Q + 2MN_q) \times \lambda Q\iota$	$2\left(\frac{M}{2} - 1\right) \times \lambda Q\iota$
Procedure 6	$2Q\iota$	0	$\lambda Q\iota$	0

TABLE 4.8 – *Complexity of procedures* 2 *to* 6 *for the two possible decoders (TC and Turbo-FSK).*

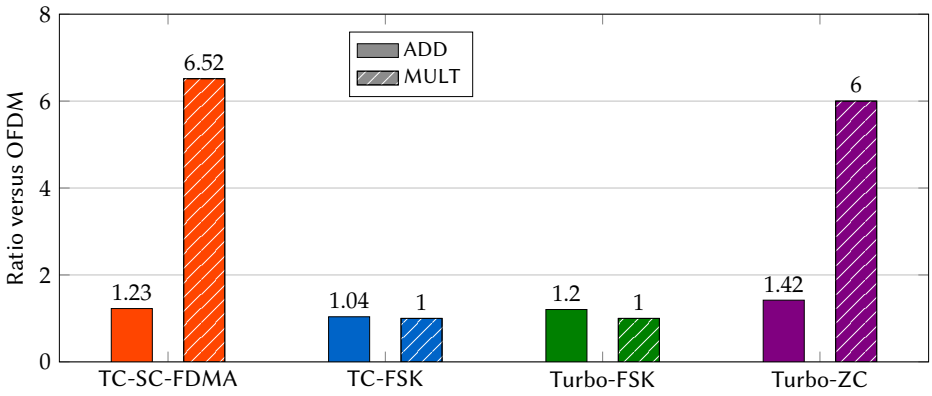

FIGURE 4.19 – *Complexity ratios with respect to the TC-OFDM, for the low throughput scenario.*

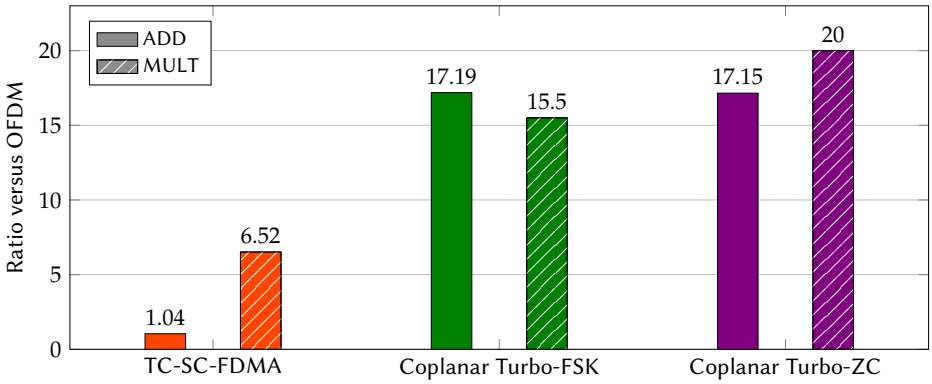

FIGURE 4.20 – *Complexity ratios with respect to the TC-OFDM, for the high throughput scenario.*

The complexity of the 4 schemes TC-SC-FDMA, TC-FSK, Coplanar Turbo-FSK and Coplanar Turbo-ZC is evaluated versus the complexity of TC-OFDM, for the two scenarios. The number of possible operations is reduced to 2: a MAX operation is considered equivalent to an ADD (it can be performed by a substraction and a test of the sign of the results) and a DIV is assimilated to a MULT (which can be considered underestimated but is sufficient for our comparison). Both the number of ADD (and MAX) of all procedures and the number of MULT (and DIV) of procedure 1 are computed for the two scenarios introduced in this section.

The complexity for the low throughput scenario is depicted in Figure 4.19. For the TC-SC-FDMA and the Turbo-ZC, the ratio of MULT traduces the increase of complexity due to the use of more complex demodulation algorithms. Specifically, these two receivers require the use of a FFT algorithm which performs a large amount of MULT and ADD. The TC-FSK and Turbo-FSK do not need additional MULT when compared to the TC-OFDM. This is because the imaginary part of the product of the output of the FFT (denoted Y) with the channel coefficient (H) is ignored, when it must be considered for the TC-OFDM. With the necessity to compute the gain of the channel ($|H|^2$) for the TC-FSK and the Turbo-FSK, the number of multiplications becomes equivalent. Concerning the ratio of ADD, the use of pre-coding in the TC-SC-FDMA induces an increase of 23%. The ratio of ADD for TC-FSK is close to one, because of the repetition. Indeed, the TC-OFDM is repeated more than 17 times while the TC-FSK is repeated approximately 2 times. The complexity increase of the TC-FSK decoding is compensated by the number of ADD necessary to recombine the LLR. The Turbo-FSK has a ratio of 20%. This ratio combines the facts that Turbo-FSK does not use repetition (hence less ADD) but has a different decoding algorithm. This means that one or several procedures of the decoder requires a large number of additions.

The complexity of the high throughput scenario is depicted in Figure 4.20. The TC-SC-FDMA exhibits the same ratio of MULT as in the other scenario, which traduces the fact that the ratio of MULT is independent of the number of symbols. The ratio of ADD is closer to 1, as less FFT operations are computed. The ratios of complexity for both Coplanar Turbo-FSK and Coplanar Turbo-ZC is much larger for this scenario. The ratio of ADD is close to 17 for both schemes while the ratio of MULT peaks at 20 for the Coplanar Turbo-ZC and at 15.5 for Coplanar Turbo-FSK. While the value N_s was reduced, the value of N_L was multiplied by 32 for this scenario. Considering the equations of complexity of Table 4.7 and Table 4.8, this affects procedures 1, 3 and 5. Particularly, procedure 3 depends on product $M \log_2(M)$ which increases rapidly with M.

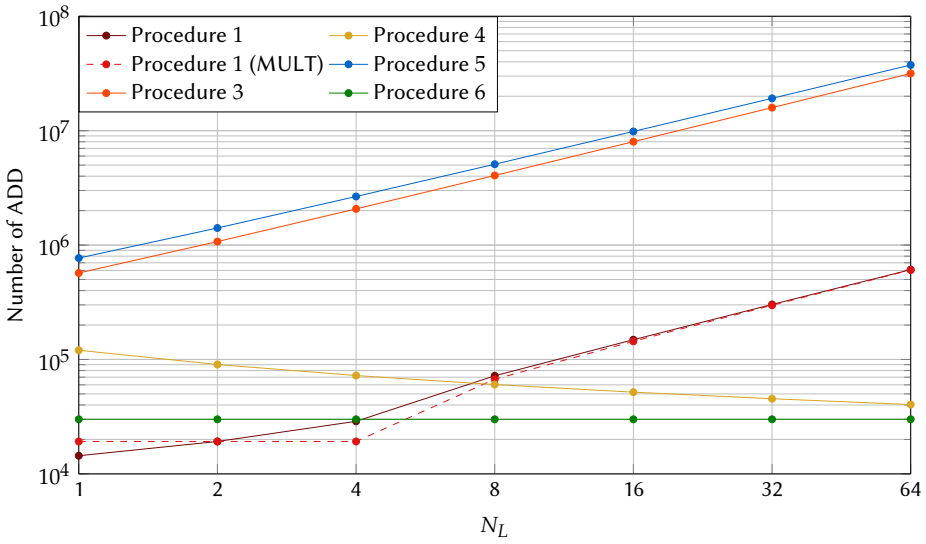

FIGURE 4.21 – *Complexity of all the procedures of the Coplanar Turbo-FSK versus the size of the linear modulation* N_L*, with* $N_s = 300$*,* $Q = 1000$*,* $N_A = 16$ *and* $\iota = 10$*.*

For a better understanding of the complexity of each procedure, complexity of Coplanar Turbo-FSK is computed for various values of N_L. The other parameters are kept constant, i.e. $N_s = 300$, $Q = 1000$, $N_A = 16$ and $\iota = 10$. The complexity for all procedures is depicted in Figure 4.21. The results confirm the linear dependency of procedures 3 and 5 with N_L. As the size of the linear modulation grows exponentially, the number of ADD for both procedures does too. Procedure 3 involves a lot of ADD as it includes the recombination of the *a priori* log-ratios into codeword probabilities. Procedure 5 recombines, for each section, the M branches of the trellis to compute the $\log_2(M) - 1$ information bits associated to the section. Because of the dependency with M, the complexity in number of ADD for these 2 procedures becomes cumbersome for very large sizes of alphabet. Procedure 1 exhibits different tendencies depending on the value of N_L. For small sizes, the computation of the likelihood indeed simplifies. However, when the size of N_L is above 8, the number of both ADD and MULT increase in a linear manner with N_L.

The complexity of the 5 schemes has been done considering the mathematical expressions only. Other simplifications or approximations could be considered in order to reduce the complexity. For the case of Coplanar Turbo-FSK, procedure 3 and 5 exhibits a linear evolution with the size of alphabet. Optimization of the computation of these procedures should be studied to reduce the complexity of the receiver.

4.3.5 SYNTHESIS

The performance of each scheme is summarized in a 5-point axis representations, in Figure 4.22 for the low throughput scenario and in Figure 4.23 for the high throughput scenario. The 5 axes represent: how constant is the envelope (which gives a low value for large variations and vice versa), the performance under the AWGN channel relative to TC-OFDM, under the Rayleigh fading channel with ETU fading profile, with both static and mobility (with $v = 50$ km·h^{-1} and $f_c = 2.4$GHz) conditions and also relative to TC-OFDM, and finally the implementation efficiency compared to TC-OFDM.

For the low throughput scenario, the Turbo-FSK offers the best compromise. Its constant envelope property distinguishes its performance from TC-OFDM. Turbo-ZC exhibits a lower implementation efficiency due to the use of an additional FFT at the receiver, and does not have a constant envelope. TC-FSK has a constant envelope and a high implementation efficiency but the combination of FSK and the TC offers a less interesting performance. Finally, the TC-SC-FDMA has a performance similar to the OFDM in AWGN and in mobility (because of the high redundancy of the scheme for this scenario) and less variations of envelope, but the use of the ZF equalizer does not allow the scheme to perform well under static ETU conditions. Moreover the FFT algorithm required at the receiver increases the complexity.

The TC-OFDM and the TC-SC-FDMA have the same performance when considering the high throughput scenario. For both schemes, increasing the throughput was done by reducing only the repetition factor. For Coplanar Turbo-FSK and Coplanar Turbo-ZC, considering a higher throughput was done by changing intrinsic characteristics of the schemes. These modifications deeply impact the performance and complexity, and also emphasize the differences in the choice of the orthogonal alphabet. The Coplanar Turbo-ZC trades the constant envelope at the benefit

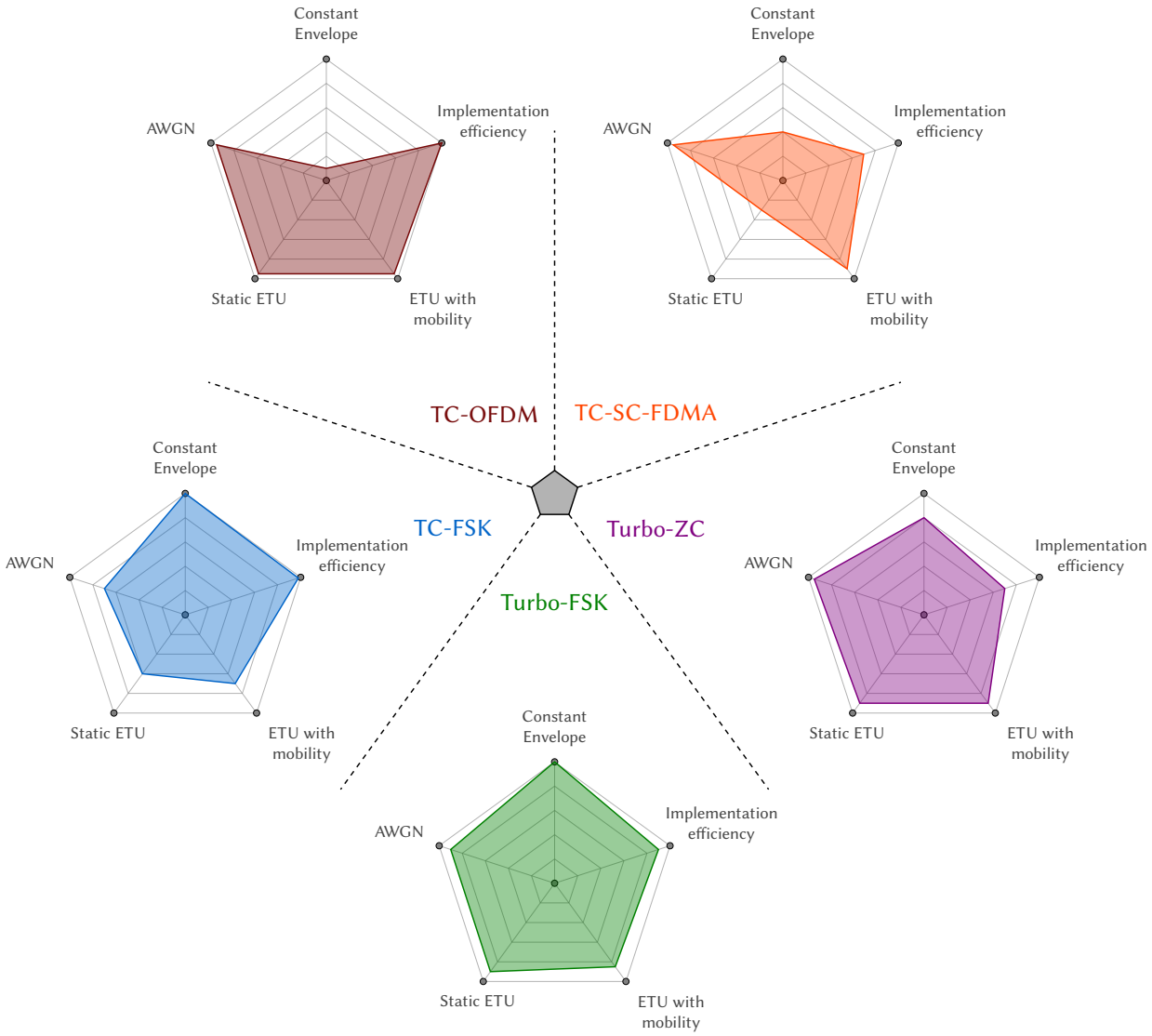

FIGURE 4.22 – *Performance of the compared schemes for the low throughput scenario.*

of a better use of the frequency diversity and a better resilience to mobility scenarios. Compared to TC-OFDM, the Coplanar Turbo-ZC trades an increased complexity for a better IAPR.

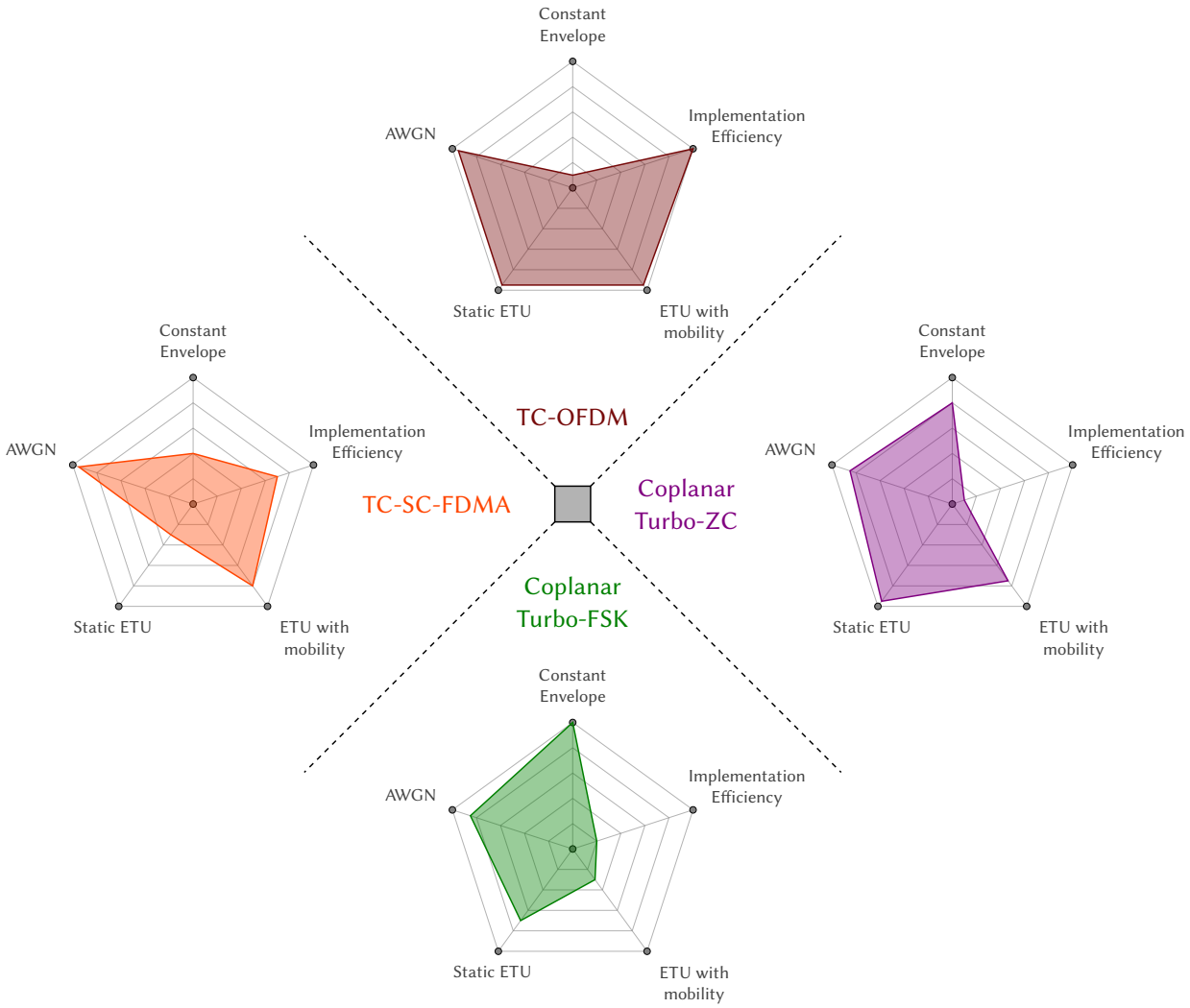

FIGURE 4.23 – *Performance of the compared schemes for the high throughput scenario.*

4.4 Conclusion

The Turbo-FSK scheme has been designed in order to address the issues related to the LPWA context. Coplanar Turbo-FSK, designed in Chapter 3, allows for a larger flexibility in spectral efficiency while reaching performance close to the minimum achievable E_b/N_0. So far, the studies have been restrained to a theoretical context. The algorithms were considered without approximations and simulations were performed under the AWGN channel. For a more practical approach, more realistic channels must be considered along with the study of a system taking into account implementation and complexity problematics. While the max-log approximation is considered for the turbo receivers, frequency selective channels are considered for the signal's propagation. The techniques of TC-OFDM, TC-SC-FDMA and TC-FSK are chosen for comparison. They all use the powerful [13 15] TC. Two use cases of the Coplanar Turbo-FSK design are considered: one using a FSK alphabet, as presented in Chapter 3, and one using an orthogonal alphabet constructed from ZC sequences, called Turbo-ZC. When a low throughput scenario is considered, Turbo-FSK equals the performance of TC-OFDM but with an IAPR equal to 0dB. This fundamental property of Turbo-FSK guarantees the use of a power and cost efficient PA, dramatically reducing the consumption of the transmitter. Turbo-FSK is thus the most suitable solution when considering low rate scenarios. When a higher throughput scenario is considered, Coplanar Turbo-ZC exhibits a better resilience to frequency selective channels versus Coplanar Turbo-FSK. The study of this scheme demonstrates that the Coplanar Turbo-FSK scheme proposed in Chapter 3 performs well even when considering other orthogonal alphabets. When compared to TC-OFDM, the Coplanar Turbo-ZC scheme trades an increased complexity for less variations of its envelope (thus a lower PAPR). Both TC-OFDM and Coplanar Turbo-ZC seems to be the most suitable solutions for scenarios where a higher throughput is considered.

In all these simulations, perfect CSI was considered, along with a perfect time and frequency synchronization. Further studies should both include imperfections in the estimation of these elements, and requirements for additional synchronization features, such as the number of pilots necessary for a acceptable channel estimation.

The work presented in this chapter will be submitted at the conference *Network of the Future* in 2017 [100].

Other implementations of the Turbo-FSK have been studied. Using off-the-shelf components, a Turbo-FSK using a 4-FSK modulation and non-coherent detection was implemented in a system using the 848MHz Industrial, Scientific and Medical (ISM) band. The implemented system outperforms the simple repetition scheme and demonstrates the sustainability of the proposed solution even on low cost components. This work was presented at the ISWCS'16 conference [101].

Chapter Summary

In this chapter, 5 schemes have been introduced. The FFT-based implementation shared by all the schemes was reviewed, along with both the Encoding/Modulating and Demodulating/Decoding procedures. For each scheme, the derivation of the decoder's metric (either LLR or likelihoods) was derived for the general expression of the likelihood of one sequence. The system was then implemented, and simulations under various conditions were performed. Two scenarios for the parameters were considered, a low throughput scenario and a high throughput scenario. Three signal propagation conditions have been studied: the AWGN channel, and the Rayleigh fading channel with an ETU fading profile with both static and mobility conditions. The IAPR of all the schemes was computed, and the complexity of each receiver was estimated based on the mathematical expressions. Finally, a graphical synthesis of the comparisons for both scenarios was presented.

Bibliography of Chapter 4

[15] J. Proakis. *Digital Communications 3rd Edition*. Communications and signal processing. McGraw-Hill, 1995.

[19] P. Bento et al. "Measuring the Magnitude of Envelope Fluctuations: Should We Use the PAPR?" In: *2014 IEEE 80th Vehicular Technology Conference (VTC2014-Fall)*. 2014, pp. 1–5.

[50] D. Chu. "Polyphase Codes with Good Periodic Correlation Properties (Corresp.)" In: *IEEE Transactions on Information Theory* 18.4 (1972), pp. 531–532.

[56] *LTE Evolved Universal Terrestrial Radio Access (E-UTRA): Physical Channels and Modulation*. 3GPP TS 36.211, V13.2.0, Release 13. 2016.

[89] S. B. Weinstein. "The History of Orthogonal Frequency-Division Multiplexing [History of Communications]". In: *IEEE Communications Magazine* 47.11 (2009), pp. 26–35.

[90] Y. Wu. "Orthogonal Frequency Division Multiplexing: A Multi-Carrier Modulation Scheme". In: *Proceedings of International Conference on Consumer Electronics*. 1995, pp. 8–.

[91] R. van Nee and R. Prasad. *OFDM for Wireless Multimedia Communications*. 1st. Norwood, MA, USA: Artech House, Inc., 2000.

[92] L. Cimini. "Analysis and Simulation of a Digital Mobile Channel Using Orthogonal Frequency Division Multiplexing". In: *IEEE Transactions on Communications* 33.7 (1985), pp. 665–675.

[93] Y. Zhao and S. G. Haggman. "Sensitivity to Doppler Shift and Carrier Frequency Errors in OFDM Systems-the Consequences and Solutions". In: *Proceedings of Vehicular Technology Conference - VTC*. Vol. 3. 1996, 1564–1568 vol.3.

[94] R. van Nee and A. de Wild. "Reducing the Peak-to-Average Power Ratio of OFDM". In: *Vehicular Technology Conference, 1998. VTC 98. 48th IEEE*. Vol. 3. 1998, 2072–2076 vol.3.

[95] Y. Rahmatallah and S. Mohan. "Peak-To-Average Power Ratio Reduction in OFDM Systems: A Survey And Taxonomy". In: *IEEE Communications Surveys Tutorials* 15.4 (2013), pp. 1567–1592.

[96] M. Geles, A. Averbuch, O. Amrani, and D. Ezri. "Performance Bounds for Maximum Likelihood Detection of Single Carrier FDMA". In: *IEEE Transactions on Communications* 60.7 (2012), pp. 1945–1952.

[97] Z. Wang and G. B. Giannakis. "Wireless Multicarrier Communications". In: *IEEE Signal Processing Magazine* 17.3 (2000), pp. 29–48.

[98] *Evolved Universal Terrestrial Radio Access (E-UTRA): Base Station (BS) Radio Transmission and Reception*. 3GPP TS 36.104, V14.3.0, Release 14. 2017.

[99] W. C. Jakes and D. C. Cox, eds. *Microwave Mobile Communications*. Wiley-IEEE Press, 1994.

[100] Y. Roth, J.-B. Doré, L. Ros, and V. Berg. "Contenders for Low Power Wide Area Networks". In: *To be submitted*. 2017.

[101] J. Estavoyer, Y. Roth, J.-B. Doré, and V. Berg. "Implementation and Analysis of a Turbo-FSK Transceiver for a New Low Power Wide Area Physical Layer". In: *2016 International Symposium on Wireless Communication Systems (ISWCS): Special sessions (ISWCS'2016 - Special sessions)*. Poznan, Poland, 2016.

Conclusion

When it comes to Low Power Wide Area (LPWA) solutions, reaching low sensitivity levels is of main concern. Low data rate transmission must be considered, and two main strategies are usually considered: the use of narrow band signaling or the choice of a low spectral efficiency technique. Following the second approach, the Turbo-FSK scheme was designed based on the pairing of 4 elements: orthogonal modulations, convolutional coding, repetition and iterative decoding. The combination of modulation and coding structures the sequence which is represented with a trellis. The transmitter sends multiple sequences corresponding to the information bit and the receiver performs iterative decoding of the various repetition. The scheme proves itself to be highly energy efficient, providing the correct metric to be chosen for the receiver's computations. Turbo-FSK allows for low levels of sensitivity to be reached. With optimized parameters, it outperfoms existing LPWA solutions. A generalization of Turbo-FSK, so-called Coplanar Turbo-FSK, was then proposed. It is based on the combination of both orthogonal and linear modulations. The scheme achieves not only low levels of sensitivity but also a flexibility in spectral efficiency. The scheme matches a wider range of applications, alike practical systems. Eventually, the scheme was compared to sophisticated techniques such as the Turbo Coded Orthogonal Frequency Division Multiplexing (TC-OFDM). The results emphasized the capacity of Turbo-FSK to offer a constant envelope while maintaining performance close to the powerful [13 15] Turbo Code (TC), even on frequency selective channels and in mobility conditions.

The **first chapter** introduced the general LPWA context. After explaining the requirements for such networks, the key system parameters were presented. This included the definition of the sensitivity, a crucial metric for our context, and a review of the channel capacity along with the interpretation of its maximum achievable spectral efficiency. The 3 main elements of the physical layer were then introduced: the channel, the modulation and the Forward Error Correction (FEC). Orthogonal modulations were introduced with their probabilistic decoding. For each modulation technique, the closed form expression of the bit error probability was presented. A review of various FEC techniques were done, concluding with the presentation of the powerful TCs. Finally, some existing LPWA schemes were presented, and a simulation environment was set. Performance of the schemes was computed and the reachable levels of sensitivity of each technique were presented. Throughout the chapter, the performances were confronted with the maximum achievable spectral efficiency as interpreted from Shannon's limit. This demonstrates the distance between the limit and selected techniques. Additionnally, this emphasizes how the orthogonal modulations reach the limit for an infinite size of alphabet or how efficient a TC can be.

The Turbo-FSK is extensively studied in the **second chapter**. The preliminary considerations and reflexions that led to the design of the scheme were presented first. The scheme relies on the use of a combination of orthogonal modulation and a convolutional code, associated with an iterative receiver. The transmitter was introduced, including the specific trellis construction. The receiver was then detailed, with a complete mathematical derivation of its procedures, and some typical performances of the scheme were presented. This demonstrates the receiver's necessity to employ the orthogonal codewords metric. The choice of the binary words metric severely impacts the performance. The study of the parameters' influence on the performance also emphasized that finding the best parameter couple is a non-trivial matter. Optimization of the parameters was thus considered, using the EXtrinsic Information Transfer (EXIT) chart tool. The EXIT chart for the specific case of the Turbo-FSK was introduced and the asymptotic performance of the scheme was evaluated. The parameter couple minimizing the E_b/N_0 corresponds to a size of alphabet $M = 512$ and the parameter $\lambda = 3$. The scheme with these parameters approaches the minimum achievable E_b/N_0 as close as 0.284dB. Performance, when the block size is set to 1000 bits, gets as close as 1.35dB to the ultimate $(E_b/N_0)_{\min}$. The Turbo-FSK with optimized parameters was then compared to the existing LPWA solutions, and outperformed the well-known [13 15] TC by 1dB. The results demonstrate the potential of Turbo-FSK as a long range solution over the Additive White Gaussian Noise (AWGN) channel.

If the Turbo-FSK scheme showed promising performance when low spectral efficiencies were considered, its

design would not suit applications requiring higher data rates. Spectral efficiency flexibility was thus introduced in the **third chapter**. The Orthogonal with Coplanar Subsets (OCS) modulation was presented as a mix of orthogonal and linear modulations. This modulation offers a flexible spectral efficiency while maintaining orthogonality in the trellis to a certain extent. The maximum likelihood receiver of the modulation was derived. The performance of the modulation itself is not remarkable, but its use associated with the Turbo-FSK technique was investigated. The new scheme, so-called Coplanar Turbo-FSK, uses both the specific alphabet defined for the OCS modulation and a puncturing procedure to achieve spectral efficiency flexibility. The transmitter including these two features was presented, as well as the receiver's architecture and its derivations. The scheme has 5 degrees of freedom: the mapping of the codewords on the trellis, the puncturing rate, the size of the orthogonal modulation, the size of the linear modulation and the number of stages. This large number of parameters makes a joint optimization cumbersome. Instead, the study focused on 4 aspects: the choice of mapping, the choice of linear modulation, the influence of puncturing and the performance versus the channel capacity. Selecting a mapping that maintains some orthogonal constraints between the transition was demonstrated to impact the performance less. Various shapes of 8-Amplitude Phase-Shift Keying (APSK) modulation were studied as the linear modulation. The 8-Phase Shift Keying (PSK) exhibited the best performance while maintaining a constant envelope. Puncturing the Coplanar Turbo-FSK increases the spectral efficiency at the expense of some performance loss. It can also be used to lower the error floor in some configurations. The performance of Coplanar Turbo-FSK was confronted to the minimum achievable E_b/N_0. The results confirmed that the scheme can reach higher levels of spectral efficiency, with an increasing performance loss as the size of the linear modulation increases.

The goal of the **fourth chapter** was to study the proposed scheme in a more practical system. An implementation on top of an Orthogonal Frequency Division Multiplexing (OFDM) transceiver was realized. Schemes based on the Turbo-FSK principle were compared to schemes based on a classic TC. Three schemes using the [13 15] TC were selected: TC-OFDM, Turbo Coded Single Carrier Frequency Division Multiple Access (TC-SC-FDMA) and Turbo Coded Frequency Shift Keying (TC-FSK) modulation. Coplanar Turbo-FSK was also considered, along with an alternative, so-called Coplanar Turbo-ZC, where the orthogonal alphabet is constructed from a Constant Amplitude Zero Auto-Correlation (CAZAC) sequence, the Zadoff-Chu (ZC) sequence. The presentation of the Fast Fourier Transform (FFT) architecture led to the expression of the likelihood of the sequence. From this expression, the metric of each receiver (either Log Likelihood Ratio (LLR) or likelihood) was derived based on the modulation method, i.e. the method of sequence construction. Using the general parameters of the mode 1.4MHz of the Long Term Evolution (LTE), two scenarios were then considered: a low throughput scenario (8kbps) and a high throughput scenario (46kbps). Each scenario has a different spectral efficiency. Specific parameters were selected for each scheme. The Instantaneous-to-Average Power Ratio (IAPR) of each scheme was computed, demonstrating the constant envelope of the Frequency Shift Keying (FSK) modulation. Performance under the AWGN channel and the Rayleigh fading channel was assessed, and both static and mobility conditions were considered. Complexity with regard to the TC-OFDM was also estimated based on the mathematical expressions of the receiver. The synthesis of the comparison revealed that for low throughput scenarios, Turbo-FSK is compelling even versus OFDM. It exhibits minor differences in complexity and performance under all conditions but benefits from a constant envelope. This undeniably reduces constraints for the Power Amplifier (PA). However, when the high throughput scenario was considered along with frequency selective channels, the Coplanar Turbo-ZC scheme outperforms the Coplanar Turbo-FSK. Its efficient use of frequency diversity thanks to its spread spectrum feature allows the Coplanar Turbo-ZC to perform better for large sizes of linear modulation. However, the complexity becomes overwhelming compared to the TC-OFDM, which remains an attractive solution for high throughputs. Nonetheless, the complexity increase is done at the benefit of reduced variations of the envelope.

Main Contributions

The LPWA networks is a trending topic. Many industrial solutions exist and a standardization by the 3rd Generation Partnership Project (3GPP) is in progress. In this context, the main contributions of this work are:

- **A solution based on the low spectral efficiency strategy which approaches the limit of the information theory**
  The existing solutions consider various technological constraints (constant envelope, complexity, etc). The Turbo-FSK [84] was designed considering the limits from the information theory. Starting from a concept, the scheme was optimized and demonstrated the ability to achieve performance close to the minimum achievable E_b/N_0 [86, 83]. Technological constraints were also considered as the transmitter of Turbo-FSK benefits from a low complexity and a constant envelope, a crucial feature in the context of low power transmission.

- **Questioning the system and improving the flexibility**
  Even if Turbo-FSK is solely designed for low data rate applications, it is also imperative to widen the range of possible applications. For this to be possible, the OCS modulation has been introduced and an extension of the Turbo-FSK using this modulation, the Coplanar Turbo-FSK, was presented. This evolution of the original scheme is capable of achieving a wide range of the spectral efficiency [87]. This technology has been patented [88].
- **Consideration of a practical scenario**
  The performance of the designed schemes has been studied further by considered practical scenarios [100], including frequency selective channels and mobility conditions. More use cases for the choice of orthogonal alphabet have been explored. The implementation on off-the-shelf component has been realized, demonstrating that the proposed scheme is supported by low power systems [101].
- **Comparison to existing LPWA solution and to the theoretical limit**
  Performance of the designed scheme has been compared to various existing LPWA solutions [85, 83]. Comparisons were always fair as the same values for spectral efficiencies were considered, or the same channel conditions were selected. The performance of all scheme has been compared to the theoretical limit. This analysis exhibits the gap of the existing technologies in terms of energy efficiency, and the benefits of using iterative receivers.

Perspectives

Based on the results presented in this thesis, several perspectives could be considered for future work.

One of the first perspectives is the consideration of the synchronization problem. As presented throughout the thesis, the ranges of Signal-to-Noise Ratio (SNR) of the Turbo-FSK technique are very low. Synchronization and channel estimation become cumbersome, or imply a large overhead in the packet sent (i.e. a spectral efficiency loss without any gain at the receiver side). Efficient ways to synchronize the system should be investigated. With the same perspective, the limits of the system in terms of resistance to imperfect synchronization should be evaluated.

Regarding the Turbo-FSK receiver, two aspects may be considered. First, the complexity of the receiver was demonstrated to increase exponentially with the size of the alphabet. The study identified the receiver's procedures that are responsible for this increase of complexity. With appropriate approximations or more efficient computing methods, the complexity of the receiver could be reduced with a minimum performance loss. The second aspect concerns the FSK detection that was considered. Only the coherent detection was studied, whereas this modulation can be detected in a non-coherent fashion. This detection technique does not require any knowledge of the phase of the received signal. This is done at the expense of some performance loss, but it would reduce the constraints for the synchronization. Preliminary work has been carried out on this topic. New optimization could be required to find the best set of parameters.

An important aspect of LPWA communications that was disregarded in this thesis is the massive access. Indeed, the number of devices accessing the channel is expected to be very large, implying problems concerning the access to the transmission medium. With regard to this problem, the performance of both Turbo-FSK and Turbo-ZC should be evaluated in presence of an interfer, i.e. when two or more devices use the same bandwidth. The sparse repartition of the use of frequency for the Turbo-FSK could be beneficial. For the Turbo-ZC, the use of ZC sequences with a difference index may allow several devices to share the same bandwidth.

Concerning the design of the Turbo-FSK, different structures may be considered. The system can be implemented using a Repeat-Accumulate structure [102], i.e. the serial concatenation of a repetition and a Convolutional-FSK encoder. While performance is expected to be quite the same, it may simplify the architecture of the receiver. Moreover, repetition could be replaced by another low rate code, or irregular repetition [103] could be considered to tune the receiver and improve the performance.

Finally, the modulation introduced for Coplanar Turbo-FSK, the OCS modulation, should be studied more. This technique offers a compromise between the high spectral efficiency of linear modulations and the high energy efficiency of orthogonal modulations. The theoretical performance of the modulation should be derived and more use cases analyzed.

APPENDICES

APPENDIX A

Non-coherent Detection of Orthogonal Modulations

This appendix is dedicated to the mathematical derivations of the non-coherent detection of M-ary orthogonal modulation. Presented in Equation (1.42), the Maximum Likelihood (ML) decision is derived, along with the likelihood of the symbols of the alphabet.

A.1 Signal Transmission

We consider the transmission of a single symbol $\boldsymbol{s}$ taken from the orthogonal alphabet of size M. The transmitted symbol is defined as

$$\boldsymbol{s} = [s_0, s_1, \ldots, s_{M-1}] = \{s_k\}_{k\in\{0,\ldots,M-1\}}$$

where one s_k is called a chip, with M the number of chips in the symbol. The power of the signal, given by Equation (1.25), is equal to

$$P_{\boldsymbol{s}} = E_b B \cdot \frac{\log_2(M)}{M}. \tag{A.1}$$

The transmitted symbol $\boldsymbol{s}$ is taken as a normalized symbol of the alphabet $\boldsymbol{s}^\ell$, with $\ell \in \{0, \ldots, M-1\}$, such that

$$\boldsymbol{s} = \sqrt{P_{\boldsymbol{s}}} \cdot \boldsymbol{s}^\ell, \tag{A.2}$$

where $\|\boldsymbol{s}^\ell\|^2 = M$.

A.1.1 Additive White Gaussian Noise Channel

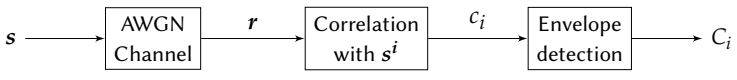

Figure A.1 – *System Model*

We consider the transmission through an Additive White Gaussian Noise (AWGN) Complex channel. The phase of the received signal is unknown. The discrete-time output of the channel is expressed, for $k \in \{0, \ldots, M-1\}$,

$$r_k = \sqrt{P_{\boldsymbol{s}}} s_k^\ell e^{j\varphi} + \nu_k, \tag{A.3}$$

where φ is an unknown phase (constant over the symbol), and ν_k a zero mean complex Gaussian noise with variance σ^2_{ch}. Considering the spectral noise density N_0 and a bandwidth $B = 1/T_c$, we have

$$\sigma^2_{\text{ch}} = N_0 \cdot B. \tag{A.4}$$

A.1.2 Signal Detection

The detector computes the correlation of the received symbol $\boldsymbol{r}$ on the alphabet of possible symbols. We consider the correlation c_i with the symbol $\boldsymbol{s}^i$, with $i \in \{0, \ldots, M-1\}$, given by

$$\begin{aligned} c_i &= \frac{1}{M}\langle \boldsymbol{r}, \boldsymbol{s}^i \rangle = \frac{1}{M}\sum_{k=0}^{M-1} r_k \overline{s_k^i} \\ &= \frac{1}{M}\sum_{k=0}^{M-1} (\sqrt{P_s} s_k^\ell e^{j\varphi} + \nu_k)\overline{s_k^i} \\ &= \frac{\sqrt{P_s}}{M}\sum_{k=0}^{M-1} s_k^\ell \overline{s_k^i} e^{j\varphi} + \frac{1}{M}\sum_{k=0}^{M-1} \nu_k \overline{s_k^i} \\ &= \frac{\sqrt{P_s}}{M} e^{j\varphi}\langle \boldsymbol{s}^\ell, \boldsymbol{s}^i \rangle + \frac{1}{M}\sum_{k=0}^{M-1} \nu_k \overline{s_k^i}. \end{aligned} \tag{A.5}$$

The first term has a different value depending on if the sent symbol was $\boldsymbol{s}^i$ or not. We therefore assume two different hypotheses

$$\begin{aligned} H_0 &: \quad \text{the symbol } \boldsymbol{s}^i \text{ was transmitted } (\ell = i) \\ H_1 &: \quad \text{the symbol } \boldsymbol{s}^i \text{ was not transmitted } (\ell \neq i). \end{aligned}$$

The correlation expression (A.5) is given by

$$c_i = \begin{cases} \sqrt{P_s} e^{j\varphi} + \gamma & \text{if } H_0 \\ \gamma & \text{if } H_1 \end{cases} \tag{A.6}$$

where P_s is the transmitted signal power.

γ is a complex AWGN noise, and is equal to the second term in Equation (A.5). As the ν_k are independant Gaussian noises, the variance of γ can be expressed

$$\begin{aligned} \mathrm{Var}(\gamma) = \sigma^2 &= \mathrm{Var}\left(\frac{1}{M}\sum_{k=0}^{M-1} \nu_k \overline{s_k^i}\right) \\ &= \frac{1}{M^2}\sum_{k=0}^{M-1} \mathrm{Var}\left(\nu_k \overline{s_k^i}\right) \\ &= \frac{1}{M^2}\sum_{k=0}^{M-1} \sigma_{\mathrm{ch}}^2 \\ &= \frac{\sigma_{\mathrm{ch}}^2}{M}. \end{aligned} \tag{A.7}$$

The relationship with the channel noise spectral density is thus

$$\sigma^2 = N_0 \cdot \frac{B}{M}, \tag{A.8}$$

which is relevant to the fact that the noise on only one of the M possible symbols is considered.

The envelope detection consists in computing the absolute value of the correlation, hence

$$C_i = |c_i| = \sqrt{(\mathrm{Re}\,(c_i))^2 + (\mathrm{Im}\,(c_i))^2}. \tag{A.9}$$

A.2 Derivation of the Likelihoods

For ML detection, the two hypothesis must be considered for every possible frequency. The closed form of the likelihood of the envelope under both hypotheses is computed.

A.2.1 Likelihood of the Envelope under Signal Presence Hypothesis

Under the assumption H_0, the received signal correlation r_i is expressed

$$c_i = \sqrt{P_s} e^{j\varphi} + \gamma \tag{A.10}$$

$$c_i = \sqrt{P_s}\cos(\varphi) + \mathrm{Re}(\gamma) + j\left(\sqrt{P_s}\sin(\varphi) + \mathrm{Im}(\gamma)\right), \tag{A.11}$$

where $\mathrm{Re}(\gamma)$ (resp. $\mathrm{Im}(\gamma)$) is the real part (resp. the imaginary part) of γ.

We consider the random variables X_1 and X_2 such that

$$X_1 \sim \mathcal{N}\left(\sqrt{P_s}\cos(\varphi),\ \sigma\right) \tag{A.12}$$

$$X_2 \sim \mathcal{N}\left(\sqrt{P_s}\sin(\varphi),\ \sigma\right), \tag{A.13}$$

where $\mathcal{N}(\mu,\ \sigma)$ refers to a Normal (Gaussian) distribution with mean μ and standard deviation σ.

Additionally, we consider the random variables Y and Z such that

$$Z = Y^2 = X_1^2 + X_2^2. \tag{A.14}$$

Since the real random variables X_1 and X_2 follow normal distributions with non-zero mean, Y^2 follows a non-central chi-squared distribution with 2 degrees of freedom. The noncentral chi-squared distribution is denoted $\chi^2(\alpha, \lambda)$, where α is the degree of freedom (i.e. the number of normal laws summed) and λ a parameter defined as

$$\lambda = \sum_{i=1}^{\alpha}\left(\frac{\mu_i}{\sigma_i}\right)^2 \tag{A.15}$$

where μ_i and σ_i are respectively the mean and the standard deviation of the i-th random variable following a normal distribution.

In order to use the classic formula of the Probability Density Function (PDF) for a noncentral chi-squared distribution, we consider the normalization of the random variable Y^2 by the variance of the normal laws. We obtain the random variable W defined by

$$W = \frac{Z}{\sigma^2} = \frac{X_1^2}{\sigma^2} + \frac{X_2^2}{\sigma^2}. \tag{A.16}$$

Using the normalization and the definition of λ from Equation (A.15), we have $W \sim \chi^2(2, P_s/\sigma^2)$. The PDF of the random variable W is defined by (noncentral chi-squared general PDF definition [15, p. 44])

$$\begin{aligned} p_{W|H_0}(w) &= \frac{1}{2} e^{-(w+\lambda)/2}\left(\frac{w}{\lambda}\right)^{\frac{\alpha}{4}-\frac{1}{2}} I_{\alpha/2-1}\left(\sqrt{\lambda w}\right) \\ &= \frac{1}{2}\exp\left\{-\frac{1}{2}\left(w + \frac{P_s}{\sigma^2}\right)\right\}\left(\frac{w\sigma^2}{P_s}\right)^0 I_0\left(\sqrt{\frac{P_s w}{\sigma^2}}\right), \end{aligned} \tag{A.17}$$

where I is the modified Bessel function of the first kind.

We can now express the PDF of the random variable Z by applying a variable change. We have

$$Z = W\sigma^2 \Rightarrow dz = \sigma^2 dw \tag{A.18}$$

and

$$p_{Z|H_0}(z)dz = p_{W|H_0}(w)dw \Leftrightarrow p_{Z|H_0}(z) = p_{W|H_0}(w)\frac{dw}{dz}, \tag{A.19}$$

hence the expression of the PDF of Z

$$\begin{aligned} p_{Z|H_0}(z) &= p_{W|H_0}\left(\frac{z}{\sigma^2}\right)\frac{1}{\sigma^2} \\ &= \frac{1}{2\sigma^2}\exp\left(-\frac{z+P_s}{2\sigma^2}\right) I_0\left(\frac{\sqrt{P_s z}}{\sigma^2}\right). \end{aligned} \tag{A.20}$$

Another variable change is required to express the PDF of the random variable Y. We have

$$Y^2 = Z \Rightarrow 2ydy = dz, \tag{A.21}$$

hence

$$\begin{aligned} p_{Y|H_0}(y) &= p_{Z|H_0}\left(y^2\right) 2y \\ &= \frac{y}{\sigma^2} \exp\left(-\frac{y^2+P_s}{2\sigma^2}\right) I_0\left(\frac{\sqrt{P_s}}{\sigma^2} y\right). \end{aligned} \tag{A.22}$$

Following the definition of the random variable Y, the likelihood of the envelope under the hypothesis H_0 is

$$p\left(C_i \mid H_0\right) = \frac{C_i}{\sigma^2} \exp\left(-\frac{C_i^2+P_s}{2\sigma^2}\right) I_0\left(\frac{\sqrt{P_s}}{\sigma^2} C_i\right). \tag{A.23}$$

A.2.2 Likelihood of the Envelope under Signal Absence Hypothesis

Under the assumption H_1, the received signal correlation r_i is expressed

$$c_i = \gamma \tag{A.24}$$

$$c_i = \gamma^{\mathcal{R}} + j\gamma^{\mathcal{I}}. \tag{A.25}$$

We consider the random variables X_1 and X_2 such that

$$X_1 \sim \mathcal{N}(0,\sigma) \tag{A.26}$$

$$X_2 \sim \mathcal{N}(0,\sigma). \tag{A.27}$$

Here again, we consider the random variables Y and Z as defined in Equation (A.14), and the random variable W as defined in Equation (A.16). W follows a chi-squared distribution with two degrees of freedom ($\alpha = 2$). The PDF of W is defined as (chi-squared general PDF definition [15, p. 42])

$$\begin{aligned} p_{W|H_1}(w) &= \frac{w^{\alpha/2-1}}{2^{\alpha/2}\Gamma(\alpha/2)} \exp\left(-\frac{w}{2}\right) \\ &= \frac{1}{2} \exp\left(-\frac{w}{2}\right) \end{aligned} \tag{A.28}$$

where $\Gamma(k)$ is the gamma function that can be expressed, for k integer,

$$\Gamma(k) = (k-1)!. \tag{A.29}$$

Here again, a variable change is needed to express the PDF of the random variable Z. Using Equation (A.18) and (A.19), we have

$$\begin{aligned} p_{Z|H_1}(z) &= p_{W|H_1}\left(\frac{z}{\sigma^2}\right) \frac{1}{\sigma^2} \\ &= \frac{1}{2\sigma^2} \exp\left(-\frac{z}{2\sigma^2}\right) \end{aligned} \tag{A.30}$$

The PDF of the random variable Y is expressed using another variable change, with

$$\begin{aligned} p_{Y|H_1}(y) &= p_{Z|H_1}\left(y^2\right) 2y \\ &= \frac{y}{\sigma^2} \exp\left(-\frac{y^2}{2\sigma^2}\right) \end{aligned} \tag{A.31}$$

Following the definition of the random variable Y, the likelihood of the envelope under the hypothesis H_1 is

$$p\left(C_i \mid H_1\right) = \frac{C_i}{\sigma^2} \exp\left(-\frac{C_i^2}{2\sigma^2}\right). \tag{A.32}$$

A.3 Maximum Likelihood Decision

Under the assumption that one symbol of the alphabet was sent, the receiver computes the ML detection by considering all possible symbols and the two possible hypotheses for each symbol. For each symbol (i.e. each index i), the likelihood ratio is related to the presence of energy at the considered correlation. The search of the maximum over the likelihood ratios thus gives the most probable symbols.

The decision of the received codeword can be done by searching

$$\begin{aligned}
\underset{i\in\{0,\dots,M-1\}}{\arg\max} \frac{p\left(C_i \mid H_0\right)}{p\left(C_i \mid H_1\right)} &= \underset{i\in\{0,\dots,M-1\}}{\arg\max} \frac{C_i \exp\left(-\frac{C_i^2+P_s}{2\sigma^2}\right) I_0\left(\frac{\sqrt{P_s}}{\sigma^2} C_i\right)}{C_i \exp\left(-\frac{C_i^2}{2\sigma^2}\right)} \\
&= \underset{i\in\{0,\dots,M-1\}}{\arg\max} \exp\left(-\frac{P_s}{2\sigma^2}\right) I_0\left(\frac{\sqrt{P_s}}{\sigma^2} C_i\right) \\
&= \underset{i\in\{0,\dots,M-1\}}{\arg\max} I_0\left(\frac{\sqrt{P_s}}{\sigma_{\text{ch}}^2} |\langle \boldsymbol{r}, \boldsymbol{s}^i \rangle|\right)
\end{aligned} \tag{A.33}$$

since $\sigma^2 = \sigma_{\text{ch}}^2 / M$ and following the definition of C_i given Equation (A.9).

Since I_0 is an increasing function, the decision may be simplified to

$$\underset{i\in\{0,\dots,M-1\}}{\arg\max} |\langle \boldsymbol{r}, \boldsymbol{s}^i \rangle| \tag{A.34}$$

Bibliography of Appendix A

[15] J. Proakis. *Digital Communications 3rd Edition*. Communications and signal processing. McGraw-Hill, 1995.

APPENDIX B

Probability of Error for M-ary Orthogonal Modulation

In this appendix, the mathematical derivations to express the probability of error for the coherent detection of the M-ary orthogonal modulations given Equation (1.54) are presented.

B.1 System Model

We consider the transmission on an AWGN channel of a single symbol $\boldsymbol{s}^i$ taken from the orthogonal alphabet of size M. The power of the signal, given by Equation (1.25), is equal to

$$P_{\boldsymbol{s}} = E_b B \cdot \frac{\log_2(M)}{M}. \tag{B.1}$$

The transmitter symbol $\boldsymbol{s}$ is taken as a normalized symbol of the alphabet $\boldsymbol{s}^i$, with $i \in \{0, \ldots, M-1\}$, such that

$$\boldsymbol{s} = \sqrt{P_{\boldsymbol{s}}} \cdot \boldsymbol{s}^i, \tag{B.2}$$

where $\|\boldsymbol{s}^i\|^2 = M$.

The output of the channel is expressed by

$$\boldsymbol{r} = \boldsymbol{s} + \boldsymbol{\nu}, \tag{B.3}$$

where $\boldsymbol{\nu}$ is a zero mean complex Gaussian noise with variance $\sigma^2_{\text{ch}} = N_0 B$, with B the bandwidth and N_0 the noise spectral density.

Given that the symbol $\boldsymbol{s}^n$ was transmitted, the output i of the correlator is given by

$$c_i = \begin{cases} \sqrt{P_{\boldsymbol{s}}} + \gamma_i & \text{if } i = n \\ \gamma_i & \text{if } i \neq n \end{cases} \tag{B.4}$$

where the terms γ_i are independent AWGN noises of variance σ^2, with the relationship

$$\sigma^2 = \frac{\sigma^2_{\text{ch}}}{M} = \frac{N_0 B}{M}. \tag{B.5}$$

B.2 Symbol Error Probability

Due to the symmetry of the alphabet, the probability of error is independent of which symbol was transmitted. We assume that the symbol $\boldsymbol{s}^0$ is transmitted. The correlation is thus

$$c_i = \begin{cases} \sqrt{P_{\boldsymbol{s}}} + \gamma_0 & \text{if } i = 0 \\ \gamma_i & \text{if } i \neq 0 \end{cases} \tag{B.6}$$

where P_s is the transmitted signal power, defined in Equation (B.1).

The noise terms γ_i are independent, zero-mean, and follow a normal distribution with variance σ_i^2. All variances are assumed equal, with $\sigma_i^2 = \sigma^2$ as defined in Equation (B.5).

The event of symbol error is denoted ε_s. The probability $\Pr(\overline{\varepsilon_s})$ of detecting the correct symbol is the joint probability that the correlation c_0 is larger than all the other correlation c_i, $\forall i$. The probability can be expressed

$$\Pr(\overline{\varepsilon_s}) = \Pr(c_1 < c_0,\, c_2 < c_0,\, \ldots,\, c_{M-1} < c_0), \tag{B.7}$$

and for which the marginalization over all the possible values of c_0 gives

$$\Pr(\overline{\varepsilon_s}) = \int_{-\infty}^{+\infty} \Pr(c_1 < c_0,\, c_2 < c_0,\, \ldots,\, c_{M-1} < c_0 \mid c_0)\, p(c_0)\, dc_0 \tag{B.8}$$

The PDF of the observation of c_0 given that $\boldsymbol{s}^0$ was sent is expressed by

$$p(c_0) = \frac{1}{\sqrt{2\pi}\sigma} \exp\left\{-\frac{(c_0 - \sqrt{P_s})^2}{2\sigma^2}\right\}, \tag{B.9}$$

while the PDF of the $M-1$ other correlations are

$$p(c_i \mid c_0) = \frac{1}{\sqrt{2\pi}\sigma} \exp\left\{-\frac{c_i^2}{2\sigma^2}\right\}. \tag{B.10}$$

The probability that $c_i < c_0$, given c_0 and that $\boldsymbol{s}^0$ was sent, is then

$$\begin{aligned}\Pr(c_i < c_0 \mid c_0) &= \int_{-\infty}^{c_0} p(c_i \mid c_0)\, dc_i \\ &= \int_{-\infty}^{c_0} \frac{1}{\sqrt{2\pi}\sigma} \exp\left\{-\frac{c_i^2}{2\sigma^2}\right\} dc_i,\end{aligned} \tag{B.11}$$

which can be expressed, by doing the change of variable $x = c_i/\sigma$,

$$\Pr(c_i < c_0 \mid c_0) = \frac{1}{\sqrt{2\pi}} \int_{-\infty}^{c_0/\sigma} \exp\left\{-\frac{x^2}{2}\right\} dx. \tag{B.12}$$

As we consider the noises independent on each correlation term, and since we averaged all the possible values for c_0, the joint probability term of (B.8) simplifies to

$$\begin{aligned}\Pr(c_1 < c_0,\, c_2 < c_0,\, \ldots,\, c_{M-1} < c_0 \mid c_0) &= \prod_{i=1}^{M-1} \Pr(c_i < c_0 \mid c_0) \\ &= \left(\frac{1}{\sqrt{2\pi}} \int_{-\infty}^{c_0/\sigma} \exp\left\{-\frac{x^2}{2}\right\} dx\right)^{M-1}\end{aligned} \tag{B.13}$$

By considering $y = c_0/\sigma$, the probability of detecting the correct symbol is then given by

$$\Pr(\overline{\varepsilon_s}) = \frac{1}{\sqrt{2\pi}} \int_{-\infty}^{+\infty} \left(\frac{1}{\sqrt{2\pi}} \int_{-\infty}^{y} e^{-x^2/2} dx\right)^{M-1} \exp\left\{-\frac{1}{2}\left(y - \frac{\sqrt{P_s}}{\sigma}\right)^2\right\} dy. \tag{B.14}$$

The symbol error probability is thus given by

$$\Pr(\varepsilon_s) = 1 - \Pr(\overline{\varepsilon_s}) \tag{B.15}$$

$$= \frac{1}{\sqrt{2\pi}} \int_{-\infty}^{+\infty} \left[1 - \left(1 - \frac{1}{2}\operatorname{erfc}\left(\frac{y}{\sqrt{2}}\right)\right)^{M-1}\right] \exp\left\{-\frac{1}{2}\left(y - \frac{\sqrt{P_s}}{\sigma}\right)^2\right\} dy, \tag{B.16}$$

as the PDF is normalized and following the definition of erfc as given in Equation (1.51). Following the definition of P_s in Equation (A.1) and of σ in Equation (A.8), the symbol error probability is expressed depending on the E_b/N_0 by

$$\Pr(\varepsilon_s) = \frac{1}{\sqrt{2\pi}} \int_{-\infty}^{+\infty} \left[1 - \left(1 - \frac{1}{2}\operatorname{erfc}\left(\frac{y}{\sqrt{2}}\right)\right)^{M-1}\right] \exp\left\{-\frac{1}{2}\left(y - \sqrt{\log_2(M)\frac{E_b}{N_0}}\right)^2\right\} dy. \tag{B.17}$$

This expression cannot be reduced further and needs to be numerically evaluated for different values of E_b/N_0.

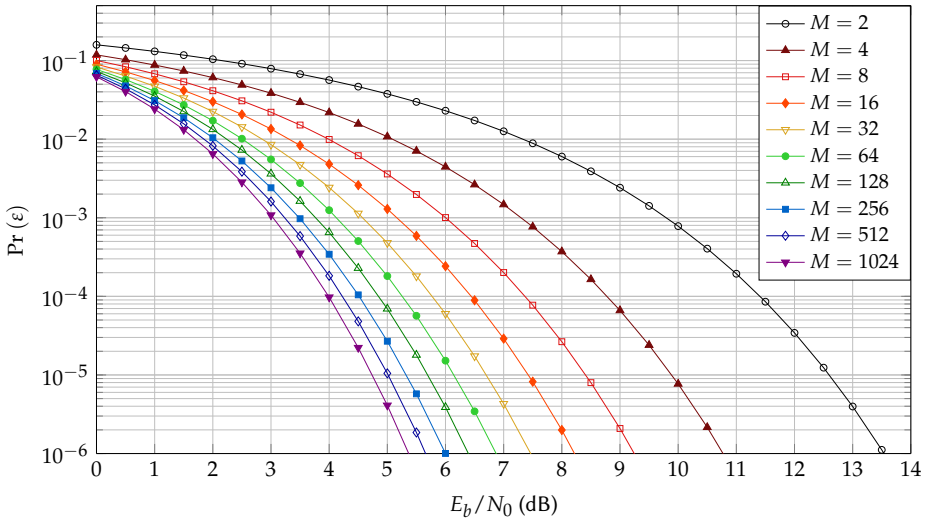

FIGURE B.1 – *Bit error probability of orthogonal modulations, for various sizes of alphabet M.*

B.3 Bit Error Probability

Due to the symmetry in the alphabet, detecting the wrong symbol $\boldsymbol{s}^i$, $i \in \{1, \ldots, M-1\}$ given that $\boldsymbol{s}^0$ was sent is equally probable, whatever the value of i. This probability is given by

$$\Pr\left(\boldsymbol{s}^i \,\middle|\, \boldsymbol{s}^0\right) = \frac{\Pr(\varepsilon_s)}{M-1}, \tag{B.18}$$

expressing the uniformity in the probability to detect the wrong symbol.

For one bit, its value 0 is represented by $M/2$ symbols, and its value 1 is represented by $M/2$ symbols. The probability of having an error on the bit is then the probability of detecting the $M/2$ symbols that represents the wrong value. The bit error probability $\Pr(\varepsilon)$ is then expressed

$$\begin{aligned}\Pr(\varepsilon) &= \frac{M}{2}\frac{\Pr(\varepsilon_s)}{M-1} \\ &= \frac{M}{2(M-1)}\Pr(\varepsilon_s).\end{aligned} \tag{B.19}$$

Finally, using Equation (B.17), the probability of a bit error is given by

$$\Pr(\varepsilon) = \frac{M}{2(M-1)}\frac{1}{\sqrt{2\pi}}\int_{-\infty}^{+\infty}\left[1-\left(1-\frac{1}{2}\operatorname{erfc}\left(\frac{y}{\sqrt{2}}\right)\right)^{M-1}\right]\exp\left\{-\frac{1}{2}\left(y-\sqrt{\log_2(M)\frac{E_b}{N_0}}\right)^2\right\}dy. \tag{B.20}$$

The bit error probability when considering various sizes of alphabet M is depicted in Figure B.1. The value of E_b/N_0 required for $\Pr(\varepsilon) = 10^{-5}$ is given for various sizes of M on the Figure 1.8.

APPENDIX C

Optimal Trellis-Decoding

The Bahl, Cocke, Jelinek and Raviv (BCJR) was initially proposed in [31], and revisited in [8] for its use in Turbo Codes (TCs). This algorithm computes the *A Posteriori* Probability (APP) of the information bits given the received codewords. This appendix is dedicated to the description of the initial BCJR algorithm, and its application for channel coding is reviewed.

C.1 *A Posteriori* Probabilities of Transitions

We consider a discrete time Markov chain with N_s possible states and N transitions. At time t the state is S_t, with $S_t \in \{0, \ldots, N_s - 1\}$ and $t \in \{0, \ldots, N\}$. By convention, $S_0 = S_N = 0$. The N observations of the transitions are denoted $\boldsymbol{R}_1^N = \{\boldsymbol{r}_1, \boldsymbol{r}_2, \ldots, \boldsymbol{r}_t, \ldots, \boldsymbol{r}_N\}$.

The goal of the algorithm is to determine the APP of the transitions $\Pr\left(S_{t-1} = s', S_t = s \,\middle|\, \boldsymbol{R}_1^N\right)$, with $\{s, s'\} \in \{0, \ldots, N_s - 1\}^2$, which can be expressed, using Bayes' law,

$$\Pr\left(S_{t-1} = s', S_t = s \,\middle|\, \boldsymbol{R}_1^N\right) = \frac{p\left(\boldsymbol{R}_1^N \,\middle|\, S_{t-1} = s', S_t = s\right) \Pr\left(S_{t-1} = s', S_t = s\right)}{\Pr\left(\boldsymbol{R}_1^N\right)}. \tag{C.1}$$

Since the probability $\Pr\left(\boldsymbol{R}_1^N\right)$ is constant for an observation $\boldsymbol{R}_1^N$, we will derive the numerator in order to have the expression of the APP' transition. Using total probabilities, the numerator can be expressed

$$\begin{aligned} p\left(S_{t-1} = s', S_t = s, \boldsymbol{R}_1^N\right) &= p\left(S_{t-1} = s', S_t = s, \boldsymbol{R}_1^{t-1}, \boldsymbol{r}_t, \boldsymbol{R}_{t+1}^N\right) \\ &= p\left(S_{t-1} = s', \boldsymbol{R}_1^{t-1}\right) p\left(S_t = s, \boldsymbol{r}_t, \boldsymbol{R}_{t+1}^N \,\middle|\, S_{t-1} = s', \boldsymbol{R}_1^{t-1}\right) \\ &= p\left(S_{t-1} = s', \boldsymbol{R}_1^{t-1}\right) p\left(S_t = s, \boldsymbol{r}_t \,\middle|\, S_{t-1} = s', \boldsymbol{R}_1^{t-1}\right) \\ &\quad \cdot p\left(\boldsymbol{R}_{t+1}^N \,\middle|\, S_t = s, S_{t-1} = s', \boldsymbol{R}_1^{t-1}, \boldsymbol{r}_t\right). \end{aligned} \tag{C.2}$$

As we considered a Markov process, if the state S_t is known, events prior to time t do not depend on the observations until t. The following terms can thus be simplified as

$$\begin{aligned} p\left(S_t = s, \boldsymbol{r}_t \,\middle|\, S_{t-1} = s', \boldsymbol{R}_1^{t-1}\right) &= p\left(S_t = s, \boldsymbol{r}_t \,\middle|\, S_{t-1} = s'\right) \\ p\left(\boldsymbol{R}_{t+1}^N \,\middle|\, S_t = s, S_{t-1} = s', \boldsymbol{R}_1^{t-1}, \boldsymbol{r}_t\right) &= p\left(\boldsymbol{R}_{t+1}^N \,\middle|\, S_t = s\right). \end{aligned}$$

We define the function gamma as

$$\gamma_t(s', s) = p\left(S_t = s, \boldsymbol{r}_t \,\middle|\, S_{t-1} = s'\right) \tag{C.3}$$

which is the joint Probability Density Function (PDF) to be in state s at index t and to observe $\boldsymbol{r}_t$, given that the state at index $t-1$ was s'. This PDF is related to the likelihood of the transition from state s to s'.

We define the probability function α such that

$$\alpha_t(s) = p\left(S_k = s,\, \boldsymbol{R}_1^t\right), \tag{C.4}$$

which is the joint PDF of being in state s at time t and to observe the received sequence up to index t, i.e. the "past" of the sequence.

We define function β as

$$\beta_t(s) = p\left(\boldsymbol{R}_{t+1}^N \,\middle|\, S_t = s\right), \tag{C.5}$$

which is the PDF of the sequence of received symbols after index t (i.e. the "future" of the sequence) given that the state at time t was s.

C.1.1 Computation of α

The value of α can be obtained recursively by summing all the possibilities for the previous states S_{t-1}

$$\begin{aligned}
\alpha_t(s) &= \sum_{s'=0}^{N_s-1} p\left(S_{t-1} = s',\, S_t = s,\, \boldsymbol{R}_1^t\right) = \sum_{s'=0}^{N_s-1} p\left(S_{t-1} = s',\, S_t = s,\, \boldsymbol{R}_1^{t-1},\, \boldsymbol{r}_t\right) \\
&= \sum_{s'=0}^{N_s-1} p\left(S_{t-1} = s',\, \boldsymbol{R}_1^{t-1}\right) p\left(S_t = s,\, \boldsymbol{r}_t \,\middle|\, S_{t-1} = s',\, \boldsymbol{R}_1^{t-1}\right) \\
&= \sum_{s'=0}^{N_s-1} p\left(S_{t-1} = s',\, \boldsymbol{R}_1^{t-1}\right) p\left(S_t = s,\, \boldsymbol{r}_t \,\middle|\, S_{t-1} = s'\right) \\
&= \sum_{s'=0}^{N_s-1} \alpha_{t-1}(s')\gamma_t(s', s)
\end{aligned} \tag{C.6}$$

where the equality between the second and third line comes from the Markov property. The values of α are thus obtained by performing a forward recursion on the trellis.

C.1.2 Computation of β

The value of β is obtained by summing all the possibilities for the next states S_{t+1}

$$\begin{aligned}
\beta_t(s) &= \sum_{s'=0}^{N_s-1} p\left(S_{t+1} = s',\, \boldsymbol{R}_{t+1}^N \,\middle|\, S_t = s\right) = \sum_{s'=0}^{N_s-1} p\left(S_{t+1} = s',\, \boldsymbol{r}_{t+1},\, \boldsymbol{R}_{t+2}^N \,\middle|\, S_t = s\right) \\
&= \sum_{s'=0}^{N_s-1} p\left(S_{t+1} = s',\, \boldsymbol{r}_{t+1} \,\middle|\, S_t = s\right) p\left(\boldsymbol{R}_{t+2}^N \,\middle|\, S_t = s,\, S_{t+1} = s',\, \boldsymbol{r}_{t+1}\right) \\
&= \sum_{s'=0}^{N_s-1} p\left(S_{t+1} = s',\, \boldsymbol{r}_{t+1} \,\middle|\, S_t = s\right) p\left(\boldsymbol{R}_{t+2}^N \,\middle|\, S_{t+1} = s'\right) \\
&= \sum_{s'=0}^{N_s-1} \gamma_{t+1}(s, s')\beta_{t+1}(s')
\end{aligned} \tag{C.7}$$

where the equality between the second and third line comes from the Markov property. The values of β are obtained with a backward recursion on the trellis.

C.1.3 Computation of γ

From the definition of γ, we have

$$\begin{aligned}
\gamma_t(s', s) &= p\left(S_t = s,\, \boldsymbol{r}_t \,\middle|\, S_{t-1} = s'\right) \\
&= p\left(\boldsymbol{r}_t \,\middle|\, S_t = s,\, S_{t-1} = s'\right) \Pr\left(S_t = s \,\middle|\, S_{t-1} = s'\right),
\end{aligned} \tag{C.8}$$

where $\Pr\left(S_t = s \,\middle|\, S_{t-1} = s'\right)$ is the *a priori* probability of a transition between two states, defined by the structure of the trellis, and $p\left(\boldsymbol{r}_t \,\middle|\, S_t = s,\, S_{t-1} = s'\right)$ is the likelihood of $\boldsymbol{r}_t$ given a specific transition. It is dependent on how the channel affects the received vector $\boldsymbol{r}_t$.

C.1.4 APP of a Transition

Following the definition of α, β and γ, the APP of a transition can be expressed

$$\begin{aligned}\Pr\left(S_{t-1}=s',\, S_t=s \,\middle|\, \boldsymbol{R}_1^N\right) &= \frac{p\left(S_{t-1}=s',\, S_t=s,\, \boldsymbol{R}_1^N\right)}{p\left(\boldsymbol{R}_1^N\right)} \\ &= \frac{\alpha_{t-1}(s')\cdot\gamma_t(s',s)\cdot\beta_t(s)}{p\left(\boldsymbol{R}_1^N\right)}\end{aligned} \tag{C.9}$$

C.2 Application to Channel Coding

In channel coding, codewords are denoted $\boldsymbol{c}^i$, $i\in\{0,\ldots,M-1\}$, with M the size of the alphabet. Each codeword is composed of N_c binary values, and encodes an information word of length q (the relation between q and N_c may vary according to the selected code). Each codeword is mapped to one or multiple transitions of the trellis. We denote by $\mathcal{T}_i$ the set of transitions from s' to s which are mapped by the codeword $\boldsymbol{c}^i$. The APP of a codeword is given by the sum of the APP of the transitions which are mapped by the codewords, i.e.

$$\Pr\left(\boldsymbol{c}^i \,\middle|\, \boldsymbol{R}_1^N\right) = \sum_{\{s',s\}\in\mathcal{T}_i} \Pr\left(S_{t-1}=s',\, S_t=s \,\middle|\, \boldsymbol{R}_1^N\right). \tag{C.10}$$

C.2.1 Log-APP of the Information Bits

The information word corresponding to the time index t is denoted $\boldsymbol{b}_t$ and has q elements $b_{k,t}$, $k\in\{0,\ldots,q-1\}$. Each bit $b_{k,t}$ is equal to $u=\pm1$, and we denote by $\mathcal{B}_u^q$ the group of codewords that encode an information word for which the bit $b_k=u$ (the index t is dropped as the mapping between information words and codewords is the same for all time index). Considering the information bit at position $k=n$, the APP of this bit b_n

$$\begin{aligned}\Pr\left(b_{n,t}=u \,\middle|\, \boldsymbol{R}_1^N\right) &= \sum_{i\in\mathcal{B}_u^n} \Pr\left(\boldsymbol{c}^i \,\middle|\, \boldsymbol{R}_1^N\right) \\ &= \sum_{i\in\mathcal{B}_u^n}\sum_{\{s',s\}\in\mathcal{T}_i} \Pr\left(S_{t-1}=s',\, S_t=s \,\middle|\, \boldsymbol{R}_1^N\right) \\ &= \frac{1}{\Pr\left(\boldsymbol{R}_1^N\right)}\sum_{i\in\mathcal{B}_u^n}\sum_{\{s',s\}\in\mathcal{T}_i} \alpha_{t-1}(s')\cdot\gamma_t(s',s)\cdot\beta_t(s)\end{aligned} \tag{C.11}$$

The log-APP of the bit $b_{n,t}$ is given by

$$\begin{aligned}L\left(b_{n,t} \,\middle|\, \boldsymbol{R}_1^N\right) &= \log\frac{\Pr\left(b_{n,t}=+1 \,\middle|\, \boldsymbol{R}_1^N\right)}{\Pr\left(b_{n,t}=-1 \,\middle|\, \boldsymbol{R}_1^N\right)} \\ &= \log\frac{\displaystyle\sum_{i\in\mathcal{B}_{+1}^n}\sum_{\{s',s\}\in\mathcal{T}_i} \alpha_{t-1}(s')\cdot\gamma_t(s',s)\cdot\beta_t(s)}{\displaystyle\sum_{i\in\mathcal{B}_{-1}^n}\sum_{\{s',s\}\in\mathcal{T}_i} \alpha_{t-1}(s')\cdot\gamma_t(s',s)\cdot\beta_t(s)}.\end{aligned} \tag{C.12}$$

C.2.2 Computation of γ

The quantity $\gamma_t(s',s)$ is related to the transition probability, and can be expressed using the codeword $\boldsymbol{c}^i$ that maps the transition from state s' to s. The *a priori* probability of having that transition is the *a priori* probability to have the codeword $\boldsymbol{c}^i$ at time index t, yielding

$$\Pr\left(S_t=s \,\middle|\, S_{t-1}=s'\right) = \Pr\left(\boldsymbol{c}_t^i\right). \tag{C.13}$$

Likewise, the likelihood of the vector $\boldsymbol{r}_t$ given that the transition m' to m happened is expressed

$$p\left(\boldsymbol{r}_t \,\middle|\, S_t=s,\, S_{t-1}=s'\right) = p\left(\boldsymbol{r}_t \,\middle|\, \boldsymbol{c}_t^i\right). \tag{C.14}$$

The term $\gamma_t(s',s)$ can thus be expressed

$$\gamma_t(s',s) = p\left(\boldsymbol{r}_t \,\middle|\, \boldsymbol{c}_t^i\right) \Pr\left(\boldsymbol{c}_t^i\right), \tag{C.15}$$

giving an expression which includes the likelihood of the codeword $\boldsymbol{c}^i$ and the *a priori* probability of having the codeword. The likelihood can be computed under some assumptions on the channel, *e.g* an Additive White Gaussian Noise (AWGN) assumption.

By convention, the codeword $\boldsymbol{c}^i$ encodes an information word $\boldsymbol{b}^i$ of length q. The *a priori* probability of having the codeword $\boldsymbol{c}^i$ is expressed

$$\Pr\left(\boldsymbol{c}^i\right) = \prod_{k=0}^{q-1} \Pr\left(b_k = b_k^i\right) \tag{C.16}$$

where b_k refers to the value of the bit at index k. The log-ratio of the *a priori* probability of bit b_k is given by

$$L_A(b_k) = \log \frac{\Pr(b_k = +1)}{\Pr(b_k = -1)}. \tag{C.17}$$

Given that $\Pr(b_k = +1) + \Pr(b_k = -1) = 1$, we have

$$\Pr(b_k = +1) = \frac{e^{L_A(b_k)}}{1 + e^{L_A(b_k)}} = \frac{e^{-\frac{1}{2}L_A(b_k)} e^{\frac{3}{2}L_A(b_k)}}{\left(1 + e^{-L_A(b_k)}\right) e^{L_A(b_k)}} = \frac{e^{-L_A(b_k)/2}}{1 + e^{-L_A(b_k)}} e^{L_A(b_k)/2}, \tag{C.18}$$

which can be generalized to the two values $u = \pm 1$ using

$$\Pr(b_k = u) = \vartheta(b_k)\, e^{L_A(b_k)u/2}, \tag{C.19}$$

with

$$\vartheta(b_k) = \frac{e^{-L_A(b_k)/2}}{1 + e^{-L_A(b_k)}}. \tag{C.20}$$

The *a priori* probability of the codeword can thus be expressed

$$\begin{aligned} \Pr\left(\boldsymbol{c}^i\right) &= \prod_{k=0}^{q-1} \vartheta(b_k)\, e^{L_A(b_k) b_k^i/2} \\ &= \left(\prod_{n=0}^{\log_2(M)-1} \vartheta(b_k)\right) \exp\left\{\frac{1}{2} \sum_{n=0}^{\log_2(M)-1} L_A(b_k) b_k^i\right\} \end{aligned} \tag{C.21}$$

The likelihood of Equation (C.15) can be computed as

$$p\left(\boldsymbol{r}_t \,\middle|\, \boldsymbol{c}_t^i\right) = \prod_{k=0}^{N_c-1} p\left(r_{k,t} \,\middle|\, c_{k,t}^i\right), \tag{C.22}$$

which gives a general expression for the terms γ_t as

$$\gamma_t(s',s) = \left(\prod_{k=0}^{q-1} \vartheta(b_{k,t})\right) \prod_{k=0}^{N_c-1} p\left(r_{k,t} \,\middle|\, c_{k,t}^i\right) \exp\left\{\frac{1}{2} \sum_{k=0}^{q-1} L_A(b_{k,t}) b_{k,t}^i\right\}. \tag{C.23}$$

When considering binary codewords, the likelihood of a codeword can be expressed, using Equation (1.63)

$$p\left(\boldsymbol{r} \,\middle|\, \boldsymbol{c}^i\right) = \left(\prod_{k=0}^{N_c-1} \vartheta(c_k)\right) \exp\left\{\frac{1}{2} \sum_{k=0}^{N_c-1} L(c_k) c_k^i\right\}, \tag{C.24}$$

where $L(c_k)$ is the Log Likelihood Ratio (LLR) of the bit c_k defined as

$$L(c_k) = \log \frac{p(r_k \mid c_k = +1)}{p(r_k \mid c_k = -1)}. \tag{C.25}$$

Using (C.21) and (C.24) in (C.15), it comes

$$\gamma_t(s',s) = \mathrm{C_{st}} \exp\left\{ \frac{1}{2} \sum_{k=0}^{N_c-1} L(c_{k,t}) c_{k,t}^i + \frac{1}{2} \sum_{k=0}^{q-1} L_A(b_{k,t}) b_{k,t}^i \right\} \tag{C.26}$$

with $\mathrm{C_{st}}$ a constant independent of i which will be cancelled out in further computations. If the code is systematic, then some positions of the codeword $\boldsymbol{c}^i$ correspond to the information word $\boldsymbol{b}^i$. The q systematic positions are denoted by $\mathcal{S}$, and the $N_c - q$ parity positions by $\mathcal{P}$. Equation (C.26) is expressed

$$\gamma_t(s',s) = \mathrm{C_{st}} \exp\left\{ \frac{1}{2} \sum_{k\in\mathcal{S}} \left((L(b_{k,t}) + L_A(b_{k,t})) b_{k,t}^i \right) + \frac{1}{2} \sum_{k\in\mathcal{P}} L(c_{k,t}) c_{k,t}^i \right\}. \tag{C.27}$$

In order to compute γ_t, the *a priori* log ratios are added to the LLR at the systematic positions.

C.2.3 Extrinsic Information

For the case of systematic binary codewords, the extrinsic information generated by the BCJR can be expressed as part of the log-APP of the bit. When considering one bit b_n, i.e. the bit at index $q = n$, the expression of $\gamma_k(s',s)$ can be factorized as

$$\begin{aligned}
\gamma_t(s',s) &= \prod_{k=0}^{N_c-1} p\left(r_{k,t} \,\middle|\, c_{k,t} = c_{k,t}^i\right) \prod_{k=0}^{q-1} \Pr\left(b_{k,t} = b_{k,t}^i\right) \\
&= p\left(r_{n,t} \,\middle|\, c_{n,t} = b_{n,t}^i\right) \Pr\left(b_{n,t} = b_{n,t}^i\right) \prod_{\substack{k=0 \\ k\neq n}}^{N_c-1} p\left(r_{k,t} \,\middle|\, c_{k,t} = c_{k,t}^i\right) \prod_{\substack{k=0 \\ k\neq n}}^{q-1} \Pr\left(b_{k,t} = b_{k,t}^i\right)
\end{aligned} \tag{C.28}$$

In the computation of the log-APP Equation (C.12), the top sum corresponds to the transitions for which the bit $b_{n,t}$ is equal to 1 and the bottom sum to the transitions for which the bit $b_{n,t}$ is -1. Using the previous factorization, it is thus possible to factorize the log-APP as

$$\begin{aligned}
L\left(b_{n,t} \,\middle|\, \boldsymbol{R}_1^N\right) = \log \frac{p\left(r_{n,t} \,\middle|\, b_{n,t} = +1\right)}{p\left(r_{n,t} \,\middle|\, b_{n,t} = -1\right)} + \log \frac{\Pr\left(b_{n,t} = +1\right)}{\Pr\left(b_{n,t} = -1\right)} \\
+ \log \frac{\displaystyle\sum_{i\in\mathcal{B}_{+1}^n} \sum_{\{s',s\}\in\mathcal{T}_i} \alpha_{t-1}(s') \cdot \prod_{\substack{k=0 \\ k\neq n}}^{N_c-1} p\left(r_{k,t} \,\middle|\, c_{k,t} = c_{k,t}^i\right) \cdot \prod_{\substack{k=0 \\ k\neq n}}^{q-1} \Pr\left(b_{k,t} = b_{k,t}^i\right) \cdot \beta_t(s)}{\displaystyle\sum_{i\in\mathcal{B}_{-1}^n} \sum_{\{s',s\}\in\mathcal{T}_i} \alpha_{t-1}(s') \cdot \prod_{\substack{k=0 \\ k\neq n}}^{N_c-1} p\left(r_{k,t} \,\middle|\, c_{k,t} = c_{k,t}^i\right) \cdot \prod_{\substack{k=0 \\ k\neq n}}^{q-1} \Pr\left(b_{k,t} = b_{k,t}^i\right) \cdot \beta_t(s)}.
\end{aligned} \tag{C.29}$$

Finally, the log-APP can be expressed as the sum of three log ratios, with

$$L\left(b_{n,t} \,\middle|\, \boldsymbol{R}_1^N\right) = L\left(b_{n,t}\right) + L_A\left(b_{n,t}\right) + L_E, \tag{C.30}$$

where L is the LLR, L_A the *a priori* log ratio, and L_E the extrinsic log ratio generated by the decoding process.

C.2.4 The BCJR Algorithm

The computation of the BCJR algorithm can be summarized in 4 steps

- $\alpha_0(s)$ and $\beta_N(s)$ are initialized according to the condition $S_0 = S_N = 0$.
- When the noisy codewords $\boldsymbol{r}_t$ are received, the transition probabilities $\gamma_t(s',s)$ are computed with (C.8), along with the forward recursion $\alpha_t(s)$ with (C.6). The computation of $\gamma_t(s',s)$ can be computed with Equation (C.23) or Equation (C.27) for the case of systematic binary codewords.
- Once the whole sequence $\boldsymbol{R}_1^N$ has been received, all the values of α and γ are known, and the backward recursion computes the values of β using (C.7).
- Once the values of α, β and γ are computed, the log-APP of the information bits can finally be computed with (C.12).

C.2.5 Example of the $[3\,1]$ Convolutional Code

The $[3\,1]$ Recursive Systematic Convolutional (RSC) code was presented Figure 1.10. The trellis has 4 transitions, and each transition has a different codeword. There are $M = 4$ codewords of length $N_c = 2$ with $\boldsymbol{c}^i = \left[x^i, y^i\right]$, where x is the systematic bit and y the parity bit. There is only one systematic bit ($q = 1$) in each codeword. The received codeword at time t is $\boldsymbol{r}_t = [x_t, y_t]$.

C.2.5.1 Computation of γ

The value of γ is given by Equation (C.27) for the case of a binary systematic code. As the 4 codewords are associated to the 4 transitions, the usual expression $\gamma_t(s', s)$ can be simplified to $\gamma_t(\boldsymbol{c}^i)$. For this code, γ is computed as

$$\gamma_t(\boldsymbol{c}^i) = C \exp\left\{\frac{1}{2}(L(x_t) + L_A(x_t))x^i + \frac{1}{2}L(y_t)y^i\right\}, \tag{C.31}$$

where x^i, y^i are binary values (equal to ± 1). If no *a priori* information is available, then $L_A(x_t) = 0$.

C.2.5.2 Computation of α and β

Following the recursive definition of α given Equation (C.6), and given the possible trellis transitions, the value of α at time index t is

$$\begin{aligned}\alpha_t(0) &= \alpha_{t-1}(0) \cdot \gamma_t([00]) + \alpha_{t-1}(1) \cdot \gamma_t([10])\\ \alpha_t(1) &= \alpha_{t-1}(0) \cdot \gamma_t([11]) + \alpha_{t-1}(1) \cdot \gamma_t([01])\end{aligned}$$

Likewise, the computation of β, given Equation (C.7), is given by

$$\begin{aligned}\beta_t(0) &= \beta_{t+1}(0) \cdot \gamma_t([00]) + \beta_{t+1}(1) \cdot \gamma_t([11])\\ \beta_t(1) &= \beta_{t+1}(0) \cdot \gamma_t([11]) + \beta_{t+1}(1) \cdot \gamma_t([01])\end{aligned}$$

Bibliography of Appendix C

[8] C. Berrou, A Glavieux, and P. Thitimajshima. "Near Shannon Limit Error-Correcting Coding and Decoding: Turbo-Codes". In: *IEEE International Conference on Communications (ICC). Geneva.* Vol. 2. 1993, pp. 1064–1070.

[31] L. Bahl, J. Cocke, F. Jelinek, and J. Raviv. "Optimal Decoding of Linear Codes for Minimizing Symbol Error Rate (Corresp.)" In: *IEEE Transactions on Information Theory* 20.2 (1974), pp. 284–287.

APPENDIX D

Extrinsic Information Transfer Chart

The EXtrinsic Information Transfer (EXIT) chart was invented by Stefan ten Brink [33] to track the exchange of information inside a turbo receiver, and to predict the behavior of the constituent decoders [36]. In this appendix, the method and principle of the EXIT chart is reviewed. The [13 15] TC is used as an example for the interpretation of the EXIT chart tool and the extension for the multi-dimensional TC is presented.

D.1 Metric and Model

The EXIT analysis is performed by simulating the response of the decoder to an *a priori* input, while considering a noisy observation of the encoded bits. The inputs and output log ratios of the decoder are represented in Figure D.1. The LLRs are obtained using the AWGN channel model with a certain noise level. A specific model is considered for the *a priori* input. The value of the parameter of the model simulates a strong *a priori* knowledge or, on the contrary, a poor *a priori* knowledge. In order to quantify the dependency between the *a priori* information fed to the decoder and the actual information, [33] suggested the use of the Mutual Information (MI).

In this section, the definition and expression of the MI is reviewed, and the model for the *a priori* information proposed in [33] is detailed, along with the expression of the extrinsic information.

D.1.1 The Mutual Information

The MI is a measure of the statistical dependency between two random variables. It can be defined using the Kullbach-Leiber divergence [104]

$$I(X, Y) = \int_x \int_y p(x, y) \log_2 \frac{p(x, y)}{p(x)\, p(y)} dx\, dy, \tag{D.1}$$

where $p(x)$ (resp. $p(y)$) is the probability of the event $X = x$ (resp. $Y = y$) and $p(x, y)$ the joint probability of the events. In the case where the two events are independent, we have $p(x, y) = p(x)\, p(y)$ and the MI is equal to 0. Otherwise, the MI is superior to 0.

With $p(x, y) = p(y \mid x)\, p(x)$, the MI is expressed

$$I(X, Y) = \int_x \int_{-\infty}^{+\infty} p(y \mid x)\, p(x) \log_2 \frac{p(y \mid x)}{p(y)} dx\, dy. \tag{D.2}$$

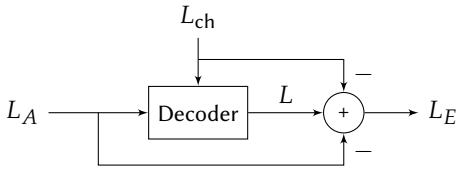

Figure D.1 – *Inputs and output* log*-ratios of a decoder in a turbo receiver.*

Further considering the random variable X as the information source, whose values are binary ($X \in \{-1, +1\}$) and equally probable, the probability of Y can be obtained by marginalizing the joint probability over the possible values of X. This gives

$$\begin{aligned} p(y) &= \int p(x, y)\, dx \\ &= \sum_{u \in \{-1, +1\}} p(y \mid x = u) \Pr(x = u) \\ &= \frac{1}{2} \left(p(y \mid x = -1) + p(y \mid x = +1) \right), \end{aligned} \tag{D.3}$$

as the binary values of X are equally probable.

Considering the range of the observation y to be from $-\infty$ to $+\infty$, Equation (D.1) can now be expressed in the form given in Equation (2.35)

$$I(X, Y) = \frac{1}{2} \sum_{u \in \{-1, +1\}} \int_y p(y \mid x = u) \log_2 \frac{2p(y \mid x = u)}{p(y \mid x = -1) + p(y \mid x = +1)} dy \tag{D.4}$$

D.1.2 *A priori* Model

In order to model the *a priori* information fed to the decoder, [33] suggested the AWGN model, based on the observation of the distribution of the *a priori* log-ratios in a turbo receiver. To develop the model, we define the variable a as

$$a = x + n, \tag{D.5}$$

where x is the information (with $x = \pm 1$) and $n \sim \mathcal{N}(0, \sigma^2)$. Using the definition of the normal distribution, the log ratio is given by

$$\begin{aligned} L_A(x) &= \frac{p(a \mid x = +1)}{p(a \mid x = -1)} \\ &= \frac{2}{\sigma^2} a \\ &= \mu_A x + n_A, \end{aligned} \tag{D.6}$$

with

$$\mu_A = \frac{2}{\sigma^2}, \tag{D.7}$$

and

$$n_A = \frac{2}{\sigma^2} n. \tag{D.8}$$

Similarly, the log ratio L_A can be said to follow a normal distribution $\mathcal{N}(\mu_A, \sigma_A)$, where

$$\sigma_A^2 = \mathrm{Var}(n_A) = \mathrm{Var}\left(\frac{2}{\sigma^2} n \right) = \frac{4}{\sigma^4} \cdot \sigma^2 = \frac{4}{\sigma^2}. \tag{D.9}$$

Using the definition of μ_A and σ_A, this gives

$$\mu_A = \frac{\sigma_A^2}{2} \tag{D.10}$$

D.1.3 Expression of the *a priori* Mutual Information

While the standard definition of the MI requires an estimation of PDFs and the computation of several integrals, its computation can be simplified using the model selected for the *a priori* log ratios. The derivation of the simplified expression of the *a priori* MI is presented here.

Denoting $y = L_A(x)$, the distribution of the *a priori* log ratio is given by

$$p_A(y \mid x) = \frac{1}{\sqrt{2\pi}\sigma_A} \exp\left\{ -\frac{\left(y - \frac{\sigma_A^2}{2} x \right)^2}{2\sigma_A^2} \right\} \tag{D.11}$$

The computation of the *a priori* MI can be expressed

$$I_A = \frac{1}{2} \sum_{u \in \{-1,+1\}} \int_{-\infty}^{+\infty} p_A(y \mid x = u) \log_2 \left(2 f(y,u)\right) dy \tag{D.12}$$

with

$$\begin{aligned} f(y,u) &= \frac{p_A(y \mid x = u)}{p_A(y \mid x = -1) + p_A(y \mid x = +1)} \\ &= \frac{p_A(y \mid x = u)}{p_A(y \mid x = +1)} \cdot \frac{1}{1 + \frac{p_A(y \mid x = -1)}{p_A(y \mid x = +1)}}. \end{aligned} \tag{D.13}$$

Using (D.11), it is easily shown that

$$\frac{p_A(y \mid x = -1)}{p_A(y \mid x = +1)} = e^{-y}, \tag{D.14}$$

which is often referred to as the consistency property of the normal distribution [105]. Likewise, the first term can be expressed

$$\begin{aligned} \frac{p_A(y \mid x = u)}{p_A(y \mid x = +1)} &= \frac{\exp\left\{-\frac{1}{2\sigma_A^2}\left(y^2 - \sigma_A^2 uy + \frac{\sigma_A^4}{4}u^2\right)\right\}}{\exp\left\{-\frac{1}{2\sigma_A^2}\left(y^2 - \sigma_A^2 y + \frac{\sigma_A^4}{4}\right)\right\}} \\ &= \exp\left\{\frac{1}{2}yu - \frac{1}{2}y - \frac{\sigma_A^2}{8}u^2 + \frac{\sigma_A^2}{8}\right\} && \text{(D.15)} \\ &= \exp\left\{\frac{1}{2}y(u-1)\right\}, && \text{(D.16)} \end{aligned}$$

where the developement from (D.15) to (D.16) comes from the fact that $u^2 = 1$ since $u = \pm 1$. Equation (D.13) can be expressed

$$f(y,u) = \exp\left\{\frac{1}{2}y(u-1)\right\} \cdot \frac{1}{1+e^{-y}}, \tag{D.17}$$

and the MI is expressed

$$I_A = \underbrace{\frac{1}{2}\int_{-\infty}^{+\infty} p_A(y \mid x = +1) \log_2\left(\frac{2}{1+e^{-y}}\right) dy}_{=I_1} + \underbrace{\frac{1}{2}\int_{-\infty}^{+\infty} p_A(y \mid x = -1) \log_2\left(\frac{2}{1+e^{y}}\right) dy}_{=I_2}. \tag{D.18}$$

The symmetry of the normal distribution gives $p_A(y \mid x = -1) = p_A(-y \mid x = +1)$, and the second integral I_2 is equal to

$$I_2 = \frac{1}{2}\int_{-\infty}^{+\infty} p_A(-y \mid x = +1) \log_2\left(\frac{2}{1+e^{y}}\right) dy. \tag{D.19}$$

By doing the variable change $z = -y$, the integral becomes

$$\begin{aligned} I_2 &= \frac{1}{2}\int_{+\infty}^{-\infty} p_A(z \mid x = +1) \log_2\left(\frac{2}{1+e^{-z}}\right)(-dz) && \text{(D.20)} \\ &= \frac{1}{2}\int_{-\infty}^{+\infty} p_A(z \mid x = +1) \log_2\left(\frac{2}{1+e^{-z}}\right) dz, && \text{(D.21)} \end{aligned}$$

which gives $I_1 = I_2$, and the MI expression becomes

$$\begin{aligned} I_A &= \int_{-\infty}^{+\infty} p_A(z \mid x = +1) \log_2\left(\frac{2}{1+e^{-z}}\right) dz && \text{(D.22)} \\ &= \int_{-\infty}^{+\infty} p_A(z \mid x = +1)\left(1 - \log_2\left(1+e^{-z}\right)\right) dz && \text{(D.23)} \\ &= 1 - \int_{-\infty}^{+\infty} p_A(z \mid x = +1) \log_2\left(1+e^{-z}\right) dz, && \text{(D.24)} \end{aligned}$$

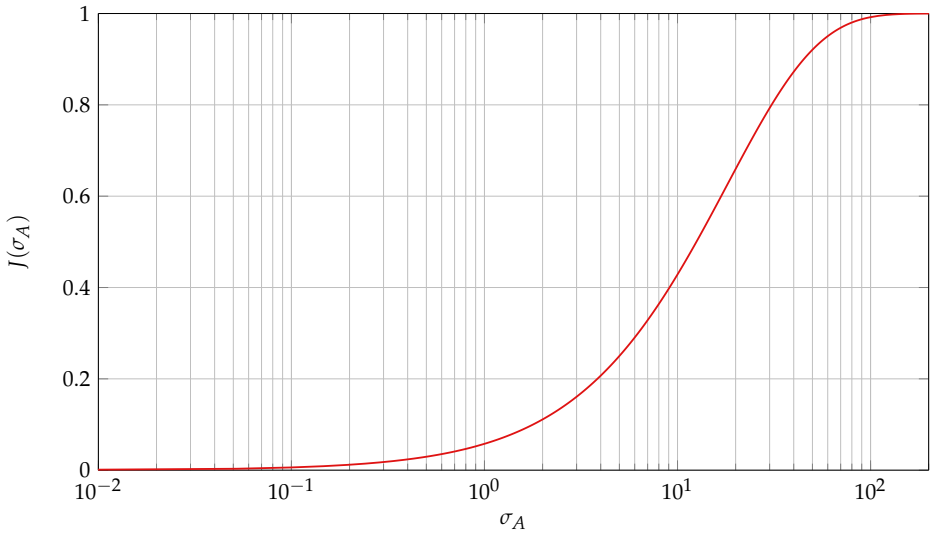

FIGURE D.2 – *The J function.*

as the PDF's integral on the range of z is equal to 1. Including (D.11), the MI is computed with

$$I_A = I_A(\sigma_A) = 1 - \int_{-\infty}^{+\infty} \frac{1}{\sqrt{2\pi}\sigma_A} \exp\left\{-\frac{1}{2\sigma_A^2}\left(z - \frac{\sigma_A^2}{2}\right)^2\right\} \log_2\left(1 + e^{-z}\right) dz, \tag{D.25}$$

which depends only on the parameter σ_A. The function J is usually defined with

$$J(\sigma) = I_A(\sigma_A = \sigma), \tag{D.26}$$

and represented in Figure D.2 for various values of σ_A.

D.1.4 Extrinsic Information

When considering a turbo receiver such as described in Section 1.3.4.5, the two decoders exchanges extrinsic information. The extrinsic information of the first decoder is used by the second decoder as *a priori* input, and then its extrinsic information is sent back to the first decoder to be used as *a priori*, and so on all along the iterations. While the BCJR algorithm computes the log-APP of the information bits L, as defined by Equation (1.71), the extrinsic information L_E is obtained with

$$L_E = L - (L_A + L_{\text{ch}}). \tag{D.27}$$

In order to compute the dependency of the extrinsic information generated by the decoder and the information source, the MI is also used. Its value is computed using Equation (D.4), which requires the evaluation of the different PDFs and their integration.

D.2 The EXIT Chart

Using the MI metric and the model described previously, the computation method of the EXIT chart and its interpretation are presented. As the EXIT Chart computation does not depend on the interleaving function, this implies statistical independence between the two stages of the decoder. Additionally, the computations need to be done using very large block sizes Q, in order to ensure a sufficient statistic for the PDF estimations.

D.2.1 Computation

The computation of the EXIT is presented in Figure D.3. The top part consists of a selected value of σ_A, with the application of the J function of Equation (D.26) to compute the *a priori* MI and uses σ_A to generate the *a priori* log ratios. The bottom part consists of the simulation of the transition through the channel. The AWGN channel is selected and after encoding of the information bits, the LLRs from the channel are computed. The simulated *a priori* log ratios are then added to the systematic bits, and the BCJR algorithm is applied to compute the log-APP of

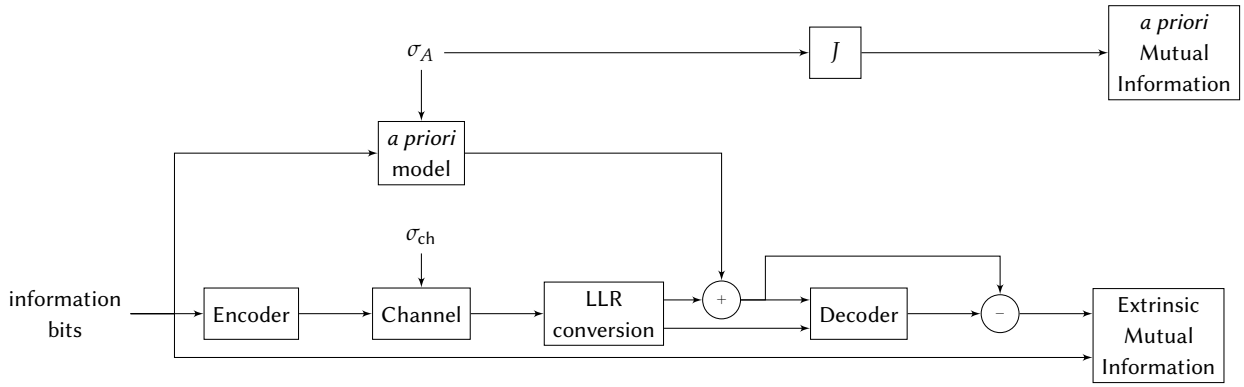

FIGURE D.3 – *Computation of the EXIT chart.*

the information bits. The extrinsic log ratios are obtained using Equation (D.27), and the extrinsic MI is computed using Equation (D.4), which requires the knowledge of the information bits to estimate the conditional PDFs.

Both the *a priori* and the extrinsic MIs are estimated for various values of σ_A for a given σ_{ch}. Usually, the values of σ_A are chosen for the *a priori* MI I_A range from 0 to 1.

D.2.2 INTERPRETATION

In order to illustrate the interpretation of the EXIT chart tool, the RSC with generators [13 15] is chosen. Its encoder and trellis are represented on the Figure 1.11. This code has a rate $R = 1/3$, and in the turbo receiver (depicted Figure 1.12 (b)), the extrinsic of one decoder is used by the other decoder as *a priori*, and vice versa.

In Figure D.4, the EXIT chart of the considered code is represented for various values of the channel parameter E_b/N_0. The *a priori* MI I_A spans from 0 (no *a priori* information) to 1 (complete knowledge of the information bits). The extrinsic MI I_E evolves differently with I_A depending on the value of E_b/N_0, and accurately reaches the coordinate $(1, 1)$ (i.e. with a perfect *a priori* knowledge, the correct information word is decoded). However, this curve only represents one of the two constituents of the turbo receiver. The other decoder, in the case where both constituent codes are the same, will have the same EXIT curve. [33] shows that in this case, the EXIT should be compared to the diagonal line going from $(0, 0)$ towards $(1, 1)$. If there is an intersection, the receiver will not be able to decode the correct information word, whatever the number of iterations. From the results depicted in Figure D.4, where the diagonal line is in dashed red, we can conclude that the receiver cannot decode correctly the information word for E_b/N_0 values of -1 and -0.1dB, but can for values above that.

In order to illustrate and clarify this, the EXIT chart of the two constituant decoders are represented in Figure D.5 for $E_b/N_0 = 1$dB, but the second one is turned over. Its *a priori* MI is on the y axis and its extrinsic MI is on

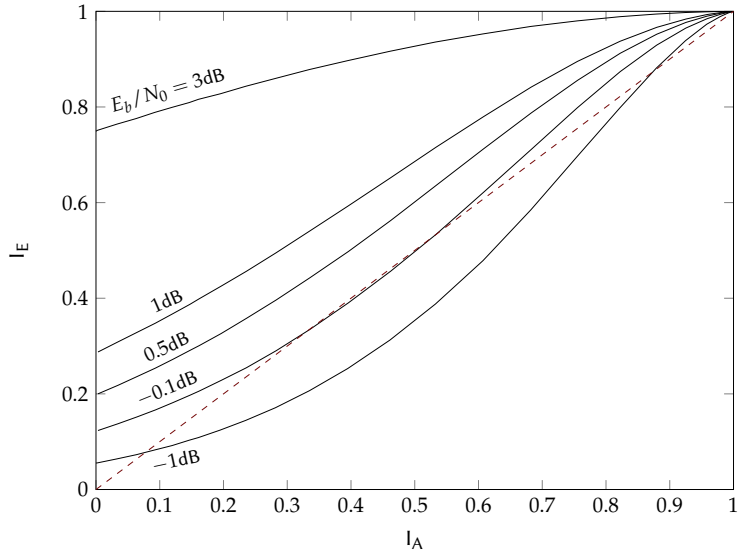

FIGURE D.4 – *EXIT charts of the* [13 15] *code for multiple values of* E_b/N_0 *and the diagonal line. The information block size is set to* $Q = 100\,000$.

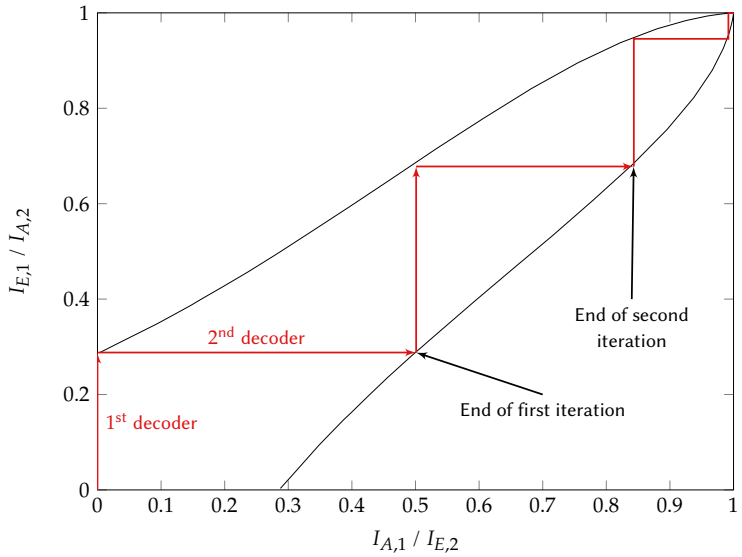

FIGURE D.5 – *One trajectory of the exchanges of information inside the receiver of the* [13 15] *TC, for* $E_b/N_0 = 1dB$. *The information block size is set to* $Q = 100\,000$.

the x axis. This way, the exchanges of extrinsic information during the decoding process, or the "trajectory" can be directly visualized:

- The system starts at the point $(0,\ 0)$. The first decoder $I_{A,1}$ is 0, and outputs the value $I_{E,1} \simeq 0.3$.
- The second decoder has for input $I_{A,2} = I_{E,1} \simeq 0.3$, and reading the reversed curve, its output is $I_{E,2} \simeq 0.5$. As the two decoders performed one estimation, this is the end of the first iteration.
- The same process is repeated to read the value of $I_{E,2}$ at the end of the second iteration.
- After roughly 4 iterations, the coordinates $(1,\ 1)$ are reached: the correct word will be decoded.

The trajectory was not drawn on the plot, but actually computed, showing that the EXIT chart predicted accurately the behavior of the system. Due to the symmetry of the system, the comparison to the diagonal line is sufficient, as previously mentioned.

In Figure D.6, the trajectories of the receiver for the values of E_b/N_0 of 0dB (a) and -1dB (b) are represented. For (a), the receiver converges toward the coordinates $(1,\ 1)$, but after significantly more iterations ($\simeq 9$) than in the case $E_b/N_0 = 1$dB presented in Figure D.5. On the opposite, the receiver for $E_b/N_0 = -1$dB converges towards the coordinates $(0.08,\ 0.08)$, showing that the correct information word cannot be retrieved for the value of E_b/N_0.

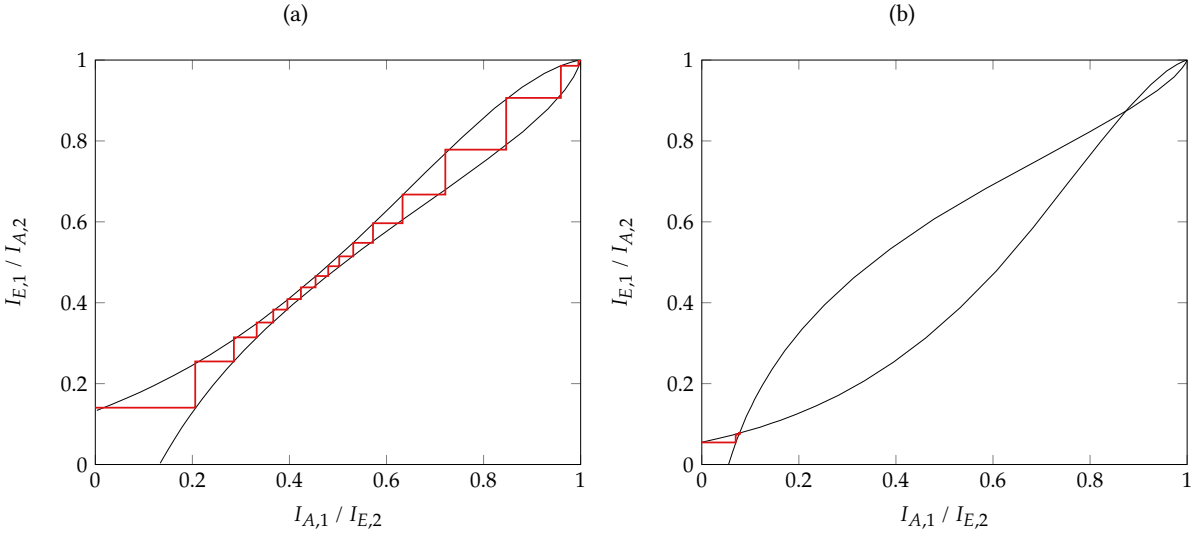

FIGURE D.6 – *One trajectory of the exchanges of information inside the receiver of the* [13 15] *TC, for (a)* $E_b/N_0 = 0dB$, *(b)* $E_b/N_0 = -1dB$. *The information block size is set to* $Q = 100\,000$.

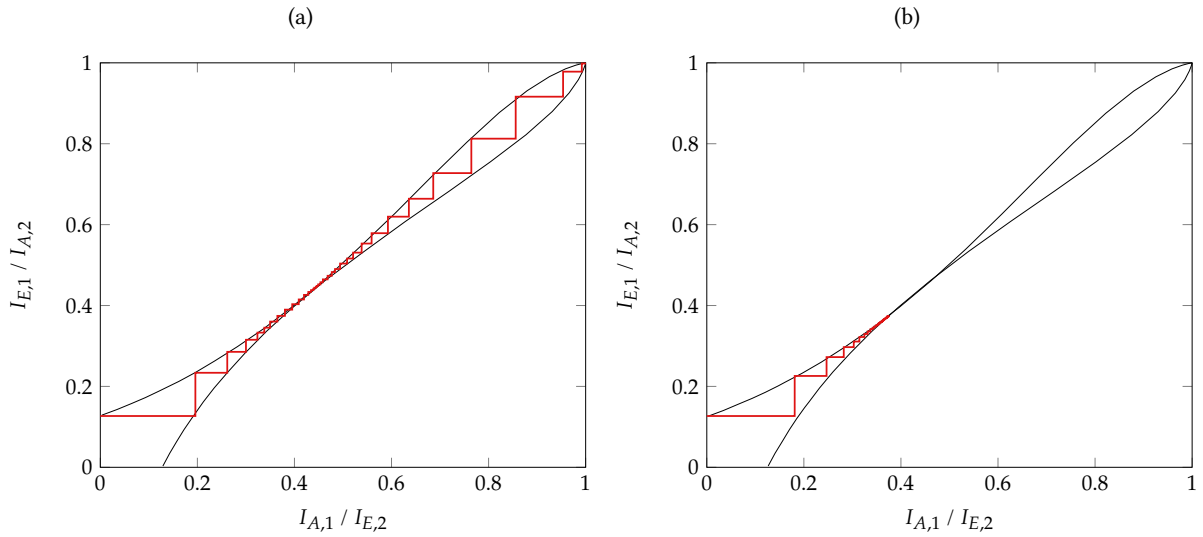

FIGURE D.7 – *One trajectory of the exchanges of information inside the receiver of the* [13 15] *TC, for (a)* $E_b/N_0 = -0.05$*dB, (b)* $E_b/N_0 = -0.07$*dB. The information block size is set to* $Q = 100\,000$.

Since the EXIT chart accurately predicts the behavior of the turbo receiver, it can also be used to estimate the threshold of the decoder (also called the turbo-cliff), i.e. the E_b/N_0 value from which the decoder can retrieve the information word correctly after an arbitrary number of iterations. From the results previously presented, this is the value of E_b/N_0 for which the EXIT curve does not intersect the diagonal line. In Figure D.7, the EXIT charts and one trajectory of the receiver for the values of E_b/N_0 of -0.05 and -0.07dB are represented. Since there is no intersection for the case $E_b/N_0 = -0.05$dB (the trajectory reaches $(1, 1)$) and intersection for the case $E_b/N_0 = 0.07$dB (the trajectory stops around $(0.35, 0.35)$), we can conclude that the threshold is between the two values of E_b/N_0.

It is important to note that the estimation of the threshold is done for very large values of information block size Q, and does not indicate the number of iterations required for the receiver to converge toward the maximum of MI. This is an asymptotic performance, i.e. a lower bound on the performance of the code.

D.3 Multi-dimensional EXIT Chart

While the initial TC [8] consists of two codes concatenated in parallel, the use of more than two constituent codes has been suggested [79]. Following this idea, Stefan ten Brink proposed an extension of the EXIT chart analysis to multi-dimensional coding schemes [80]. In this type of receiver, the *a priori* information fed to one decoder consists of the sum of the extrinsic of the other decoders.

In the general case with λ parallel concatenated codes, the representation of the exchanges of information needs to be done with λ dimensions. This becomes inconvenient when $\lambda > 3$. However, in the specific case where all the codes are the same, the process can be simplified by computing a two dimensional projection. This projection is obtained by computing the EXIT chart of one decoder while considering that the *a priori* input consists in the sum of the extrinsic of the other decoders. This implies a correction in the computation of the *a priori* MI.

In order to express the correction, the more convenient case of $\lambda = 3$ is considered first. In this case, the *a priori* of the first decoder L_{A_1} (after at least one iteration) is given by

$$L_{A_1} = L_{E_2} + L_{E_3} \tag{D.28}$$

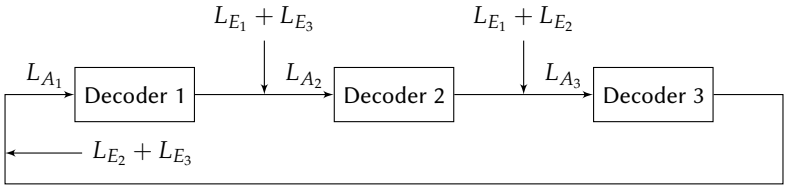

FIGURE D.8 – *Illustration of the exchange of information between the three decoders.*

where L_{E_2} (resp. L_{E_3}) is the extrinsic log ratio of the second (resp. the third) decoder. The exchange of information in the three dimensions receiver is depicted on the Figure D.8.

Assuming a Gaussian distribution for the log ratios and the independence of the extrinsic observations [80],

$$\sigma_{A_1}^2 = \sigma_{E_2}^2 + \sigma_{E_3}^2. \tag{D.29}$$

Using $I = J(\sigma)$, and inversely $\sigma = J^{-1}(I)$, the *a priori* MI is given by

$$\begin{aligned} I_{A_1} = J(\sigma_{A_1}) &= J\left(\sqrt{\sigma_{E_2}^2 + \sigma_{E_3}^2}\right) \\ &= J\left(\sqrt{\left(J^{-1}(I_{E_2})\right)^2 + \left(J^{-1}(I_{E_3})\right)^2}\right). \end{aligned} \tag{D.30}$$

By setting $I_{E_2} = I_{E_3}$, then

$$I_{A_1} = J\left(\sqrt{2} \cdot J^{-1}(I_{E_2})\right). \tag{D.31}$$

With the same *a priori* model with variance σ_A^2 described in Section D.1.2, the *a priori* MI is thus given by

$$I_{A_1} = J\left(\sqrt{2} \cdot \sigma_A\right), \tag{D.32}$$

which can be generalized to λ decoders as

$$I_A = J\left(\sqrt{\lambda - 1} \cdot \sigma_A\right). \tag{D.33}$$

In order to obtain the two dimensions' projection, the *a priori* MI is computed with Equation (D.33), and for various values of σ_A, the extrinsic MI is computed. When the transition in the channel is modeled, the overall rate of the code is considered.

Bibliography of Appendix D

[8] C. Berrou, A Glavieux, and P. Thitimajshima. "Near Shannon Limit Error-Correcting Coding and Decoding: Turbo-Codes". In: *IEEE International Conference on Communications (ICC). Geneva.* Vol. 2. 1993, pp. 1064–1070.

[33] S. ten Brink. "Convergence Behavior of Iteratively Decoded Parallel Concatenated Codes". In: *IEEE Transactions on Communications* 49.10 (2001), pp. 1727–1737.

[36] M. El-Hajjar and L. Hanzo. "EXIT Charts for System Design and Analysis". In: *IEEE Communications Surveys Tutorials* 16.1 (2014), pp. 127–153.

[79] C. Berrou, M. Jezequel, and C. Douillard. "Multidimensional Turbo Codes". In: *1999 Information Theory and Networking Workshop (Cat. No.99EX371).* 1999, pp. 27–.

[80] S. ten Brink. "Convergence of Multidimensional Iterative Decoding Schemes". In: *Conference Record of the Thirty-Fifth Asilomar Conference on Signals, Systems and Computers.* Vol. 1. 2001, 270–274 vol.1.

[104] S. Kullback and R. A. Leibler. "On Information and Sufficiency". In: *Ann. Math. Statist.* 22.1 (Mar. 1951), pp. 79–86.

[105] F. Alberge. "On Some Properties of the Mutual Information Between Extrinsics With Application to Iterative Decoding". In: *IEEE Transactions on Communications* 63.5 (2015), pp. 1541–1553.

Bibliography

[1] *4G LTE World Coverage Map*. http://www.worldtimezone.com/4g.html. Accessed: July 26, 2017.

[2] *5G White Paper*. NGMN 5G Initiative. 2015.

[3] M. R. Palattella et al. "Internet of Things in the 5G Era: Enablers, Architecture, and Business Models". In: *IEEE Journal on Selected Areas in Communications* 34.3 (2016), pp. 510–527.

[4] T. Rebbeck, M. Mackenzie, and N. Afonso. *Low-Powered Wireless Solutions Have the Potential to Increase the M2M Market by Over 3 Billion Connections*. Analysys Mason. 2014.

[5] D. Evans. *The Internet of Things - How the Next Evolution of the Internet is Changing Everything*. Cisco White Paper. 2011.

[6] U. Raza, P. Kulkarni, and M. Sooriyabandara. "Low Power Wide Area Networks: an Overview". In: *IEEE Communications Surveys Tutorials* PP.99 (2017), pp. 1–1.

[7] C. Shannon. "A Mathematical Theory of Communication". In: *The Bell System Technical Journal* 27.3 (1948), pp. 379–423.

[8] C. Berrou, A Glavieux, and P. Thitimajshima. "Near Shannon Limit Error-Correcting Coding and Decoding: Turbo-Codes". In: *IEEE International Conference on Communications (ICC). Geneva.* Vol. 2. 1993, pp. 1064–1070.

[9] R. G. Gallager. "Low-Density Parity-Check Codes". PhD thesis. 1963.

[10] E. Arikan. "Channel Polarization: A Method for Constructing Capacity-Achieving Codes for Symmetric Binary-Input Memoryless Channels". In: *IEEE Transactions on Information Theory* 55.7 (2009), pp. 3051–3073.

[11] Machina Research. *LPWA Technologies - Unlock New IoT Market Potential*. A White Paper prepared for the LoRa Alliance. 2014.

[12] H. T. Friis. "A Note on a Simple Transmission Formula". In: *Proceedings of the IRE* 34.5 (1946), pp. 254–256.

[13] M. Loy. *Understanding and Enhancing Sensitivity in Receivers for Wireless Applications*. Texas Instrument, Wireless Communication Business Unit, Technical Brief SWRA030. 1999.

[14] H. Kwon and T. Birdsall. "Channel Capacity in Bits per Joule". In: *IEEE Journal of Oceanic Engineering* 11.1 (1986), pp. 97–99.

[15] J. Proakis. *Digital Communications 3rd Edition*. Communications and signal processing. McGraw-Hill, 1995.

[16] F. H. Raab et al. "Power Amplifiers and Transmitters for RF and Microwave". In: *IEEE Transactions on Microwave Theory and Techniques* 50.3 (2002), pp. 814–826.

[17] S. C. Thompson. "Constant Envelope OFDM Phase Modulation". PhD thesis. University of California, San Diego, 2005.

[18] S. Cui, A. J. Goldsmith, and A. Bahai. "Energy-Constrained Modulation Optimization". In: *IEEE Transactions on Wireless Communications* 4.5 (2005), pp. 2349–2360.

[19] P. Bento et al. "Measuring the Magnitude of Envelope Fluctuations: Should We Use the PAPR?" In: *2014 IEEE 80th Vehicular Technology Conference (VTC2014-Fall)*. 2014, pp. 1–5.

[20] S. Benedetto and E. Biglieri. *Principles of Digital Transmission: With Wireless Applications*. Norwell, MA, USA: Kluwer Academic Publishers, 1999.

[21] J. Hagenauer, E. Offer, and L. Papke. "Iterative Decoding of Binary Block and Convolutional Codes". In: *IEEE Transactions on Information Theory* 42.2 (1996), pp. 429–445.

[22] K. Cho and D. Yoon. "On the General BER Expression of one- and two-Dimensional Amplitude Modulations". In: *IEEE Transactions on Communications* 50.7 (2002), pp. 1074–1080.

[23] J. Costello D.J. and J. Forney G.D. “Channel Coding: The Road to Channel Capacity”. In: *Proceedings of the IEEE* 95.6 (2007), pp. 1150–1177.

[24] R. W. Hamming. “Error Detecting and Error Correcting Codes”. In: *The Bell System Technical Journal* 29.2 (1950), pp. 147–160.

[25] P. Elias. “Coding for Noisy Channels”. In: *IRE Convention Record* 3.2 (1955), pp. 37–46.

[26] H. Ma and J. Wolf. “On Tail Biting Convolutional Codes”. In: *IEEE Transactions on Communications* 34.2 (1986), pp. 104–111.

[27] A. Viterbi. “Error Bounds for Convolutional Codes and an Asymptotically Optimum Decoding Algorithm”. In: *IEEE Transactions on Information Theory* 13.2 (1967), pp. 260–269.

[28] A. Viterbi. “Convolutional Codes and Their Performance in Communication Systems”. In: *IEEE Transactions on Communication Technology* 19.5 (1971), pp. 751–772.

[29] J. Heller and I. Jacobs. “Viterbi Decoding for Satellite and Space Communication”. In: *IEEE Transactions on Communication Technology* 19.5 (1971), pp. 835–848.

[30] J. Hagenauer and P. Hoeher. “A Viterbi Algorithm with Soft-Decision Outputs and its Applications”. In: *Global Telecommunications Conference and Exhibition ’Communications Technology for the 1990s and Beyond’ (GLOBECOM), 1989. IEEE.* 1989, 1680–1686 vol.3.

[31] L. Bahl, J. Cocke, F. Jelinek, and J. Raviv. “Optimal Decoding of Linear Codes for Minimizing Symbol Error Rate (Corresp.)” In: *IEEE Transactions on Information Theory* 20.2 (1974), pp. 284–287.

[32] G. D. Forney. *Concatenated Codes.* Cambridge, 1966.

[33] S. ten Brink. “Convergence Behavior of Iteratively Decoded Parallel Concatenated Codes”. In: *IEEE Transactions on Communications* 49.10 (2001), pp. 1727–1737.

[34] S. Benedetto and G. Montorsi. “Average Performance of Parallel Concatenated Block Codes”. In: *Electronics Letters* 31.3 (1995), pp. 156–158.

[35] L. C. Perez, J. Seghers, and D. J. Costello. “A Distance Spectrum Interpretation of Turbo Codes”. In: *IEEE Transactions on Information Theory* 42.6 (1996), pp. 1698–1709.

[36] M. El-Hajjar and L. Hanzo. “EXIT Charts for System Design and Analysis”. In: *IEEE Communications Surveys Tutorials* 16.1 (2014), pp. 127–153.

[37] J. Hagenauer and L. Papke. “Decoding "Turbo"-Codes with the Soft Output Viterbi Algorithm (SOVA)”. In: *Proceedings of 1994 IEEE International Symposium on Information Theory.* 1994, pp. 164–.

[38] M. P. C. Fossorier, F. Burkert, S. Lin, and J. Hagenauer. “On the Equivalence Between SOVA and max-log-MAP Decodings”. In: *IEEE Communications Letters* 2.5 (1998), pp. 137–139.

[39] P. Robertson, P. Hoeher, and E. Villebrun. “Optimal and Sub-Optimal Maximum a Posteriori Algorithms Suitable for Turbo Decoding”. In: *European Transactions on Telecommunications* 8.2 (1997), pp. 119–125.

[40] J. Vogt and A. Finger. “Improving the max-log-MAP Turbo Decoder”. In: *Electronics Letters* 36.23 (2000), pp. 1937–1939.

[41] P. Frenger, P. Orten, and T. Ottosson. “Convolutional Codes with Optimum Distance Spectrum”. In: *IEEE Communications Letters* 3.11 (1999), pp. 317–319.

[42] S.-Y. Chung, G. D. Forney, T. J. Richardson, and R. Urbanke. “On the Design of Low-Density Parity-Check Codes Within 0.0045 dB of the Shannon Limit”. In: *IEEE Communications Letters* 5.2 (2001), pp. 58–60.

[43] L. Liu and C. Zhang. “Circuits and Systems for 5G Network: Massive MIMO and Advanced Coding”. In: *2015 IEEE 11th International Conference on ASIC (ASICON).* 2015, pp. 1–4.

[44] *Low Throughput Networks (LTN): Protocol and Interfaces.* ETSI Group Specification GS LTN 003, V 1.1.1. 2014.

[45] A. Augustin, J. Yi, T. Clausen, and W. M. Townsley. “A Study of LoRa: Long Range & Low Power Networks for the Internet of Things”. In: *Sensors* 16.9 (2016), p. 1466. URL: http://www.mdpi.com/1424-8220/16/9/1466.

[46] *SigFox website.* http://www.sigfox.com/. Accessed: July 26, 2017.

[47] *LoRa Alliance.* https://www.lora-alliance.org/. Accessed: July 26, 2017.

[48] O. Seller and N. Sornin. “Low Power Long Range Transmitter”. Patent US 20140219329 A1. 2014.

[49] A. Springer et al. “Spread Spectrum Communications Using Chirp Signals”. In: *IEEE/AFCEA EUROCOMM 2000. Information Systems for Enhanced Public Safety and Security (Cat. No.00EX405).* 2000, pp. 166–170.

[50] D. Chu. "Polyphase Codes with Good Periodic Correlation Properties (Corresp.)" In: *IEEE Transactions on Information Theory* 18.4 (1972), pp. 531–532.

[51] *LoRa Modulation Theory*. Semtech Technical Brief. 2014.

[52] *802.15.4k: Low-Rate Wireless Personal Area Networks (LR-WPANs) Amendment 5: Physical Layer Specifications for Low Energy, Critical Infrastructure Monitoring Networks*. IEEE Standard for Local and metropolitan area networks. 2013.

[53] X. Xiong et al. "Low Power Wide Area Machine-to-Machine Networks: Key Techniques and Prototype". In: *IEEE Communications Magazine* 53.9 (2015), pp. 64–71.

[54] *How RPMA Works*. A White Paper by Ingenu. Retrieved from the Ingenu website.

[55] T. Myers. "Random Phase Multiple Access System With Meshing". Patent US 7,773,664 B2. 2010.

[56] *LTE Evolved Universal Terrestrial Radio Access (E-UTRA): Physical Channels and Modulation*. 3GPP TS 36.211, V13.2.0, Release 13. 2016.

[57] *Whitepaper Narrowband Internet of Things*. Rohde & Schwarz. 2016.

[58] *LTE Evolved Universal Terrestrial Radio Access (E-UTRA): Multiplexing and Channel Coding*. 3GPP TS 36.212, V12.6.0, Release 12. 2015.

[59] R. Ratasuk, B. Vejlgaard, N. Mangalvedhe, and A. Ghosh. "NB-IoT System for M2M Communication". In: *2016 IEEE Wireless Communications and Networking Conference*. 2016, pp. 1–5.

[60] Y. P. E. Wang et al. "A Primer on 3GPP Narrowband Internet of Things". In: *IEEE Communications Magazine* 55.3 (2017), pp. 117–123.

[61] H. G. Myung, J. Lim, and D. J. Goodman. "Single Carrier FDMA for Uplink Wireless Transmission". In: *IEEE Vehicular Technology Magazine* 1.3 (2006), pp. 30–38.

[62] *SX1272 from Semtech, datasheet*. http://www.semtech.com/wireless-rf/rf-transceivers/sx1272/. Accessed: July 26, 2017.

[63] K. Kikuchi and M. Osaki. "Highly-Sensitive Coherent Optical Detection of M-ary Frequency-Shift Keying Signal". In: *Optics Express* 19.26 (2011), B32–B39.

[64] L. Ping and S. Chan. "Iterative Decoding of Concatenated Hadamard Codes". In: *IEEE International Conference on Communications (ICC)*. Vol. 1. 1998, 136–140 vol.1.

[65] L. Ping, W. Leung, and K. Y. Wu. "Low-Rate Turbo-Hadamard Codes". In: *IEEE Transactions on Information Theory* 49.12 (2003), pp. 3213–3224.

[66] S. Benedetto and G. Montorsi. "Unveiling Turbo Codes: Some Results on Parallel Concatenated Coding Schemes". In: *IEEE Transactions on Information Theory* 42.2 (1996), pp. 409–428.

[67] Y.-J. Wu and L. Ping. "On the Limiting Performance of Turbo-Hadamard Codes". In: *IEEE Communications Letters* 8.7 (2004), pp. 449–451.

[68] N. Shimanuki, B. M. Kurkoski, K. Yamaguchi, and K. Kobayashi. "Improvements and Extensions of Low-Rate Turbo-Hadamard Codes". In: 2006.

[69] L. Ping, L. Liu, K. Y. Wu, and W. K. Leung. "Approaching the Capacity of Multiple Access Channels Using Interleaved Low-Rate Codes". In: *IEEE Communications Letters* 8.1 (2004), pp. 4–6.

[70] X. Wu, Z. Yang, J. Yan, and J. Cui. "Low-Rate Turbo-Hadamard Coding Approach for Narrow-Band Interference Suppression". In: *2014 IEEE International Conference on Communications (ICC)*. 2014, pp. 2130–2134.

[71] J. W. Cooley, P. A. W. Lewis, and P. D. Welch. "The Fast Fourier Transform and its Applications". In: *IEEE Transactions on Education* 12.1 (1969), pp. 27–34.

[72] G. Caire, G. Taricco, and E. Biglieri. "Bit-Interleaved Coded Modulation". In: *IEEE Transactions on Information Theory* 44.3 (1998), pp. 927–946.

[73] X. Li and J. A. Ritcey. "Bit-Interleaved Coded Modulation with Iterative Decoding". In: *IEEE Communications Letters* 1.6 (1997), pp. 169–171.

[74] S. Cheng and M. C. Valenti. "Bit-Interleaved Turbo-Coded Noncoherent Orthogonal Modulation with Iterative Demodulation and Decoding: Capacity Limits and Convergence Analysis". In: *Conference Record of the Thirty-Eighth Asilomar Conference on Signals, Systems and Computers, 2004*. Vol. 2. 2004, 2020–2024 Vol.2.

[75] M. C. Valenti, E. Hueffmeier, B. Bogusch, and J. Fryer. "Towards the Capacity of Noncoherent Orthogonal Modulation: BICM-ID for Turbo Coded NFSK". In: *IEEE MILCOM 2004. Military Communications Conference, 2004.* Vol. 3. 2004, 1549–1555 Vol. 3.

[76] J. Panaro. "Simple Iterative Decoding for Bit-Interleaved Coded Orthogonal Modulation". In: *Joint IST Workshop on Mobile Future. SympoTIC '06.* 2006, pp. 16–19.

[77] M. Fu. "Stochastic Analysis of Turbo Decoding". In: *IEEE Transactions on Information Theory* 51.1 (2005), pp. 81–100.

[78] H. E. Gamal and A. R. Hammons. "Analyzing the Turbo Decoder Using the Gaussian Approximation". In: *IEEE Transactions on Information Theory* 47.2 (2001), pp. 671–686.

[79] C. Berrou, M. Jezequel, and C. Douillard. "Multidimensional Turbo Codes". In: *1999 Information Theory and Networking Workshop (Cat. No.99EX371).* 1999, pp. 27–.

[80] S. ten Brink. "Convergence of Multidimensional Iterative Decoding Schemes". In: *Conference Record of the Thirty-Fifth Asilomar Conference on Signals, Systems and Computers.* Vol. 1. 2001, 270–274 vol.1.

[81] J. W. Lee and R. E. Blahut. "Convergence Analysis and BER Performance of Finite-Length Turbo Codes". In: *IEEE Transactions on Communications* 55.5 (2007), pp. 1033–1043.

[82] Y. Polyanskiy, H. V. Poor, and S. Verdu. "Channel Coding Rate in the Finite Blocklength Regime". In: *IEEE Transactions on Information Theory* 56.5 (2010), pp. 2307–2359.

[83] Y. Roth, J.-B. Doré, L. Ros, and V. Berg. "Turbo-FSK, a Physical Layer for Low-Power Wide-Area Networks: Analysis and Optimization". In: *Elsevier Comptes Rendus Physique* 18.2 (2017). Energy and radiosciences, pp. 178 –188. URL: //www.sciencedirect.com/science/article/pii/S163107051630158X.

[84] Y. Roth, J.-B. Doré, L. Ros, and V. Berg. "Turbo-FSK: A New Uplink Scheme for Low Power Wide Area Networks". In: *2015 IEEE 16th International Workshop on Signal Processing Advances in Wireless Communications (SPAWC).* Stockholm, Sweden, 2015, pp. 81–85.

[85] Y. Roth, J.-B. Doré, L. Ros, and V. Berg. "A Comparison of Physical Layers for Low Power Wide Area Networks". In: *11th EAI International Conference on Cognitive Radio Oriented Wireless Networks (Crowncom).* Grenoble, France, 2016.

[86] Y. Roth, J.-B. Doré, L. Ros, and V. Berg. "EXIT Chart Optimization of Turbo-FSK: Application to Low Power Wide Area Networks". In: *9th International Symposium on Turbo Codes & Iterative Information Processing 2016 (ISTC'16).* Brest, France, Sept. 2016.

[87] Y. Roth, J.-B. Doré, L. Ros, and V. Berg. "Coplanar Turbo-FSK: A Flexible and Power Efficient Modulation for the Internet-of-Thing". In: *To be submitted* (2017).

[88] Y. Roth, J.-B. Doré, L. Ros, and V. Berg. "Transmission/Reception System Based on the Use of a Joint Orthogonal and Linear Modulation". Patent EUR. 2017.

[89] S. B. Weinstein. "The History of Orthogonal Frequency-Division Multiplexing [History of Communications]". In: *IEEE Communications Magazine* 47.11 (2009), pp. 26–35.

[90] Y. Wu. "Orthogonal Frequency Division Multiplexing: A Multi-Carrier Modulation Scheme". In: *Proceedings of International Conference on Consumer Electronics.* 1995, pp. 8–.

[91] R. van Nee and R. Prasad. *OFDM for Wireless Multimedia Communications.* 1st. Norwood, MA, USA: Artech House, Inc., 2000.

[92] L. Cimini. "Analysis and Simulation of a Digital Mobile Channel Using Orthogonal Frequency Division Multiplexing". In: *IEEE Transactions on Communications* 33.7 (1985), pp. 665–675.

[93] Y. Zhao and S. G. Haggman. "Sensitivity to Doppler Shift and Carrier Frequency Errors in OFDM Systems-the Consequences and Solutions". In: *Proceedings of Vehicular Technology Conference - VTC.* Vol. 3. 1996, 1564–1568 vol.3.

[94] R. van Nee and A. de Wild. "Reducing the Peak-to-Average Power Ratio of OFDM". In: *Vehicular Technology Conference, 1998. VTC 98. 48th IEEE.* Vol. 3. 1998, 2072–2076 vol.3.

[95] Y. Rahmatallah and S. Mohan. "Peak-To-Average Power Ratio Reduction in OFDM Systems: A Survey And Taxonomy". In: *IEEE Communications Surveys Tutorials* 15.4 (2013), pp. 1567–1592.

[96] M. Geles, A. Averbuch, O. Amrani, and D. Ezri. "Performance Bounds for Maximum Likelihood Detection of Single Carrier FDMA". In: *IEEE Transactions on Communications* 60.7 (2012), pp. 1945–1952.

[97] Z. Wang and G. B. Giannakis. "Wireless Multicarrier Communications". In: *IEEE Signal Processing Magazine* 17.3 (2000), pp. 29–48.

[98] *Evolved Universal Terrestrial Radio Access (E-UTRA): Base Station (BS) Radio Transmission and Reception*. 3GPP TS 36.104, V14.3.0, Release 14. 2017.

[99] W. C. Jakes and D. C. Cox, eds. *Microwave Mobile Communications*. Wiley-IEEE Press, 1994.

[100] Y. Roth, J.-B. Doré, L. Ros, and V. Berg. "Contenders for Low Power Wide Area Networks". In: *To be submitted*. 2017.

[101] J. Estavoyer, Y. Roth, J.-B. Doré, and V. Berg. "Implementation and Analysis of a Turbo-FSK Transceiver for a New Low Power Wide Area Physical Layer". In: *2016 International Symposium on Wireless Communication Systems (ISWCS): Special sessions (ISWCS'2016 - Special sessions)*. Poznan, Poland, 2016.

[102] H. J. D. Divsalar and R. J. McEliece. "Coding Theorems for 'Turbo-Like' Codes". In: *Proc. 36th Allerton Conf. on Communication, Control and Computing*. 1998, pp. 201–210.

[103] H. Jin, A. Khandekar, A. Kh, and R. J. McEliece. *Irregular Repeat Accumulate Codes*. 2000.

[104] S. Kullback and R. A. Leibler. "On Information and Sufficiency". In: *Ann. Math. Statist.* 22.1 (Mar. 1951), pp. 79–86.

[105] F. Alberge. "On Some Properties of the Mutual Information Between Extrinsics With Application to Iterative Decoding". In: *IEEE Transactions on Communications* 63.5 (2015), pp. 1541–1553.